INFORMATION TO USERS

This manuscript has been reproduced from the microfilm master. UMI films the text directly from the original or copy submitted. Thus, some thesis and dissertation copies are in typewriter face, while others may be from any type of computer printer.

The quality of this reproduction is dependent upon the quality of the copy submitted. Broken or indistinct print, colored or poor quality illustrations and photographs, print bleedthrough, substandard margins, and improper alignment can adversely affect reproduction.

In the unlikely event that the author did not send UMI a complete manuscript and there are missing pages, these will be noted. Also, if unauthorized copyright material had to be removed, a note will indicate the deletion.

Oversize materials (e.g., maps, drawings, charts) are reproduced by sectioning the original, beginning at the upper left-hand corner and continuing from left to right in equal sections with small overlaps.

ProQuest Information and Learning
300 North Zeeb Road, Ann Arbor, MI 48106-1346 USA
800-521-0600



Downloaded from SHAREOK. Persistent Handle URL: https://hdl.handle.net/11244/542

NOTE TO USERS

This reproduction is the best copy available.

UMI®

THE UNIVERSITY OF OKLAHOMA

GRADUATE COLLEGE

TRANSFORMED INTEGRAL EQUATIONS OF RADIATIVE TRANSFER AND COMBINED CONVECTION-RADIATION HEAT TRANSFER ENHANCEMENT WITH POROUS INSERT

A Dissertation

SUBMITTED TO THE GRADUATE FACULTY

in partial fulfillment of the requirements for the

degree of

Doctor of Philosophy

By

Xuelei Chen
Norman, Oklahoma
2003

UMI Number: 3073700

UMI®

UMI Microform 3073700
Copyright 2003 by ProQuest Information and Learning Company.
All rights reserved. This microform edition is protected against
unauthorized copying under Title 17, United States Code.

ProQuest Information and Learning Company
300 North Zeeb Road
P.O. Box 1346
Ann Arbor, MI 48106-1346

© Copyright by XUELEI CHEN 2003
All Rights Reserved

TRANSFORMED INTEGRAL EQUATIONS OF RADIATIVE TRANSFER AND COMBINED CONVECTION-RADIATION HEAT TRANSFER ENHANCEMENT WITH POROUS INSERT

A Dissertation APPROVED FOR THE
SCHOOL OF AEROSPACE AND MECHANICAL ENGINEERING

BY

Dr. William H. Sutton (Chair)

Dr. Ajay K. Agrawal

Dr. M. Cengiz Altan

Dr. Tom J. Jr. Love

Dr. Richard G. Mallinson

Dr. Ramkumar N. Parthasarathy

ACKNOWLEDGMENTS

It is with deep gratitude and sincere appreciation that the author acknowledges the tremendous guidance, patience and understanding of Dr. William H. Sutton. His constant encouragement made possible the completion of this investigation.

The author wants to express her gratitude to Dr. Ajay K. Agrawal and Dr. Tom J. Love for their encouragement and professional help in this work. The author is grateful to all other members of her graduate committee, Dr. M. Cengiz Altan, Dr. Richard G. Mallinson, and Dr. Ramkumar N. Parthasarathy for their ideas, suggestions and aid during this investigation, and finally for their careful evaluation of her dissertation. The special gratitude goes to Dr. Feng-Chyuan Lai for his generous help although he is not a committee member.

The author would also like to thank the staff of the School of Aerospace and Mechanical Engineering. They are always kind, generous, and helpful whenever help is needed.

Finally, the author wishes to thank her parents for their love and tremendous encouragement, her husband and son for their patience, sacrifice and great support throughout this work.

TABLE OF CONTENTS

Page

LIST OF TABLES ix

LIST OF FIGURES x

ABSTRACT xix

1. INTRODUCTION 1

1.1 References 5

2. RADIATIVE TRANSFER IN FINITE CYLINDRICAL MEDIA USING TRANSFORMED INTEGRAL EQUATIONS 7

2.1 Introduction 7

2.2 Integral Equations of Transfer for General Cylindrical Geometry 9

2.2.1 Incident Radiation and Heat Fluxes 11

2.2.2 Boundary Conditions 15

2.3 Coordinate Transformation 16

2.3.1 Integration of the Volume 16

2.3.2 Integration of the Bottom Surface (z_1=0) 19

2.3.3 Integration of the Top Surface (z_2=L) 20

2.3.4 Integration of the Side Surface (r_3=R) 21

2.3.5 The Transformation of Boundary Conditions 24

2.4 Numerical Method 24

2.5 Results and Discussions 27

2.5.1 Two-Dimensional Results 27

2.5.2 Three-Dimensional Results 29

2.6 Conclusions 34

2.7 Nomenclature 35

2.8 References 52

2.9 Appendix A 54

3. A GENERAL INTEGRATION METHOD FOR RADIATIVE TRANSFER IN 3-D NON-HOMOGENEOUS CYLINDRICAL MEDIA WITH ANISOTROPIC SCATTERING 57

3.1 Introduction 57

3.2 Integral Equations of Transfer 59

3.2.1 General Equations in Finite Hollow Cylinders 60

3.2.1.1 Equations for finite solid and infinite hollow cylinders 67

3.2.2 The Radiation Intensity 68

3.2.3 Boundary Conditions 70

3.3 Numerical Methods 71

3.4 Results and Discussions 74

3.4.1 Continuous-Changing Property 2-D Results 74

3.4.2 Continuous-Changing Property 3-D Results 77

3.4.3 Step-Changing Property Results 79

3.5 Conclusions 85

3.6 Nomenclature 85

3.7 References 103

3.8 Appendix B 105

4. ENHANCEMENT OF HEAT TRANSFER: COMBINED CONVECTION AND RADIATION IN THE ENTRANCE REGION OF CIRCULAR DUCTS WITH POROUS INSERTS 107

4.1 Introduction 107
4.2 Governing Equations 109
4.2.1 Equations of Radiative Heat Transfer 111
4.2.2 Dimensionless Form of Governing Equations 113
4.3 Numerical Methods 116
4.3.1 Numerical Method for Momentum and Energy Equations 116
4.3.1.1 The interface property 119
4.3.2 Numerical Method for Radiative Transfer Equations 120
4.3.2.1 Intensity 123
4.4 Results and Discussions 126
4.4.1 Combined Heat Transfer without Porous Insert 128
4.4.1.1 The upstream and downstream externally incident radiation 129
4.4.1.2 The emissivity and temperature of the cooling wall 132
4.4.1.3 The extinction coefficient of the fluid 133
4.4.1.4 The scattering albedo of the fluid 133
4.4.1.5 Reynolds number 134
4.4.2 Combined Heat Transfer with Porous Insert 135
4.4.2.1 The radius of the porous insert 137
4.4.2.2 The upstream externally incident radiation 138
4.4.2.3 The cooling wall temperature 139
4.4.2.4 Reynolds number 139
4.4.2.5 The scattering albedo of the porous insert 140
4.4.2.6 The extinction coefficient of the porous insert 140

4.4.2.7 Darcy number Da 141

4.4.3 Error Analysis 143

4.5 Conclusions 145

4.6 Nomenclature 146

4.7 References 174

4.8 Appendix C 177

LIST OF TABLES

Page

Table 2-1 Case conditions for 3-D radiative heat transfer computations..... 30

Table 3-1 Case conditions for continuous-changing property 2-D solutions..... 75

Table 3-2 Case conditions for continuous-changing property 3-D solutions..... 77

Table 3-3 Case conditions for step-changing property 2-D solutions..... 83

Table 3-4 The effects of linear anisotropic scattering coefficient on hemispherical reflectivity for a cold solid cylindrical medium with transparent boundary, $f_3(R_{out})=1/\pi$, $R_m=1$, $R_{out}=2$ 84

Table 3-5 Hemispherical reflectivity for a cold hollow cylindrical medium with transparent boundary, $f_3(R_{out})=1/\pi$, $f_4(R_{in})=0$, and $R_{in}=1$, $R_m=2$, $R_{out}=3$ 84

LIST OF FIGURES

Page

Figure 2-1 Illustration of the physical system and coordinates. 37

Figure 2-2 Schematic diagram of the physical model and radiation transfer path. 37

Figure 2-3 Schematic diagram of the coordinates and the radiant ray direction. 38

Figure 2-4 Schematic diagram of coordinates transformation. 38

Figure 2-5 Top view of the cylinder coordinates transformation. Capital S is the projection of point s and capital S′ is the projection of point s′..... 39

Figure 2-6 The enlarged illustration of coordinates transformation. Capital S is the projection of point s and capital S′ is the projection of point s′..... 39

Figure 2-7 The effects of the scattering albedo on the radial heat flux $q_r(\tau_z,R)$ for a hot cylindrical medium enclosed by cold walls, $\varepsilon_1=\varepsilon_2=\varepsilon_3=0.5$, L=2R=1.0. 40

Figure 2-8 The effects of the scattering albedo on the distribution of centerline incident radiation $G(\tau_z,0)$ and axial heat flux $q_z(\tau_z,0)$, for a hot cylindrical medium enclosed by cold walls, $\varepsilon_1=\varepsilon_2=\varepsilon_3=0.5$, L=2R=1.0. 40

Figure 2-9 The effects of the scattering albedo on the distributions of incident radiation $G(L/2,\tau_r)$ and heat flux $q_r(L/2,\tau_r)$ with respect to τ_r/R, for a hot cylindrical medium enclosed by cold walls, $\varepsilon_1=\varepsilon_2=\varepsilon_3=0.5$, L=2R=1.0. ... 41

Figure 2-10 The effects of the scattering albedo on the distribution of axial heat flux $q_z(L,\tau_r)$ with respect to τ_r/R, for a hot cylindrical medium enclosed by cold walls, $\varepsilon_1=\varepsilon_2=\varepsilon_3=0.5$, L=2R=1.0. 41

Figure 2-11 The distributions of the incident radiation $G(L/2,\tau_r)$ and its compositions $Gv(L/2,\tau_r)$, $G1(L/2,\tau_r)$, $G2(L/2,\tau_r)$ and $G3(L/2,\tau_r)$ with respect to τ_r/R, for a hot cylindrical medium enclosed by cold walls, $\varepsilon_1=\varepsilon_2=\varepsilon_3=0.5$, $\omega=0.5$, L=2R=1.0. 42

Figure 2-12 The distributions of $q_r(L/2,\tau_r)$, $q_rv(L/2,\tau_r)$, $q_r1(L/2,\tau_r)$, $q_r2(L/2,\tau_r)$ and $q_r3(L/2,\tau_r)$ with respect to τ_r/R, for a hot medium enclosed by cold walls, $\varepsilon_1=\varepsilon_2=\varepsilon_3=0.5$, $\omega=0.5$, L=2R=1.0. 42

Figure 2-13 The effects of the optical thickness on the distribution of $q_r(\tau_z,R)$ with respect to normalized optical thickness τ_z/L, for a hot medium enclosed by cold walls, $\varepsilon_1=\varepsilon_2=\varepsilon_3=0.5$, $\omega=0.5$. 43

Figure 2-14 The effects of scattering albedo on heat fluxes $q_r(\tau_z,R,0)$ and $q_\phi(\tau_z,R,0)$ of a 3-D hot cylinder enclosed by cold walls with $\varepsilon_1=\varepsilon_2=1.0$, $\varepsilon_3=0.5(1-\sin\phi)$, see case 1 in table 2-1. 43

Figure 2-15 The effects of scattering albedo on the distribution of heat fluxes $q_r(0.5L,\tau_r,0)$ and $q_\phi(0.5L,\tau_r,0)$ with respect to normalized optical thickness τ_r/R for case 1 in table 2-1. 44

Figure 2-16 The effects of scattering albedo on the distribution of incident radiation at mid-plane $\tau_z=0.5L$ with respect to angular coordinate ϕ for case 1..... 44

Figure 2-17 The distribution of heat fluxes q_r and q_ϕ at mid-plane $\tau_z=0.5L$, but with different radial position, with respect to angular coordinate ϕ for case 1, $\omega=0.5$..... 45

Figure 2-18 The distribution of heat fluxes q_z at bottom or top surface, but with different radial position, with respect to angular coordinate ϕ for case 1, $\omega=0.5$..... 45

Figure 2-19 The comparison between case 1 ($\omega=0.5$) and case 2 for heat flux $q_r(0.5L,0,\phi)$ and $q_r(0.5L,R,\phi)$ with respect to angular coordinate ϕ. 46

Figure 2-20 The distribution of incident radiation $G(0.5L,0.5R,\phi)$ and heat flux $q_\phi(0.5L,0,\phi)$ with respect to angular direction ϕ for case 2, case 3 and case 4 in table 2-1. 46

Figure 2-21 The distribution of heat flux q_z at bottom surface, but at different radial position, with respect to angular coordinate ϕ for case 2, case 3 and case 4 in table 2-1 47

Figure 2-22 The comparison between case 3 and case 4 for heat flux $q_r(0.5L,0,\phi)$ and $q_r(0.5L,0.5R,\phi)$ with respect to angular coordinate ϕ. 47

Figure 2-23 The distribution of incident radiation and heat flux q_z at angular position $\phi=\pi/2$, but at different radial position, with respect to normalized optical thickness τ_z/L for case 3 and case 5 in table 2-1..... 48

Figure 2-24 The distribution of heat flux $q_r(\tau_z,0,\pi/2)$ and $q_r(\tau_z,0.5R,\pi/2)$ with respect to normalized optical thickness τ_z/L for case 3 and case 5. 48

Figure 2-25 The effects of linear anisotropic scattering coefficient a1 on the distribution of incident radiation $G(0.5L,\tau_r,0)$ with respect to normalized optical thickness τ_r/R for case 6 in table 2-1 49

Figure 2-26 The effects of linear anisotropic scattering coefficient a1 on the distribution of heat flux $q_r(\tau_z,0,0)$ and $q_\phi(\tau_z,0,0)$ with respect to normalized optical thickness τ_z/L for case 6 in table 2-1. 49

Figure 2-27 The effects of linear anisotropic scattering coefficient a1 on the distribution of q_r at mid-plane $\tau_z=0.5L$, but on different radial position, with respect to angular coordinate ϕ for case 6 in table 2-1. 50

Figure 2-28 The effects of linear anisotropic scattering coefficient a1 on the distribution of incident radiation $G(0.5L,0,\phi)$ and $G(0.5L,R,\phi)$ with respect to angular coordinate ϕ for case 6 in table 2-1 50

Figure 2-29 The effects of linear anisotropic scattering coefficient a1 on the distribution of incident radiation G at different radial position with respect to angular direction ϕ. 51

Figure 3-1 Illustration of the ray path, direction and boundary condition..... 88

Figure 3-2 Schematic diagram of the cylindrical coordinate and the radiant ray direction. 88

Figure 3-3 Schematic diagram of surface integration domain in a hollow cylinder. . 89

Figure 3-4 Top view of the coordinates transformation. Capital S is the projection of point s and capital S_i is the projection of point s_i..... 89

Figure 3-5 The scattering albedo changes with normalized radial distance τ_r/R in three different cases. 90

Figure 3-6 The effects of the scattering albedo on the radial heat flux $q_r(\tau_z,R)$ for a hot solid cylindrical medium enclosed by cold black walls, L=R=1.0..... 90

Figure 3-7 The combined effects of scattering albedo and linear anisotropic coefficient on the distributions of incident radiation $G(0.5L,\tau_r)$ and heat flux $q_r(0.5L,\tau_r)$ with respect to τ_r/R for case 1 in table 3-1 91

Figure 3-8 The combined effects of the optical thickness and linear anisotropic coefficient on the distribution of heat flux $q_z(0,\tau_r)$ with respect to τ_r/R for case 1 with $\omega_2=1-0.75(\tau_r/R)$..... 91

Figure 3-9 The combined effects of scattering albedo and linear anisotropic coefficient on the distributions of incident radiation $G(0.5L,\tau_r)$ and heat flux $q_r(0.5L,\tau_r)$ with respect to normalized optical thickness τ_r/R for a non-isothermal hot cylindrical medium (case 2 in table 3-1)..... 92

Figure 3-10 The extinction coefficient changes with normalized radial distance τ_r/R in three different cases. 92

Figure 3-11 The effects of extinction coefficient on the distributions of incident radiation $G(0.5L,\tau_r)$ and heat flux $q_r(0.5L,\tau_r)$ with respect to normalized optical thickness τ_r/R for case 3 in table 3-1..... 93

Figure 3-12 The effects of inner cylinder radius on the distributions of incident radiation $G(0.5L,\tau_r)$ and heat flux $q_r(0.5L,\tau_r)$ with respect to normalized optical thickness τ_r/R_{out}, for a hot hollow cylindrical medium enclosed by cold black walls (case 4 in table 3-1)..... 93

Figure 3-13 The effects of inner wall emissivity on the distributions of incident radiation $G(0.5L,\tau_r)$ and heat flux $q_r(0.5L,\tau_r)$, for a hot hollow cylindrical medium (case 4 in table 3-1)..... 94

Figure 3-14 The combined effects of inner wall emissivity and linear anisotropic coefficient on incident radiation $G(0.5L,\tau_r)$ for a hot hollow cylindrical medium (case 4 in table 3-1)..... 94

Figure 3-15 The comparison of present work and previous work [6] for the effects of scattering albedo on the distributions of $q_r(\tau_z,R,0)$ and $q_\phi(\tau_z,R,0)$ with respect to τ_z/L for case 5 in table 3-2..... 95

Figure 3-16 The comparison of present work and previous work [6] for the effects of scattering albedo on the distributions of $q_r(0.5L,\tau_r,0)$ and $q_\phi(0.5L,\tau_r,0)$ with respect to radial position for case 5 in table 3-2. 95

Figure 3-17 The comparison of present work and previous work [6] for the distributions of incident radiation and heat fluxes q_r and q_ϕ at mid-plane $\tau_z=0.5L$, but with different radial positions, with respect to angular coordinate ϕ for case 5 in table 3-2, $\omega=0.5$..... 96

Figure 3-18 The effects of spatial change albedo on the distributions of heat fluxes q_r and q_z with respect to axial position for case 6, a1=0. 96

Figure 3-19 The effects of spatial change albedo on the distributions of heat fluxes $q_r(0.5L,\tau_r,0)$ and $q_\phi(0.5L,\tau_r,0)$ with respect to radial position for case 6 in table 3-2, a1=0. 97

Figure 3-20 The distributions of incident radiation and heat flux q_r at mid-plane τ_z=0.5L, but with different radial position, with respect to angular direction ϕ for case 6 with spatial change albedo ω_2. 97

Figure 3-21 The distributions of q_ϕ at mid-plane, q_z at bottom surface, but both with different radial positions, with respect to angular coordinate ϕ for case 6 with spatial change albedo ω_2. 98

Figure 3-22 The effects of linear anisotropic coefficient on the incident radiation $G(0.5L,\tau_r,0)$ and heat flux $q_r(0.5L,\tau_r,0)$ for case 6 in table 3-2 with spatial change albedo ω_2. 98

Figure 3-23 The effects of spatial change extinction coefficient on the distributions of heat fluxes $q_r(0.5L,\tau_r,0)$ and $q_\phi(0.5L,\tau_r,0)$ at angular position ϕ=0 with respect to radial position for case 7 in table 3-2 99

Figure 3-24 The effects of spatial change extinction coefficient on the distributions of heat fluxes $q_r(0.5L,0,\phi)$ and $q_\phi(0.5L,0,\phi)$ with respect to angular position for case 7 in table 3-2 99

Figure 3-25 Schematic diagram for two-layer hollow cylindrical medium when tracing a ray to compute optical thickness ($r \le R_m$). 100

Figure 3-26 Schematic diagram for two-layer hollow cylindrical medium when tracing a ray to compute optical thickness ($r > R_m$). 100

Figure 3-27 The effects of different combinations of scattering albedo on the distributions of incident radiation and heat flux q_r with respect to radial distance for case 8 in table 3-3 101

Figure 3-28 The effects of different combinations of extinction coefficient on the distributions of incident radiation and heat flux q_r with respect to radial distance for case 8 in table 3-3 101

Figure 3-29 The effects of cylinder length on the distributions of heat flux $q_r(0.5L,r)$ with respect to radial distance r for case 8 in table 3-3 102

Figure 4-1 Schematic diagram of the flow system and coordinates. 149

Figure 4-2 Schematic diagram of the cylindrical coordinate and the radiant ray direction. 149

Figure 4-3 A typical control volume in cylindrical coordinate. 149

Figure 4-4 Illustration of the heat flux at the interface between the fluid layer and porous layer 150

Figure 4-5 Illustration of the 'ghost' point at the interface between the fluid layer and porous layer..... 150

Figure 4-6 Schematic diagram of the transformed coordinates..... 151

Figure 4-7 Top view of the transformed coordinates, S and S_i are the projection points of s and s_i..... 151

Figure 4-8 Schematic diagram for two-layer media when tracing a ray to compute optical thickness ($r \leq R_m$)..... 152

Figure 4-9 Schematic diagram for two-layer media when tracing a ray to compute optical thickness ($r > R_m$)..... 152

Figure 4-10 The comparison of current work with Kays etc. for the laminar flow in the entrance region with simultaneously developing velocity and temperature profiles..... 153

Figure 4-11 The comparision of velocity developing profiles for Pr=0.7158 and constant wall temperature T_w=500K..... 153

Figure 4-12 The distributions of radiative heat flux along the wall at different upstream externally incident radiation conditions..... 154

Figure 4-13 The distributions of radiative heat flux from upstream along radial coordinate at different upstream incident radiation conditions..... 154

Figure 4-14 The distributions of radiative heat flux to downstream along radial coordinate at different upstream incident radiation conditions..... 155

Figure 4-15 The distribution of radiative heat flux from upstream along radial coordinate when e_l=0.05 and T_w=800K..... 155

Figure 4-16 The distributions of net heat flux component q_z along axial direction at different upstream incident radiation conditions..... 156

Figure 4-17 The temperature developing profiles for Re=100, e_l=0.05 and T_w=800K. 156

Figure 4-18 The distributions of radiative heat flux along the wall at different downstream incident radiation conditions..... 157

Figure 4-19 The distributions of radiative heat flux along the wall at different wall temperature and emissivity conditions..... 157

Figure 4-20 The distributions of net heat flux component q_z along axial direction at different wall temperature and emissivity conditions. 158

Figure 4-21 The distributions of radiative heat flux along the wall at different fluid extinction coefficients. 158

Figure 4-22 The distributions of net heat flux component q_z along axial direction at different fluid extinction coefficients 159

Figure 4-23 The distributions of radiative heat flux along the wall at different fluid scattering albedos. 159

Figure 4-24 The distributions of radiative heat flux along the wall at different Reynolds numbers. 160

Figure 4-25 The distributions of convective and radiative heat flux along the wall at different Reynolds numbers 160

Figure 4-26 The comparison of convective Nusselt number between pure convection and combined convection-radiation. 161

Figure 4-27 The velocity developing profiles for in-pipe flow with the porous insert R_m=0.5(dimensionless). 161

Figure 4-28 The comparision of temperature fields between pure convection and combined convection-radiation cases with and without the porous insert (T_{in}=1200K, T_w=500K). 162

Figure 4-29 The comparision of convective Nusselt number between pure convection and combined convection-radiation cases with and without the porous insert. 163

Figure 4-30 The distributions of convective and radiative heat fluxes at the wall for the pipe with and without the porous insert. 163

Figure 4-31 The comparison of convective and radiative Nusselt number between the cases with and without the porous insert. 164

Figure 4-32 The distributions of net flux component q_z at the inlet and outlet for cases with and without the porous insert. 164

Figure 4-33 The velocity developing profiles for in-pipe flow with the porous insert R_m=0.2(dimensionless). 165

Figure 4-34 The temperature developing field for in-pipe flow with the porous insert (Da=0.01, T_{in}=1200K, T_w=500K, ε_w=0.8, e_1=e_2=0.05, β_{fluid}=0.5m^{-1}, ω_{fluid}=0, β_{porous}=200m^{-1}, ω_{porous}=0.8). 165

Figure 4-35 The distributions of convective and radiative heat fluxes along the wall at different dimensionless R_m. 166

Figure 4-36 The distributions of convective and radiative heat fluxes at different upstream incident radiation conditions with R_m=0.2. 166

Figure 4-37 The comparison of radiative heat fluxes with and without the porous insert at different upstream incident radiation conditions. 167

Figure 4-38 The distributions of net flux component q_z at the inlet at different upstream incident radiaiton conditions. 167

Figure 4-39 The distributions of radiative heat flux at the wall for T_w=500K and 800K. 168

Figure 4-40 The velocity developing profiles for in-pipe flow with the porous insert R_m=0.2(dimensionless) and Re=100. 168

Figure 4-41 The comparison of outlet temperature at different Reynolds numbers... 169

Figure 4-42 The distributions of bulk mean temperature at different Reynolds numbers. 169

Figure 4-43 The comparison of the enhancement of radiative heat flux by the porous insert at different Reynolds numbers. 170

Figure 4-44 The distributions of radiative heat flux at the wall under different porous scattering albedo conditions. 170

Figure 4-45 The distributions of radiative heat flux at the wall under different porous extinction coefficients. 171

Figure 4-46 The velocity developing profiles for in-pipe flow with the porous insert R_m=0.2(dimensionless) and Da=0.001. 171

Figure 4-47 The velocity developing profiles for in-pipe flow with the porous insert R_m=0.2(dimensionless) and Da=0.1. 172

Figure 4-48 The distributions of radiative heat flux at different Darcy numbers..... 172

Figure 4-49 The distributions of bulk mean temperature at different Darcy numbers. 173

Figure 4-50 The distributions of relative pressure at different Darcy numbers. 173

ABSTRACT

In this dissertation, Chapter One has given an introduction including literature review. A modified direct integration method is presented in Chapter Two to solve 3-D radiative transfer in emitting, absorbing and linear-anisotropic scattering finite cylindrical media. This scheme effectively avoids an integral singularity in the coupled Fredholm type integral equations of radiative transfer. The scheme leads to faster and more accurate results, which are needed in combined mode and non-gray problems. The calculated incident radiation and heat fluxes agree well with published results by discrete ordinates method. Using the transformed integral equations, the effects of boundary emission and reflection can also be easily handled. In Chapter Three, a general set of integral equations is presented to solve 3-D radiative heat transfer problems in emitting, absorbing and linear anisotropic scattering finite hollow or solid cylinders with non-homogeneous media. By tracing a ray to compute the intensity, it is much easier to handle the spatial changing properties including extinction coefficient. Both the continuous changing property and step-changing property are dealt with without difficulties. The solid angle integration of the incident radiation and heat fluxes is represented by the bounding surface integration. In order to avoid the singularity near the bounding surface, the surface integrations are transformed to new modified integral equations like in Chapter two. By doing so, we get more flexible general integral equations applicable to all cases like 3-D solid cylinders, 3-D hollow cylinders, finite cylinders or infinite cylinders. This scheme has been verified by comparing the results with published data in the literature. It is believed that this method is useful in combined radiation and convection heat transfer problems. Finally in Chapter Four, the combined convective and radiative heat transfer in

the entrance length of a pipe with or without the porous insert is solved by control volume method and integral equation scheme. The results are compared between the pipe flow with the porous insert and flow without the porous insert. The porous insert in a pipe will enhance both the convective and radiative heat transfer under certain parameters. The effects of several important parameters on this enhancement are discussed in detail.

CHAPTER ONE

1. INTRODUCTION

In the past twenty years, with increase in energy consumers and the development of high temperature equipment, radiative heat transfer in participating media has received tremendous consideration and attention in industry. A lot of applications which we can find include combustion chambers, cooling systems of nuclear reactors, solar energy recovery equipment, and high temperature heat exchangers. Among these applications, the cylindrical geometry is the most common and important.

Actually, going through the literature, one can find many methods available to solve radiative heat transfer problems. The method of spherical harmonics was first suggested by Jeans [1.1] and described in the book by Kourganoff [1.2]. The Monte Carlo method based on the statistical characteristics of physical processes in radiative heat transfer was reviewed by Howell [1.3], and discrete ordinates method was thoroughly studied [1.4-1.8] and recently extended to combined modes [1.9], thereby keeping compatibility with the CFD approach. Here, our interests focus on the exact integral method of radiative heat transfer.

The integral method is an accurate and efficient way to solve radiative transfer problems. We can see, later, that it couples easily with the differential equations governing the transport of mass, momentum and energy in combined heat transfer numerical models. Lin [1.10] and Thynell [1.11] presented integral equations for axisymmetric finite cylindrical participating media. Zhang and Sutton [1.12] gave the

SV-type (surface & volume) integral equations of transfer for 3-D non-homogeneous cylindrical media, although they just discuss the 2-D results. Later they developed efficient S-type (surface) integral equations for cylindrical media [1.13] to overcome singularity problem in volume integrations. But a singularity still exists in surface integrations especially near the boundaries.

In order to totally escape the singularity problem while still using a simple numerical integration method, like the Gauss-Legendre Quadrature method, and fill the blank of lacking 3-D cylindrical results in the literature, in Chapter 2 of this dissertation the transformed integral equations are derived and used to solve 3-D anisotropic scattering radiation problems. The effects of scattering albedo to the distributions of incident radiation and three net heat flux components in z, r, and ϕ direction are presented. Also the effects of linear anisotropic coefficient are known in 3-D cases. It has been found that the transformed integral equations are much easier to handle than original integral equations while doing numerical computation. The computation is fast and stable.

In Chapter 3 of this work, a general integration method based on the transformed equations and S-type equations is formulated and solved for variable properties. This scheme is much more powerful and flexible than equations in Chapter 2 in solving radiative heat transfer problems in cylindrical coordinates. The method provides the foundation for solving the combined convection radiation problems later in Chapter 4. The general integral equations for 3-D finite hollow cylinders are presented, and reduced to simplified equations for finite solid cylinders and infinite hollow cylinders automatically when certain variables are defined. By these equations, we can solve

radiative transfer problems for non-homogeneous media with space-dependent scattering albedo and extinction coefficient. In addition to the problems with continuous-change of properties, we can also deal with problems of step-change in properties. That means layered cylindrical problems, which have many applications such as thermal insulation and laminated biotissues, can be solved with the general integral equations. The results of 3-D radiative transfer with spatially changing properties are discussed in detail. The effects of linear anisotropic scattering coefficient on the hemispherical reflectivity for a layered solid cylinder and effects of different layer material on the hemispherical reflectivity for a hollow cylinder are presented.

In Chapter 4, the combined convective and radiative heat transfer of both hydraulically and thermally developing flow with porous insert in the flow pipe of a high temperature heat exchanger, which uses the flue gas as working fluid, is programmed and computed. For the porous layer, we use Brinkman type extension of the Darcy law and include convective terms in the momentum equation. The whole domain is divided by non-overlapping grids, so the staggered grids are used for different variables. The governing equations of continuity, momentum, and energy are solved by control volume methods (SIMPLE) and the radiation source term in the energy equation is solved by integral method developed in Chapter 3. First, we calculated the combined heat transfer in the entrance region without the porous insert, second we consider the combined transfer in the entrance region with the porous insert. Then for different parametric cases, we compare the results of these two situations to find the advantages of using the porous insert in high temperature heat exchangers. Two dimensional radiative heat transfer results give us detail of the radiative transfer from upstream, downstream and the cooling

wall. As a result, we have knowledge about when and how to use the porous insert to enhance the total heat transfer and efficiency of the equipment. The effects of important flow parameters like Reynolds number, flue gas properties like emissivity and extinction coefficient, and porous material properties like Darcy number are discussed in detail. All these data are currently limited in the literature.

1.1 References:

[1.1] J. H. Jeans, the equations of radiative transfer of energy, Monthly Notices Roy. Astron. Soc., **78**, 28-36, 1917.

[1.2] V. Kourganoff, Basic methods in transfer problems, Dover Publications, New York, 1963.

[1.3] J. R. Howell, the Monte Carlo method in radiative heat transfer, Journal of Heat Transfer, transactions of the ASME, August 1998, Vol. 120, pp. 547-560.

[1.4] J. S. Truelove, Three-dimensional radiation in absorbing-emitting-scattering media using the discrete-ordinates approximation, J. Quant. Spectrosc. Radiat. Transfer 1988, Vol. 39, No. 1, pp. 27-31.

[1.5] H. Y. Li, M. N. Ozisik, and J. R. Tsai, Two-dimensional radiation in a cylinder with spatially varying albedo, Journal of Thermophysics and Heat Transfer 1992, Vol. 6, No. 1, pp. 180-182.

[1.6] Slah Jendoubi, HaeOk Skarda Lee, and Tae-Kuk Kim, Discrete ordinates solutions for radiatively participating media in a cylindrical enclosure, Journal of Thermophysics and Heat Transfer, April-June 1993, Vol. 7, No. 2, pp. 213-219.

[1.7] Do Young Byun, Seung Wook Baek, and Man Young Kim, Thermal radiation in a discretely heated irregular geometry using the Monte-Carlo, finite volume, and modified discrete ordinates interpolation method, Numerical Heat Transfer 2000, Part A, 37:1-18.

[1.8] Nevin Selcuk and Gorkem Kirbas, the method of lines solution of the discrete ordinates method for radiative heat transfer in enclosures, Numerical Heat Transfer 2000, Part B, 37:379-392.

[1.9] K. B. Cheong and T. H. Song, an alternative discrete ordinates method with interpolation and source differencing for two-dimensional radiative transfer problems, Numerical Heat Transfer 1997, Part B, Vol. 32, pp. 107-125.

[1.10] Jenn-Der Lin, Exact expressions for radiative transfer in an arbitrary geometry exposed to radiation, J. Quant. Spectrosc. Radiat. Transfer 1987, Vol. 37, No. 6, pp. 591-601.

[1.11] S. T. Thynell, the integral form of the equation of transfer in finite, two-dimensional, cylindrical media, J. Quant. Spectrosc. Radiat. Transfer 1989, Vol. 42, No. 2, pp. 117-136.

[1.12] J. M. Zhang and W. H. Sutton, Multidimensional radiative transfer in absorbing emitting and linearly anisotropic scattering cylindrical medium with space-dependent properties, J. Quant. Spectrosc. Radiat. Transfer 1994, Vol. 52, No. 6, pp. 791-808.

[1.13] J. Zhang and W. Sutton, Predictions of radiative transfer in two-dimensional non-homogeneous participating cylindrical media based on the S-type integral equation of transfer, ASME/AIAA National Heat Transfer Conference, 1995, Portland, OR. AIAA-95-3519.

CHAPTER TWO

2. RADIATIVE TRANSFER IN FINITE CYLINDRICAL MEDIA USING TRANSFORMED INTEGRAL EQUATIONS

A modified direct integration method is presented to solve 3-D radiative transfer in emitting, absorbing and linear-anisotropic scattering finite cylindrical media. This scheme effectively avoids an integral singularity in the coupled Fredholm type integral equations of radiative transfer. The scheme leads to faster and more accurate results, which are needed in combined mode and nongray problems. The calculated incident radiation and heat fluxes agree well with published results obtained by discrete ordinates method. Using the transformed integral equations, the effects of boundary emission and reflection can also be easily handled.

2.1 Introduction

Radiative heat transfer in cylindrical media is important in industrial applications such as the design of combustion chambers, furnaces and high temperature heat exchangers. There are many papers dealing with the radiative transfer in multidimensional cylindrical enclosures with participating media. Lin [2.1] in 1987 presented mathematical formulas for radiative transfer in cylindrical, rectangular, triangular, and spherical absorbing and isotropically scattering media. Thynell [2.2], Tan [2.3], Zhang and Sutton [2.4] also gave the exact integral equations of transfer for radiation in various cylindrical cases.

The radiative transfer equation can be cast as coupled Fredholm integral equations of the second kind. Some terms in these equations have a strong singularity behavior, for example, the equation of heat flux q_r in radial direction. Efforts have been made to remove the singularity when evaluating these equations numerically; Crosbie and Schrenker [2.5] gave an application of a technique called the method of removing the singularity by Squire [2.6] for numerically handling singularities. This method subtracts a weighted function from the singular integral, thus removing the singularity, while leaving the integral of the kernel to be evaluated analytically. This remainder is singular also, but in some cases can be transformed to known functions or integrated analytically. As in Crosbie and Schrenker [2.5] research on the radiative transfer in a two-dimensional rectangular medium, the integration of the kernel can be finally integrated analytically because the good performance of the kernel and regularity of the geometry. Loyalka [2.7] applied this technique to Milne's problem in neutron transport, the remainder of the kernel integration becomes the well-known exponential integral $E_n(x)$. This method needs much work to evaluate the integration of the kernel and in some complex cases the remainder cannot be evaluated analytically. So, the singularity cannot be predictably solved in the general case.

A partition-extrapolation technique was provided by Wu and Wu [2.8], [2.9], but the method is complicated and time consuming.

Thynell [2.2], [2.10], and Lin [2.1], used the relation of the Bickley function and the modified Bessel function to solve the incident radiation and heat fluxes in 1-D or 2-D infinitely long geometries. The functional form of kernel changes for the analogous 3-D problem.

The objective of this work is to develop a modified or transformed integral equation of transfer in general 3-D cylindrical media. These transformed equations of transfer in absorbing, emitting, and linear-anisotropic scattering media can be numerically evaluated easily without singularity.

2.2 Integral Equations of Transfer for General Cylindrical Geometry

The radiative transfer in absorbing, emitting, and linear-anisotropic scattering cylindrical media bounded by diffusely emitting and reflecting opaque walls is expressed by the following equations. For a gray medium or a single frequency [2.15],

$$\frac{1}{\beta(s)}\frac{dI(s,\hat{\Omega})}{ds}+I(s,\hat{\Omega})=S(s,\hat{\Omega}), \tag{2-1}$$

where s represents the position (z,r,ϕ) of the radiation intensity in cylindrical coordinate. $\hat{\Omega}$ is the unit vector representing the intensity direction (θ,φ) in 4π solid angle. Please refer to Figure 2-1. β is the extinction coefficient of the medium and I is the radiation intensity. The source term in equation (2-1) is defined as

$$S(s,\hat{\Omega})\equiv(1-\omega)I_b[T(z,r,\phi)]+\frac{\omega}{4\pi}\int_{4\pi}p(\hat{\Omega}'\cdot\hat{\Omega})\cdot I(s,\hat{\Omega}')d\Omega'. \tag{2-2}$$

where ω is the scattering albedo of the medium and the linear-anisotropic scattering phase function is

$$p(\hat{\Omega}',\hat{\Omega})=1+a_1\hat{\Omega}\cdot\hat{\Omega}'. \tag{2-3}$$

The incident radiation $G(z,r,\phi)$, radiation heat fluxes $q_r(z,r,\phi)$ in r direction, $q_z(z,r,\phi)$ in z direction, and $q_\phi(z,r,\phi)$ in ϕ direction are, respectively, defined by

$$G(z,r,\phi)=\int_{4\pi}I(z,r,\phi,\hat{\Omega})\cdot d\Omega, \tag{2-4a}$$

$$q_r(z,r,\phi) = \int_{4\pi} I(z,r,\phi,\hat{\Omega}) \cdot \cos(\hat{e}_r,\hat{\Omega}) \cdot d\Omega, \tag{2-4b}$$

$$q_z(z,r,\phi) = \int_{4\pi} I(z,r,\phi,\hat{\Omega}) \cdot \cos(\hat{e}_z,\hat{\Omega}) \cdot d\Omega, \tag{2-4c}$$

$$q_\phi(z,r,\phi) = \int_{4\pi} I(z,r,\phi,\hat{\Omega}) \cdot \cos(\hat{e}_\phi,\hat{\Omega}) \cdot d\Omega. \tag{2-4d}$$

The source term defined by equation (2-2) can be further expressed as

$$S(s,\hat{\Omega}) = (1-\omega) I_b(T) + \frac{\omega}{4\pi}\left\{G(s) + a_1\left[q_r(s)\cos(\hat{e}_r,\hat{\Omega}) + q_z(s)\cos(\hat{e}_z,\hat{\Omega}) + q_\phi(s)\cos(\hat{e}_\phi,\hat{\Omega})\right]\right\}. \tag{2-5}$$

The formal solution [2.15] of the intensity in equation (2-1) is

$$I(s,\hat{\Omega}) = I_i \exp\left[-\int_{s_i}^{s}\beta(s')ds'\right] + \int_{s_i}^{s}\beta(s')S(s',\hat{\Omega})\exp\left[-\int_{s'}^{s}\beta(s'')ds''\right]ds', \tag{2-6a}$$

Referencing Figure 2-2, I_i is the intensity leaving the bounding surface i (i=1, 2, 3 for bottom, top, and side surface of the cylinder respectively) into the medium. For comparison with published cases, one might take the extinction coefficient β as constant in the medium. In that case, the intensity in (2-6a) is given as

$$I(s,\hat{\Omega}) = I_i(s_i,\hat{\Omega})e^{-\beta(s-s_i)} + \int_{s_i}^{s} S(s',\hat{\Omega})e^{-\beta(s-s')}\beta \cdot ds'. \tag{2-6b}$$

The physical meaning of the above equation is clear. The intensity of radiation at any point s and in a given direction $\hat{\Omega}$ results from the contribution of the radiation leaving the boundary and the contribution of energy source term of all interior points like s'. All have exponential decay because of the extinction along the ray path.

2.2.1 Incident Radiation and Heat Fluxes

Considering the cylinder shown in Figure 2-2, the incident radiation and heat fluxes are evaluated by the respective integration over the whole 4π solid angle. Using the following relation from Viskanta [2.11]

$$d\Omega = \frac{\cos\theta_i \cdot dA_i}{d^2(s,s_i)}, \tag{2-7a}$$

$$ds'd\Omega = \frac{dV'}{d^2(s,s')}, \tag{2-7b}$$

where θ_i is the angle between the unit normal vector $\hat{n}_i$ of surface i and the intensity direction $\hat{\Omega}$. The term $d(s,s_i)$ is the distance from s_i to s while $d(s,s')$ is the distance from s' to s. The coordinates of point s_1 on surface 1, point s_2 on surface 2, point s_3 on surface 3, and point s' in the volume are respectively (z_1,r_1,ϕ_1), (z_2,r_2,ϕ_2), (z_3,r_3,ϕ_3), and (z',r',ϕ'). Substituting equations (2-6b), (2-7a), and (2-7b) into equations (2-4a) to (2-4d), yields

$$G(s) = \sum_{i=1}^{3} \int_{A_i} I_i e^{-\beta \cdot d(s,s_i)} \cdot \frac{\cos\theta_i \cdot dA_i}{d^2(s,s_i)} + \int_V \left\{ \begin{array}{l} (1-\omega) I_b(T) + \\ \frac{\omega}{4\pi}\left[G + a_1 q_r \cos(\hat{e}_r,\hat{\Omega}) + a_1 q_z \cos(\hat{e}_z,\hat{\Omega}) + a_1 q_\phi \cos(\hat{e}_\phi,\hat{\Omega}) \right] \end{array} \right\} e^{-\beta \cdot d(s,s')} \frac{\beta dV'}{d^2(s,s')}, \tag{2-8a}$$

$$q_r(s) = \sum_{i=1}^{3} \int_{A_i} I_i e^{-\beta \cdot d(s,s_i)} \frac{\cos\theta_i \cdot \cos(\hat{e}_r,\hat{\Omega}) dA_i}{d^2(s,s_i)} + \int_V \left\{ \begin{array}{l} (1-\omega) I_b(T) + \\ \frac{\omega}{4\pi}\left[G + a_1 q_r \cos(\hat{e}_r,\hat{\Omega}) + a_1 q_z \cos(\hat{e}_z,\hat{\Omega}) + a_1 q_\phi \cos(\hat{e}_\phi,\hat{\Omega}) \right] \end{array} \right\} e^{-\beta \cdot d(s,s')} \frac{\cos(\hat{e}_r,\hat{\Omega}) \beta dV'}{d^2(s,s')}, \tag{2-8b}$$

$$q_z(s)=\sum_{i=1}^{3}\int_{A_i} I_i e^{-\beta\cdot d(s,s_i)}\frac{\cos\theta_i\cdot\cos(\hat{e}_z,\hat{\Omega})dA_i}{d^2(s,s_i)}+$$
$$\int_V\left\{\begin{array}{l}(1-\omega)I_b(T)+\\ \frac{\omega}{4\pi}\left[G+a_1q_r\cos(\hat{e}_r,\hat{\Omega})+a_1q_z\cos(\hat{e}_z,\hat{\Omega})+a_1q_\phi\cos(\hat{e}_\phi,\hat{\Omega})\right]\end{array}\right\}e^{-\beta\cdot d(s,s')}\frac{\cos(\hat{e}_z,\hat{\Omega})\beta dV'}{d^2(s,s')} \quad \text{,(2-8c)}$$

and

$$q_\phi(s)=\sum_{i=1}^{3}\int_{A_i} I_i e^{-\beta\cdot d(s,s_i)}\frac{\cos\theta_i\cdot\cos(\hat{e}_\phi,\hat{\Omega})dA_i}{d^2(s,s_i)}+$$
$$\int_V\left\{\begin{array}{l}(1-\omega)I_b(T)+\\ \frac{\omega}{4\pi}\left[G+a_1q_r\cos(\hat{e}_r,\hat{\Omega})+a_1q_z\cos(\hat{e}_z,\hat{\Omega})+a_1q_\phi\cos(\hat{e}_\phi,\hat{\Omega})\right]\end{array}\right\}e^{-\beta\cdot d(s,s')}\frac{\cos(\hat{e}_\phi,\hat{\Omega})\beta dV'}{d^2(s,s')} \quad \text{.(2-8d)}$$

Where in cylindrical coordinates, the distance between any two points s(z,r,ϕ) and s′(z′,r′,ϕ′) is expressed as

$$d(s,s')=\left[r^2+r'^2-2rr'\cos(\phi-\phi')+(z-z')^2\right]^{1/2}. \quad \text{(2-9)}$$

There exist the following equations for cosines. For details, please refer to Zhang and Sutton [2.4].

$$\cos\theta_1=\cos(\hat{n}_1,\hat{\Omega})=\frac{z}{\left[r^2+r_1^2-2rr_1\cos(\phi-\phi_1)+z^2\right]^{1/2}}, \quad \text{(2-10a)}$$

$$\cos\theta_2=\cos(\hat{n}_2,\hat{\Omega})=\frac{L-z}{\left[r^2+r_2^2-2rr_2\cos(\phi-\phi_2)+(L-z)^2\right]^{1/2}}, \quad \text{(2-10b)}$$

$$\cos\theta_3=\cos(\hat{n}_3,\hat{\Omega})=\frac{R-r\cos(\phi-\phi_3)}{\left[r^2+R^2-2rR\cos(\phi-\phi_3)+(z_3-z)^2\right]^{1/2}}. \quad \text{(2-10c)}$$

Where equation (2-10a), (2-10b), or (2-10c) is respectively for surface 1, 2, and 3. In Figure 2-3, the intensity in the direction of $\hat{\Omega}$ starting from point s′(z′,r′,ϕ′) to point s(z,r,ϕ), yields the following relations.

$$\cos(\hat{e}_z,\hat{\Omega}) = \frac{z-z'}{\left[r^2+r'^2-2rr'\cos(\phi-\phi')+(z-z')^2\right]^{1/2}}, \tag{2-11a}$$

$$\cos(\hat{e}_r,\hat{\Omega}) = \frac{r-r'\cos(\phi-\phi')}{\left[r^2+r'^2-2rr'\cos(\phi-\phi')+(z-z')^2\right]^{1/2}}, \tag{2-11b}$$

$$\cos(\hat{e}_\phi,\hat{\Omega}) = \frac{r'\sin(\phi-\phi')}{\left[r^2+r'^2-2rr'\cos(\phi-\phi')+(z-z')^2\right]^{1/2}}. \tag{2-11c}$$

If the point $s'(z',r',\phi')$ is at surface 1, the coordinate becomes $s_1(0,r_1,\phi_1)$, and then substitute $(0,r_1,\phi_1)$ in place of (z',r',ϕ') in the above equations. It is the same situation if the point $s'(z',r',\phi')$ is on surface 2 or surface 3.

By substituting equations (2-10) to (2-11) into equations (2-8), resultant expressions for incident radiation and heat fluxes are

$$G(z,r,\phi) = \int_0^{2\pi}\int_0^{R} I_1 e^{-\beta\cdot d(s,s_1)}\frac{z\cdot r_1 dr_1 d\phi_1}{d^3(s,s_1)} + \int_0^{2\pi}\int_0^{R} I_2 e^{-\beta\cdot d(s,s_2)}\frac{(L-z)\cdot r_2 dr_2 d\phi_2}{d^3(s,s_2)} +$$
$$\int_0^{2\pi}\int_0^{L} I_3 e^{-\beta\cdot d(s,s_3)}\frac{[R-r\cos(\phi-\phi_3)]\cdot R dz_3 d\phi_3}{d^3(s,s_3)} + \tag{2-12a}$$
$$\int_0^{2\pi}\int_0^{R}\int_0^{L}\left\{(1-\omega)I_b(T)+\frac{\omega}{4\pi}\left[G + a_1 q_r\frac{r-r'\cos(\phi-\phi')}{d(s,s')} + a_1 q_z\frac{z-z'}{d(s,s')} + a_1 q_\phi\frac{r'\sin(\phi-\phi')}{d(s,s')}\right]\right\}\cdot$$
$$e^{-\beta\cdot d(s,s')}\frac{\beta\cdot r' dz' dr' d\phi'}{d^2(s,s')}$$

$$q_r(z,r,\phi) = \int_0^{2\pi}\int_0^{R} I_1 e^{-\beta\cdot d(s,s_1)}\frac{z\cdot[r-r_1\cos(\phi-\phi_1)]\cdot r_1 dr_1 d\phi_1}{d^4(s,s_1)} +$$
$$\int_0^{2\pi}\int_0^{R} I_2 e^{-\beta\cdot d(s,s_2)}\frac{(L-z)\cdot[r-r_2\cos(\phi-\phi_2)]\cdot r_2 dr_2 d\phi_2}{d^4(s,s_2)} +$$
$$\int_0^{2\pi}\int_0^{L} I_3 e^{-\beta\cdot d(s,s_3)}\frac{[R-r\cos(\phi-\phi_3)]\cdot[r-R\cos(\phi-\phi_3)]\cdot R dz_3 d\phi_3}{d^4(s,s_3)} + \tag{2-12b}$$
$$\int_0^{2\pi}\int_0^{R}\int_0^{L}\left\{(1-\omega)I_b(T)+\frac{\omega}{4\pi}\left[G + a_1 q_r\frac{r-r'\cos(\phi-\phi')}{d(s,s')} + a_1 q_z\frac{z-z'}{d(s,s')} + a_1 q_\phi\frac{r'\sin(\phi-\phi')}{d(s,s')}\right]\right\}\cdot$$
$$e^{-\beta\cdot d(s,s')}\frac{[r-r'\cos(\phi-\phi')]\cdot\beta\cdot r' dz' dr' d\phi'}{d^3(s,s')}$$

$$q_z(z,r,\phi)=\int_0^{2\pi R}\int_0 I_1 e^{-\beta\cdot d(s,s_1)}\frac{z\cdot(z-0)\cdot r_1 dr_1 d\phi_1}{d^4(s,s_1)}+$$
$$\int_0^{2\pi R}\int_0 I_2 e^{-\beta\cdot d(s,s_2)}\frac{(L-z)\cdot(z-L)\cdot r_2 dr_2 d\phi_2}{d^4(s,s_2)}+$$
$$\int_0^{2\pi L}\int_0 I_3 e^{-\beta\cdot d(s,s_3)}\frac{[R-r\cos(\phi-\phi_3)]\cdot(z-z_3)\cdot R dz_3 d\phi_3}{d^4(s,s_3)}+ \qquad (2\text{-}12c)$$
$$\int_0^{2\pi R}\int_0^{L}\int_0\left\{(1-\omega)I_b(T)+\frac{\omega}{4\pi}\left[G+a_1 q_r\frac{r-r'\cos(\phi-\phi')}{d(s,s')}+a_1 q_z\frac{z-z'}{d(s,s')}+a_1 q_\phi\frac{r'\sin(\phi-\phi')}{d(s,s')}\right]\right\}\cdot$$
$$e^{-\beta\cdot d(s,s')}\frac{(z-z')\cdot\beta\cdot r' dz' dr' d\phi'}{d^3(s,s')}$$

and

$$q_\phi(z,r,\phi)=\int_0^{2\pi R}\int_0 I_1 e^{-\beta\cdot d(s,s_1)}\frac{z\cdot[r_1\sin(\phi-\phi_1)]\cdot r_1 dr_1 d\phi_1}{d^4(s,s_1)}+$$
$$\int_0^{2\pi R}\int_0 I_2 e^{-\beta\cdot d(s,s_2)}\frac{(L-z)\cdot[r_2\sin(\phi-\phi_2)]\cdot r_2 dr_2 d\phi_2}{d^4(s,s_2)}+$$
$$\int_0^{2\pi L}\int_0 I_3 e^{-\beta\cdot d(s,s_3)}\frac{[R-r\cos(\phi-\phi_3)]\cdot[R\sin(\phi-\phi_3)]\cdot R dz_3 d\phi_3}{d^4(s,s_3)}+ \qquad (2\text{-}12d)$$
$$\int_0^{2\pi R}\int_0^{L}\int_0\left\{(1-\omega)I_b(T)+\frac{\omega}{4\pi}\left[G+a_1 q_r\frac{r-r'\cos(\phi-\phi')}{d(s,s')}+a_1 q_z\frac{z-z'}{d(s,s')}+a_1 q_\phi\frac{r'\sin(\phi-\phi')}{d(s,s')}\right]\right\}\cdot$$
$$e^{-\beta\cdot d(s,s')}\frac{[r'\sin(\phi-\phi')]\cdot\beta\cdot r' dz' dr' d\phi'}{d^3(s,s')}$$

Equations (2-12) are the exact integral equations for three-dimensional cylindrical enclosures with absorbing, emitting, and anisotropically scattering media. Defining the first integral terms in equations (2-12a)-(2-12d) as G1, q_r1, q_z1, and q_ϕ1, respectively, these represent the effects of surface 1 for emitting and reflecting. Similarly, the second terms and the third terms are represented by G2, q_r2, q_z2, q_ϕ2, G3, q_r3, q_z3, and q_ϕ3. The volume integration terms in equations (2-12a)-(2-12d) denoted as Gv, q_rv, q_zv, and q_ϕv, represent the effects of medium emitting and in-scattering. Summarizing,

$$G(z,r,\phi)=G1(z,r,\phi)+G2(z,r,\phi)+G3(z,r,\phi)+Gv(z,r,\phi), \qquad (2\text{-}13a)$$

$$q_r(z,r,\phi) = q_r1(z,r,\phi) + q_r2(z,r,\phi) + q_r3(z,r,\phi) + q_rv(z,r,\phi), \qquad (2\text{-}13b)$$

$$q_z(z,r,\phi) = q_z1(z,r,\phi) + q_z2(z,r,\phi) + q_z3(z,r,\phi) + q_zv(z,r,\phi), \qquad (2\text{-}13c)$$

$$q_\phi(z,r,\phi) = q_\phi1(z,r,\phi) + q_\phi2(z,r,\phi) + q_\phi3(z,r,\phi) + q_\phi v(z,r,\phi). \qquad (2\text{-}13d)$$

2.2.2 Boundary Conditions

Considering diffusely emitting and reflecting opaque walls with unit refractive index the following relations result:

$$I_1(0,r,\phi) = \frac{J_1(0,r,\phi)}{\pi}, \qquad (2\text{-}14a)$$

$$I_2(L,r,\phi) = \frac{J_2(L,r,\phi)}{\pi}, \qquad (2\text{-}14b)$$

$$I_3(z,R,\phi) = \frac{J_3(z,R,\phi)}{\pi}, \qquad (2\text{-}14c)$$

where

$$J_1(0,r,\phi) = \varepsilon_1\sigma T_1^4(0,r,\phi) + \rho_1 \int_{2\pi} I(0,r,\phi)\cdot\cos(-\hat{e}_z,\hat{\Omega})\cdot d\Omega, \qquad (2\text{-}15a)$$

$$J_2(L,r,\phi) = \varepsilon_2\sigma T_2^4(L,r,\phi) + \rho_2 \int_{2\pi} I(L,r,\phi)\cdot\cos(\hat{e}_z,\hat{\Omega})\cdot d\Omega, \qquad (2\text{-}15b)$$

$$J_3(z,R,\phi) = \varepsilon_3\sigma T_3^4(z,R,\phi) + \rho_3 \int_{2\pi} I(z,R,\phi)\cdot\cos(\hat{e}_r,\hat{\Omega})\cdot d\Omega. \qquad (2\text{-}15c)$$

Where J_1, J_2, and J_3 are the radiosities of surface 1, surface 2, and surface 3 respectively. The radiosity is the radiant energy leaving the surface per unit of time and area. It is equal to the emission plus the reflected part of the incident energy. I_1, I_2, and I_3 are the entering

intensities on the bounding surface 1, surface 2, and surface 3. Equations (2-15) can be further expressed as

$$J_1(0,r,\phi) = \varepsilon_1 \sigma T_1^4(0,r,\phi) + \rho_1\{-q_z 2(0,r,\phi) - q_z 3(0,r,\phi) - q_z v(0,r,\phi)\}, \quad (2\text{-}16a)$$

$$J_2(L,r,\phi) = \varepsilon_2 \sigma T_2^4(L,r,\phi) + \rho_2\{q_z 1(L,r,\phi) + q_z 3(L,r,\phi) + q_z v(L,r,\phi)\}, \quad (2\text{-}16b)$$

$$J_3(z,R,\phi) = \varepsilon_3 \sigma T_3^4(z,R,\phi) + \rho_3\{q_r 1(z,R,\phi) + q_r 2(z,R,\phi) + q_r 3(z,R,\phi) + q_r v(z,R,\phi)\} \quad (2\text{-}16c)$$

Because surface 3 is a concave surface, a $q_r 3$ term appears in the above equation of J_3.

2.3 Coordinate Transformation

The equations (2-12) are Fredholm second kind integral equations with a singularity when the distance $d(s,s_i)$ or $d(s,s')$ tends to zero or very small (as s' approaches s). Methods using multiple orders/types of quadrature methods to integrate the equations, which may remove an apparent singularity, resulted in numerically oscillating results. It is not practical to avoid all possible grid lines or points (z, r, ϕ) approaching integration points (z', r', ϕ'), especially when computing the heat flux q_r. A trigonometric coordinate transform method was therefore used for the purpose of avoiding this difficulty in the numerical calculation.

2.3.1 Integration of the Volume

First, one may consider the volume integration terms in equations (2-12). The transformed coordinates are shown in Figure 2-4 to Figure 2-6. If the incident radiation and heat fluxes calculated at the point $s(z,r,\phi)$, then the integration precedes over the

volume with respect to (z',r',ϕ'). The angle α (below) is defined as in Figure 2-4, yielding the following relations:

$$\rho = \rho(r, r', \phi - \phi') = \left[r^2 + r'^2 - 2rr'\cos(\phi - \phi')\right]^{1/2}, \tag{2-17}$$

$$d(s, s') = \rho \cdot \sec\alpha, \tag{2-18}$$

$$z' = z + \rho \cdot \tan\alpha, \quad dz' = \rho \cdot \sec^2\alpha \cdot d\alpha, \tag{2-19a,b}$$

$$\alpha_1 = \arctan\frac{0 - z}{\rho}, \quad \alpha_2 = \arctan\frac{L - z}{\rho}. \tag{2-20a,b}$$

Using above equations, the integration with respect to z' becomes the integration over α. In the projected view of the cylinder (Figure 2-5 and Figure 2-6), the original point is moved from O(0,0) to S(r,ϕ). The coordinates of S' will change from the previous (r',ϕ') to (ρ,χ). The boundary points of r'=R will have the following equation in the new coordinates while χ goes from 0 to 2π:

$$\rho(r' = R) = \rho_R = \sqrt{R^2 - r^2\sin^2(\phi - \chi)} - r \cdot \cos(\phi - \chi). \tag{2-21}$$

There are also

$$r' = \sqrt{r^2 + \rho^2 + 2r\rho \cdot \cos(\phi - \chi)}, \tag{2-22}$$

$$\tan\phi' = \frac{r\sin\phi + \rho \cdot \sin\chi}{r\cos\phi + \rho \cdot \cos\chi}. \tag{2-23}$$

The Jacobian of this transformation is

$$|J| = \left|\frac{\partial(r', \phi')}{\partial(\rho, \chi)}\right| = \frac{\rho}{r'}, \tag{2-24}$$

So we have (referring to Figure 2-6)

$$r'dr'd\phi' = \rho \cdot d\rho \cdot d\chi. \tag{2-25}$$

From the triangle relations shown in Figure 2-6, there are

$$r - r'\cos(\phi - \phi') = -\rho \cdot \cos(\phi - \chi), \tag{2-26a}$$

$$r' \cdot \sin(\phi - \phi') = \rho \cdot \sin(\phi - \chi). \tag{2-26b}$$

By utilizing above relations, the integration of (r'dz'dr'dϕ') can be easily transformed to ($\rho^2\sec^2\alpha \cdot d\alpha d\rho d\chi$), yielding nonsingular forms that are easier to evaluate numerically.

$$Gv(z,r,\phi) = \int_0^{2\pi}\int_0^{\rho_R}\int_{\alpha_1}^{\alpha_2} \left\{(1-\omega)I_b(T) + \frac{\omega}{4\pi}\left[G - a_1 q_r \cos(\phi-\chi)\cos\alpha - a_1 q_z \sin\alpha + a_1 q_\phi \sin(\phi-\chi)\cos\alpha\right]\right\} \cdot e^{-\beta\cdot\rho\cdot\sec\alpha} \cdot d\alpha(\beta d\rho)d\chi \tag{2-27a}$$

$$q_r v(z,r,\phi) = \int_0^{2\pi}\int_0^{\rho_R}\int_{\alpha_1}^{\alpha_2} \left\{(1-\omega)I_b(T) + \frac{\omega}{4\pi}\left[G - a_1 q_r \cos(\phi-\chi)\cos\alpha - a_1 q_z \sin\alpha + a_1 q_\phi \sin(\phi-\chi)\cos\alpha\right]\right\} \cdot e^{-\beta\cdot\rho\cdot\sec\alpha}(-1)\cos(\phi-\chi)\cos\alpha \cdot d\alpha(\beta d\rho)d\chi \tag{2-27b}$$

$$q_z v(z,r,\phi) = \int_0^{2\pi}\int_0^{\rho_R}\int_{\alpha_1}^{\alpha_2} \left\{(1-\omega)I_b(T) + \frac{\omega}{4\pi}\left[G - a_1 q_r \cos(\phi-\chi)\cos\alpha - a_1 q_z \sin\alpha + a_1 q_\phi \sin(\phi-\chi)\cos\alpha\right]\right\} \cdot e^{-\beta\cdot\rho\cdot\sec\alpha}(-\sin\alpha) \cdot d\alpha(\beta d\rho)d\chi \tag{2-27c}$$

and

$$q_\phi v(z,r,\phi) = \int_0^{2\pi}\int_0^{\rho_R}\int_{\alpha_1}^{\alpha_2} \left\{(1-\omega)I_b(T) + \frac{\omega}{4\pi}\left[G - a_1 q_r \cos(\phi-\chi)\cos\alpha - a_1 q_z \sin\alpha + a_1 q_\phi \sin(\phi-\chi)\cos\alpha\right]\right\} \cdot e^{-\beta\cdot\rho\cdot\sec\alpha}\sin(\phi-\chi)\cos\alpha \cdot d\alpha(\beta d\rho)d\chi \tag{2-27d}$$

where

$$I_b(T) = I_b\left[T(z',r',\phi')\right] = I_b\left\{T\left[z'(z,\alpha,\rho), r'(r,\phi,\rho,\chi), \phi'(r,\phi,\rho,\chi)\right]\right\}, \tag{2-28a}$$

$$G = G\left[z'(z,\alpha,\rho), r'(r,\phi,\rho,\chi), \phi'(r,\phi,\rho,\chi)\right], \tag{2-28b}$$

$$q_r = q_r\left[z'(z,\alpha,\rho), r'(r,\phi,\rho,\chi), \phi'(r,\phi,\rho,\chi)\right], \tag{2-28c}$$

$$q_z = q_z\left[z'(z,\alpha,\rho), r'(r,\phi,\rho,\chi), \phi'(r,\phi,\rho,\chi)\right], \tag{2-28d}$$

$$q_\phi = q_\phi\left[z'(z,\alpha,\rho), r'(r,\phi,\rho,\chi), \phi'(r,\phi,\rho,\chi)\right]. \tag{2-28e}$$

2.3.2 Integration of the Bottom Surface (z_1=0)

Similarly, for the integration of the bottom surface (z_1=0) on the cylinder, the following relations result where the point (z',r',ϕ') is replaced by point (0,r_1,ϕ_1).

$$\alpha_1 = \arctan\frac{z_1 - z}{\rho} = \arctan\frac{-z}{\rho}, \tag{2-29}$$

$$\rho(r_1 = R) = \rho_R = \sqrt{R^2 - r^2\sin^2(\phi - \chi)} - r\cdot\cos(\phi - \chi), \tag{2-30}$$

$$r_1 = \sqrt{r^2 + \rho^2 + 2r\rho\cdot\cos(\phi - \chi)}, \tag{2-31}$$

$$\tan\phi_1 = \frac{r\sin\phi + \rho\cdot\sin\chi}{r\cos\phi + \rho\cdot\cos\chi}, \tag{2-32}$$

$$r_1 d\phi_1 dr_1 = \rho\cdot d\chi\cdot d\rho, \tag{2-33}$$

and

$$r - r_1\cos(\phi - \phi_1) = -\rho\cdot\cos(\phi - \chi), \qquad r_1\cdot\sin(\phi - \phi_1) = \rho\cdot\sin(\phi - \chi) \tag{2-34a,b}$$

By utilizing above relations, the integration of ($r_1 dr_1 d\phi_1$) can be easily transformed to ($\rho d\rho d\chi$) as follows:

$$G1(z,r,\phi) = \int_0^{2\pi}\int_0^{\rho_R(\chi)} I_1 \frac{e^{-\beta\cdot\rho\cdot\sec\alpha_1}}{\rho}(-1)\sin\alpha_1\cos^2\alpha_1 d\rho d\chi, \tag{2-35a}$$

$$q_r1(z,r,\phi) = \int_0^{2\pi}\int_0^{\rho_R(\chi)} I_1 \frac{e^{-\beta\cdot\rho\cdot\sec\alpha_1}}{\rho}\sin\alpha_1\cos^3\alpha_1\cos(\phi - \chi) d\rho d\chi, \tag{2-35b}$$

$$q_z1(z,r,\phi) = \int_0^{2\pi}\int_0^{\rho_R(\chi)} I_1 \frac{e^{-\beta\cdot\rho\cdot\sec\alpha_1}}{\rho}\sin^2\alpha_1\cos^2\alpha_1 d\rho d\chi, \tag{2-35c}$$

$$q_\phi1(z,r,\phi) = \int_0^{2\pi}\int_0^{\rho_R(\chi)} I_1 \frac{e^{-\beta\cdot\rho\cdot\sec\alpha_1}}{\rho}(-1)\sin\alpha_1\cos^3\alpha_1\sin(\phi - \chi) d\rho d\chi, \tag{2-35d}$$

where

$$I_1 = I_1[0, r_1(r,\phi,\rho,\chi), \phi_1(r,\phi,\rho,\chi)]. \tag{2-36}$$

2.3.3 Integration of the Top Surface (z_2=L)

For integration of the top surface

$$\alpha_2 = \arctan\frac{z_2 - z}{\rho} = \arctan\frac{L - z}{\rho}, \tag{2-37}$$

$$\rho(r_2 = R) = \rho_R = \sqrt{R^2 - r^2\sin^2(\phi - \chi)} - r\cdot\cos(\phi - \chi), \tag{2-38}$$

$$r_2 = \sqrt{r^2 + \rho^2 + 2r\rho\cdot\cos(\phi - \chi)}, \tag{2-39}$$

$$\tan\phi_2 = \frac{r\sin\phi + \rho\cdot\sin\chi}{r\cos\phi + \rho\cdot\cos\chi}, \tag{2-40}$$

$$r_2 d\phi_2 dr_2 = \rho\cdot d\chi\cdot d\rho, \tag{2-41}$$

and

$$r - r_2\cos(\phi - \phi_2) = -\rho\cdot\cos(\phi - \chi), \qquad r_2\cdot\sin(\phi - \phi_2) = \rho\cdot\sin(\phi - \chi) \tag{2-42a,b}$$

By utilizing above relations, the integration of ($r_2 dr_2 d\phi_2$) can be easily transformed to ($\rho d\rho d\chi$) as follows:

$$G2(z,r,\phi) = \int_0^{2\pi}\int_0^{\rho_R(\chi)} I_2 \frac{e^{-\beta\cdot\rho\cdot\sec\alpha_2}}{\rho}\sin\alpha_2\cos^2\alpha_2 d\rho d\chi, \tag{2-43a}$$

$$q_r 2(z,r,\phi) = \int_0^{2\pi}\int_0^{\rho_R(\chi)} I_2 \frac{e^{-\beta\cdot\rho\cdot\sec\alpha_2}}{\rho}(-1)\sin\alpha_2\cos^3\alpha_2\cos(\phi - \chi) d\rho d\chi, \tag{2-43b}$$

$$q_z 2(z,r,\phi) = \int_0^{2\pi}\int_0^{\rho_R(\chi)} I_2 \frac{e^{-\beta\cdot\rho\cdot\sec\alpha_2}}{\rho}(-1)\sin^2\alpha_2\cos^2\alpha_2 d\rho d\chi, \tag{2-43c}$$

$$q_\phi 2(z,r,\phi) = \int_0^{2\pi}\int_0^{\rho_R(\chi)} I_2 \frac{e^{-\beta\cdot\rho\cdot\sec\alpha_2}}{\rho}\sin\alpha_2\cos^3\alpha_2\sin(\phi - \chi) d\rho d\chi. \tag{2-43d}$$

where

$$I_2 = I_2\left[L, r_2(r,\phi,\rho,\chi), \phi_2(r,\phi,\rho,\chi)\right] \tag{2-44}$$

2.3.4 Integration of the Side Surface (r_3=R)

These are similar to above sections, except point (z',r',ϕ') being replaced by point (z_3,R,ϕ_3).

$$\rho(r_3 = R) = \rho_R = \sqrt{R^2 - r^2\sin^2(\phi-\chi)} - r\cdot\cos(\phi-\chi), \tag{2-45}$$

$$d(s,s_3) = \rho_R \cdot \sec\alpha, \tag{2-46}$$

$$z_3 = z + \rho_R \cdot \tan\alpha, \quad dz_3 = \rho_R \cdot \sec^2\alpha \cdot d\alpha, \tag{2-47a,b}$$

$$\alpha_1 = \arctan\frac{0-z}{\rho_R}, \quad \alpha_2 = \arctan\frac{L-z}{\rho_R}, \tag{2-48a,b}$$

$$\tan\phi_3 = \frac{r\sin\phi + \rho_R\cdot\sin\chi}{r\cos\phi + \rho_R\cdot\cos\chi}, \tag{2-49}$$

$$R\cdot d\phi_3 = \frac{\rho_R\cdot d\chi}{\cos(\phi_3-\chi)}, \tag{2-50}$$

and

$$R - r\cos(\phi-\phi_3) = \rho_R\cdot\cos(\phi_3-\chi), \tag{2-51a}$$

$$r - R\cos(\phi-\phi_3) = -\rho_R\cdot\cos(\phi-\chi), \tag{2-51b}$$

$$R\cdot\sin(\phi-\phi_3) = \rho_R\cdot\sin(\phi-\chi). \tag{2-51c}$$

By utilizing above relations, the integration of ($Rdz_3d\phi_3$) can be easily transformed to $\frac{\rho_R{}^2\cdot\sec^2\alpha}{\cos(\phi_3-\chi)}d\alpha\cdot d\chi$ as follows.

$$G3(z,r,\phi) = \int_0^{2\pi}\int_{\alpha_1}^{\alpha_2} I_3 e^{-\beta\cdot\rho_R\cdot\sec\alpha}\cos\alpha\cdot d\alpha d\chi, \tag{2-52a}$$

$$q_r 3(z,r,\phi) = \int_0^{2\pi}\int_{\alpha_1}^{\alpha_2} I_3 e^{-\beta\cdot\rho_R\cdot\sec\alpha}(-1)\cos^2\alpha\cos(\phi-\chi)\cdot d\alpha d\chi\,, \tag{2-52b}$$

$$q_z 3(z,r,\phi) = \int_0^{2\pi}\int_{\alpha_1}^{\alpha_2} I_3 e^{-\beta\cdot\rho_R\cdot\sec\alpha}(-1)\sin\alpha\cos\alpha\cdot d\alpha d\chi\,, \tag{2-52c}$$

$$q_\phi 3(z,r,\phi) = \int_0^{2\pi}\int_{\alpha_1}^{\alpha_2} I_3 e^{-\beta\cdot\rho_R\cdot\sec\alpha}\cos^2\alpha\sin(\phi-\chi)\cdot d\alpha d\chi\,. \tag{2-52d}$$

where

$$I_3 = I_3\left[z_3(z,r,\phi,\alpha,\chi), R, \phi_3(r,\phi,\chi)\right] \tag{2-53}$$

All necessary transformed integral equations are obtained for finite cylindrical geometry. Substituting equations (2-27a)-(2-27d), (2-35a)-(2-35d), (2-43a)-(2-43d), (2-52a)-(2-52d) into equations (2-13a)-(2-13d) respectively, give the expressions for G(z,r,ϕ), q_r(z,r,ϕ), q_z(z,r,ϕ), and q_ϕ(z,r,ϕ) as

$$\begin{aligned}
G(z,r,\phi) = {} & \int_0^{2\pi}\int_0^{\rho_R(\chi)} I_1 \frac{e^{-\beta\cdot\rho\cdot\sec\alpha_1}}{\rho}(-1)\sin\alpha_1\cos^2\alpha_1 d\rho d\chi + \\
& \int_0^{2\pi}\int_0^{\rho_R(\chi)} I_2 \frac{e^{-\beta\cdot\rho\cdot\sec\alpha_2}}{\rho}\sin\alpha_2\cos^2\alpha_2 d\rho d\chi + \\
& \int_0^{2\pi}\int_{\alpha_1}^{\alpha_2} I_3 e^{-\beta\cdot\rho_R\cdot\sec\alpha}\cos\alpha\cdot d\alpha d\chi + \\
& \int_0^{2\pi}\int_0^{\rho_R}\int_{\alpha_1}^{\alpha_2}\left\{(1-\omega)I_b(T) + \frac{\omega}{4\pi}\left[G - a_1 q_r\cos(\phi-\chi)\cos\alpha - a_1 q_z\sin\alpha + a_1 q_\phi\sin(\phi-\chi)\cos\alpha\right]\right\}\cdot \\
& e^{-\beta\cdot\rho\cdot\sec\alpha}\cdot d\alpha(\beta d\rho)d\chi
\end{aligned} \tag{2-54a}$$

$$q_r(z,r,\phi)=\int_0^{2\pi}\int_0^{\rho_R(\chi)} I_1\frac{e^{-\beta\cdot\rho\cdot\sec\alpha_1}}{\rho}\sin\alpha_1\cos^3\alpha_1\cos(\phi-\chi)d\rho d\chi+$$

$$\int_0^{2\pi}\int_0^{\rho_R(\chi)} I_2\frac{e^{-\beta\cdot\rho\cdot\sec\alpha_2}}{\rho}(-1)\sin\alpha_2\cos^3\alpha_2\cos(\phi-\chi)d\rho d\chi+$$

$$\int_0^{2\pi}\int_{\alpha_1}^{\alpha_2} I_3 e^{-\beta\cdot\rho_R\cdot\sec\alpha}(-1)\cos^2\alpha\cos(\phi-\chi)\cdot d\alpha d\chi+ \qquad \text{(2-54b)}$$

$$\int_0^{2\pi}\int_0^{\rho_R}\int_{\alpha_1}^{\alpha_2}\left\{(1-\omega)I_b(T)+\frac{\omega}{4\pi}\left[G-a_1q_r\cos(\phi-\chi)\cos\alpha-a_1q_z\sin\alpha+a_1q_\phi\sin(\phi-\chi)\cos\alpha\right]\right\}\cdot$$

$$e^{-\beta\cdot\rho\cdot\sec\alpha}(-1)\cos(\phi-\chi)\cos\alpha\cdot d\alpha(\beta d\rho)d\chi$$

$$q_z(z,r,\phi)=\int_0^{2\pi}\int_0^{\rho_R(\chi)} I_1\frac{e^{-\beta\cdot\rho\cdot\sec\alpha_1}}{\rho}\sin^2\alpha_1\cos^2\alpha_1 d\rho d\chi+$$

$$\int_0^{2\pi}\int_0^{\rho_R(\chi)} I_2\frac{e^{-\beta\cdot\rho\cdot\sec\alpha_2}}{\rho}(-1)\sin^2\alpha_2\cos^2\alpha_2 d\rho d\chi+$$

$$\int_0^{2\pi}\int_{\alpha_1}^{\alpha_2} I_3 e^{-\beta\cdot\rho_R\cdot\sec\alpha}(-1)\sin\alpha\cos\alpha\cdot d\alpha d\chi+ \qquad \text{(2-54c)}$$

$$\int_0^{2\pi}\int_0^{\rho_R}\int_{\alpha_1}^{\alpha_2}\left\{(1-\omega)I_b(T)+\frac{\omega}{4\pi}\left[G-a_1q_r\cos(\phi-\chi)\cos\alpha-a_1q_z\sin\alpha+a_1q_\phi\sin(\phi-\chi)\cos\alpha\right]\right\}\cdot$$

$$e^{-\beta\cdot\rho\cdot\sec\alpha}(-\sin\alpha)\cdot d\alpha(\beta d\rho)d\chi$$

$$q_\phi(z,r,\phi)=\int_0^{2\pi}\int_0^{\rho_R(\chi)} I_1\frac{e^{-\beta\cdot\rho\cdot\sec\alpha_1}}{\rho}(-1)\sin\alpha_1\cos^3\alpha_1\sin(\phi-\chi)d\rho d\chi+$$

$$\int_0^{2\pi}\int_0^{\rho_R(\chi)} I_2\frac{e^{-\beta\cdot\rho\cdot\sec\alpha_2}}{\rho}\sin\alpha_2\cos^3\alpha_2\sin(\phi-\chi)d\rho d\chi+$$

$$\int_0^{2\pi}\int_{\alpha_1}^{\alpha_2} I_3 e^{-\beta\cdot\rho_R\cdot\sec\alpha}\cos^2\alpha\sin(\phi-\chi)\cdot d\alpha d\chi+ \qquad \text{(2-54d)}$$

$$\int_0^{2\pi}\int_0^{\rho_R}\int_{\alpha_1}^{\alpha_2}\left\{(1-\omega)I_b(T)+\frac{\omega}{4\pi}\left[G-a_1q_r\cos(\phi-\chi)\cos\alpha-a_1q_z\sin\alpha+a_1q_\phi\sin(\phi-\chi)\cos\alpha\right]\right\}\cdot$$

$$e^{-\beta\cdot\rho\cdot\sec\alpha}\sin(\phi-\chi)\cos\alpha\cdot d\alpha(\beta d\rho)d\chi$$

2.3.5 The Transformation of Boundary Conditions

The transformation of boundary conditions utilizes equations (2-16). Solving the integrations in J_1 and J_2 follows the earlier transformations. Substituting (z,r,ϕ) by $(0,r,\phi)$ or (L,r,ϕ) in the q_z1 equation (2-35c), q_z2 equation (2-43c), q_z3 equation (2-52c) and q_zv equation (2-27c), each term in equations (2-16a) and (2-16b) for J_1 and J_2 is obtained.

For integral terms in J_3, when you substitute (z,r,ϕ) by (z,R,ϕ) in the q_r1, q_r2, q_r3, and q_rv equations, ρ_R will be zero when $\cos(\phi-\chi)>0$, so there are

$$q_r1(z,R,\phi)=\int_{\frac{\pi}{2}+\phi}^{\frac{3\pi}{2}+\phi}\int_0^{\rho_R(\chi)} I_1\frac{e^{-\beta\cdot\rho\cdot\sec\alpha_1}}{\rho}\sin\alpha_1\cos^3\alpha_1\cos(\phi-\chi)d\rho d\chi, \qquad (2\text{-}55a)$$

$$q_r2(z,R,\phi)=\int_{\frac{\pi}{2}+\phi}^{\frac{3\pi}{2}+\phi}\int_0^{\rho_R(\chi)} I_2\frac{e^{-\beta\cdot\rho\cdot\sec\alpha_2}}{\rho}(-1)\sin\alpha_2\cos^3\alpha_2\cos(\phi-\chi)d\rho d\chi, \qquad (2\text{-}55b)$$

$$q_r3(z,R,\phi)=\int_{\frac{\pi}{2}+\phi}^{\frac{3\pi}{2}+\phi}\int_{\alpha_1}^{\alpha_2} I_3e^{-\beta\cdot\rho_R\cdot\sec\alpha}(-1)\cos^2\alpha\cos(\phi-\chi)\cdot d\alpha d\chi, \qquad (2\text{-}55c)$$

$$q_rv(z,R,\phi)=\int_{\frac{\pi}{2}+\phi}^{\frac{3\pi}{2}+\phi}\int_0^{\rho_R}\int_{\alpha_1}^{\alpha_2}\left\{(1-\omega)I_b(T)+\frac{\omega}{4\pi}\left[G-a_1q_r\cos(\phi-\chi)\cos\alpha-a_1q_z\sin\alpha+a_1q_\phi\sin(\phi-\chi)\cos\alpha\right]\right\}\cdot e^{-\beta\cdot\rho\cdot\sec\alpha}(-1)\cos(\phi-\chi)\cos\alpha\cdot d\alpha(\beta d\rho)d\chi \qquad (2\text{-}55d)$$

Put above equations in (2-16c), we get the expression for J_3.

2.4 Numerical Method

In order to evaluate coupled equations (2-54), uniform grids 24×24 divide the domain. Piecewise linear or second order Lagrange polynomial interpolation are assumed

for the incident radiation and heat fluxes and 20 point Gauss-Legendre quadrature was used to integrate equations. Iteration method was used to solve them simultaneously. It is found the convergence is fast while the criterion can be set very small (10^{-5} to 10^{-8}).

The values of incident radiation and heat fluxes on the boundaries are obtained by direct computation from the integrals as:

The values on surface 1

$$\begin{aligned} G|_{surface1} &= \lim_{z\to 0} G(z,r,\phi) \\ &= \lim_{z\to 0}\left[G1(z,r,\phi)+G2(z,r,\phi)+G3(z,r,\phi)+Gv(z,r,\phi)\right], \\ &= 2J_1(0,r,\phi)+G2(0,r,\phi)+G3(0,r,\phi)+Gv(0,r,\phi) \end{aligned} \tag{2-56a}$$

$$\begin{aligned} q_r|_{surface1} &= \lim_{z\to 0} q_r(z,r,\phi) \\ &= \lim_{z\to 0}\left[q_r1(z,r,\phi)+q_r2(z,r,\phi)+q_r3(z,r,\phi)+q_rv(z,r,\phi)\right], \\ &= 0+q_r2(0,r,\phi)+q_r3(0,r,\phi)+q_rv(0,r,\phi) \end{aligned} \tag{2-56b}$$

$$\begin{aligned} q_z|_{surface1} &= \lim_{z\to 0} q_z(z,r,\phi) \\ &= \lim_{z\to 0}\left[q_z1(z,r,\phi)+q_z2(z,r,\phi)+q_z3(z,r,\phi)+q_zv(z,r,\phi)\right], \\ &= J_1(0,r,\phi)+q_z2(0,r,\phi)+q_z3(0,r,\phi)+q_zv(0,r,\phi) \end{aligned} \tag{2-56c}$$

$$\begin{aligned} q_\phi|_{surface1} &= \lim_{z\to 0} q_\phi(z,r,\phi) \\ &= \lim_{z\to 0}\left[q_\phi1(z,r,\phi)+q_\phi2(z,r,\phi)+q_\phi3(z,r,\phi)+q_\phi v(z,r,\phi)\right] \\ &= 0+q_\phi2(0,r,\phi)+q_\phi3(0,r,\phi)+q_\phi v(0,r,\phi) \end{aligned} \tag{2-56d}$$

The values on surface 2

$$\begin{aligned} G|_{surface2} &= \lim_{z\to L} G(z,r,\phi) \\ &= \lim_{z\to L}\left[G1(z,r,\phi)+G2(z,r,\phi)+G3(z,r,\phi)+Gv(z,r,\phi)\right], \\ &= G1(L,r,\phi)+2J_2(L,r,\phi)+G3(L,r,\phi)+Gv(L,r,\phi) \end{aligned} \tag{2-57a}$$

$$\begin{aligned} q_r|_{surface2} &= \lim_{z\to L} q_r(z,r,\phi) \\ &= \lim_{z\to L}\left[q_r1(z,r,\phi)+q_r2(z,r,\phi)+q_r3(z,r,\phi)+q_rv(z,r,\phi)\right], \\ &= q_r1(L,r,\phi)+0+q_r3(L,r,\phi)+q_rv(L,r,\phi) \end{aligned} \tag{2-57b}$$

$$
\begin{aligned}
q_z\big|_{surface2} &= \lim_{z\to L} q_z(z,r,\phi) \\
&= \lim_{z\to L}\left[q_z1(z,r,\phi)+q_z2(z,r,\phi)+q_z3(z,r,\phi)+q_zv(z,r,\phi)\right], \\
&= q_z1(L,r,\phi)-J_2(L,r,\phi)+q_z3(L,r,\phi)+q_zv(L,r,\phi)
\end{aligned}
\qquad \text{(2-57c)}
$$

$$
\begin{aligned}
q_\phi\big|_{surface2} &= \lim_{z\to L} q_\phi(z,r,\phi) \\
&= \lim_{z\to L}\left[q_\phi1(z,r,\phi)+q_\phi2(z,r,\phi)+q_\phi3(z,r,\phi)+q_\phi v(z,r,\phi)\right] \\
&= q_\phi1(L,r,\phi)+0+q_\phi3(L,r,\phi)+q_\phi v(L,r,\phi)
\end{aligned}
\qquad \text{(2-57d)}
$$

The values on surface 3

$$
\begin{aligned}
G\big|_{surface3} &= \lim_{r\to R} G(z,r,\phi) \\
&= \lim_{r\to R}\left[G1(z,r,\phi)+G2(z,r,\phi)+G3(z,r,\phi)+Gv(z,r,\phi)\right] \\
&= G1(z,R,\phi)+G2(z,R,\phi)+\left[2J_3(z,R,\phi)+G3(z,R,\phi)\right]+Gv(z,R,\phi)
\end{aligned}
\qquad \text{(2-58a)}
$$

$$
\begin{aligned}
q_r\big|_{surface3} &= \lim_{r\to R} q_r(z,r,\phi) \\
&= \lim_{r\to R}\left[q_r1(z,r,\phi)+q_r2(z,r,\phi)+q_r3(z,r,\phi)+q_rv(z,r,\phi)\right] \\
&= q_r1(z,R,\phi)+q_r2(z,R,\phi)+\left[-J_3(z,R,\phi)+q_r3(z,R,\phi)\right]+q_rv(z,R,\phi)
\end{aligned}
\qquad \text{(2-58b)}
$$

$$
\begin{aligned}
q_z\big|_{surface3} &= \lim_{r\to R} q_z(z,r,\phi) \\
&= \lim_{r\to R}\left[q_z1(z,r,\phi)+q_z2(z,r,\phi)+q_z3(z,r,\phi)+q_zv(z,r,\phi)\right] \\
&= q_z1(z,R,\phi)+q_z2(z,R,\phi)+\left[0+q_z3(z,R,\phi)\right]+q_zv(z,R,\phi)
\end{aligned}
\qquad \text{(2-58c)}
$$

$$
\begin{aligned}
q_\phi\big|_{surface3} &= \lim_{r\to R} q_\phi(z,r,\phi) \\
&= \lim_{r\to R}\left[q_\phi1(z,r,\phi)+q_\phi2(z,r,\phi)+q_\phi3(z,r,\phi)+q_\phi v(z,r,\phi)\right] \\
&= q_\phi1(z,R,\phi)+q_\phi2(z,R,\phi)+\left[0+q_\phi3(z,R,\phi)\right]+q_\phi v(z,R,\phi)
\end{aligned}
\qquad \text{(2-58d)}
$$

We can see at the boundaries, some values of incident radiation and heat fluxes are not the same as calculated or expressed by the integral equations (2-12) and transformed integral equations (2-54). In other words, equations (2-12) and (2-54) are invalid at boundaries. The incident radiation and heat fluxes at the intersection of boundary surfaces are obtained by multidimensional extrapolation.

2.5 Results and Discussions

In order to validate the current code, some 2-D cases in the literature were run and compared with the available data. The method is then extended to 3-D problems. The description for those problems is presented below.

2.5.1 Two-Dimensional Results

For simplicity, the application of the current method is illustrated in a 2-D axisymmetric cylinder (finite in z) for comparison to published results. Assuming axisymmetric loading on the boundary, the heat flux q_ϕ will disappear. The incident radiation and other two heat fluxes will become the functions of only two variables (z,r). The 3-D equations are easily resolved to 2-D for comparison to published results (see Appendix A).

The resultant equations are coupled, so we need to solve them simultaneously including boundary conditions. In specific computations, cold boundaries are considered, i.e., $I_i=0$, i=1,2,3, but the walls diffusely reflect radiation, i.e., $\varepsilon_1=\varepsilon_2=\varepsilon_3=0.5$. The medium is at a uniform temperature such that $I_b[T(\tau_z,\tau_r)]=1$. The effects of the scattering albedo ω on the incident radiation and heat fluxes are evaluated. Figure 2-7 shows the distribution of the heat flux $q_r(\tau_z,R)$ versus axial optical thickness compared with Li, Ozisik, and Tsai [2.13] and Thynell [2.14] results. There is good overall agreement of the present work with these results. However, there is difference near the boundary z=0 and z=L, particularly with smaller ω.

The effects of ω on the distribution of centerline incident radiation G and heat flux q_z in axial direction are shown in Figure 2-8. Both the incident radiation and heat

flux q_z are symmetric to z=L/2 plane and decrease with increasing scattering albedo. Furthermore, results become more uniform with larger scattering albedo.

Figure 2-9 is about the distributions of the incident radiation and heat flux q_r at the middle plane z=L/2 with respect to normalized optical thickness τ_r/R. The distribution of the heat flux q_z on the top surface with respect to normalized optical thickness τ_r/R is illustrated in Figure 2-10. We can see they are symmetric to the center axis r=0 and radial heat flux q_r is zero at the centerline.

Figure 2-11 shows the contributions of each integrals term to the total incident radiation. The term Gv comes from the integration of the volume source term, i.e., the last integral term in equation (2-59a). G1, G2, and G3 are the contributions of the bottom, top, and side surface emitting and reflecting respectively, i.e., the first, the second, and the third integral term in equation (2-59a). The sum of them is the total incident radiation G. In the case of cold walls with $\varepsilon_1=\varepsilon_2=\varepsilon_3=0.5$, Gv contributes most; G1 and G2 are the same at the middle plane (average 3.6 percent of G).

Figure 2-12 shows the distributions of the individual integrals of heat flux $q_r(0.5L,\tau_r)$ vs. normalized radial optical thickness. The effect of sidewall emitting and reflecting $q_r3(0.5L,\tau_r)$ is negative. Therefore, the total heat flux is smaller than the heat flux q_rv, which is the result of the volume source term integration including medium emitting and scattering. q_r1 or q_r2 contribute about 12 percent of the total radial heat flux while q_r3 contributes about 75 percent of the total heat flux (negative effect).

In Figure 2-13, one can see the effects of the optical thickness on the heat flux at the sidewall. Again, there exists a difference at the boundary edges compared with Li, Ozisik, and Tsai [2.13] and Thynell [2.14] results. For larger optical thickness, there is

larger difference at the edge. The Thynell [2.14] solution was constructed using power series expansions and collocation methods based on discrete ordinates. Here, the non-grid terms in the integral are interpolated or extrapolated during integration; however, the grid values are iterated to the convergence criteria noted earlier. In the limit as grid spacing decreases in the current method, the exact solution should result. So there may exist some approximation, while the present work uses exact integral equations.

Most of the data presented in above figures used 19 iterations with a convergence criterion of 10^{-5}. Typical computation time was about 5 minutes in Digital Fortran 5.0 on a generic PC with 1GB memory and an AMD Athlon™ XP 1.2 GHz processor.

2.5.2 Three-Dimensional Results

Radiative heat transfer with absorbing, emitting and scattering medium in a three-dimensional cylinder (L=2R=1.0) is considered. The boundaries are diffusely emitting and reflecting opaque walls. The bottom and top boundaries are cold and black. The medium is at uniform temperature such that $I_b[T(\tau_z,\tau_r,\tau_\Phi)]=1$. The following 6 cases will be computed for comparison purpose. Note that these 3-D cases represent opaque partial side wall diffuse emission and/or reflection. Cases 1-2 have continuous side wall radiosity change around angular coordinate along the full height of the finite cylinder, and present a true ϕ variation. Cases 3 to 5 present true non-symmetric partial wall cases. Case 6 has highly forward and backward scatter.

Table 2-1 Case conditions for 3-D radiative heat transfer computations

	Side surface emitting property (surface 3)	**Side surface ε (surface 3)**
Case 1	Cold wall, $I_3=0$	$\varepsilon_3=1/2(1-\sin\phi)$ ($\omega=0.1,0.5,0.9$, $a_l=0$)
Case 2	$J_3=\pi(1+\sin\phi)$, or $I_3=(1+\sin\phi)$	Black wall $\varepsilon_3=1.0$ ($\omega=0.5$, $a_l=0$)
Case 3	Half of the wall $[0,\pi]$ & [0,L] emitting, $J_3=\pi$ ($I_3=1$); Another half $J_3=0$.	Black wall $\varepsilon_3=1.0$ ($\omega=0.5$, $a_l=0$)
Case 4	Quarter of the wall $[0,\pi/2]$ & [0,L] emitting, $J_3=\pi$ ($I_3=1$); Another part $J_3=0$.	Black wall $\varepsilon_3=1.0$ ($\omega=0.5$, $a_l=0$)
Case 5	Quarter of the wall $[0,\pi]$ & [L/2,L] emitting, $J_3=\pi$ ($I_3=1$); Another part $J_3=0$.	Black wall $\varepsilon_3=1.0$ ($\omega=0.5$, $a_l=0$)
Case 6	Same as case 1, except anisotropically scattering	Same as case1, $\omega=0.5$ (but $a_l=0.99$, -0.99)

The effects of ω on the distribution of heat fluxes $q_r(\tau_z,R,0)$ and $q_\phi(\tau_z,R,0)$ in axial position are shown in Figure 2-14. We can see that $q_r(\tau_z,R,0)$ decreases with increasing scattering albedo as in 2-D cases, the magnitude of $q_\phi(\tau_z,R,0)$ also decreases with increasing albedo. Both of them become more uniform with larger albedo.

Figure 2-15 shows the distribution of heat fluxes $q_r(0.5L,\tau_r,0)$ and $q_\phi(0.5L,\tau_r,0)$ with respect to radial position τ_r/R. The heat flux $q_\phi(0.5L,\tau_r,0)$ in angular ϕ direction is also symmetric to the center axis r=0.

The incident radiation at mid-plane $\tau_z=0.5L$, but different radial position is shown in Figure 2-16 changing with angle ϕ. At side surface r=R, $G(0.5L,R,\phi)$ changes the most with the angle; while at center line r=0, $G(0.5L,0,\phi)$ remains constant. We can

also see the effects of scattering albedo from the Figure. The smallest albedo makes the biggest change around angle ϕ.

The heat fluxes q_r and q_ϕ at mid-plane τ_z=0.5L, but different radial position is shown in Figure 2-17 changing with angle ϕ. Unlike incident radiation, center line heat fluxes $q_r(0.5L,0,\phi)$ and $q_\phi(0.5L,0,\phi)$ change with ϕ instead of remaining constant, but they tend toward sinusoidal change around the zero horizontal axis. One interesting phenomenon is that the magnitude of heat flux at side surface $q_r(0.5L,R,\phi)$ may be larger than $q_r(0.5L,0,\phi)$, while the magnitude of $q_\phi(0.5L,R,\phi)$ is always smaller than $q_\phi(0.5L,0,\phi)$.

Figure 2-18 shows the distribution of heat flux q_z around angle ϕ. We see that q_z at the bottom surface τ_z=0 and the top surface τ_z=L are symmetric to the zero horizontal axis. Like incident radiation, center line heat flux $q_z(0,0,\phi)$ or $q_z(L,0,\phi)$ does not change with angle ϕ.

The comparison of heat flux q_r at mid-plane τ_z=0.5L for Case 1 and Case 2 is shown in Figure 2-19. The magnitude of $q_r(0.5L,0,\phi)$ and $q_r(0.5L,R,\phi)$ of Case 2 is much bigger than that of Case 1. At side surface, $q_r(0.5L,R,\phi)$ can not be negative for Case 1, only reflecting situation. But for Case 2, black wall emitting boundary, $q_r(0.5L,R,\phi)$ could be negative or positive.

Figure 2-20 gives the comparison of incident radiation $G(0.5L,0.5R,\phi)$ and heat flux $q_\phi(0.5L,0,\phi)$ for Case 2, Case 3 and Case 4. Both the incident radiation and heat flux of Case 3, which is half wall emitting, change around ϕ in a similar tendency as that of Case 2, which is sidewall continuous emitting in sine function of ϕ. This is reasonable

conceptually. The $G(0.5L,0.5R,\phi)$ and $q_\phi(0.5L,0,\phi)$ of Case 4, which has a quarter of the wall emitting, changes along ϕ differently as shown in Figure 2-20. During the range $[0,\pi/2]$, the incident radiation reaches the local maximum value, which is expected.

The distribution of heat flux q_z around ϕ is shown in Figure 2-21 for Case 2, Case 3 and Case 4. The heat flux $q_z(0,0,\phi)$ at the bottom surface and center point remains constant in three cases, but $q_z(0,0.5R,\phi)$ changes with ϕ. We see again here that $q_z(0,0.5R,\phi)$ of Case 3 changes along ϕ with similar shape as Case 2. The $q_z(0,0.5R,\phi)$ of Case 4 follows a similar curve coinciding with the quarter wall $[0,\pi/2]$ emitting boundary condition.

Figure 2-22 displays the changes of $q_r(0.5L,0,\phi)$ and $q_r(0.5L,0.5R,\phi)$ along ϕ for Case 3 and Case 4. The magnitude of $q_r(0.5L,0.5R,\phi)$ is larger than $q_r(0.5L,0,\phi)$ in Case 4 during $[0,\pi/2]$, while smaller than $q_r(0.5L,0,\phi)$ in Case 3 during $[0,\pi]$. This is due to the extremely asymmetry of Case 4.

Figure 2-23 demonstrates the different distributions of incident radiation and heat flux q_z for Case 3 and Case 5. The $G(\tau_z,0,\pi/2)$, $G(\tau_z,0.5R,\pi/2)$ and $G(\tau_z,R,\pi/2)$ reach local maximum in the range of [0.5L,L] for Case 5. In Case 3 $q_z(\tau_z,0,\pi/2)$ is zero at $\tau_z=0.5L$, while the zero point of $q_z(\tau_z,0,\pi/2)$ will move higher to above 0.6L in Case 5. This is because the upper sidewall is emitting in Case 5.

The comparison between Case 3 and Case 5 is also shown in Figure 2-24 for heat flux q_r. Because the upper partial wall emission, we see the distributions as shown in the Figure. The heat flux $q_z(\tau_z,0.5R,\pi/2)$ are larger than $q_z(\tau_z,0,\pi/2)$ in magnitude in the range [0.5L,L] for Case 5.

The influences of linear anisotropic scattering coefficient a1 are shown in Figure 2-25 to Figure 2-29. There are no big differences among isotropic scattering, forward scattering and backward scattering, especially on the boundary, for the cases considered. From Figure 2-27, we can see the a1's influence in the range $[0,\pi]$ is weaker than the influence when ϕ in $[\pi,2\pi]$, that is because the side wall reflection ($0.5<\rho_3<1.0$) is stronger in the range of $[0,\pi]$ than the reflection ($0<\rho_3<0.5$) in $[\pi,2\pi]$.

However we can see in Figure 2-29, how $G(L/2,0,\phi)$, $G(L/2,R/48,\phi)$ and $G(L/2,R/16,\phi)$, which are grid point 1, 2 and 3 from the original point in r coordinate respectively, change with ϕ in isotropic case, forward scattering and backward scattering cases. This is interesting and because in forward scattering and backward scattering cases, the heat fluxes like q_r go into the source term. So the values of $G(0.5L,0,\phi)$ are not exactly constant when a1=0.99 and a1=-0.99 because of the numerical computation. But the values of $G(0.5L,0,\phi)$ will lie on the constant lines, without the expanded scale in Figure 28, for this case with an albedo of 0.5. The highly forward scatter case (a1=0.99) gives results slightly more than 1% lower on average than isotropic incident radiation, while highly backward scatter (a1=-0.99) gives slightly less than 1% greater than isotropic.

Computation times, on the same generic PC referred to earlier, ranged 5 to 6 hours for fully 3-D cases, this may be compared to about 5 minutes for 2-D cases.

For grid convergence, when we use double grid number to divide the domain, the average difference or error is about 0.1 percent. So we consider the current grid size is enough to get the convergent results.

2.6 Conclusions

A set of transformed integral equations for radiative transfer in a 3-D finite cylinder was developed that can be easily integrated by numerical method without singularity effects. Although there is a ρ in the denominator of the surface integral term (similar to the volume term in 1-D), it is well-behaved first order term and does not cause oscillations. The transformed 3-D equations were also cast into 2-D axisymmetric cylindrical media for comparison purposes. The numerical results show good agreement with published data except in extreme cases. Computational time for most of the 2-D comparisons was about 5 minutes on a good PC. A strong benefit of the current method is a detailed knowledge of each contribution of the volume and boundary to the total incident radiation and heat fluxes, which allows one to attack those computational terms giving the most difficulty with more robust methods, in future work.

Several simple 3-D cases were computed with the new integration strategy. Several of these cases included results for simple ϕ variation in the sidewall diffuse emission/reflection. Unlike 2-D cylindrically symmetric cases, G shows a small variation with ϕ along the cylinder axis for 3-D anisotropic scatter (Case 6). Other cases included true 3-D partial (in both z and ϕ) sidewall emission. The computational time for these new 3-D cases was still fairly large for the current generation of 1 to 2 GHz class PCs (5 to 6 hours). More efficient computational methods, such as those presented, allow application to more realistic modeling of nongray pure radiation and combined modes of heat transfer problems.

2.7 Nomenclature

a_l linear anisotropic scattering coefficient

A differential surface area, m^2

d distance, m

G incident radiation, W/m^2

I the radiation intensity, W/m^2

J the radiosity of the surface, W/m^2

L the cylinder height, m

q components of net radiative heat flux, W/m^2

R the cylinder out radius, m

S radiation source term, W/m^2

T temperature, K

V differential volume, m^3

Greek symbols

α the specified angle, transformed coordinate

β extinction coefficient, 1/m

ε the emissivity of the surface

θ angle between surface normal vector and the intensity direction

ρ the reflectivity of the surface, or the specified distance (transformed coordinate)

ϕ cylindrical angular coordinate

χ the specified angle, transformed coordinate

ω single scattering albedo

Ω the unit vector of the intensity direction, or the solid angle

Subscripts

b black body

i surface i

r radial direction

R at out radius position

z axial direction

ϕ angular direction

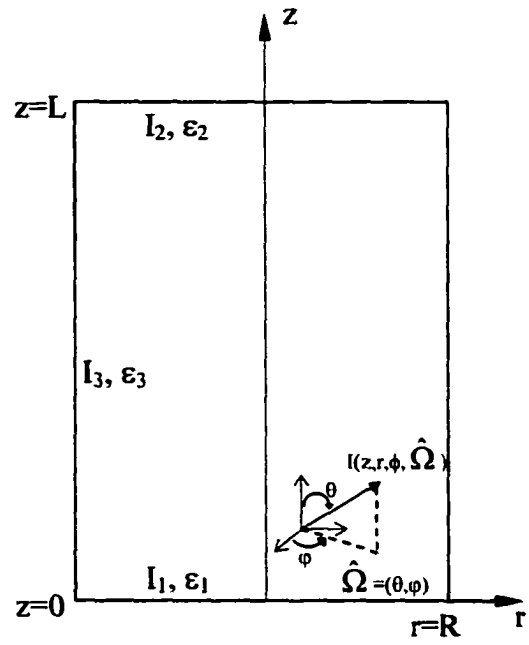

Figure 2-1 Illustration of the physical system and coordinates.

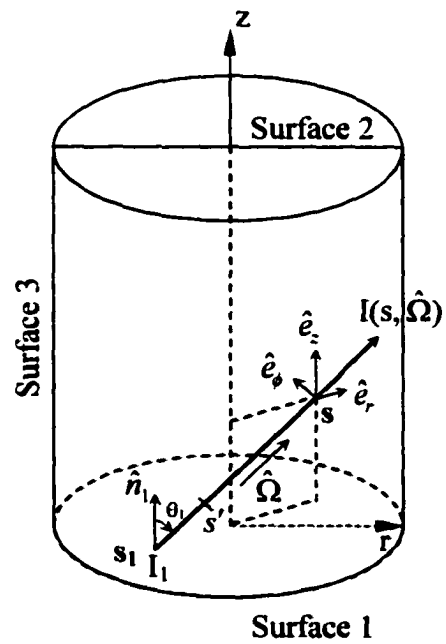

Figure 2-2 Schematic diagram of the physical model and radiation transfer path.

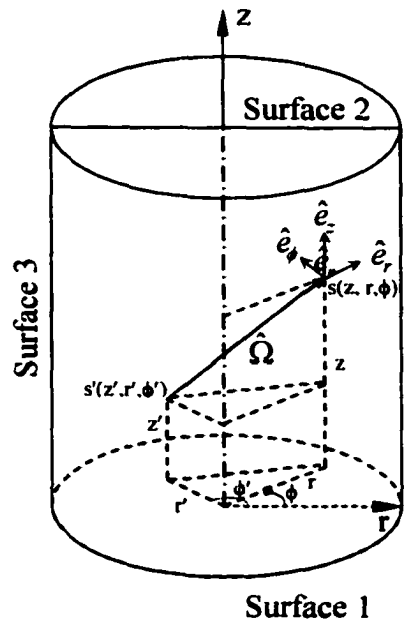

Figure 2-3 Schematic diagram of the coordinates and the radiant ray direction.

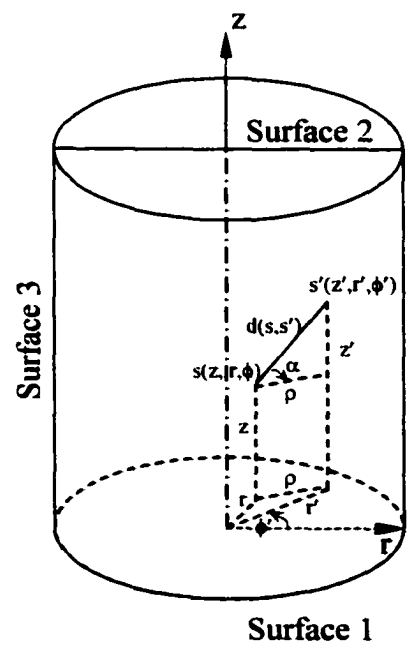

Figure 2-4 Schematic diagram of coordinates transformation.

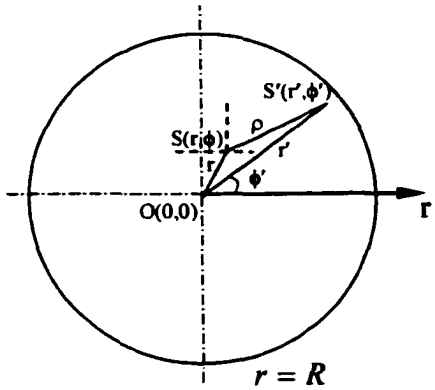

Figure 2-5 Top view of the cylinder coordinates transformation. Capital S is the projection of point s and capital S′ is the projection of point s′.

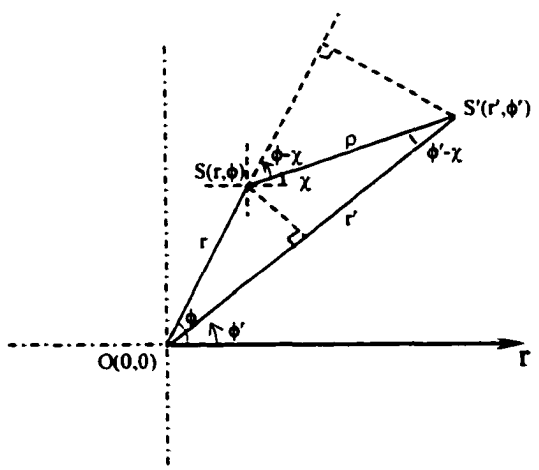

Figure 2-6 The enlarged illustration of coordinates transformation. Capital S is the projection of point s and capital S′ is the projection of point s′.

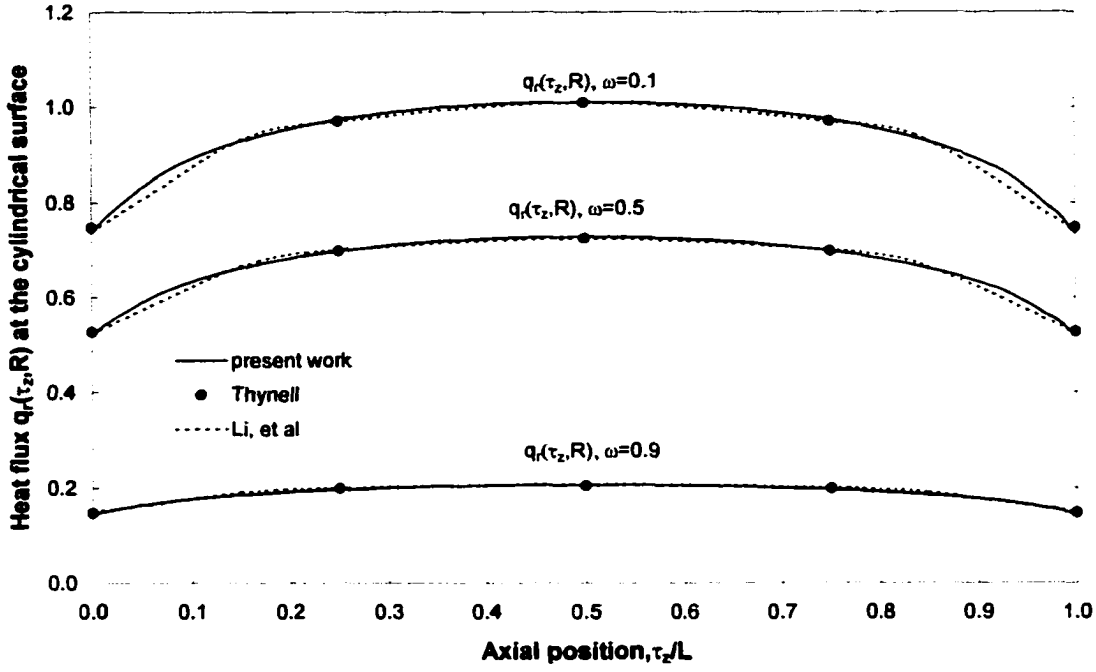

Figure 2-7 The effects of the scattering albedo on the radial heat flux $q_r(\tau_z,R)$ for a hot cylindrical medium enclosed by cold walls, $\varepsilon_1=\varepsilon_2=\varepsilon_3=0.5$, L=2R=1.0.

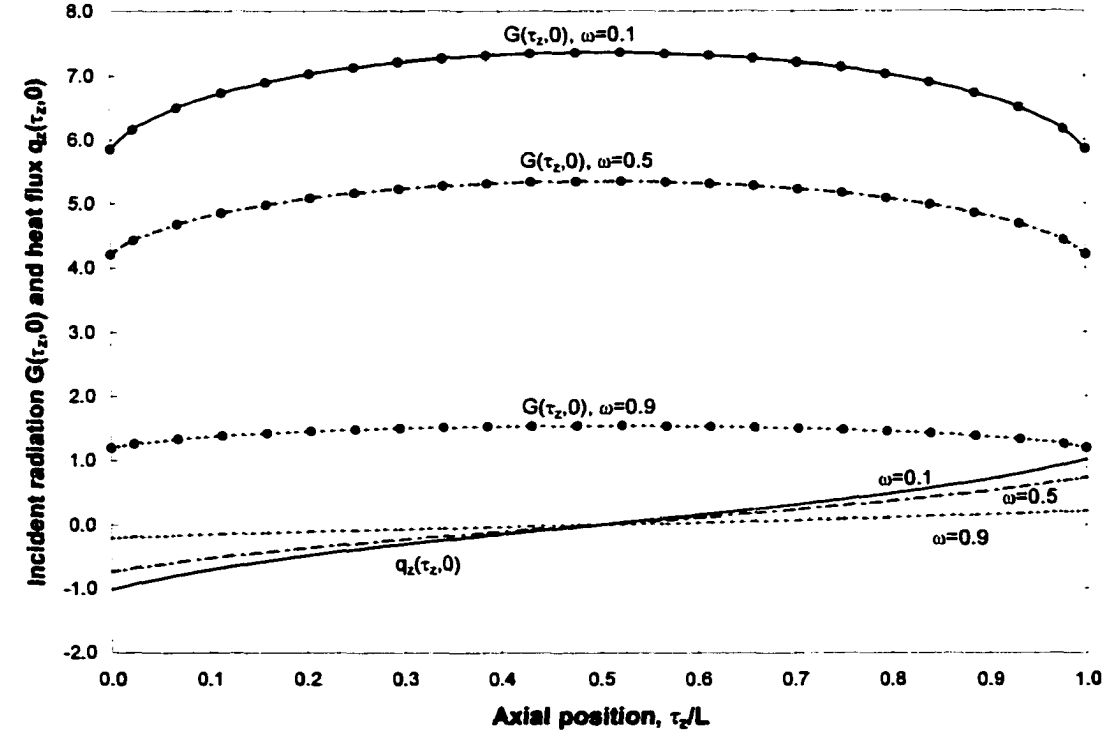

Figure 2-8 The effects of the scattering albedo on the distribution of centerline incident radiation $G(\tau_z,0)$ and axial heat flux $q_z(\tau_z,0)$, for a hot cylindrical medium enclosed by cold walls, $\varepsilon_1=\varepsilon_2=\varepsilon_3=0.5$, L=2R=1.0.

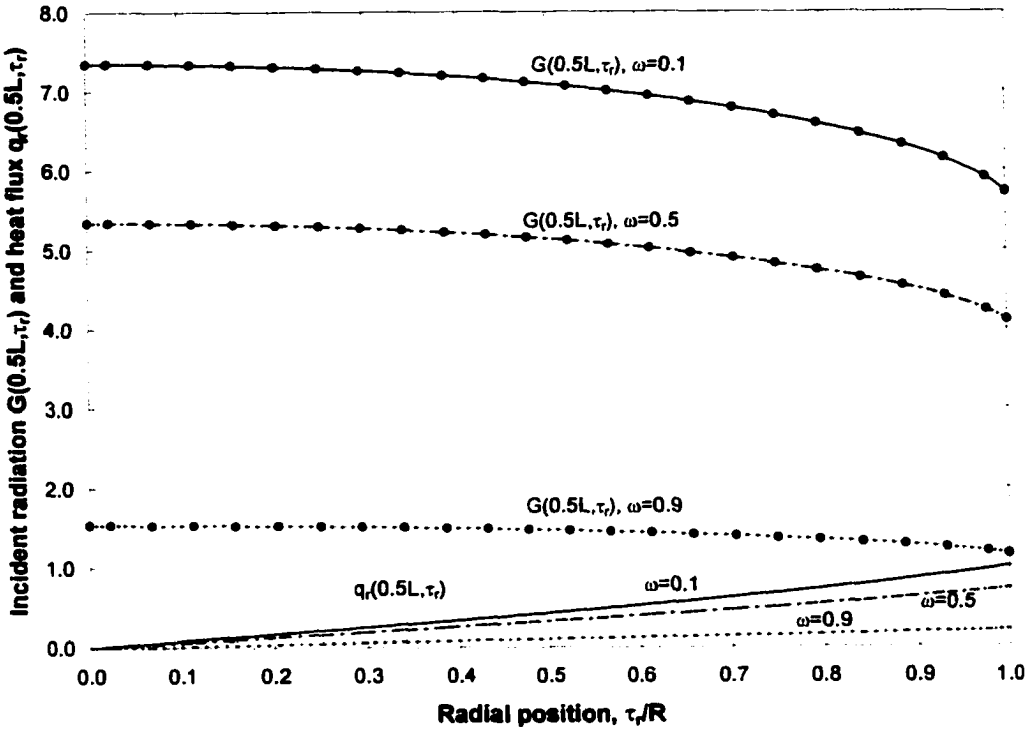

Figure 2-9 The effects of the scattering albedo on the distributions of incident radiation $G(L/2,\tau_r)$ and heat flux $q_r(L/2,\tau_r)$ with respect to τ_r/R, for a hot cylindrical medium enclosed by cold walls, $\varepsilon_1=\varepsilon_2=\varepsilon_3=0.5$, $L=2R=1.0$.

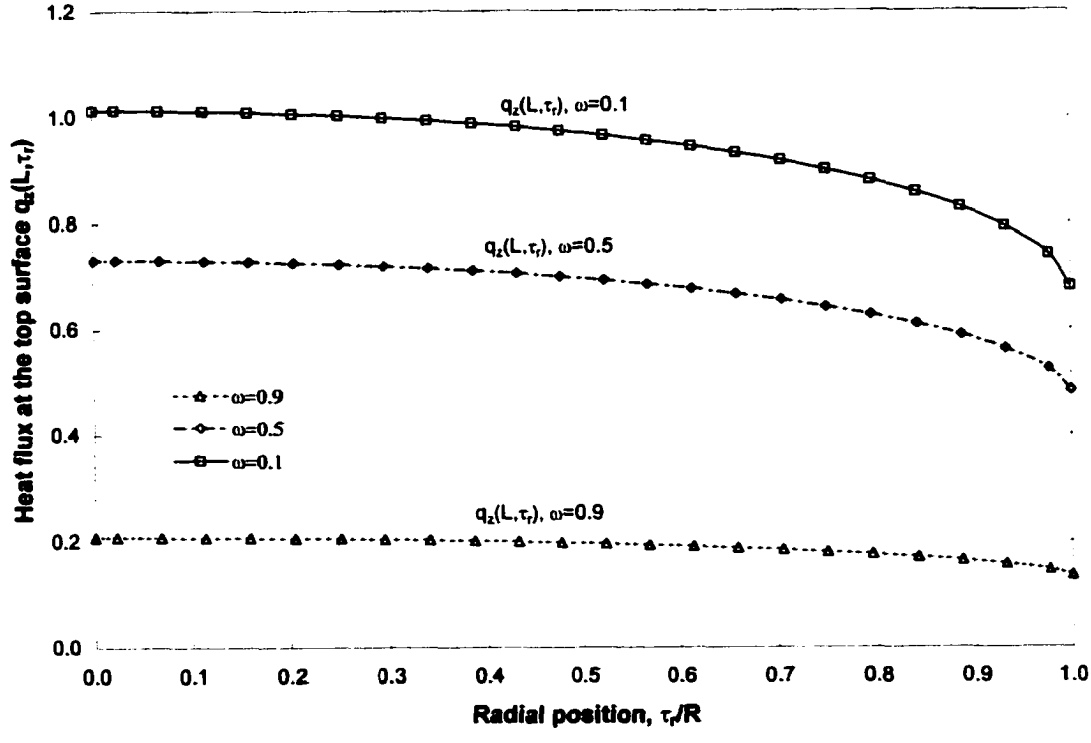

Figure 2-10 The effects of the scattering albedo on the distribution of axial heat flux $q_z(L,\tau_r)$ with respect to τ_r/R, for a hot cylindrical medium enclosed by cold walls, $\varepsilon_1=\varepsilon_2=\varepsilon_3=0.5$, $L=2R=1.0$.

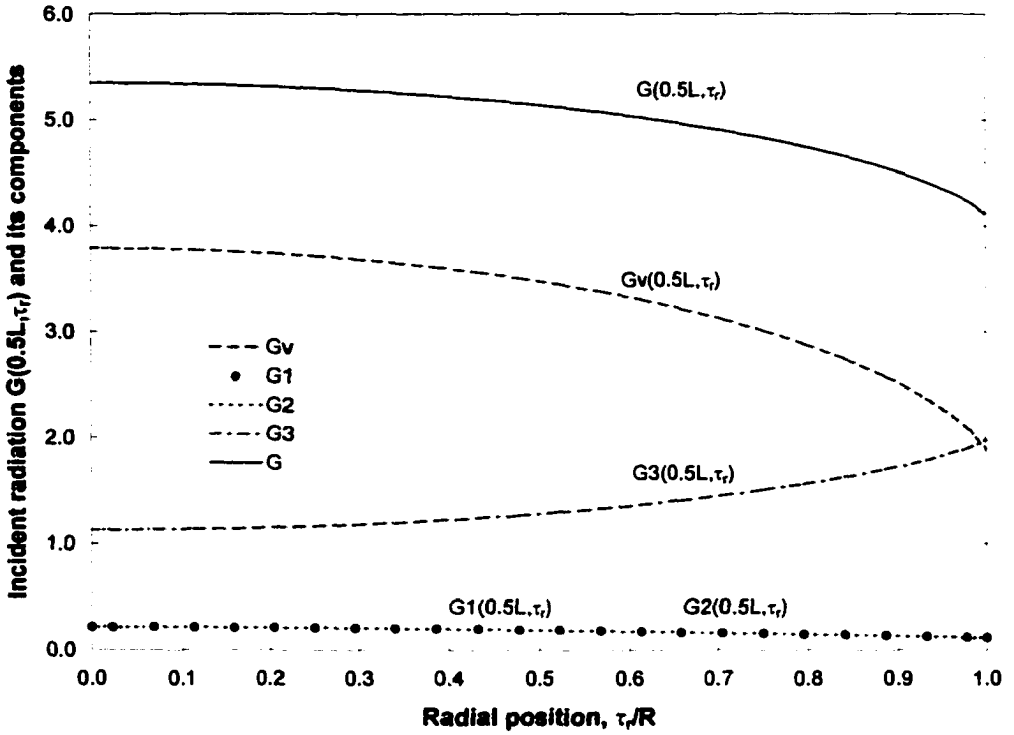

Figure 2-11 The distributions of the incident radiation $G(L/2,\tau_r)$ and its compositions $Gv(L/2,\tau_r)$, $G1(L/2,\tau_r)$, $G2(L/2,\tau_r)$ and $G3(L/2,\tau_r)$ with respect to τ_r/R, for a hot cylindrical medium enclosed by cold walls, $\varepsilon_1=\varepsilon_2=\varepsilon_3=0.5$, $\omega=0.5$, $L=2R=1.0$.

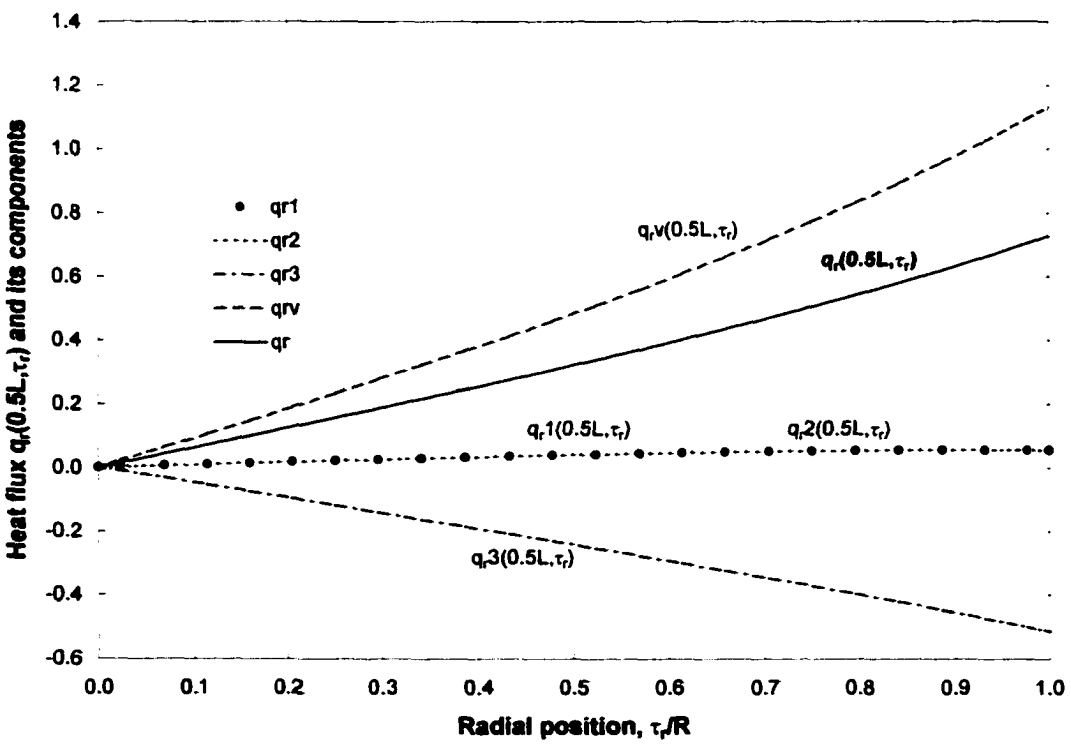

Figure 2-12 The distributions of $q_r(L/2,\tau_r)$, $q_rv(L/2,\tau_r)$, $q_r1(L/2,\tau_r)$, $q_r2(L/2,\tau_r)$ and $q_r3(L/2,\tau_r)$ with respect to τ_r/R, for a hot medium enclosed by cold walls, $\varepsilon_1=\varepsilon_2=\varepsilon_3=0.5$, $\omega=0.5$, $L=2R=1.0$.

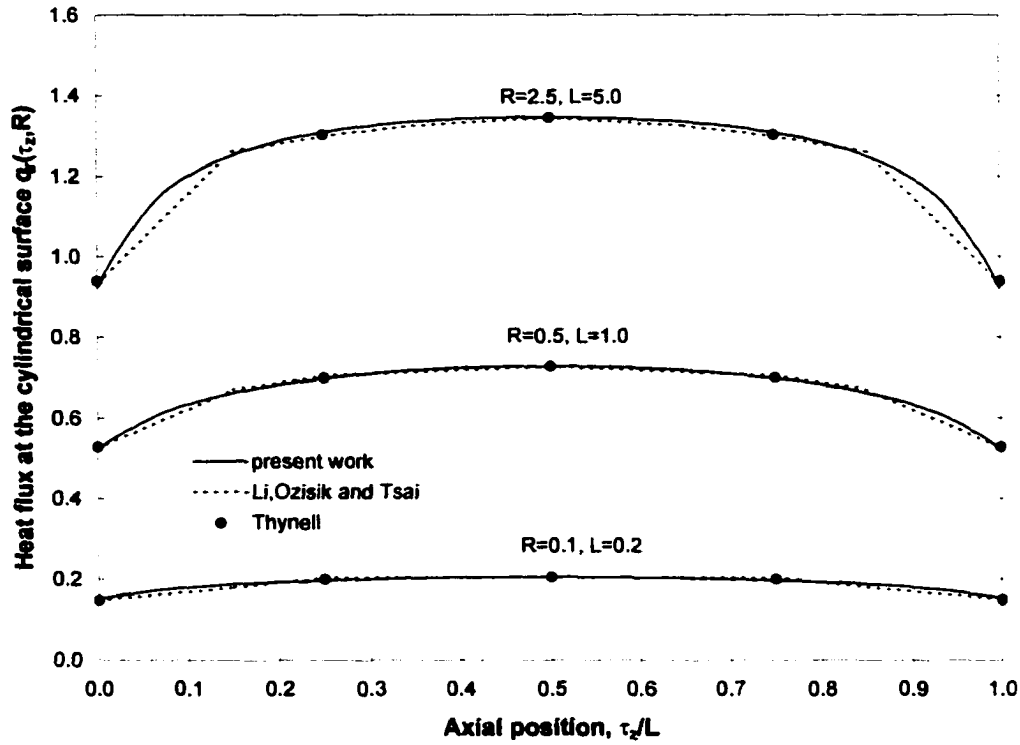

Figure 2-13 The effects of the optical thickness on the distribution of $q_r(\tau_z,R)$ with respect to normalized optical thickness τ_z/L, for a hot medium enclosed by cold walls, $\varepsilon_1=\varepsilon_2=\varepsilon_3=0.5$, $\omega=0.5$.

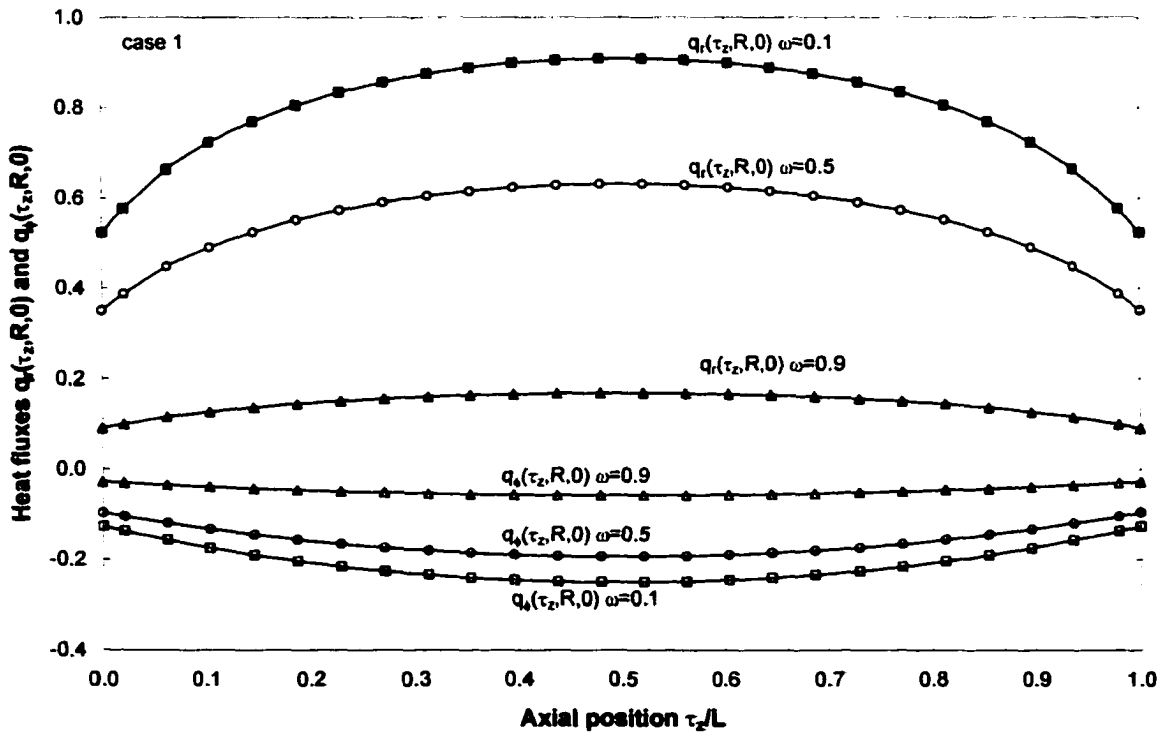

Figure 2-14 The effects of scattering albedo on heat fluxes $q_r(\tau_z,R,0)$ and $q_\phi(\tau_z,R,0)$ of a 3-D hot cylinder enclosed by cold walls with $\varepsilon_1=\varepsilon_2=1.0$, $\varepsilon_3=0.5(1-\sin\phi)$, see case 1 in table 2-1.

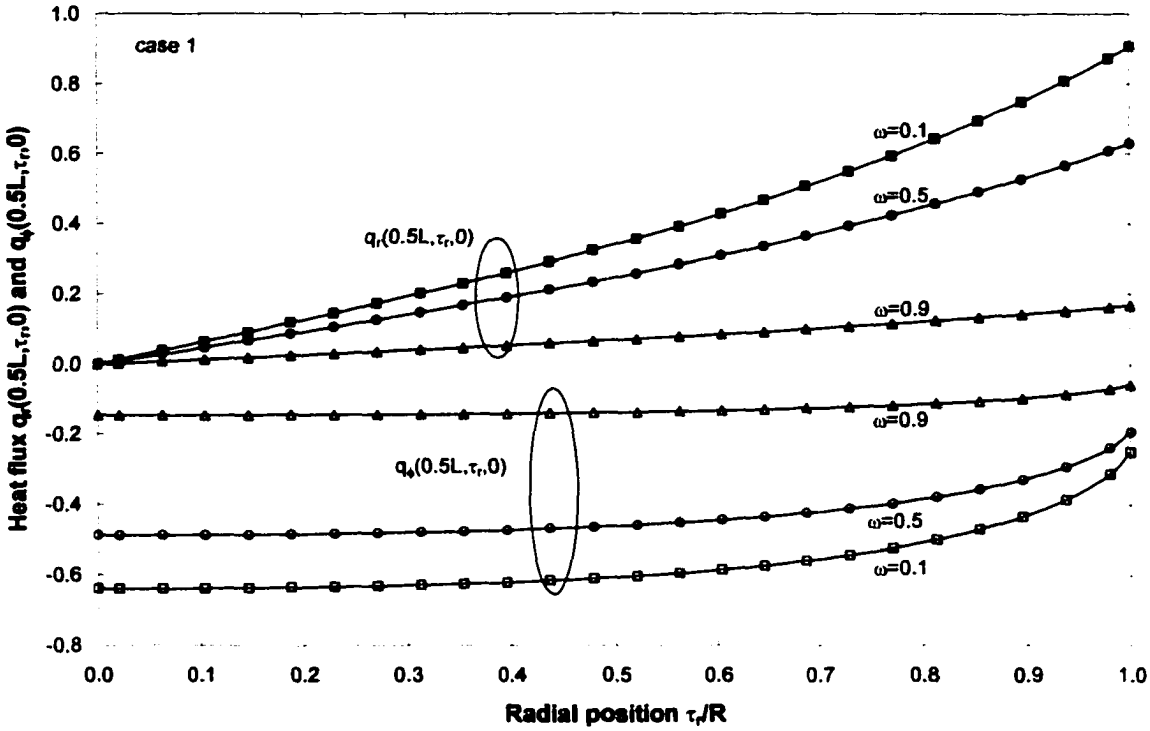

Figure 2-15 The effects of scattering albedo on the distribution of heat fluxes $q_r(0.5L,\tau_r,0)$ and $q_\phi(0.5L,\tau_r,0)$ with respect to normalized optical thickness τ_r/R for case 1 in table 2-1.

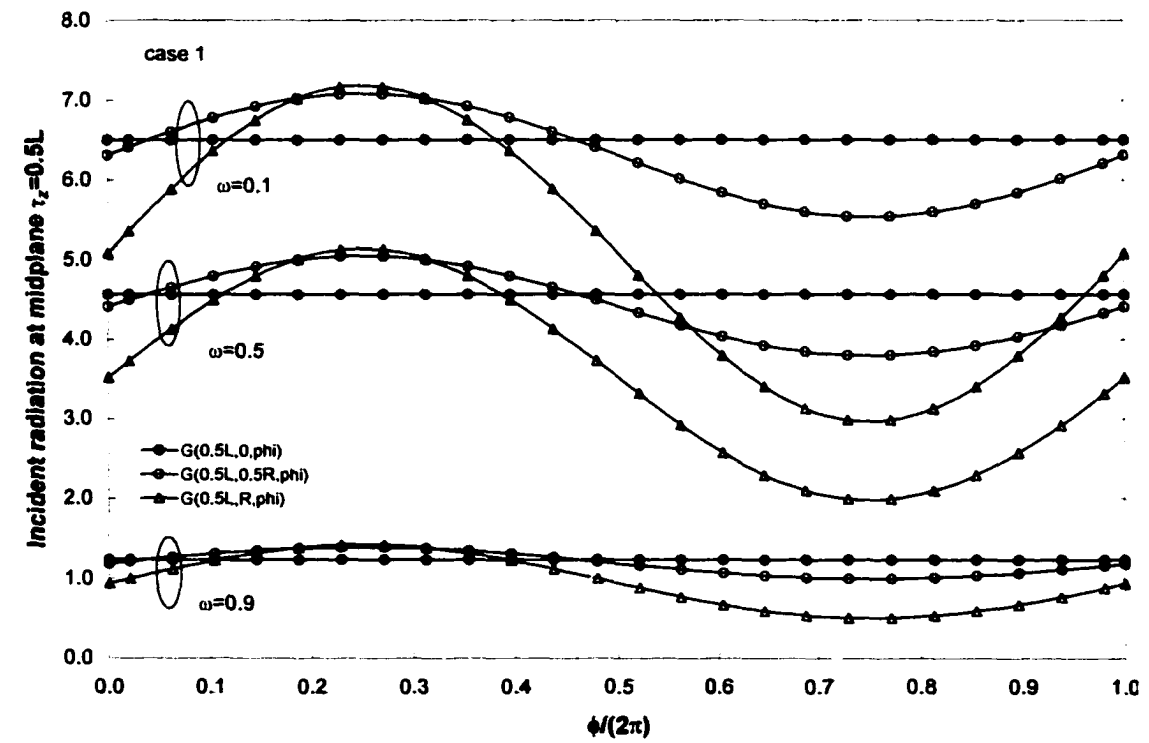

Figure 2-16 The effects of scattering albedo on the distribution of incident radiation at mid-plane τ_z=0.5L with respect to angular coordinate ϕ for case 1 in table 2-1.

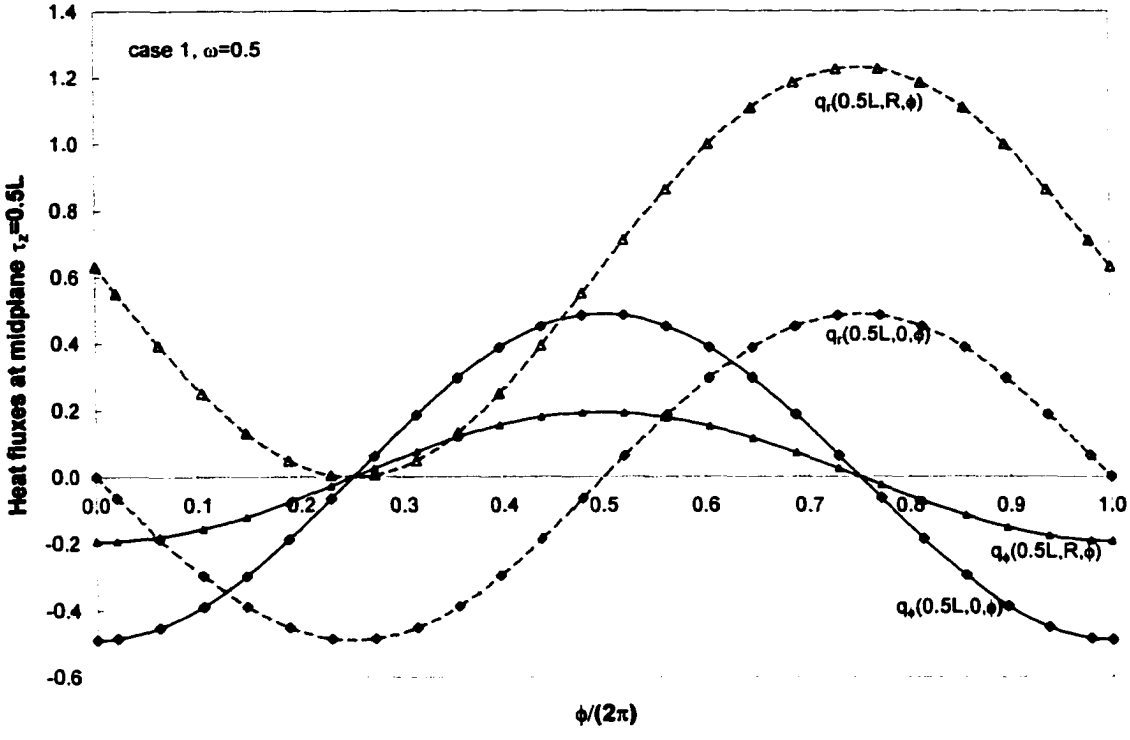

Figure 2-17 The distribution of heat fluxes q_r and q_ϕ at mid-plane τ_z=0.5L, but with different radial position, with respect to angular coordinate ϕ for case 1, ω=0.5.

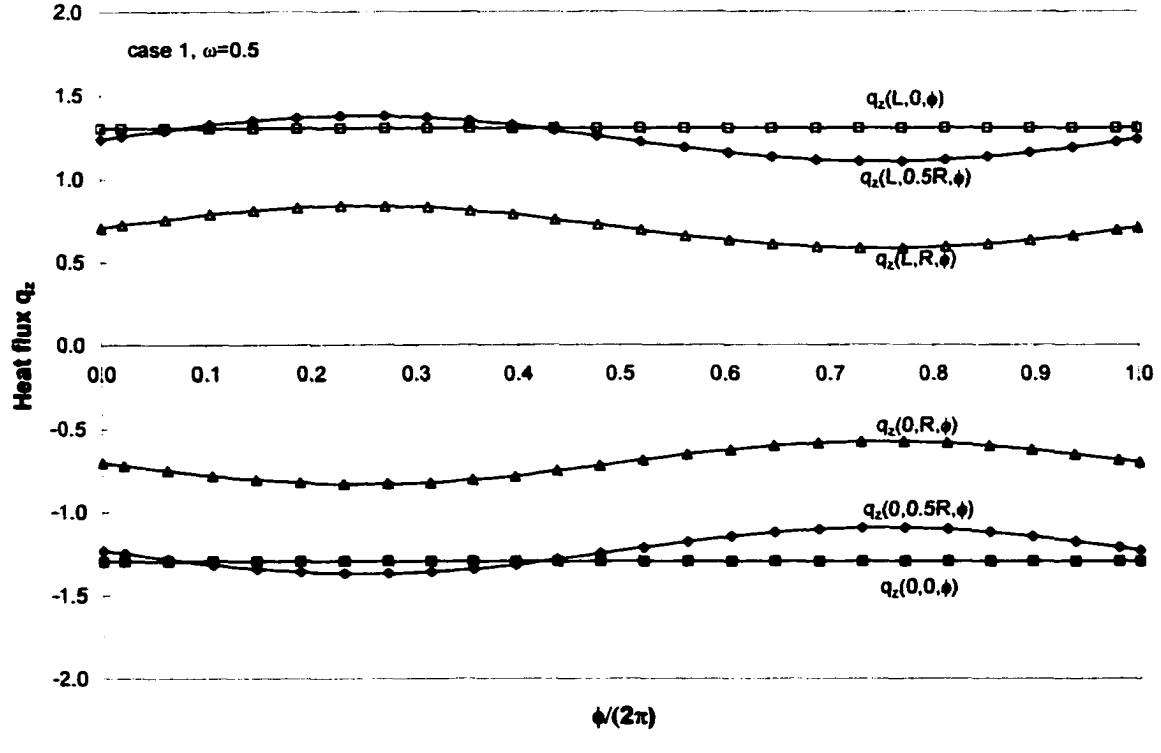

Figure 2-18 The distribution of heat fluxes q_z at bottom or top surface, but with different radial position, with respect to angular coordinate ϕ for case 1, ω=0.5.

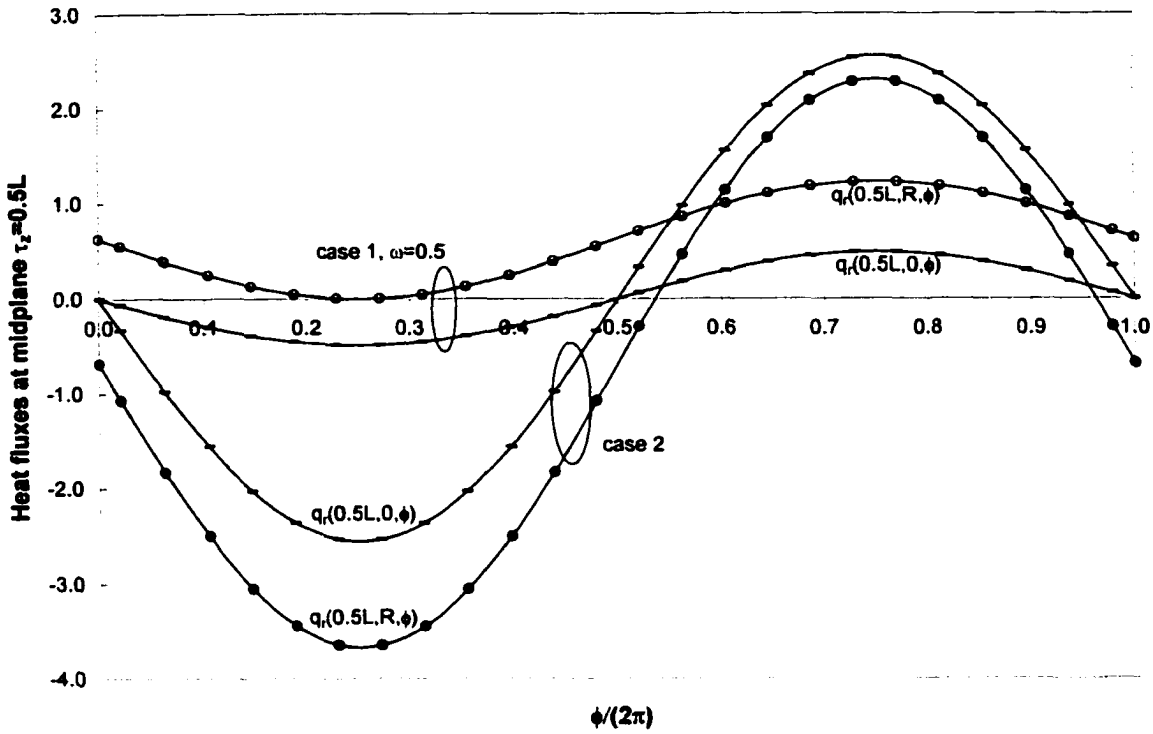

Figure 2-19 The comparison between case 1 (ω=0.5) and case 2 for heat flux $q_r(0.5L,0,\phi)$ and $q_r(0.5L,R,\phi)$ with respect to angular coordinate ϕ.

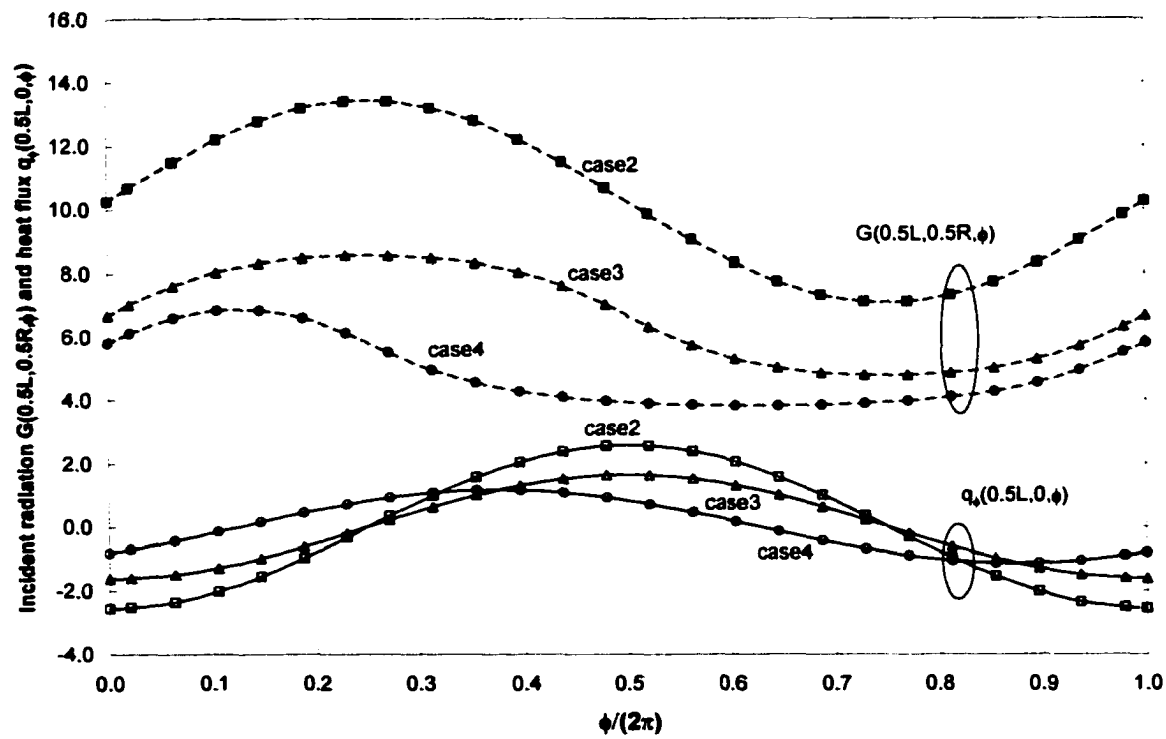

Figure 2-20 The distribution of incident radiation G(0.5L,0.5R,ϕ) and heat flux $q_\phi(0.5L,0,\phi)$ with respect to angular direction ϕ for case 2, case 3 and case 4 in table 2-1.

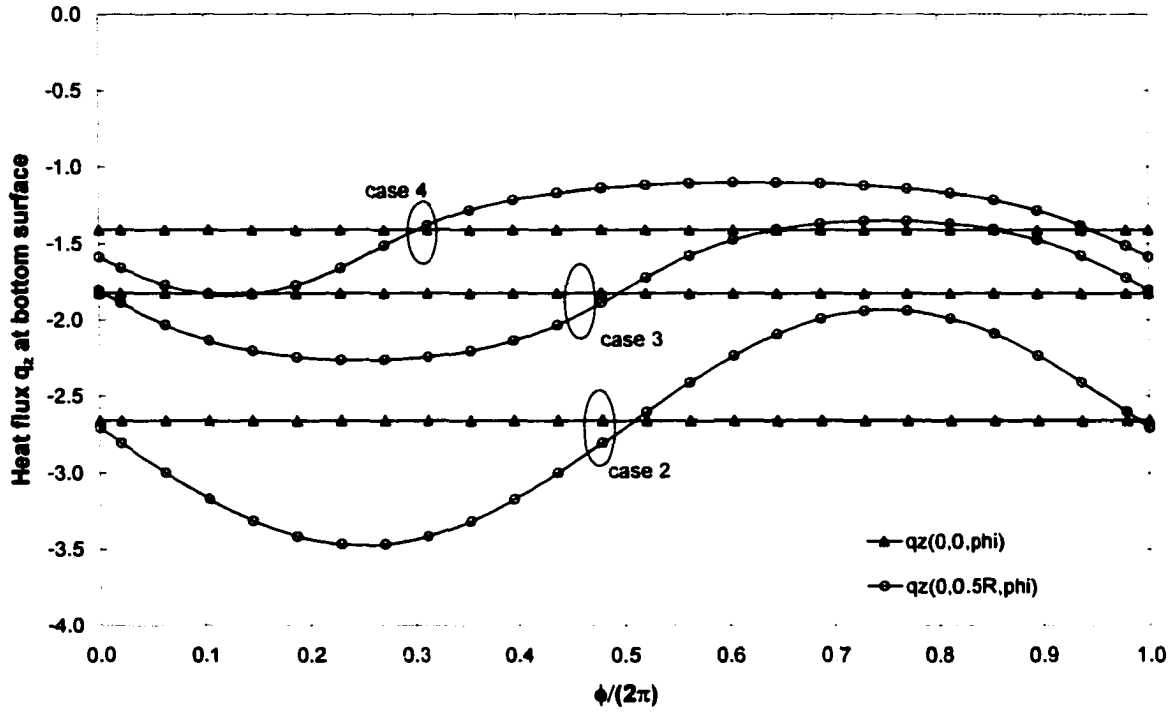

Figure 2-21 The distribution of heat flux q_z at bottom surface, but at different radial position, with respect to angular coordinate ϕ for case 2, case 3 and case 4 in table 2-1.

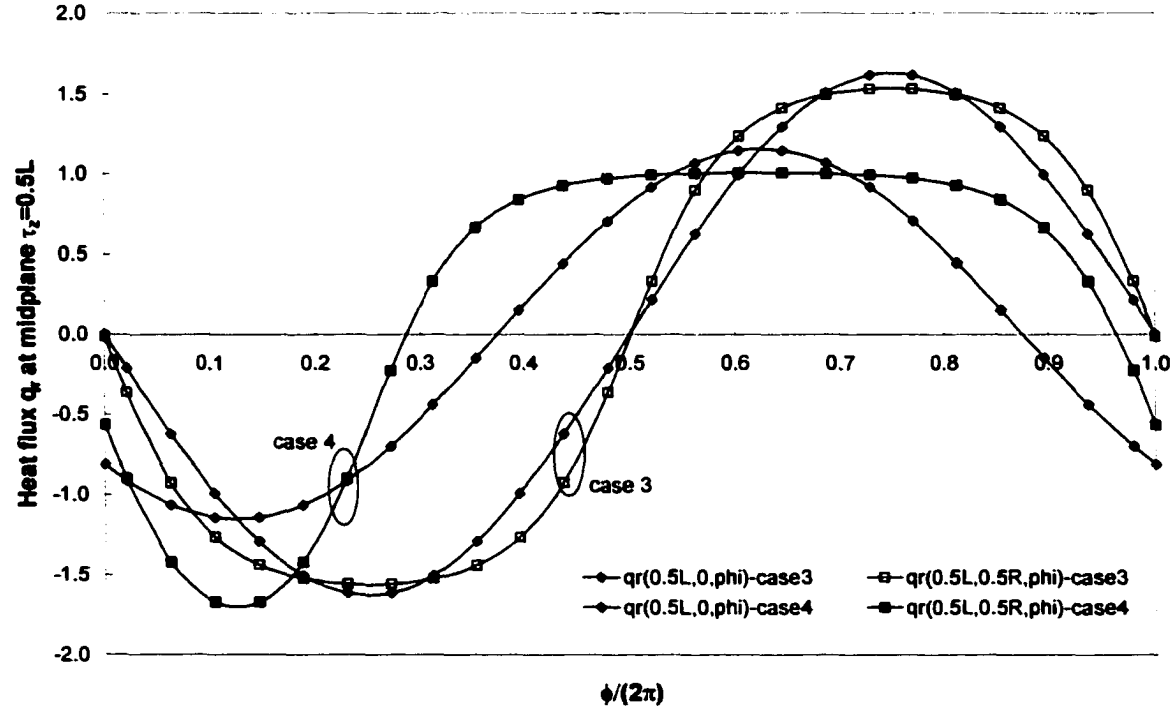

Figure 2-22 The comparison between case 3 and case 4 for heat flux $q_r(0.5L,0,\phi)$ and $q_r(0.5L,0.5R,\phi)$ with respect to angular coordinate ϕ.

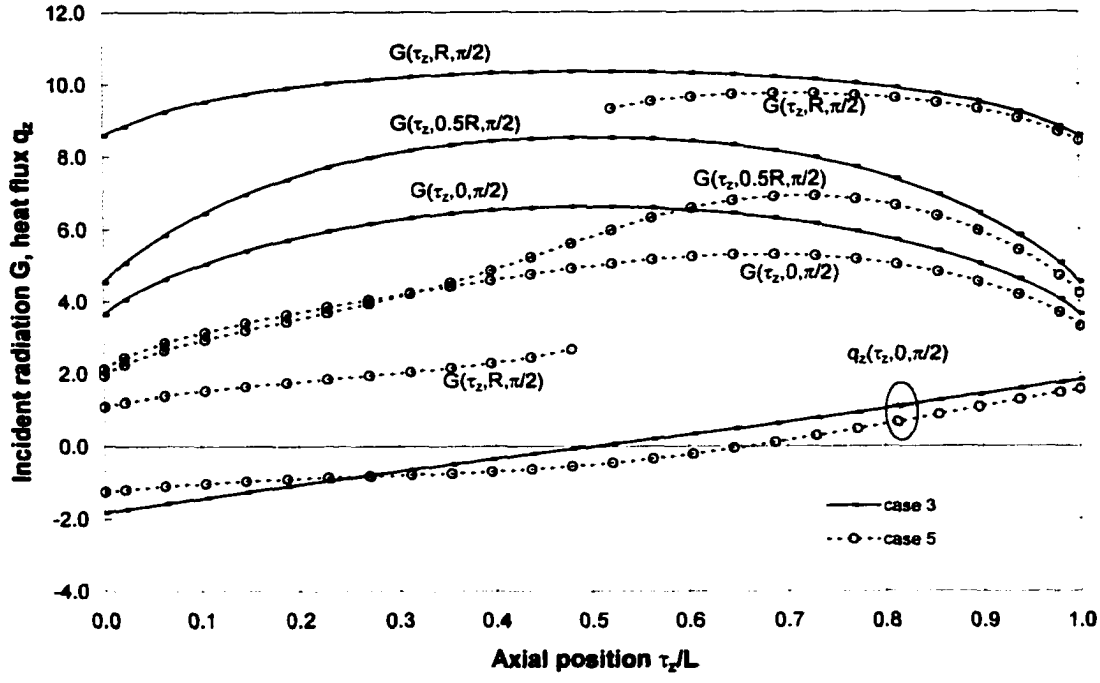

Figure 2-23 The distribution of incident radiation and heat flux q_z at angular position $\phi=\pi/2$, but at different radial position, with respect to normalized optical thickness τ_z/L for case 3 and case 5.

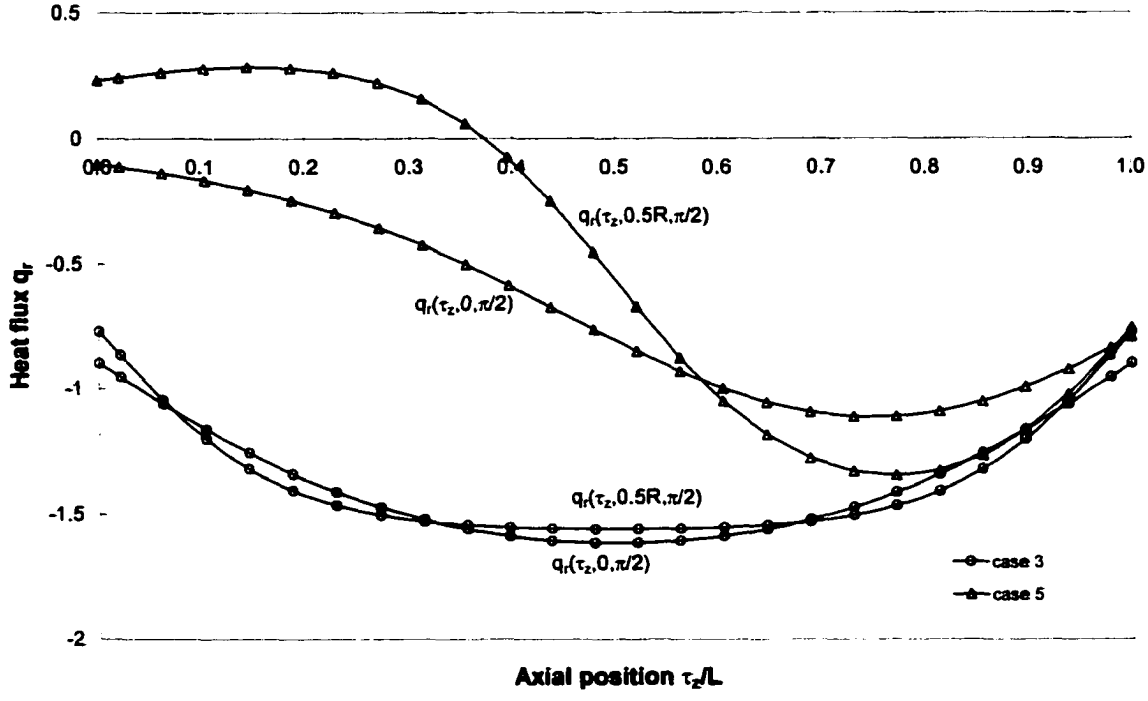

Figure 2-24 The distribution of heat flux $q_r(\tau_z,0,\pi/2)$ and $q_r(\tau_z,0.5R,\pi/2)$ with respect to normalized optical thickness τ_z/L for case 3 and case 5 in table 2-1.

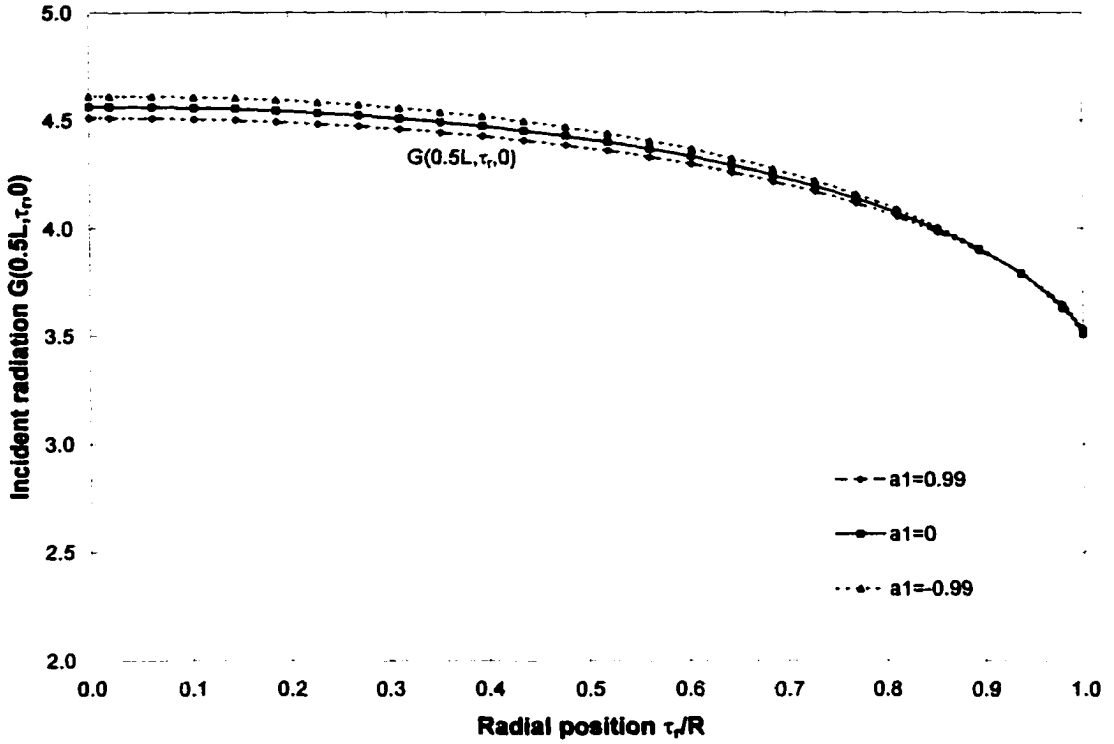

Figure 2-25 The effects of linear anisotropic scattering coefficient a1 on the distribution of incident radiation $G(0.5L,\tau_r,0)$ with respect to normalized optical thickness τ_r/R for case 6.

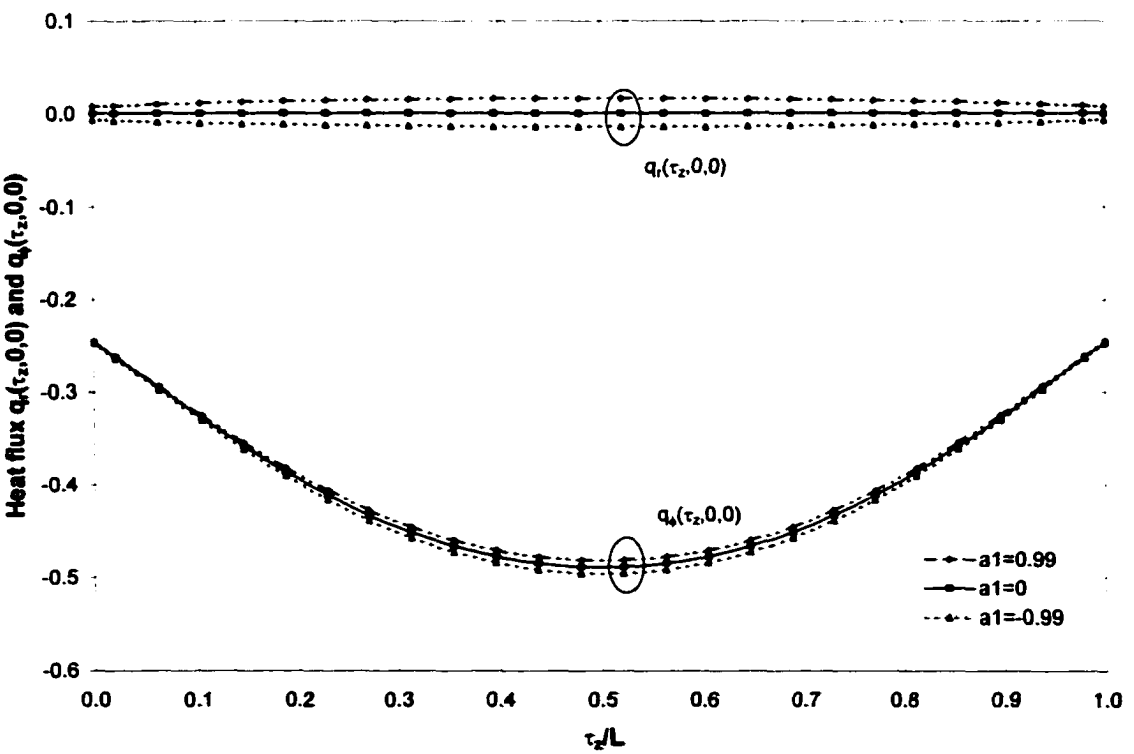

Figure 2-26 The effects of linear anisotropic scattering coefficient a1 on the distribution of heat flux $q_r(\tau_z,0,0)$ and $q_\phi(\tau_z,0,0)$ with respect to normalized optical thickness τ_z/L for case 6 in table 2-1.

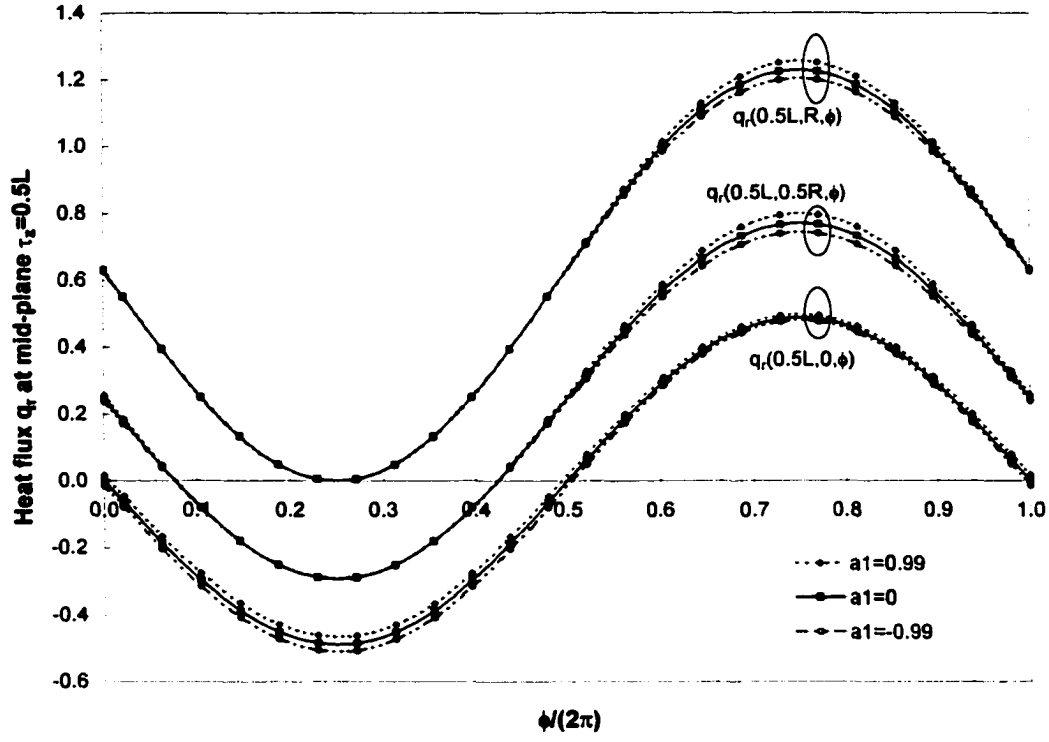

Figure 2-27 The effects of linear anisotropic scattering coefficient a1 on the distribution of q_r at mid-plane τ_z=0.5L, but on different radial position, with respect to angular coordinate ϕ for case 6.

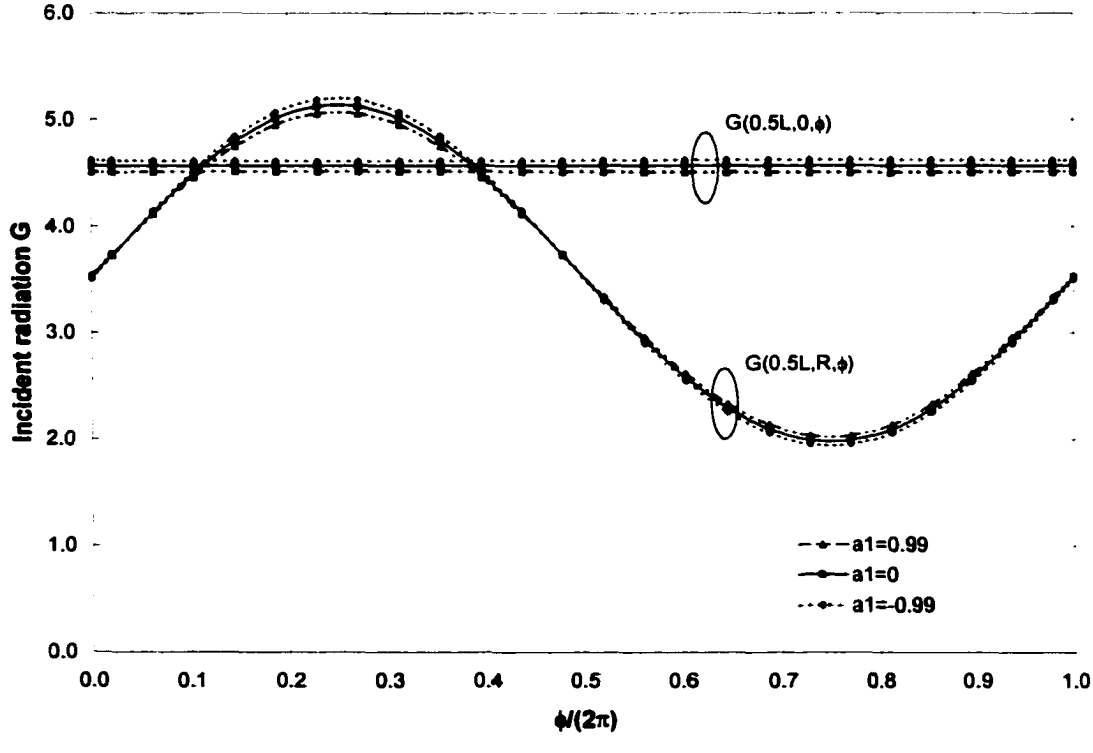

Figure 2-28 The effects of linear anisotropic scattering coefficient a1 on the distribution of incident radiation $G(0.5L,0,\phi)$ and $G(0.5L,R,\phi)$ with respect to angular coordinate ϕ for case 6 in table 2-1.

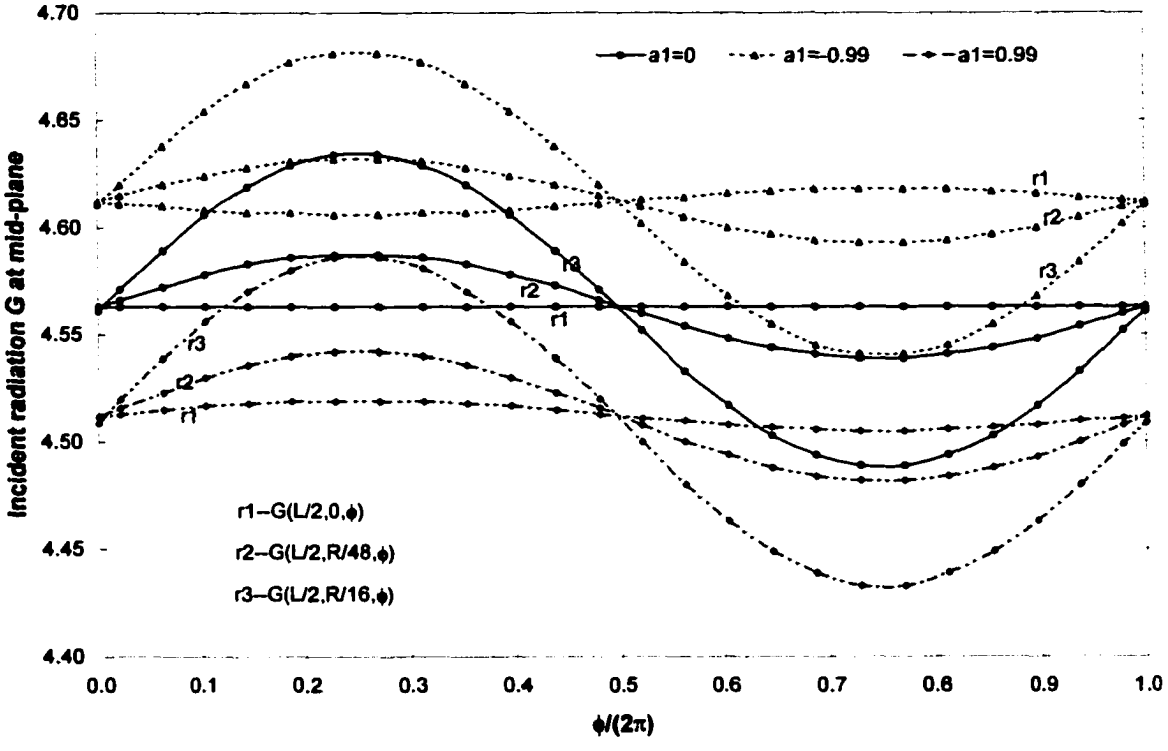

Figure 2-29 The effects of linear anisotropic scattering coefficient a1 on the distribution of incident radiation G at different radial position with respect to angular direction ϕ.

2.8 References:

[2.1] Jenn-Der Lin. Exact expressions for radiative transfer in an arbitrary geometry exposed to radiation. J. Quant. Spectrosc. Radiat. Transfer 1987, Vol. 37, No. 6, pp. 591-601.

[2.2] S. T. Thynell. The integral form of the equation of transfer in finite, two-dimensional, cylindrical media. J. Quant. Spectrosc. Radiat. Transfer 1989, Vol. 42, No. 2, pp. 117-136.

[2.3] Zhiqiang Tan. Radiative heat transfer in multidimensional emitting, absorbing, and anisotropic scattering media-mathematical formulation and numerical method. Journal of Heat Transfer 1989, Vol. 111, No. 1, pp. 141-147.

[2.4] J. M. Zhang and W. H. Sutton. Multidimensional radiative transfer in absorbing, emitting, and linearly anisotropic scattering cylindrical medium with space-dependent properties. J. Quant. Spectrosc. Radiat. Transfer 1994, Vol. 52, No. 6, pp. 791-808.

[2.5] A. L. Crosbie and R. G. Schrenker. Radiative transfer in a two-dimensional rectangular medium exposed to diffuse radiation. J. Quant. Spectrosc. Radiat. Transfer 1984, Vol. 31, No. 4, pp. 339-372.

[2.6] W. Squire. Integration for engineers and scientists. Chap. 4. Elsevier, New York.

[2.7] S. K. Loyalka. A numerical method for solving integral equations of neutron transport. Nucl. Sci. Engng 1975; 56, pp.317-319.

[2.8] Chih-Yang Wu and Shang-Chen Wu. Radiative transfer in a two-layer medium on a cylinder. Int. J. Heat Mass Transfer 1993, Vol. 36, No. 5, pp. 1147-1158.

[2.9] Shang-Chen Wu and Chih-Yang Wu. Partition-extrapolation integration applied to radiative transfer in cylindrical media. J. Quant. Spectrosc. Radiat. Transfer 1992, Vol. 48, No. 3, pp. 279-286.

[2.10] S. T. Thynell and M. N. Ozisik. Integration form of the equation of transfer for an isotropically scattering, inhomogeneous solid cylinder. J. Quant. Spectrosc. Radiat. Transfer 1986, Vol. 36, No. 6, pp. 497-503.

[2.11] R. Viskanta. Radiation transfer and interaction of convection with radiation heat transfer. Advances in Heat Transfer 1966, Vol. 3, pp. 176-252.

[2.12] S. T. Thynell and M. N. Ozisik. Radiation transfer in absorbing, emitting, isotropically scattering, homogeneous cylindrical media. J. Quant. Spectrosc. Radiat. Transfer 1987, Vol. 38, No. 6, pp. 413-426.

[2.13] H. Y. Li, M. N. Ozisik, and J. R. Tsai. Two-dimensional radiation in a cylinder with spatially varying albedo. Journal of Thermophysics and Heat Transfer 1992, Vol. 6, No. 1, pp. 180-182.

[2.14] S. T. Thynell. Treatment of radiation heat transfer in absorbing, emitting, scattering two-dimensional cylindrical media. Numerical Heat Transfer Part A, 1990, Vol. 17, pp. 449-472.

[2.15] M. N. Ozisik. Radiative transfer and interactions with conduction and convection. Wiley, New York, NY (1973).

2.9 Appendix A

Two-Dimensional Equations

In converting the 3-D analysis to 2-D for comparison to published results, consider for isotropic scattering, the transformed integral equations (2-54) reduce to:

$$G(z,r)=\int_0^{2\pi}\int_0^{\rho_R(\chi)} I_1\frac{e^{-\beta\cdot\rho\cdot\sec\alpha_1}}{\rho}(-1)\sin\alpha_1\cos^2\alpha_1 d\rho d\chi +$$
$$\int_0^{2\pi}\int_0^{\rho_R(\chi)} I_2\frac{e^{-\beta\cdot\rho\cdot\sec\alpha_2}}{\rho}\sin\alpha_2\cos^2\alpha_2 d\rho d\chi +$$
$$\int_0^{2\pi}\int_{\alpha_1}^{\alpha_2} I_3 e^{-\beta\cdot\rho_R\cdot\sec\alpha}\cos\alpha\cdot d\alpha\cdot d\chi +$$
$$\int_0^{2\pi}\int_0^{\rho_R}\int_{\alpha_1}^{\alpha_2}\left[(1-\omega)I_b(T)+\frac{\omega}{4\pi}G(z+\rho\tan\alpha,\sqrt{r^2+\rho^2+2r\rho\cdot\cos\chi})\right]\cdot$$
$$e^{-\beta\cdot\rho\cdot\sec\alpha}d\alpha(\beta d\rho)d\chi \qquad \text{(A1a)}$$

$$q_r(z,r)=\int_0^{2\pi}\int_0^{\rho_R(\chi)} I_1\frac{e^{-\beta\cdot\rho\cdot\sec\alpha_1}}{\rho}\sin\alpha_1\cos^3\alpha_1\cos\chi\cdot d\rho d\chi +$$
$$\int_0^{2\pi}\int_0^{\rho_R(\chi)} I_2\frac{e^{-\beta\cdot\rho\cdot\sec\alpha_2}}{\rho}(-1)\sin\alpha_2\cos^3\alpha_2\cos\chi d\rho d\chi +$$
$$\int_0^{2\pi}\int_{\alpha_1}^{\alpha_2} I_3 e^{-\beta\cdot\rho_R\cdot\sec\alpha}(-1)\cos^2\alpha\cdot\cos\chi d\alpha\cdot d\chi +$$
$$\int_0^{2\pi}\int_0^{\rho_R}\int_{\alpha_1}^{\alpha_2}\left[(1-\omega)I_b(T)+\frac{\omega}{4\pi}G(z+\rho\tan\alpha,\sqrt{r^2+\rho^2+2r\rho\cdot\cos\chi})\right]\cdot$$
$$e^{-\beta\cdot\rho\cdot\sec\alpha}(-\cos\chi\cos\alpha)d\alpha(\beta d\rho)d\chi \qquad \text{(A1b)}$$

and

$$
\begin{aligned}
q_z(z,r) = & \int_0^{2\pi}\int_0^{\rho_R(\chi)} I_1 \frac{e^{-\beta\cdot\rho\cdot\sec\alpha_1}}{\rho}\sin^2\alpha_1\cos^2\alpha_1\cdot d\rho d\chi + \\
& \int_0^{2\pi}\int_0^{\rho_R(\chi)} I_2 \frac{e^{-\beta\cdot\rho\cdot\sec\alpha_2}}{\rho}(-1)\sin^2\alpha_2\cos^2\alpha_2\cdot d\rho d\chi + \\
& \int_0^{2\pi}\int_{\alpha_1}^{\alpha_2} I_3 e^{-\beta\cdot\rho_R\cdot\sec\alpha}(-1)\sin\alpha\cdot\cos\alpha\cdot d\alpha\cdot d\chi + \\
& \int_0^{2\pi}\int_0^{\rho_R}\int_{\alpha_1}^{\alpha_2}\left[(1-\omega)I_b(T)+\frac{\omega}{4\pi}G(z+\rho\tan\alpha,\sqrt{r^2+\rho^2+2r\rho\cos\chi})\right]\cdot \\
& e^{-\beta\cdot\rho\cdot\sec\alpha}(-\sin\alpha)d\alpha(\beta d\rho)d\chi
\end{aligned}
\tag{A1c}
$$

The radiosities of boundary surfaces by equation (2-15) are expressed as

$$
\begin{aligned}
J_1(0,r) = \varepsilon_1\sigma T_1^4(0,r) + \rho_1\Bigg\{ & -\int_0^{2\pi}\int_0^{\rho_R(\chi)} I_2\frac{e^{-\beta\cdot\rho\cdot\sec\alpha_2}}{\rho}(-1)\sin^2\alpha_2\cos^2\alpha_2 d\rho d\chi - \\
& \int_0^{2\pi}\int_0^{\alpha_2} I_3 e^{-\beta\cdot\rho_R\cdot\sec\alpha}(-1)\sin\alpha\cos\alpha\cdot d\alpha d\chi - \\
& \int_0^{2\pi}\int_0^{\rho_R}\int_0^{\alpha_2}\left\{(1-\omega)I_b(T)+\frac{\omega}{4\pi}G\right\}\cdot \\
& e^{-\beta\cdot\rho\cdot\sec\alpha}(-\sin\alpha)\cdot d\alpha(\beta d\rho)d\chi \Bigg\}
\end{aligned}
\tag{A2a}
$$

$$
\begin{aligned}
J_2(L,r) = \varepsilon_2\sigma T_2^4(L,r) + \rho_2\Bigg\{ & \int_0^{2\pi}\int_0^{\rho_R(\chi)} I_1\frac{e^{-\beta\cdot\rho\cdot\sec\alpha_1}}{\rho}\sin^2\alpha_1\cos^2\alpha_1 d\rho d\chi + \\
& \int_0^{2\pi}\int_{\alpha_1}^{0} I_3 e^{-\beta\cdot\rho_R\cdot\sec\alpha}(-1)\sin\alpha\cos\alpha\cdot d\alpha d\chi + \\
& \int_0^{2\pi}\int_0^{\rho_R}\int_{\alpha_1}^{0}\left\{(1-\omega)I_b(T)+\frac{\omega}{4\pi}G\right\}\cdot \\
& e^{-\beta\cdot\rho\cdot\sec\alpha}(-\sin\alpha)\cdot d\alpha(\beta d\rho)d\chi \Bigg\}
\end{aligned}
\tag{A2b}
$$

$$J_3(z,R)=\varepsilon_3\sigma T_3^{\ 4}(z,R)+\rho_3\left\{\begin{array}{l}\int_{\frac{\pi}{2}+\phi}^{\frac{3\pi}{2}+\phi}\int_0^{\rho_R(\chi)} I_1\frac{e^{-\beta\cdot\rho\cdot\sec\alpha_1}}{\rho}\sin\alpha_1\cos^3\alpha_1\cos\chi d\rho d\chi+\\ \int_{\frac{\pi}{2}+\phi}^{\frac{3\pi}{2}+\phi}\int_0^{\rho_R(\chi)} I_2\frac{e^{-\beta\cdot\rho\cdot\sec\alpha_2}}{\rho}(-1)\sin\alpha_2\cos^3\alpha_2\cos\chi d\rho d\chi+\\ \int_{\frac{\pi}{2}+\phi}^{\frac{3\pi}{2}+\phi}\int_{\alpha_1}^{\alpha_2} I_3 e^{-\beta\cdot\rho_R\cdot\sec\alpha}(-1)\cos^2\alpha\cos\chi\cdot d\alpha d\chi+\\ \int_{\frac{\pi}{2}+\phi}^{\frac{3\pi}{2}+\phi}\int_0^{\rho_R}\int_{\alpha_1}^{\alpha_2}\left\{(1-\omega)I_b(T)+\frac{\omega}{4\pi}G\right\}\cdot\\ e^{-\beta\cdot\rho\cdot\sec\alpha}(-1)\cos\chi\cos\alpha\cdot d\alpha(\beta d\rho)d\chi\end{array}\right\} \qquad \text{(A2c)}$$

CHAPTER THREE

3. A GENERAL INTEGRATION METHOD FOR RADIATIVE TRANSFER IN 3-D NON-HOMOGENEOUS CYLINDRICAL MEDIA WITH ANISOTROPIC SCATTERING

A general set of integral equations is presented to solve 3-D radiative heat transfer problems in emitting, absorbing and linear anisotropic scattering finite hollow or solid cylinders with non-homogeneous media. By tracing a ray to compute the intensity, it is much easier to handle the spatial change properties including extinction coefficient. Both the continuous change property and step-change property are dealt with without difficulties. The solid angle integration in getting the incident radiation and heat fluxes is represented by the bounding surface integration. In order to avoid the singularity problem near the bounding surface, the surface integrations are transformed to new modified integral equations by mathematic methods. By doing so, we get more flexible general integral equations applicable to all cases like 3-D solid cylinders, 3-D hollow cylinders, finite cylinders or infinite cylinders. This scheme has been verified by comparing the results with published data in the literature. It is believed that this method is useful in combined radiation and convection heat transfer problems.

3.1 Introduction

Radiative heat transfer in cylindrical media is important in various industrial applications such as combustion chambers and high temperature heat exchangers. We can find many papers dealing with radiation in multidimensional cylindrical media by

integral equations of transfer [3.1]-[3.4]. According to Zhang and Sutton [3.5], most integral equations in the literature are SV-type, which is surface integration plus volume integration for participating media. They suggested a new way to solve radiative heat transfer problem by so-called S-type integral equations, which only include surface integration, in cylindrical media. The S-type integral method can easily be developed to other geometries as well. The intensity at each point in the medium is obtained by tracing the ray starting from the bounding surface, integrated along the line. Once obtained the intensity at the point in every direction, the incident radiation and heat fluxes can be determined by the integration over 4π solid angles. The solid angle integration is transformed to the integration of bounding surfaces around the medium.

For most interior points of the medium, there are no singularity problems in S-type integral equations. There do exist singularity points near the boundaries. This singularity comes from the transformation of solid angle integration to surface integration. To avoid this difficulty while computing the incident radiation and heat fluxes in the whole domain, a same coordinate transformation is adopted here as in a previous paper [3.6] for surface integrations.

Here, we give a more general form of integral equations for radiative transfer in finite 3-D non-homogeneous participating media with anisotropic scattering in solid or hollow cylinders. Not only will the spatial variation of albedo be treated, but also that of the extinction coefficient. Further, non-smooth or abrupt step change of extinction coefficient in cylindrical layers will also be considered.

3.2 Integral Equations of Transfer

When the radiative properties of the medium are independent of frequency, the radiative transfer equation will take the form [3.7]

$$\frac{1}{\beta(s)}\frac{dI(s,\hat{\Omega})}{ds}+I(s,\hat{\Omega})=S(s,\hat{\Omega}) \tag{3-1}$$

where the source term in above equation is defined as

$$S(s,\hat{\Omega})\equiv(1-\omega)\frac{n^2\overline{\sigma}T^4}{\pi}+\frac{\omega}{4\pi}\int_{4\pi}p(\hat{\Omega}'\cdot\hat{\Omega})\cdot I(s,\hat{\Omega}')d\Omega' \tag{3-2}$$

and n is the refractive index of the medium, ω is the scattering albedo. If a linear-anisotropic scattering phase function is assumed, then

$$p(\hat{\Omega}',\hat{\Omega})=1+a_1\hat{\Omega}\cdot\hat{\Omega}' \tag{3-3}$$

Considering a specified boundary condition (Figure 3-1):

$$I(s,\hat{\Omega})=I_i \quad \text{at } s=s_i \tag{3-4}$$

Then the formal integration of the transfer equation (3-1) along the path s in the direction $\hat{\Omega}$ subject to this boundary condition is expressed as

$$I(s,\hat{\Omega})=I_i\exp\left[-\int_{s_i}^{s}\beta(s')ds'\right]+\int_{s_i}^{s}\beta(s')S(s',\hat{\Omega})\exp\left[-\int_{s'}^{s}\beta(s'')ds''\right]ds' \tag{3-5}$$

For the simplicity in expression, we define

$$\tau(s_i,s)=\int_{s_i}^{s}\beta(s')ds' \tag{3-6}$$

So the intensity in equation (3-5) can be expressed simply as

$$I(s,\hat{\Omega})=I_i\exp[-\tau(s_i,s)]+\int_{s_i}^{s}\beta(s')S(s',\hat{\Omega})\exp[-\tau(s',s)]ds' \tag{3-7}$$

The incident radiation and heat flux at a particular point can be evaluated by the integration of the intensity at that point around the whole 4π solid angle. In cylindrical coordinates (Figure 3-2), they are expressed in following forms:

$$G(z,r,\phi) = \int_{4\pi} I(z,r,\phi,\hat{\Omega}) \cdot d\Omega, \tag{3-8a}$$

$$q_r(z,r,\phi) = \int_{4\pi} I(z,r,\phi,\hat{\Omega}) \cdot \cos(\hat{e}_r,\hat{\Omega}) \cdot d\Omega, \tag{3-8b}$$

$$q_z(z,r,\phi) = \int_{4\pi} I(z,r,\phi,\hat{\Omega}) \cdot \cos(\hat{e}_z,\hat{\Omega}) \cdot d\Omega, \tag{3-8c}$$

$$q_\phi(z,r,\phi) = \int_{4\pi} I(z,r,\phi,\hat{\Omega}) \cdot \cos(\hat{e}_\phi,\hat{\Omega}) \cdot d\Omega. \tag{3-8d}$$

The source term in cylindrical coordinates with linear anisotropic scattering medium is given by

$$\begin{aligned} S(s,\hat{\Omega}) &= S(z,r,\phi,\hat{\Omega}) \\ &= (1-\omega) I_b(T) + \frac{\omega}{4\pi} \left\{ \begin{array}{l} G(z,r,\phi) + \\ a_1 \left[q_r(z,r,\phi)\cos(\hat{e}_r,\hat{\Omega}) + q_z(z,r,\phi)\cos(\hat{e}_z,\hat{\Omega}) + q_\phi(z,r,\phi)\cos(\hat{e}_\phi,\hat{\Omega}) \right] \end{array} \right\} \end{aligned} \tag{3-9}$$

3.2.1 General Equations in Finite Hollow Cylinders

If the medium is enclosed by several bounding surfaces i (i=1,2,3...), the solid angle integration in equations (3-8) could be transformed to surface integrations. A 3-D hollow cylinder is shown in Figure 3-3. The point s(z,r,ϕ) is surrounded by a bottom surface, a top surface, outer cylinder and inner cylinder, which are surface 1, surface 2, surface 3 and surface 4 respectively. The incident radiation and heat fluxes are expressed as

$$G(z,r,\phi) = \sum_{i=1}^{4} \iint_i I(z,r,\phi,\hat{\Omega}) \cdot \frac{\cos\theta_i}{d^2(s_i,s)} dA_i \tag{3-10a}$$

$$q_r(z,r,\phi)=\sum_{i=1}^{4}\iint_i I(z,r,\phi,\hat{\Omega})\cdot\cos(\hat{e}_r,\hat{\Omega})\frac{\cos\theta_i}{d^2(s_i,s)}dA_i \tag{3-10b}$$

$$q_z(z,r,\phi)=\sum_{i=1}^{4}\iint_i I(z,r,\phi,\hat{\Omega})\cdot\cos(\hat{e}_z,\hat{\Omega})\frac{\cos\theta_i}{d^2(s_i,s)}dA_i \tag{3-10c}$$

$$q_\phi(z,r,\phi)=\sum_{i=1}^{4}\iint_i I(z,r,\phi,\hat{\Omega})\cdot\cos(\hat{e}_\phi,\hat{\Omega})\frac{\cos\theta_i}{d^2(s_i,s)}dA_i \tag{3-10d}$$

where θ_i is the angle between the unit normal vector $\hat{n}_i$ of surface i and the intensity direction $\hat{\Omega}$ (Figure 3-2). The term $d(s_i,s)$ is the distance from point s_i on the boundary i (i=1,2,3,4) to point s in the medium and can be computed by

$$d(s_i,s)=\left[r_i^2+r^2-2r_i r\cos(\phi-\phi_i)+(z-z_i)^2\right]^{1/2} \tag{3-11}$$

The actual integration of surface 1 is on the area A_1-B_1-C_1-f_1-e_1-d_1-A_1 shown shadowed in Figure 3-3. The same area of surface 2 is A_2-B_2-C_2-f_2-e_2-d_2-A_2. The surface 3 integration is on the outer cylindrical surface in between A_1-B_1-C_1 and A_2-B_2-C_2. The integration to surface 4 is the integration of the inner cylindrical surface in between f_1-e_1-d_1 and f_2-e_2-d_2.

The equations for cosines in above equations (3-10) are from Zhang and Sutton [3.4], Chen and Sutton [3.6] and listed in Appendix B.

By substituting all cosines into equations (3-10), the resultant expressions for incident radiation and heat fluxes are

$$G(z,r,\phi) = \iint_{surface1} I(z,r,\phi,\hat{\Omega})\frac{z\cdot dA_1}{d^3(s_1,s)} + \iint_{surface2} I(z,r,\phi,\hat{\Omega})\frac{(L-z)\cdot dA_2}{d^3(s_2,s)} + \iint_{surface3} I(z,r,\phi,\hat{\Omega})\frac{[R_{out}-r\cos(\phi-\phi_3)]\cdot dA_3}{d^3(s_3,s)} + \iint_{surface4} I(z,r,\phi,\hat{\Omega})\frac{[r\cos(\phi-\phi_4)-R_{in}]\cdot dA_4}{d^3(s_4,s)} \quad (3\text{-}12a)$$

$$q_r(z,r,\phi) = \iint_{surface1} I(z,r,\phi,\hat{\Omega})\frac{z\cdot[r-r_1\cos(\phi-\phi_1)]\cdot dA_1}{d^4(s_1,s)} + \iint_{surface2} I(z,r,\phi,\hat{\Omega})\frac{(L-z)\cdot[r-r_2\cos(\phi-\phi_2)]\cdot dA_2}{d^4(s_2,s)} + \iint_{surface3} I(z,r,\phi,\hat{\Omega})\frac{[R_{out}-r\cos(\phi-\phi_3)]\cdot[r-R_{out}\cos(\phi-\phi_3)]\cdot dA_3}{d^4(s_3,s)} + \iint_{surface4} I(z,r,\phi,\hat{\Omega})\frac{[r\cos(\phi-\phi_4)-R_{in}]\cdot[r-R_{in}\cos(\phi-\phi_4)]\cdot dA_4}{d^4(s_4,s)} \quad (3\text{-}12b)$$

$$q_z(z,r,\phi) = \iint_{surface1} I(z,r,\phi,\hat{\Omega})\frac{z\cdot(z-0)\cdot dA_1}{d^4(s_1,s)} + \iint_{surface2} I(z,r,\phi,\hat{\Omega})\frac{(L-z)\cdot(z-L)\cdot dA_2}{d^4(s_2,s)} + \iint_{surface3} I(z,r,\phi,\hat{\Omega})\frac{[R_{out}-r\cos(\phi-\phi_3)]\cdot(z-z_3)\cdot dA_3}{d^4(s_3,s)} + \iint_{surface4} I(z,r,\phi,\hat{\Omega})\frac{[r\cos(\phi-\phi_4)-R_{in}]\cdot(z-z_4)\cdot dA_4}{d^4(s_4,s)} \quad (3\text{-}12c)$$

and

$$q_\phi(z,r,\phi) = \iint_{surface1} I(z,r,\phi,\hat{\Omega}) \frac{z\cdot[r_1 \sin(\phi-\phi_1)]\cdot dA_1}{d^4(s_1,s)} + \iint_{surface2} I(z,r,\phi,\hat{\Omega}) \frac{(L-z)\cdot[r_2 \sin(\phi-\phi_2)]\cdot dA_2}{d^4(s_2,s)} + \iint_{surface3} I(z,r,\phi,\hat{\Omega}) \frac{[R_{out} - r\cos(\phi-\phi_3)]\cdot R_{out}\sin(\phi-\phi_3)\cdot dA_3}{d^4(s_3,s)} + \iint_{surface4} I(z,r,\phi,\hat{\Omega}) \frac{[r\cos(\phi-\phi_4) - R_{in}]\cdot R_{in}\sin(\phi-\phi_4)\cdot dA_4}{d^4(s_4,s)} \quad (3\text{-}12d)$$

Equations (3-12) are the exact integral equations for 3-dimensional hollow cylindrical enclosures with absorbing, emitting, and anisotropically scattering media. Defining the first integral terms in equations (3-12a)-(3-12d) as G1, q_r1, q_z1, and q_ϕ1 respectively and so on with the second, third and forth terms, we have

$$G(z,r,\phi) = G1(z,r,\phi) + G2(z,r,\phi) + G3(z,r,\phi) + G4(z,r,\phi), \quad (3\text{-}13a)$$

$$q_r(z,r,\phi) = q_r1(z,r,\phi) + q_r2(z,r,\phi) + q_r3(z,r,\phi) + q_r4(z,r,\phi), \quad (3\text{-}13b)$$

$$q_z(z,r,\phi) = q_z1(z,r,\phi) + q_z2(z,r,\phi) + q_z3(z,r,\phi) + q_z4(z,r,\phi), \quad (3\text{-}13c)$$

$$q_\phi(z,r,\phi) = q_\phi1(z,r,\phi) + q_\phi2(z,r,\phi) + q_\phi3(z,r,\phi) + q_\phi4(z,r,\phi). \quad (3\text{-}13d)$$

The integration of surface 1 will be separated into two parts (Figure 3-4). One part is the integration of area S-f_1-e_1-d_1-S; other part is the integration of area S-d_1-A_1-B_1-C_1-f_1-S. The integration of surface 2 is the same as surface 1.

In order to calculate the integrations without the singularity problem, we use the same coordinate transformation method as by Chen and Sutton [3.6], which is moving the original point from O(0,0,0) to S(z,r,ϕ) referring to Figure 3-3 and Figure 3-4. By doing so, the integration point coordinate (z_i,r_i,ϕ_i) is transformed to a new defined coordinate (α,γ,χ), where α is the angle defined as in Figure 3-3; γ is the distance from projection point (r_i,ϕ_i) to (r,ϕ); and χ is the angle defined as in Figure 3-4. The

transformed expressions for incident radiation and heat fluxes are (for more details, see Appendix B):

$$G1(z,r,\phi)=\int_{-(\frac{\pi}{2}+\phi_{in})}^{(\frac{\pi}{2}+\phi_{in})}\int_{0}^{\gamma_{R_2}}\frac{I}{\gamma}(-\sin\alpha_1)\cos^2\alpha_1 d\gamma d\chi+\int_{(\frac{\pi}{2}+\phi_{in})}^{(\frac{3\pi}{2}-\phi_{in})}\int_{0}^{\gamma_{R_1}}\frac{I}{\gamma}(-\sin\alpha_1)\cos^2\alpha_1 d\gamma d\chi \quad (3\text{-}14a)$$

$$G2(z,r,\phi)=\int_{-(\frac{\pi}{2}+\phi_{in})}^{(\frac{\pi}{2}+\phi_{in})}\int_{0}^{\gamma_{R_2}}\frac{I}{\gamma}\sin\alpha_2\cos^2\alpha_2 d\gamma d\chi+\int_{(\frac{\pi}{2}+\phi_{in})}^{(\frac{3\pi}{2}-\phi_{in})}\int_{0}^{\gamma_{R_1}}\frac{I}{\gamma}\sin\alpha_2\cos^2\alpha_2 d\gamma d\chi \quad (3\text{-}14b)$$

$$G3(z,r,\phi)=\int_{-(\frac{\pi}{2}+\phi_{in})}^{(\frac{\pi}{2}+\phi_{in})}\int_{\alpha_1}^{\alpha_2} I\cdot\cos\alpha\cdot d\alpha d\chi \quad (3\text{-}14c)$$

$$G4(z,r,\phi)=\int_{(\frac{\pi}{2}+\phi_{in})}^{(\frac{3\pi}{2}-\phi_{in})}\int_{\alpha_1}^{\alpha_2} I\cdot\cos\alpha\cdot d\alpha d\chi \quad (3\text{-}14d)$$

$$q_r1(z,r,\phi)=\int_{-(\frac{\pi}{2}+\phi_{in})}^{(\frac{\pi}{2}+\phi_{in})}\int_{0}^{\gamma_{R_2}}\frac{I}{\gamma}\sin\alpha_1\cos^3\alpha_1\cos\chi d\gamma d\chi+\int_{(\frac{\pi}{2}+\phi_{in})}^{(\frac{3\pi}{2}-\phi_{in})}\int_{0}^{\gamma_{R_1}}\frac{I}{\gamma}\sin\alpha_1\cos^3\alpha_1\cos\chi d\gamma d\chi \quad (3\text{-}15a)$$

$$q_r2(z,r,\phi)=\int_{-(\frac{\pi}{2}+\phi_{in})}^{(\frac{\pi}{2}+\phi_{in})}\int_{0}^{\gamma_{R_2}}\frac{I}{\gamma}\sin\alpha_2\cos^3\alpha_2(-\cos\chi)d\gamma d\chi+\int_{(\frac{\pi}{2}+\phi_{in})}^{(\frac{3\pi}{2}-\phi_{in})}\int_{0}^{\gamma_{R_1}}\frac{I}{\gamma}\sin\alpha_2\cos^3\alpha_2(-\cos\chi)d\gamma d\chi \quad (3\text{-}15b)$$

$$q_r3(z,r,\phi)=\int_{-(\frac{\pi}{2}+\phi_{in})}^{(\frac{\pi}{2}+\phi_{in})}\int_{\alpha_1}^{\alpha_2} I\cdot\cos^2\alpha(-\cos\chi)d\alpha d\chi \quad (3\text{-}15c)$$

$$q_r4(z,r,\phi)=\int_{(\frac{\pi}{2}+\phi_{in})}^{(\frac{3\pi}{2}-\phi_{in})}\int_{\alpha_1}^{\alpha_2} I\cdot\cos^2\alpha(-\cos\chi)d\alpha d\chi \quad (3\text{-}15d)$$

$$q_z1(z,r,\phi)=\int_{-(\frac{\pi}{2}+\phi_{in})}^{(\frac{\pi}{2}+\phi_{in})}\int_{0}^{\gamma_{R2}}\frac{I}{\gamma}\sin^2\alpha_1\cos^2\alpha_1 d\gamma d\chi+\int_{(\frac{\pi}{2}+\phi_{in})}^{(\frac{3\pi}{2}-\phi_{in})}\int_{0}^{\gamma_{R1}}\frac{I}{\gamma}\sin^2\alpha_1\cos^2\alpha_1 d\gamma d\chi \tag{3-16a}$$

$$q_z2(z,r,\phi)=\int_{-(\frac{\pi}{2}+\phi_{in})}^{(\frac{\pi}{2}+\phi_{in})}\int_{0}^{\gamma_{R2}}\frac{I}{\gamma}(-1)\sin^2\alpha_2\cos^2\alpha_2 d\gamma d\chi+\int_{(\frac{\pi}{2}+\phi_{in})}^{(\frac{3\pi}{2}-\phi_{in})}\int_{0}^{\gamma_{R1}}\frac{I}{\gamma}(-1)\sin^2\alpha_2\cos^2\alpha_2 d\gamma d\chi \tag{3-16b}$$

$$q_z3(z,r,\phi)=\int_{-(\frac{\pi}{2}+\phi_{in})}^{(\frac{\pi}{2}+\phi_{in})}\int_{\alpha_1}^{\alpha_2}I\cdot(-\sin\alpha)\cos\alpha\cdot d\alpha d\chi \tag{3-16c}$$

$$q_z4(z,r,\phi)=\int_{(\frac{\pi}{2}+\phi_{in})}^{(\frac{3\pi}{2}-\phi_{in})}\int_{\alpha_1}^{\alpha_2}I\cdot(-\sin\alpha)\cos\alpha\cdot d\alpha d\chi \tag{3-16d}$$

and

$$q_\phi1(z,r,\phi)=\int_{-(\frac{\pi}{2}+\phi_{in})}^{(\frac{\pi}{2}+\phi_{in})}\int_{0}^{\gamma_{R2}}\frac{I}{\gamma}\sin\alpha_1\cos^3\alpha_1\sin\chi d\gamma d\chi+\int_{(\frac{\pi}{2}+\phi_{in})}^{(\frac{3\pi}{2}-\phi_{in})}\int_{0}^{\gamma_{R1}}\frac{I}{\gamma}\sin\alpha_1\cos^3\alpha_1\sin\chi d\gamma d\chi \tag{3-17a}$$

$$q_\phi2(z,r,\phi)=\int_{-(\frac{\pi}{2}+\phi_{in})}^{(\frac{\pi}{2}+\phi_{in})}\int_{0}^{\gamma_{R2}}\frac{I}{\gamma}\sin\alpha_2\cos^3\alpha_2(-\sin\chi)d\gamma d\chi+\int_{(\frac{\pi}{2}+\phi_{in})}^{(\frac{3\pi}{2}-\phi_{in})}\int_{0}^{\gamma_{R1}}\frac{I}{\gamma}\sin\alpha_2\cos^3\alpha_2(-\sin\chi)d\gamma d\chi \tag{3-17b}$$

$$q_\phi3(z,r,\phi)=\int_{-(\frac{\pi}{2}+\phi_{in})}^{(\frac{\pi}{2}+\phi_{in})}\int_{\alpha_1}^{\alpha_2}I\cdot\cos^2\alpha(-\sin\chi)\cdot d\alpha d\chi \tag{3-17c}$$

$$q_\phi4(z,r,\phi)=\int_{(\frac{\pi}{2}+\phi_{in})}^{(\frac{3\pi}{2}-\phi_{in})}\int_{\alpha_1}^{\alpha_2}I\cdot\cos^2\alpha(-\sin\chi)\cdot d\alpha d\chi \tag{3-17d}$$

where

$$\phi_{in}=\cos^{-1}\frac{R_{in}}{r} \tag{3-18}$$

$$\gamma_{Ro} = \sqrt{R_{out}^{\ 2} - r^2 \sin^2 \chi} - r\cos\chi \tag{3-19a}$$

$$\gamma_{Ri} = -\sqrt{R_{in}^{\ 2} - r^2 \sin^2 \chi} - r\cos\chi \tag{3-19b}$$

$$\alpha_1 = \arctan\frac{0-z}{\gamma},\ \alpha_2 = \arctan\frac{L-z}{\gamma} \tag{3-20}$$

Here γ_{Ro} or γ_{Ri} is the distance from a point on outer cylinder or inner cylinder to the concerned point S(r,ϕ) in the projection view. When calculating α_1 and α_2 limits in the above integrations, use γ_{Ro} or γ_{Ri} instead of γ in equation (3-20).

In order to compute the radiation intensity, the old coordinate value (z_i,r_i,ϕ_i) is required. Once the new coordinate (α,γ,χ) is known, the coordinate (z_i,r_i,ϕ_i) can be obtained by

$$z_i = \gamma\tan\alpha + z \tag{3-21a}$$

$$r_i = \sqrt{r^2 + \gamma^2 + 2r\gamma\cos\chi} \tag{3-21b}$$

$$\phi_i = \tan^{-1}\frac{y_i}{x_i} \quad \text{if } x_i > 0 \text{ and } y_i > 0 \tag{3-21c}$$

$$\phi_i = 2\pi + \tan^{-1}\frac{y_i}{x_i} \quad \text{if } x_i > 0 \text{ and } y_i < 0 \tag{3-21d}$$

$$\phi_i = \pi + \tan^{-1}\frac{y_i}{x_i} \quad \text{if } x_i < 0 \tag{3-21e}$$

where

$$x_i = r\cos\phi + \gamma\cos(\phi+\chi),\quad y_i = r\sin\phi + \gamma\sin(\phi+\chi) \tag{3-22}$$

In above equations, γ is replaced by γ_{Ro} in surface 3 integrations and by γ_{Ri} in surface 4 integrations.

Equations (3-14)-(3-17) plus equation (3-7) are the complete set of descriptive equations to solve for incident radiation, heat fluxes, and the intensity.

3.2.1.1 Equations for finite solid and infinite hollow cylinders

An interesting point of above equations is when $R_{in}=0$, then $\phi_{in}=\pi/2$, equations (3-14)-(3-17) become the equations for solid cylinders automatically. The second term of G1 and G2 will equal to zero, as does G4. The same thing happens with the second term of q_r1, q_r2, q_z1, q_z2, $q_\phi1$ and $q_\phi2$; and the whole terms q_r4, q_z4 and $q_\phi4$ vanish. The following equations hold for 3-D solid cylinders.

$$G(z,r,\phi)=\int_{-\pi}^{\pi}\int_{0}^{\gamma_{R_o}}\frac{I}{\gamma}(-\sin\alpha_1)\cos^2\alpha_1 d\gamma d\chi+\int_{-\pi}^{\pi}\int_{0}^{\gamma_{R_o}}\frac{I}{\gamma}\sin\alpha_2\cos^2\alpha_2 d\gamma d\chi+\int_{-\pi}^{\pi}\int_{-\pi\alpha_1}^{\alpha_2} I\cdot\cos\alpha\cdot d\alpha d\chi \tag{3-23a}$$

$$q_r(z,r,\phi)=\int_{-\pi}^{\pi}\int_{0}^{\gamma_{R_o}}\frac{I}{\gamma}\sin\alpha_1\cos^3\alpha_1\cos\chi d\gamma d\chi+\int_{-\pi}^{\pi}\int_{0}^{\gamma_{R_o}}\frac{I}{\gamma}\sin\alpha_2\cos^3\alpha_2(-\cos\chi)d\gamma d\chi+\int_{-\pi}^{\pi}\int_{-\pi\alpha_1}^{\alpha_2} I\cdot\cos^2\alpha(-\cos\chi)d\alpha d\chi \tag{3-23b}$$

$$q_z(z,r,\phi)=\int_{-\pi}^{\pi}\int_{0}^{\gamma_{R_o}}\frac{I}{\gamma}\sin^2\alpha_1\cos^2\alpha_1 d\gamma d\chi+\int_{-\pi}^{\pi}\int_{0}^{\gamma_{R_o}}\frac{I}{\gamma}(-1)\sin^2\alpha_2\cos^2\alpha_2 d\gamma d\chi+\int_{-\pi}^{\pi}\int_{-\pi\alpha_1}^{\alpha_2} I\cdot(-\sin\alpha)\cos\alpha\cdot d\alpha d\chi \tag{3-23c}$$

$$q_\phi(z,r,\phi)=\int_{-\pi}^{\pi}\int_{0}^{\gamma_{R_o}}\frac{I}{\gamma}\sin\alpha_1\cos^3\alpha_1\sin\chi d\gamma d\chi+\int_{-\pi}^{\pi}\int_{0}^{\gamma_{R_o}}\frac{I}{\gamma}\sin\alpha_2\cos^3\alpha_2(-\sin\chi)d\gamma d\chi+\int_{-\pi}^{\pi}\int_{-\pi\alpha_1}^{\alpha_2} I\cdot\cos^2\alpha(-\sin\chi)\cdot d\alpha d\chi \tag{3-23d}$$

In addition it may be noted that when $\alpha_1=-\pi/2$ and $\alpha_2=\pi/2$, the whole set of equations (3-14)-(3-17) become the equations for infinitely long hollow cylinders automatically. Because all the integrations of surface 1 and surface 2 will equal to zero, these are:

$$G(r,\phi)=\int_{-(\frac{\pi}{2}+\phi_{in})}^{(\frac{\pi}{2}+\phi_{in})}\int_{-\frac{\pi}{2}}^{\frac{\pi}{2}} I\cdot\cos\alpha d\alpha d\chi+\int_{(\frac{\pi}{2}+\phi_{in})}^{(\frac{3\pi}{2}-\phi_{in})}\int_{-\frac{\pi}{2}}^{\frac{\pi}{2}} I\cdot\cos\alpha d\alpha d\chi \qquad (3\text{-}24a)$$

$$q_r(r,\phi)=\int_{-(\frac{\pi}{2}+\phi_{in})}^{(\frac{\pi}{2}+\phi_{in})}\int_{-\frac{\pi}{2}}^{\frac{\pi}{2}} I\cdot\cos^2\alpha(-\cos\chi)d\alpha d\chi+\int_{(\frac{\pi}{2}+\phi_{in})}^{(\frac{3\pi}{2}-\phi_{in})}\int_{-\frac{\pi}{2}}^{\frac{\pi}{2}} I\cdot\cos^2\alpha(-\cos\chi)d\alpha d\chi \qquad (3\text{-}24b)$$

$$q_\phi(r,\phi)=\int_{-(\frac{\pi}{2}+\phi_{in})}^{(\frac{\pi}{2}+\phi_{in})}\int_{-\frac{\pi}{2}}^{\frac{\pi}{2}} I\cdot\cos^2\alpha(-\sin\chi)\cdot d\alpha d\chi+\int_{(\frac{\pi}{2}+\phi_{in})}^{(\frac{3\pi}{2}-\phi_{in})}\int_{-\frac{\pi}{2}}^{\frac{\pi}{2}} I\cdot\cos^2\alpha(-\sin\chi)\cdot d\alpha d\chi \qquad (3\text{-}24c)$$

In above equations, the first term is the integration of outer cylinder, in which γ_{Ro} is used to determine the start point coordinate (z_i,r_i,ϕ_i) of intensity; while the second term is the integration of inner cylinder, in which γ_{Ri} is used to determine the coordinate (z_i,r_i,ϕ_i). Gauss-Legendre quadrature is suggested to compute the integration of angle α from $-\pi/2$ to $\pi/2$, so a suitable z_i value can be obtained from equation (3-21a) by assuming $z=0$ because the characteristics of tangent function. If a 20-point quadrature is used, z_i can be handled and accurate integration results will be obtained at the same time.

3.2.2 The Radiation Intensity

The surface integrations are purely a geometric evaluation. Radiative properties are considered in the intensity computation. The intensity from boundary point $s_i(z_i,r_i,\phi_i)$ to concerned point $s(z,r,\phi)$ in the medium is given by

$$I(z,r,\phi,\hat{\Omega}) = I_i \exp[-\tau(s_i,s)] + \int_0^l \beta(z',r',\phi')S(z',r',\phi',\hat{\Omega})\exp[-\tau(s',s)]\cdot d(s_i,s)dt \quad (3\text{-}25)$$

where $d(s_i,s)$ is determined by equation (3-11), point $s'(z',r',\phi')$ lays between the start point $s_i(z_i,r_i,\phi_i)$ and end point $s(z,r,\phi)$. We have

$$s' = s_i + (s - s_i)t; \qquad 1 \geq t \geq 0 \quad (3\text{-}26)$$

then

$$z' = z_i + (z - z_i)\cdot t \quad (3\text{-}27a)$$

$$r' = \sqrt{x'^2 + y'^2} \quad (3\text{-}27b)$$

$$\phi' = \tan^{-1}\frac{y'}{x'} \quad \text{if } x' > 0 \text{ and } y' > 0 \quad (3\text{-}27c)$$

$$\phi' = 2\pi + \tan^{-1}\frac{y'}{x'} \quad \text{if } x' > 0 \text{ and } y' < 0 \quad (3\text{-}27d)$$

$$\phi' = \pi + \tan^{-1}\frac{y'}{x'} \quad \text{if } x' < 0 \quad (3\text{-}27e)$$

where

$$x' = r_i\cos\phi_i + (r\cos\phi - r_i\cos\phi_i)\cdot t \qquad y' = r_i\sin\phi_i + (r\sin\phi - r_i\sin\phi_i)\cdot t \quad (3\text{-}28)$$

The optical thickness in equation (3-25) is simply integrated by

$$\tau(s_i,s) = \int_{s_i}^{s}\beta(s')ds' = \int_0^l \beta(z',r',\phi')\cdot d(s_i,s)\cdot dt \quad (3\text{-}29a)$$

The optical thickness from point s' to point s can be obtained by the same procedure except point $s_i(z_i,r_i,\phi_i)$ replaced by point $s'(z',r',\phi')$ as

$$\tau(s',s) = \int_{s'}^{s}\beta(s'')ds'' = \int_0^l \beta(z'',r'',\phi'')\cdot d(s',s)\cdot dt \quad (3\text{-}29b)$$

Using these equations, the intensity from any start point s_i to point s can be easily determined even in non-homogeneous medium, because the distribution changes of extinction coefficient and scattering albedo are considered in the integral calculation. Note that, even though this is illustrated for gray properties, the same general procedure would apply for monochromatic radiation.

3.2.3 Boundary Conditions

The boundary conditions can be generally expressed as

$$I_1(0,r,\phi) = f_1(0,r,\phi) + \varepsilon_1 I_{b1}(0,r,\phi) + \frac{\rho_1}{\pi}\int_{2\pi} I(0,r,\phi)\cdot\cos(-\hat{e}_z,\hat{\Omega})\cdot d\Omega \qquad (3\text{-}30a)$$

$$I_2(L,r,\phi) = f_2(L,r,\phi) + \varepsilon_2 I_{b2}(L,r,\phi) + \frac{\rho_2}{\pi}\int_{2\pi} I(L,r,\phi)\cdot\cos(\hat{e}_z,\hat{\Omega})\cdot d\Omega \qquad (3\text{-}30b)$$

$$I_3(z,R_{out},\phi) = f_3(z,R_{out},\phi) + \varepsilon_3 I_{b3}(z,R_{out},\phi) + \frac{\rho_3}{\pi}\int_{2\pi} I(z,R_{out},\phi)\cdot\cos(\hat{e}_r,\hat{\Omega})\cdot d\Omega \qquad (3\text{-}30c)$$

$$I_4(z,R_{in},\phi) = f_4(z,R_{in},\phi) + \varepsilon_4 I_{b4}(z,R_{in},\phi) + \frac{\rho_4}{\pi}\int_{2\pi} I(z,R_{in},\phi)\cdot\cos(-\hat{e}_r,\hat{\Omega})\cdot d\Omega \qquad (3\text{-}30d)$$

Where we have considered only diffuse reflection. f_1, f_2, f_3 and f_4 are possible externally incident radiations at the boundaries. When the boundary is transparent, the second and third terms do not apply. If it is opaque, the first term is eliminated. Equations (3-30) can be further expressed as

$$I_1(0,r,\phi) = f_1(0,r,\phi) + \varepsilon_1 I_{b1}(0,r,\phi) + \frac{\rho_1}{\pi}\{-q_z 2(0,r,\phi) - q_z 3(0,r,\phi) - q_z 4(0,r,\phi)\} \qquad (3\text{-}31a)$$

$$I_2(L,r,\phi) = f_2(L,r,\phi) + \varepsilon_2 I_{b2}(L,r,\phi) + \frac{\rho_2}{\pi}\{q_z 1(L,r,\phi) + q_z 3(L,r,\phi) + q_z 4(L,r,\phi)\} \qquad (3\text{-}31b)$$

$$I_3(z,R_{out},\phi) = f_3(z,R_{out},\phi) + \varepsilon_3 I_{b3}(z,R_{out},\phi) + \frac{\rho_3}{\pi}\{q_r1(z,R_{out},\phi) + q_r2(z,R_{out},\phi) + q_r3(z,R_{out},\phi) + q_r4(z,R_{out},\phi)\} \quad (3\text{-}31c)$$

$$I_4(z,R_{in},\phi) = f_4(z,R_{in},\phi) + \varepsilon_4 I_{b4}(z,R_{in},\phi) + \frac{\rho_4}{\pi}\{q_r1(z,R_{in},\phi) + q_r2(z,R_{in},\phi) + q_r3(z,R_{in},\phi)\} \quad (3\text{-}31d)$$

Because surface 3 is a concave surface, a q_r3 term appears in the I_3 equation. When calculating $q_r1(z,R_{out},\phi)$, $q_r2(z,R_{out},\phi)$ and $q_r3(z,R_{out},\phi)$, γ_{Ro} will be zero when $-\frac{\pi}{2} \le \chi \le \frac{\pi}{2}$, so the integrations in equations (3-15) become

$$\int_{-(\frac{\pi}{2}+\phi_{in})}^{(\frac{\pi}{2}+\phi_{in})} = \int_{-(\frac{\pi}{2}+\phi_{in})}^{\frac{\pi}{2}} + \int_{\frac{\pi}{2}}^{(\frac{\pi}{2}+\phi_{in})} \quad (3\text{-}32)$$

Note that the incident radiation and heat fluxes on the outer cylindrical surface will also utilize this relation.

3.3 Numerical Methods

In order to evaluate the coupled equations above, the uniform grids 26×26 ×26 divide the domain. Piecewise second order Lagrange polynomial interpolation is assumed for the incident radiation, heat fluxes and entering intensity at the boundaries. 20 point Gauss-Legendre quadrature is used for all integrations and iteration is used to solve the resultant equations simultaneously. It is found that the convergence is fast (criteria 10^{-5} to 10^{-8}). The values of incident radiation and heat fluxes on the boundaries are obtained by direct computation from the integrals as:

surface 1

$$G|_{surface1} = \lim_{z\to 0} G(z,r,\phi)$$
$$= \lim_{z\to 0}[G1(z,r,\phi) + G2(z,r,\phi) + G3(z,r,\phi) + G4(z,r,\phi)] \quad (3\text{-}33a)$$
$$= 2J_1(0,r,\phi) + G2(0,r,\phi) + G3(0,r,\phi) + G4(0,r,\phi)$$

$$q_r|_{surface1} = \lim_{z\to 0} q_r(z,r,\phi)$$
$$= \lim_{z\to 0}[q_r1(z,r,\phi) + q_r2(z,r,\phi) + q_r3(z,r,\phi) + q_r4(z,r,\phi)] \quad (3\text{-}33b)$$
$$= 0 + q_r2(0,r,\phi) + q_r3(0,r,\phi) + q_r4(0,r,\phi)$$

$$q_z|_{surface1} = \lim_{z\to 0} q_z(z,r,\phi)$$
$$= \lim_{z\to 0}[q_z1(z,r,\phi) + q_z2(z,r,\phi) + q_z3(z,r,\phi) + q_z4(z,r,\phi)] \quad (3\text{-}33c)$$
$$= J_1(0,r,\phi) + q_z2(0,r,\phi) + q_z3(0,r,\phi) + q_z4(0,r,\phi)$$

$$q_\phi|_{surface1} = \lim_{z\to 0} q_\phi(z,r,\phi)$$
$$= \lim_{z\to 0}[q_\phi1(z,r,\phi) + q_\phi2(z,r,\phi) + q_\phi3(z,r,\phi) + q_\phi4(z,r,\phi)] \quad (3\text{-}33d)$$
$$= 0 + q_\phi2(0,r,\phi) + q_\phi3(0,r,\phi) + q_\phi4(0,r,\phi)$$

surface 2

$$G|_{surface2} = \lim_{z\to L} G(z,r,\phi)$$
$$= \lim_{z\to L}[G1(z,r,\phi) + G2(z,r,\phi) + G3(z,r,\phi) + G4(z,r,\phi)] \quad (3\text{-}34a)$$
$$= G1(L,r,\phi) + 2J_2(L,r,\phi) + G3(L,r,\phi) + G4(L,r,\phi)$$

$$q_r|_{surface2} = \lim_{z\to L} q_r(z,r,\phi)$$
$$= \lim_{z\to L}[q_r1(z,r,\phi) + q_r2(z,r,\phi) + q_r3(z,r,\phi) + q_r4(z,r,\phi)] \quad (3\text{-}34b)$$
$$= q_r1(L,r,\phi) + 0 + q_r3(L,r,\phi) + q_r4(L,r,\phi)$$

$$q_z|_{surface2} = \lim_{z\to L} q_z(z,r,\phi)$$
$$= \lim_{z\to L}[q_z1(z,r,\phi) + q_z2(z,r,\phi) + q_z3(z,r,\phi) + q_z4(z,r,\phi)] \quad (3\text{-}34c)$$
$$= q_z1(L,r,\phi) - J_2(L,r,\phi) + q_z3(L,r,\phi) + q_z4(L,r,\phi)$$

$$q_\phi|_{surface2} = \lim_{z\to L} q_\phi(z,r,\phi)$$
$$= \lim_{z\to L}[q_\phi1(z,r,\phi) + q_\phi2(z,r,\phi) + q_\phi3(z,r,\phi) + q_\phi4(z,r,\phi)] \quad (3\text{-}34d)$$
$$= q_\phi1(L,r,\phi) + 0 + q_\phi3(L,r,\phi) + q_\phi4(L,r,\phi)$$

surface 3

$$G\big|_{surface3} = \lim_{r\to R_{out}} G(z,r,\phi)$$
$$= \lim_{r\to R_{out}} \left[G1(z,r,\phi)+G2(z,r,\phi)+G3(z,r,\phi)+G4(z,r,\phi)\right] \quad (3\text{-}35a)$$
$$= G1(z,R_{out},\phi)+G2(z,R_{out},\phi)+[2J_3(z,R_{out},\phi)+G3(z,R_{out},\phi)]+G4(z,R_{out},\phi)$$

$$q_r\big|_{surface3} = \lim_{r\to R_{out}} q_r(z,r,\phi)$$
$$= \lim_{r\to R_{out}} \left[q_r1(z,r,\phi)+q_r2(z,r,\phi)+q_r3(z,r,\phi)+q_r4(z,r,\phi)\right] \quad (3\text{-}35b)$$
$$= q_r1(z,R_{out},\phi)+q_r2(z,R_{out},\phi)+[-J_3(z,R_{out},\phi)+q_r3(z,R_{out},\phi)]+q_r4(z,R_{out},\phi)$$

$$q_z\big|_{surface3} = \lim_{r\to R} q_z(z,r,\phi)$$
$$= \lim_{r\to R_{out}} \left[q_z1(z,r,\phi)+q_z2(z,r,\phi)+q_z3(z,r,\phi)+q_z4(z,r,\phi)\right] \quad (3\text{-}35c)$$
$$= q_z1(z,R_{out},\phi)+q_z2(z,R_{out},\phi)+\left[0+q_z3(z,R_{out},\phi)\right]+q_z4(z,R_{out},\phi)$$

$$q_\phi\big|_{surface3} = \lim_{r\to R_{out}} q_\phi(z,r,\phi)$$
$$= \lim_{r\to R_{out}} \left[q_\phi1(z,r,\phi)+q_\phi2(z,r,\phi)+q_\phi3(z,r,\phi)+q_\phi4(z,r,\phi)\right] \quad (3\text{-}35d)$$
$$= q_\phi1(z,R_{out},\phi)+q_\phi2(z,R_{out},\phi)+\left[0+q_\phi3(z,R_{out},\phi)\right]+q_\phi4(z,R_{out},\phi)$$

surface 4

$$G\big|_{surface4} = \lim_{r\to R_{in}} G(z,r,\phi)$$
$$= \lim_{r\to R_{in}} \left[G1(z,r,\phi)+G2(z,r,\phi)+G3(z,r,\phi)+G4(z,r,\phi)\right] \quad (3\text{-}36a)$$
$$= G1(z,R_{in},\phi)+G2(z,R_{in},\phi)+G3(z,R_{in},\phi)+2J_4(z,R_{in},\phi)$$

$$q_r\big|_{surface4} = \lim_{r\to R_{in}} q_r(z,r,\phi)$$
$$= \lim_{r\to R_{in}} \left[q_r1(z,r,\phi)+q_r2(z,r,\phi)+q_r3(z,r,\phi)+q_r4(z,r,\phi)\right] \quad (3\text{-}36b)$$
$$= q_r1(z,R_{in},\phi)+q_r2(z,R_{in},\phi)+q_r3(z,R_{in},\phi)+J_4(z,R_{in},\phi)$$

$$q_z\big|_{surface4} = \lim_{r\to R_{in}} q_z(z,r,\phi)$$
$$= \lim_{r\to R_{in}} \left[q_z1(z,r,\phi)+q_z2(z,r,\phi)+q_z3(z,r,\phi)+q_z4(z,r,\phi)\right] \quad (3\text{-}36c)$$
$$= q_z1(z,R_{in},\phi)+q_z2(z,R_{in},\phi)+q_z3(z,R_{in},\phi)$$

$$
\begin{aligned}
q_\phi\big|_{surface4} &= \lim_{r\to R} q_\phi(z,r,\phi) \\
&= \lim_{r\to R_{in}} \left[q_\phi 1(z,r,\phi) + q_\phi 2(z,r,\phi) + q_\phi 3(z,r,\phi) + q_\phi 4(z,r,\phi) \right] \\
&= q_\phi 1(z,R_{in},\phi) + q_\phi 2(z,R_{in},\phi) + q_\phi 3(z,R_{in},\phi)
\end{aligned}
\qquad \text{(3-36d)}
$$

where $J_i=\pi\cdot I_i$ for the diffuse i^{th} boundary in above equations. We can see some values of incident radiation and heat fluxes are invalid at boundaries (not the same as expressed by the transformed integral equations). The incident radiation and heat fluxes at the intersection of boundary surfaces are obtained by multidimensional extrapolation.

3.4 Results and Discussions

In this work, we solve some typical radiative heat transfer problems by above-mentioned surface integral equations. Considering a non-homogeneous medium, we have continuous change properties and step-change properties (as in layered materials). In order to compare with available data in the literature, we start from the 2-D results.

3.4.1 Continuous-Changing Property 2-D Results

In the axisymmetric cylindrical medium, the incident radiation and heat fluxes will be the function of only z and r. The heat flux q_ϕ vanishes also. The whole set of equations are easily obtained from 3-D equations (3-14)-(3-17) by omitting the ϕ variable or setting ϕ equal zero. In order to compare with available data in the literature, the following cases are computed to test the current scheme.

Table 3-1 Case conditions for continuous-changing property 2-D solutions

	Geometry	Medium property	Surfaces
Case 1	***Solid cylinder*** R=L=1.0	β=uniform, $I_b(\tau_z,\tau_r)=1.0$, ω=0.5, $1-0.75(\frac{\tau_r}{R})$, $0.375(\frac{\tau_r}{R})+0.5(\frac{\tau_r}{R})^2$ a1=0, 0.99, -0.99	All cold walls $\varepsilon_1=1.0$, $\varepsilon_2=1.0$, $\varepsilon_3=1.0$
Case 2	***Solid cylinder*** R=L=1.0	β=uniform, $I_b(\tau_z,\tau_r)=1-(\tau_r/R)^2$, ω=0.5, $1-0.75(\frac{\tau_r}{R})$, $0.375(\frac{\tau_r}{R})+0.5(\frac{\tau_r}{R})^2$ a1=0, 0.99, -0.99	All cold walls $\varepsilon_1=1.0$, $\varepsilon_2=1.0$, $\varepsilon_3=1.0$
Case 3	***Solid cylinder*** R=L=1.0	$I_b(\tau_z,\tau_r)=1.0$, ω=0.5, β=1.0, $0.5+0.75(\frac{\tau_r}{R})$, $1.2-0.4(\frac{\tau_r}{R})^2$ a1=0 (isotropic scattering)	All cold walls $\varepsilon_1=1.0$, $\varepsilon_2=1.0$, $\varepsilon_3=1.0$
Case 4	***Hollow cylinder*** R_{in}=0.1,0.5,0.8 R_{out}=L=1.0	β=1.0, $I_b(\tau_z,\tau_r)=1.0$, ω=0.5 a1=0, 0.99, -0.99	All cold walls $\varepsilon_1=1.0$,$\varepsilon_2=1.0$, $\varepsilon_3=1.0$, ε_4=0, 1.0

If we consider the scattering albedo change [3.5,3.8] in the medium with optical thickness as shown in Figure 3-5 The scattering albedo changes with normalized radial distance τ_r/R in three different cases., the effect of this albedo change on the heat flux $q_r(\tau_z,R)$ is presented in Figure 3-6. There is a good agreement between current work and the results of Zhang and Sutton [3.5].

The effects of scattering albedo and linear anisotropic coefficient on the incident radiation and heat flux q_r are shown in Figure 3-7. As expected, we can see that the bigger the local scattering albedo in the medium, the smaller the incident radiation and heat flux q_r. The linear anisotropic coefficient a1's influence is small compared with scattering albedo. The difference of forward scattering and backward scattering on the incident radiation will increase when albedo increases. But, the difference of forward and

backward scattering on the heat flux q_r will decrease with the albedo increase because of cylinder geometry (diameter larger than height, R=L=1).

Figure 3-8 shows the influence of the linear anisotropic coefficient a1 on the heat flux at the bottom surface. The effects of a1 will increase with the increase of optical thickness and the increase of scattering albedo (see Figure 3-5). The data presented here agree well with published results [3.8].

Figure 3-9 shows the combined effects of scattering albedo ω and medium emission intensity. We can see similar incident radiation and heat flux changes with albedo as that shown in Figure 3-7. But, the effects of albedo on G and q_r will decrease as local medium emission decreases. This is illustrated in the figure especially near the cylindrical boundary. The linear anisotropic coefficient influence is similar to that shown in Figure 3-7.

If the medium is non-homogeneous and the extinction coefficient changes in three different combinations as shown in Figure 3-10, the distributions of incident radiation $G(0.5L,\tau_r)$ and heat flux $q_r(0.5L,\tau_r)$ with normalized optical thickness τ_r/R are presented in Figure 3-11. The larger the local extinction coefficient β, the larger the incident radiation and heat flux q_r. This is because the optical thickness increases with β.

The present scheme also is verified in hollow cylinder cases. Figure 3-12 gives the distributions of incident radiation and heat flux q_r with respect to normalized optical thickness τ_r/R_{out} in different inner cylinder radii and black surface boundaries. Figure 3-13 shows the effects of inner cylindrical wall emissivity ε_4 on the distribution of G and q_r along radial direction. When ε_4 equals zero, due to total reflection on the inner cylindrical surface, the heat flux q_r at the inner wall should be zero as shown in the

figure. The incident radiation when ε_4=0 will be much greater than that when ε_4=1 (black surface). Both the effects of the inner radius and inner wall emissivity on the results are shown.

Figure 3-14 shows the effect of anisotropic scattering on the incident radiation. The inner wall emissivity will affect this effect of scattering coefficient a1. The greater the inner wall emissivity is, the smaller the effect of a1 on incident radiation G. This is especially obvious near the inner wall.

3.4.2 Continuous-Changing Property 3-D Results

The equations (3-14)-(3-17) can be directly applied to solve 3-D cylindrical radiative heat transfer problems. Considering a non-homogeneous medium, the following cases are analyzed to compare with available data in the literature.

Table 3-2 Case conditions for continuous-changing property 3-D solutions

	Geometry	Medium property	Surfaces
Case 5	***Solid cylinder*** 2R=L=1.0	β=uniform, $I_b(\tau_z,\tau_r,\tau_\phi)$=1.0 ω=0.1, 0.5, 0.9 a1=0 (isotropic scattering)	All cold walls ε_1=1.0, ε_2=1.0, ε_3=1/2(1-sinϕ)
Case 6	***Solid cylinder*** R=L=1.0	β=uniform, $I_b(\tau_z,\tau_r,\tau_\phi)$=1.0 ω=0.5, $1-0.75(\frac{\tau_r}{R})$, $0.375(\frac{\tau_r}{R})+0.5(\frac{\tau_r}{R})^2$ a1=0, 0.99, -0.99	All cold walls ε_1=1.0, ε_2=1.0, ε_3=1/2(1-sinϕ)
Case 7	***Solid cylinder*** R=L=1.0	$I_b(\tau_z,\tau_r,\tau_\phi)$=1.0, ω=0.5 β=1.0, $0.5+0.75(\frac{\tau_r}{R})$, $1.2-0.4(\frac{\tau_r}{R})^2$ a1=0 (isotropic scattering)	All cold walls ε_1=1.0, ε_2=1.0, ε_3=1/2(1-sinϕ)

Figure 3-15 to Figure 3-17 have shown the comparison of current work to previous results [3.6], which used the Surface-Volume integration method, for case 5 in table 3-2. There is good agreement between the two methods. Figure 3-15 presents the effects of scattering albedo on the two heat fluxes q_r and q_ϕ. The magnitudes of both heat fluxes decrease with increasing albedo. Figure 3-16 illustrates the distributions of q_r and q_ϕ in the radial direction. We can see the typical effects of albedo on the distributions. Figure 3-17 has variations of incident radiation and heat fluxes q_r and q_ϕ around angular coordinate. The incident radiation $G(0.5L,0,\phi)$ at center line r=0 remains constant along different angular positions while the heat fluxes $q_r(0.5L,0,\phi)$, $q_\phi(0.5L,0,\phi)$ tend toward sinusoidal change around the zero horizontal axis. The distributions at different radial positions r=0, 0.5R, R are also given in the figure.

Under spatial change, for the albedo situations shown in Figure 3-5, the distributions of heat flux $q_r(\tau_z,R,0)$ at cylindrical surface and heat flux $q_z(\tau_z,0,0)$ at centerline are expressed in Figure 3-18. Heat flux q_z is always symmetric to the mid-plane $\tau_z/L=0.5$. The distributions of two net flux components $q_r(0.5L,\tau_r,0)$ and $q_\phi(0.5L,\tau_r,0)$ at mid-plane along radial direction are shown in Figure 3-19. Compared with Figure 3-16, the effects of spatial change albedo are clear. The higher the scattering albedo, the smaller the heat fluxes. At somewhere higher albedo, q_r will be negative.

For case 6 listed in table 3-2, the variations of incident radiation and heat flux q_r along the angular coordinate are shown in Figure 3-20. The incident radiation $G(0.5L,0,\phi)$ at the centerline remains constant as before in Figure 3-17. The heat flux $q_r(0.5L,0,\phi)$ tends toward sinusoidal change around the zero horizontal axis also. But the distributions when r=0.5R and r=R are at different relative positions compared with that

in Figure 3-17 because albedo ω_2 changes with the r coordinate. The distributions of the two net flux components q_ϕ and q_z around angular direction are shown in Figure 3-21. We can see the difference at different r (0, 0.5R, R) positions.

The effects of linear anisotropic scattering coefficient a1 are shown in Figure 3-22. The difference of forward scattering and backward scattering on the heat flux q_r is not obvious. But for the incident radiation, this difference reaches 8 percent maximum at the centerline. As expected, the greater the local scattering albedo is, the bigger the difference between forward scattering and backward scattering.

Figure 3-23 presents the effects of extinction coefficient on two net flux components q_r and q_ϕ. The non-homogeneous property change is represented by β change as shown in figure 10. The greater the local β is, the larger the heat flux q_r but the smaller the magnitude of q_ϕ at angular position ϕ=0. Figure 3-24 shows the distributions of center point (0.5L, 0) heat fluxes q_r and q_ϕ around angular coordinate at different β conditions. It is interesting to note that at smaller center β condition, both heat fluxes tend toward larger magnitude sinusoidal change around the zero horizontal axis.

3.4.3 Step-Changing Property Results

For multi-layer systems, there are many potential applications (like composite layers for thermal insulation and laminated biotissues). One can find numerous methods [3.9-3.12] reported in the literature. Those methods are usually 1-D problems. The researchers gave different equations for step-change non-homogeneous cases and continuous change cases. However for variable property cases here, the solid angle integration is simply a geometric evaluation. The same integral equations (3-14)-(3-17)

apply. The importance lies in the calculation of intensity. When a ray is traced to calculate the intensity (the interface between two layers is assumed free and non-reflecting), all radiation related factors go into the given intensity equation (3-7). The only difference here in step-change property is to apply Gauss Quadrature integration by segments.

For a two layer, 3-D radiation problem, assume step-change extinction coefficient and scattering albedo (Figure 3-25) in the radial direction:

$$\beta(z',r',\phi') = \beta_{in}, \quad \omega(z',r',\phi') = \omega_{in}, \quad \text{when } R_{in} \le r' \le R_m \tag{3-37a}$$

$$\beta(z',r',\phi') = \beta_{out}, \quad \omega(z',r',\phi') = \omega_{out}, \quad \text{when } R_m \le r' \le R_{out} \tag{3-37b}$$

where 'in' and 'out' refer to the inside and outside layers respectively. When R_{in}=0, this becomes a two-layer solid cylinder problem automatically as before. If the radiation loading on the boundary (temperature or externally incident radiation) is not axisymmetric, it could be a true 3-D problem although the properties are symmetric. The integral equations (3-14)-(3-17) behave the same. First we consider computation of the intensity from start point $s_i(z_i,r_i,\phi_i)$ to point $s(z,r,\phi)$ if the line $\overline{s_i s}$ across two layers.

If any point $s'(z',r',\phi')$ lays on and between the line $\overline{s_i s}$, there are

$$z' = z_i + (z - z_i)\cdot t \quad \text{where} \quad 1 \ge t \ge 0 \tag{3-38a}$$

$$r' = \sqrt{x'^2 + y'^2} \tag{3-38b}$$

where

$$x' = x_i + (x - x_i)\cdot t = r_i\cos\phi_i + (r\cos\phi - r_i\cos\phi_i)\cdot t \tag{3-39a}$$

$$y' = y_i + (y - y_i)\cdot t = r_i\sin\phi_i + (r\sin\phi - r_i\sin\phi_i)\cdot t \tag{3-39b}$$

The cross point of the line $\overline{s_i s}$ with the circle r=R_m is determined by

$$x'^2 + y'^2 = R_m^{\ 2} \tag{3-40a}$$

that is

$$[r_i \cos\phi_i + (r\cos\phi - r_i\cos\phi_i)t]^2 + [r_i \sin\phi_i + (r\sin\phi - r_i\sin\phi_i)t]^2 = R_m^{\ 2} \tag{3-40b}$$

we solve above equation for t as follows:

$$t_{1,2} = \frac{r_i[r_i - r\cos(\phi - \phi_i)] \pm \sqrt{r_i^2[r_i - r\cos(\phi - \phi_i)]^2 + \gamma^2(R_m^{\ 2} - r_i^2)}}{\gamma^2} \tag{3-41}$$

where

$$\gamma = [r^2 + r_i^2 - 2rr_i\cos(\phi - \phi_i)]^{1/2} \tag{3-42}$$

In equation (3-42), the '–' operation in the numerator goes with solution t_1 and the '+' operation goes with solution t_2. So the root t_2 is always greater than t_1. Usually, we may have three situations. One is no solution or both t_1 and t_2 do not belong to [0,1], so there is no intersection between line $\overline{s_i s}$ and middle cylindrical plane r=R_m; another situation is only one of t_1 and t_2 belongs to [0,1], so there is only one intersection; the last situation is both of t_1 and t_2 fall in the range [0,1], so there are two intersections. From systematic analysis of equation (3-41), we have following possibilities:

If $r \le R_m$ (Figure 3-25)

1) When $t_1, t_2 \notin [0,1]$

$$I(z,r,\phi,\hat{\Omega}) = I_i \exp[-\beta_{in} d(s_i,s)] + \int_0^1 \beta_{in} S(\omega_{in}) \exp[-\beta_{in}(1-t) d(s_i,s)] d(s_i,s) dt \tag{3-43a}$$

2) When only $t_1 \in [0,1]$

$$I(z,r,\phi,\hat{\Omega}) = I_i \exp\{-[\beta_{out} t_1 + \beta_{in}(1-t_1)]d(s_i,s)\} +$$
$$\int_0^{t_1} \beta_{out} S(\omega_{out}) \exp\{-[\beta_{out}(t_1 - t) + \beta_{in}(1-t_1)]d(s_i,s)\} d(s_i,s) dt + \quad (3\text{-}43b)$$
$$\int_{t_1}^{1} \beta_{in} S(\omega_{in}) \exp[-\beta_{in}(1-t) d(s_i,s)] d(s_i,s) dt$$

If $r > R_m$ (Figure 3-26)

3) When no solution or $t_1, t_2 \notin [0,1]$

$$I(z,r,\phi,\hat{\Omega}) = I_i \exp[-\beta_{out} d(s_i,s)] + \int_0^1 \beta_{out} S(\omega_{out}) \exp[-\beta_{out}(1-t) d(s_i,s)] d(s_i,s) dt \quad (3\text{-}43c)$$

4) When only $t_2 \in [0,1]$

$$I(z,r,\phi,\hat{\Omega}) = I_i \exp\{-[\beta_{in} t_2 + \beta_{out}(1-t_2)]d(s_i,s)\} +$$
$$\int_0^{t_2} \beta_{in} S(\omega_{in}) \exp\{-[\beta_{in}(t_2 - t) + \beta_{out}(1-t_2)]d(s_i,s)\} d(s_i,s) dt + \quad (3\text{-}43d)$$
$$\int_{t_2}^{1} \beta_{out} S(\omega_{out}) \exp[-\beta_{out}(1-t) d(s_i,s)] d(s_i,s) dt$$

5) When both $t_1, t_2 \in [0,1]$

$$I(z,r,\phi,\hat{\Omega}) = I_i \exp\{-[\beta_{out} t_1 + \beta_{in}(t_2 - t_1) + \beta_{out}(1-t_2)]d(s_i,s)\} +$$
$$\int_0^{t_1} \beta_{out} S(\omega_{out}) \exp\{-[\beta_{out}(t_1 - t) + \beta_{in}(t_2 - t_1) + \beta_{out}(1-t_2)]d(s_i,s)\} d(s_i,s) dt$$
$$\int_{t_1}^{t_2} \beta_{in} S(\omega_{in}) \exp\{-[\beta_{in}(t_2 - t) + \beta_{out}(1-t_2)]d(s_i,s)\} d(s_i,s) dt + \quad (3\text{-}43e)$$
$$\int_{t_2}^{1} \beta_{out} S(\omega_{out}) \exp[-\beta_{out}(1-t) d(s_i,s)] d(s_i,s) dt$$

Until now we certainly find it's not difficult to solve for the intensity. It is even easier in step-change property case, because we don't need to integrate to obtain the optical thickness.

In order to compare with available data in the previous paper [3.11], we consider axisymmetric radiative transfer in following cases listed in table 3-3.

Table 3-3 Case conditions for step-changing property 2-D solutions

	Geometry	Medium property	Boundaries
Case 8 (2-D)	***Solid cylinder*** R_m=1, R_{out}=2 L=1, 5, ∞	$I_b(\tau_z,\tau_r)$=1.0 β_{in}=0.8, 1.0, 1.2, β_{out}=0.8, 1.0, 1.2 ω_{in}=0.1, 0.5, 0.9, ω_{out}=0.1, 0.5, 0.9 a1=0 (isotropic scattering)	All cold walls ε_1=1, ε_2=1, I_3=f_3=0(trans.)
Case 9 (1-D)	***Solid cylinder*** R_m=1, R_{out}=2 L=∞	$I_b(\tau_z,\tau_r)$=0 β_{in}=1.0 β_{out}=1.0 ω_{in}=0.1, 0.5, 0.9, ω_{out}=0.1, 0.5, 0.9 a1=0, 0.99, -0.99	Transparent boundary f_3=1/π
Case 10 (1-D)	***Hollow cylinder*** R_{in}=1,R_m=2,R_{out}=3 L=∞	$I_b(\tau_z,\tau_r)$=0, β_{in}=0.8, 1.0, 1.2, β_{out}=0.8, 1.0, 1.2 ω_{in}=0.2, 0.5, 0.8, ω_{out}=0.2, 0.5, 0.8 a1=0 (isotropic scattering)	Transparent boundary f_3=1/π, f_4=0

The distributions of incident radiation and heat flux q_r for a hot solid cylindrical media in case 8 are shown in Figure 3-27, Figure 3-28. The effects of two layers with different scattering albedo but same extinction coefficient are presented in Figure 3-27, while the effects of two layers with different extinction coefficient but same albedo are presented in Figure 3-28. Smaller albedo or greater extinction coefficient leads to greater incident radiation and heat flux.

The effect of cylinder length is illustrated in Figure 3-29. The result of L=5 is almost the same as the result for infinite long cylinder.

Considering case 9 listed in table 3-3, the dependence of hemispherical reflectivity on the scattering albedo and linear anisotropic coefficient for a solid infinite long layered cylinder is presented in table 3-4. The influence of step change albedo is not negligible. So the homogeneous assumption for a layered medium may cause a large

error in the solution and may not be used in actual design and application. The forward scattering and backward scattering also have certain effects on the reflectivity as we can see from table 3-4. The isotropic assumption may lead to an average 10 percent error.

Table 3-4 The effects of linear anisotropic scattering coefficient on hemispherical reflectivity for a cold solid cylindrical medium with transparent boundary, $f_3(R_{out})=1/\pi$, $R_{in}=1$, $R_{out}=2$

ω_{in}	ω_{out}	Current work		
		a1=-0.99	a1=0	a1=0.99
0.1	0.9	0.62113	0.56406	0.48665
0.5	0.5	0.29457	0.25981	0.21805
0.9	0.1	0.11659	0.10914	0.10099

Considering case 10 listed in table 3-3, the effects of various combinations of β_{in} and β_{out}, ω_{in} and ω_{out} on the hemispherical reflectivity are shown in table 3-5. The results of current work agree well with the results of Wu and Wu [11]. At the same scattering albedo, the reflectivity increases with the increasing in-layer coefficient β_{in}. Under the same extinction coefficient, the reflectivity decreases with the increasing in-layer scattering albedo ω_{in}.

Table 3-5 Hemispherical reflectivity for a cold hollow cylindrical medium with transparent boundary, $f_3(R_{out})=1/\pi$, $f_4(R_{in})=0$, and $R_{in}=1$, $R_m=2$, $R_{out}=3$

ω_{in}	ω_{out}	Current work			C.Y. Wu and S.C. Wu [11]		
		$\beta_{in}=0.8$ $\beta_{out}=1.2$	$\beta_{in}=1.0$ $\beta_{out}=1.0$	$\beta_{in}=1.2$ $\beta_{out}=0.8$	$\beta_{in}=0.8$ $\beta_{out}=1.2$	$\beta_{in}=1.0$ $\beta_{out}=1.0$	$\beta_{in}=1.2$ $\beta_{out}=0.8$
0.2	0.8	0.38066	0.37876	0.37631	0.38044	0.37861	0.37640
0.5	0.5	0.19159	0.20245	0.21833	0.19133	0.20226	0.21824
0.8	0.2	0.08058	0.09535	0.11940	0.08046	0.09527	0.11935

From all above discussions, we can see the current scheme is how flexible in computing radiative heat transfer in cylindrical medium.

3.5 Conclusions

A general and flexible integration scheme is illustrated to solve radiative heat transfer problems in cylindrical non-homogeneous media. Results for 2-D continuous property change problems; 3-D continuous property change problems and 2-D step-change property problems are presented for hollow or solid, finite or infinite long cylinders. Some of them agree well with results of other people. The computer program is very stable and converges fast. Usually it takes about 1 minute to compute for a 1-D cases, 30 minutes for a 2-D step-change property cases, 60 minutes for a 2-D continuous property change cases and more than 15 hours for a 3-D continuous property change cases in Digital Fortran 5.0 on a generic PC with 1GB memory and an AMD Athlon™ XP 1.2 GHz processor.

It is believed that this method contribute to the combined heat transfer computation, which is also our future work.

3.6 Nomenclature

a_l linear anisotropic scattering coefficient

A differential surface area, m^2

d distance, m

f external incident radiation at the boundaries

G incident radiation, W/m^2

I the radiation intensity, W/m^2

J the radiosity of the surface, W/m^2

L the cylinder height, m

q components of net radiative heat flux, W/m^2

R_{in} the inside cylindrical radius, m

R_{out} the outside cylindrical radius, m

S radiation source term, W/m^2

T temperature, K

Greek symbols

α the specified angle, transformed coordinate

β extinction coefficient, 1/m

ε the emissivity of the surface

θ angle between surface normal vector and the intensity direction

γ the specified distance, transformed coordinate

ρ surface reflectivity

τ optical thickness

ϕ cylindrical angular coordinate

χ the specified angle, transformed coordinate

ω single scattering albedo

Ω the unit vector of the intensity direction, or the solid angle

Subscripts

b	black body
i	surface i
r	radial direction
R_i	at inside radius position
R_o	at outside radius position
z	axial direction
ϕ	angular direction

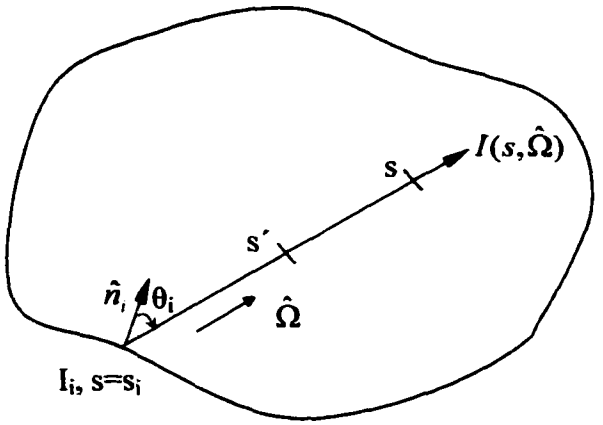

Figure 3-1 Illustration of the ray path, direction and boundary condition.

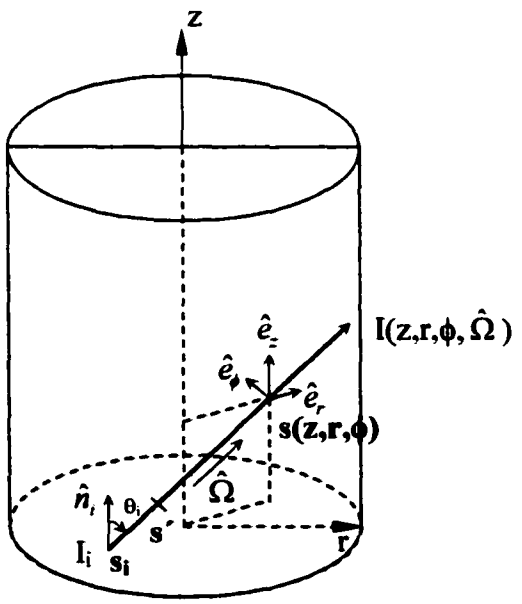

Figure 3-2 Schematic diagram of the cylindrical coordinate and the radiant ray direction.

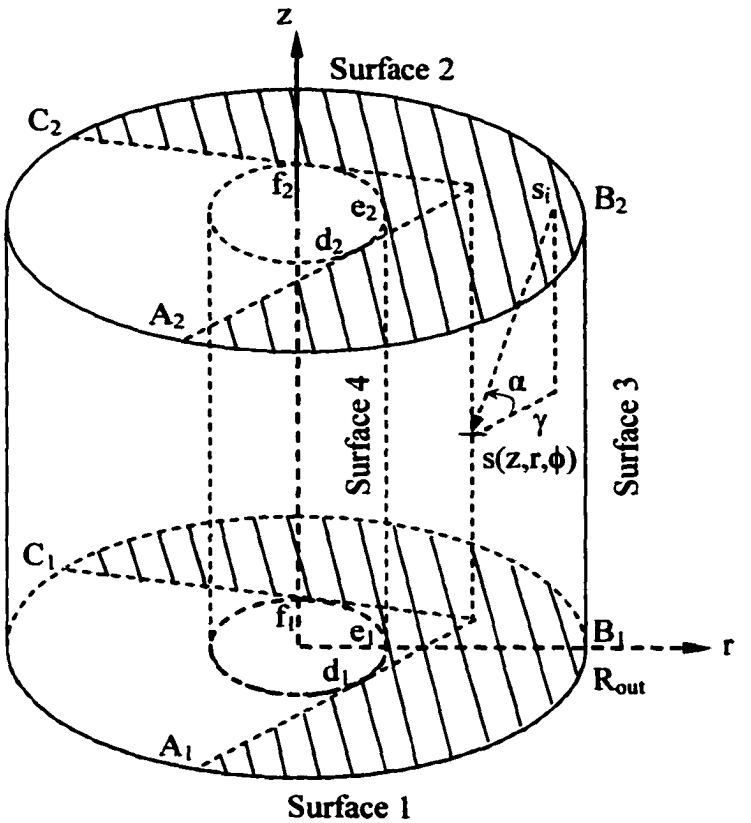

Figure 3-3 Schematic diagram of surface integration domain in a hollow cylinder.

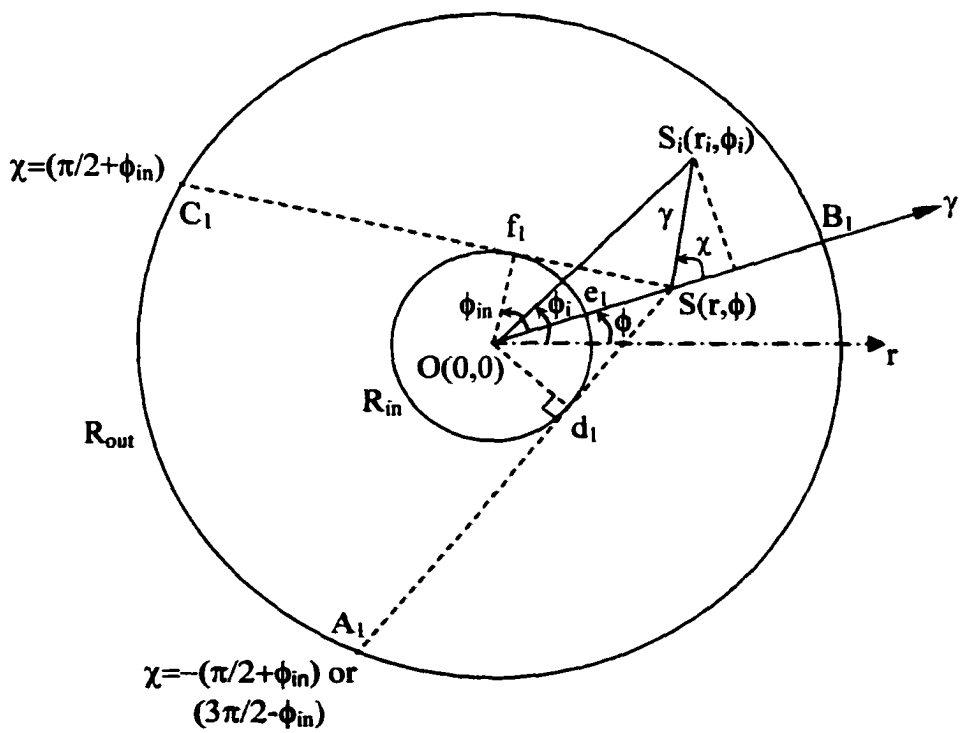

Figure 3-4 Top view of the coordinates transformation. Capital S is the projection of point s and capital S_i is the projection of point s_i.

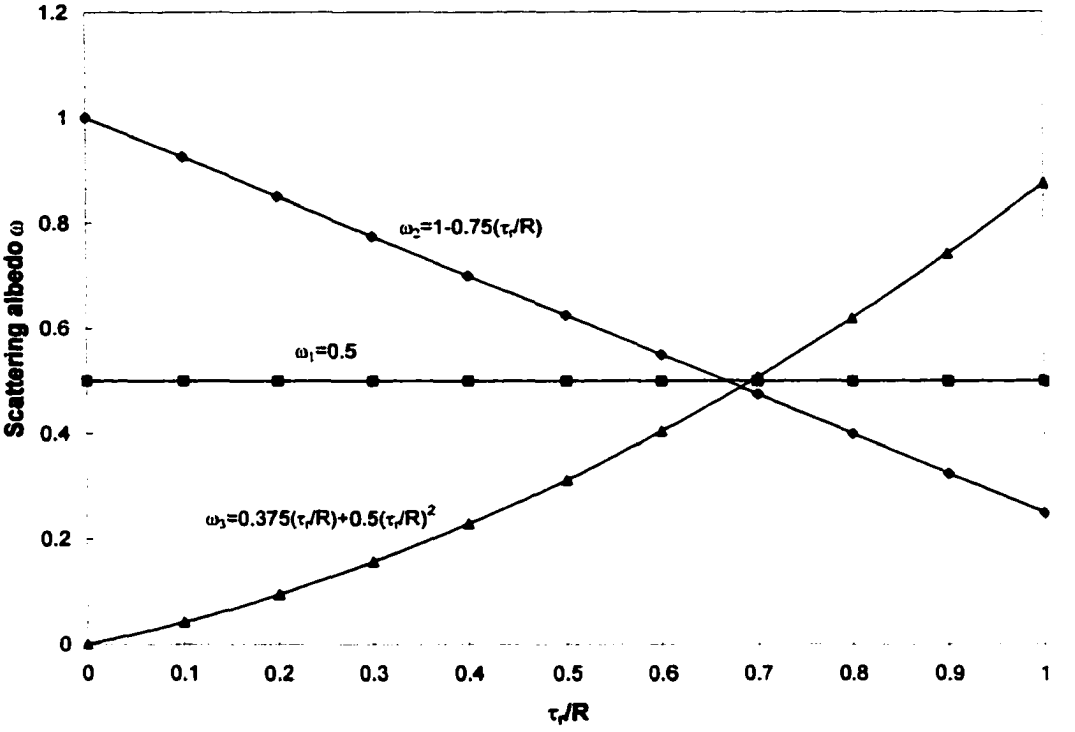

Figure 3-5 The scattering albedo changes with normalized radial distance τ_r/R in three different cases.

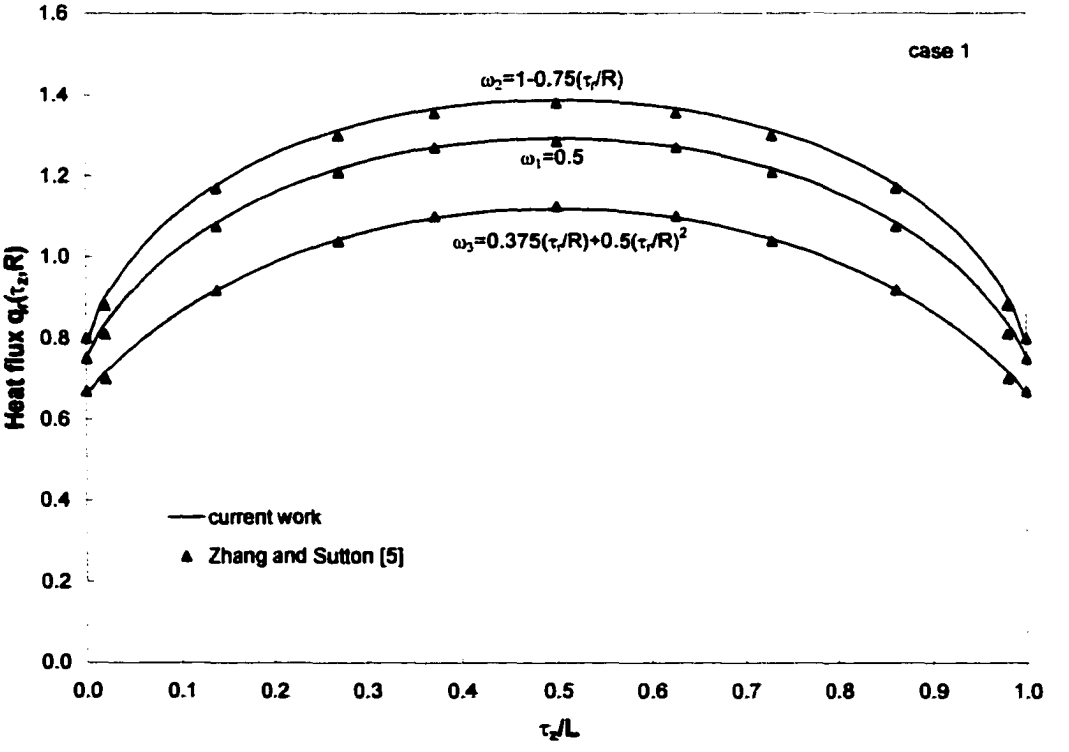

Figure 3-6 The effects of the scattering albedo on the radial heat flux $q_r(\tau_z,R)$ for a hot solid cylindrical medium enclosed by cold black walls, L=R=1.0.

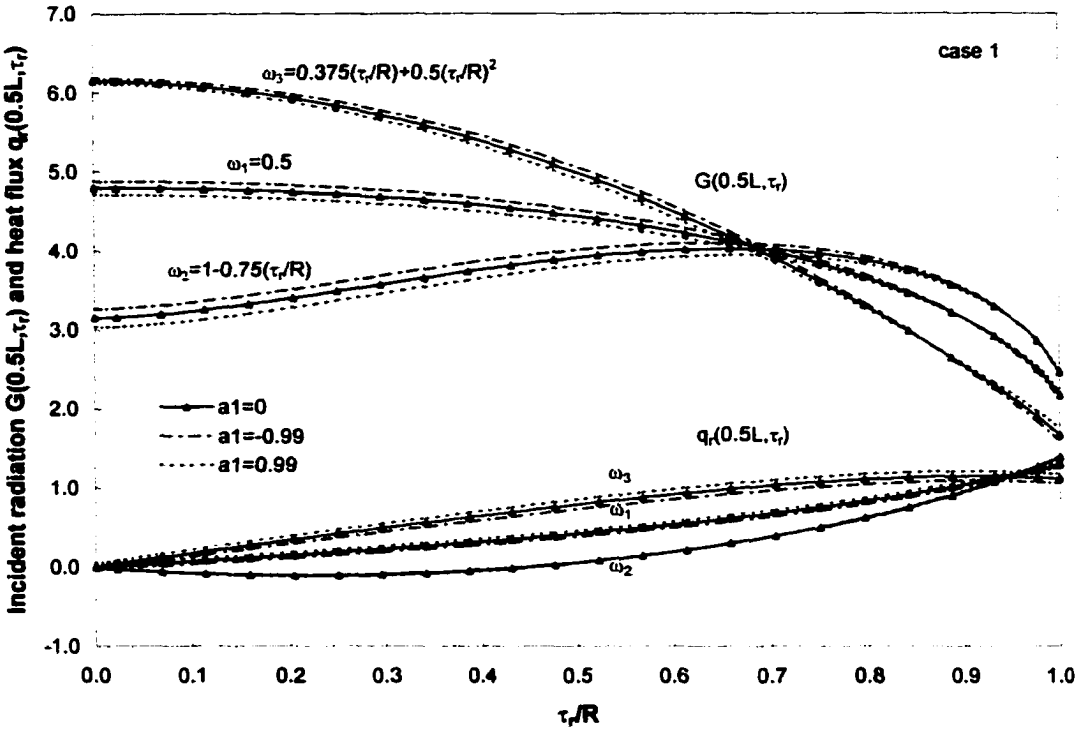

Figure 3-7 The combined effects of scattering albedo and linear anisotropic coefficient on the distributions of incident radiation $G(0.5L,\tau_r)$ and heat flux $q_r(0.5L,\tau_r)$ with respect to τ_r/R for case 1 in table 3-1.

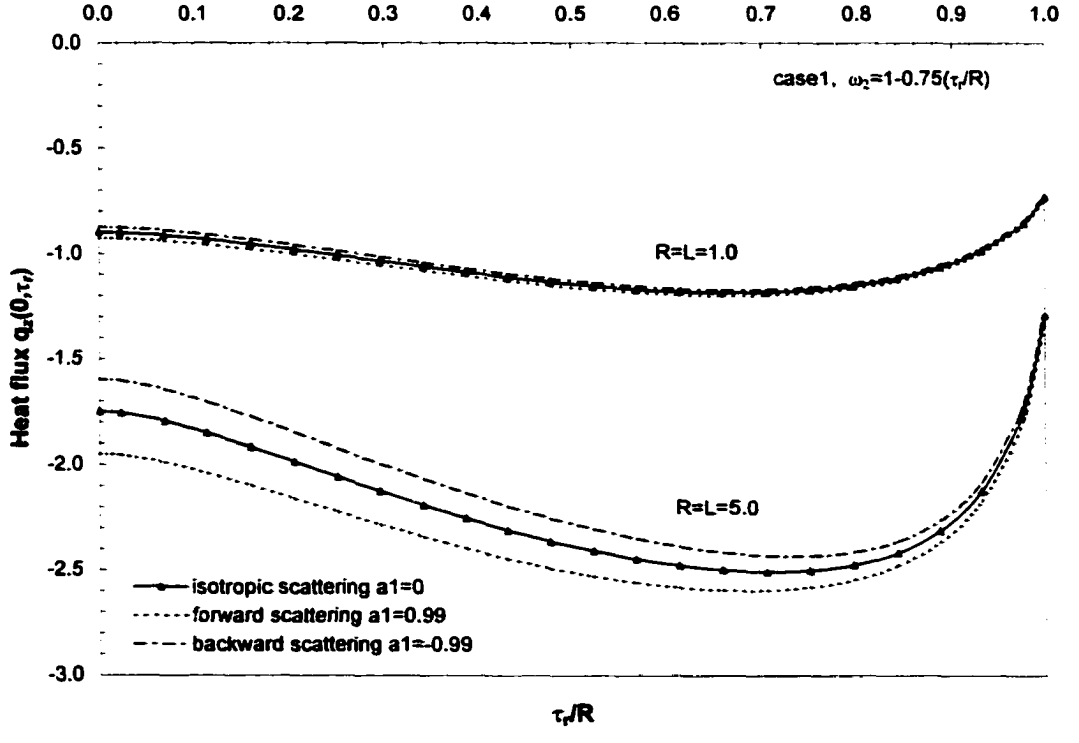

Figure 3-8 The combined effects of the optical thickness and linear anisotropic coefficient on the distribution of heat flux $q_r(0,\tau_r)$ with respect to τ_r/R for case 1 in table 3-1 with ω_2=1-0.75(τ_r/R).

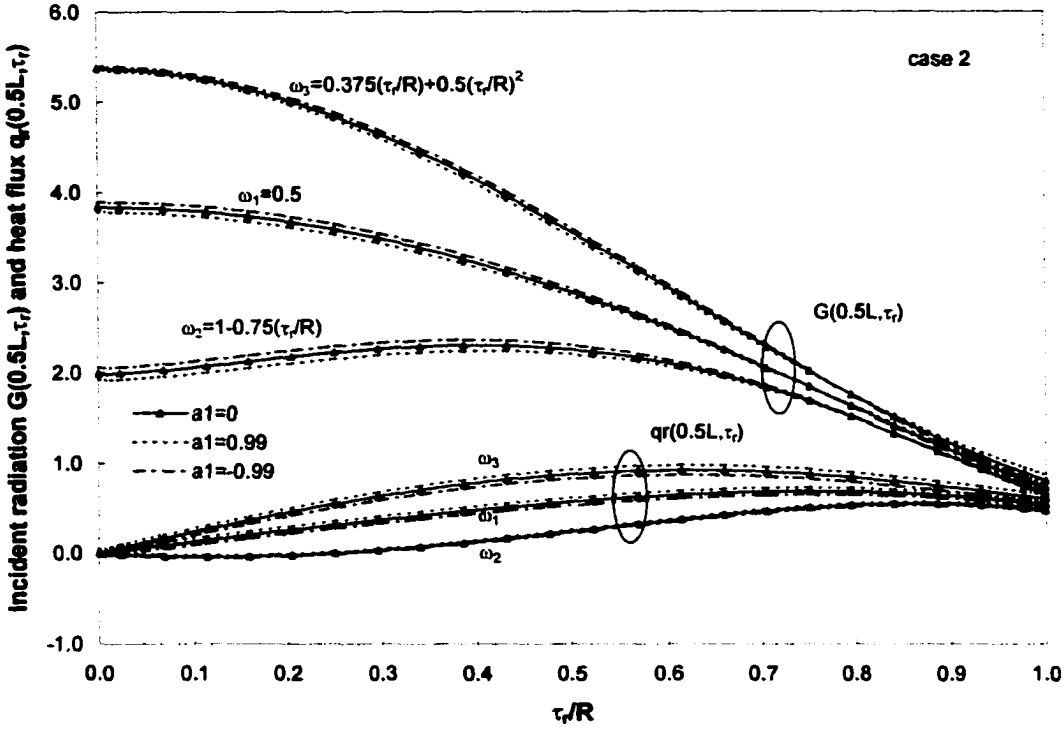

Figure 3-9 The combined effects of scattering albedo and linear anisotropic coefficient on the distributions of incident radiation G(0.5L,τ_r) and heat flux q_r(0.5L,τ_r) with respect to normalized optical thickness τ_r/R for a non-isothermal hot cylindrical medium (case 2 in table 3-1).

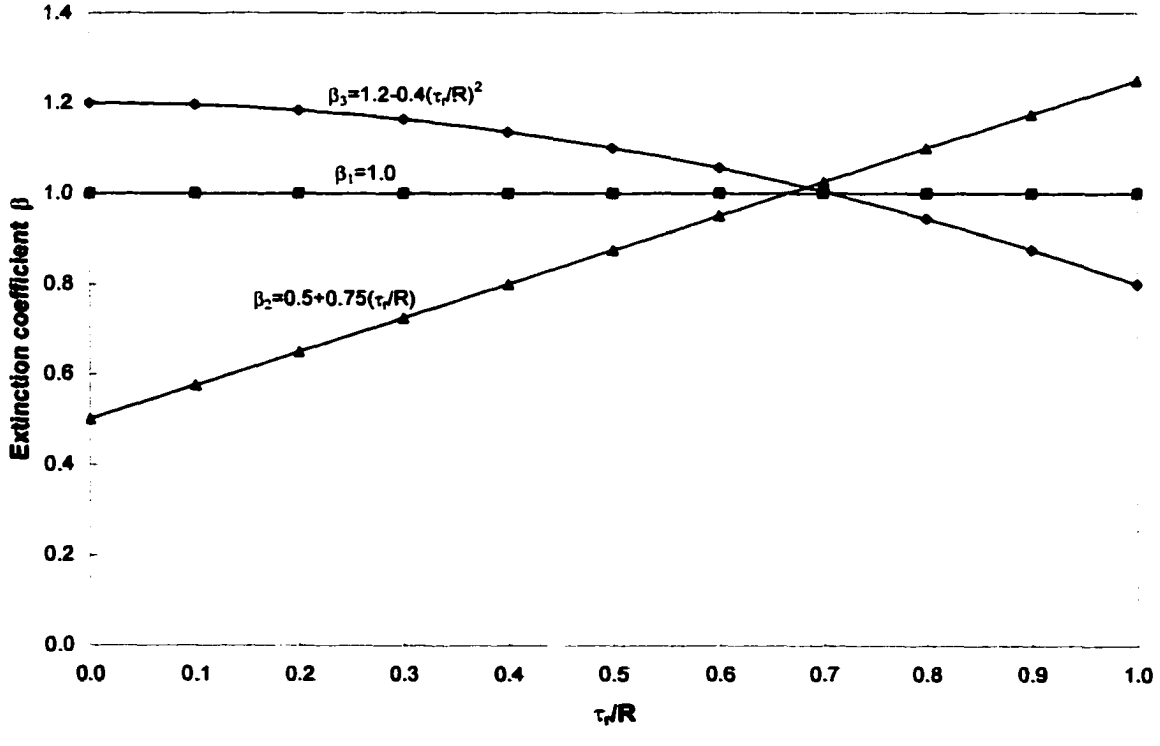

Figure 3-10 The extinction coefficient changes with normalized radial distance τ_r/R in three different cases.

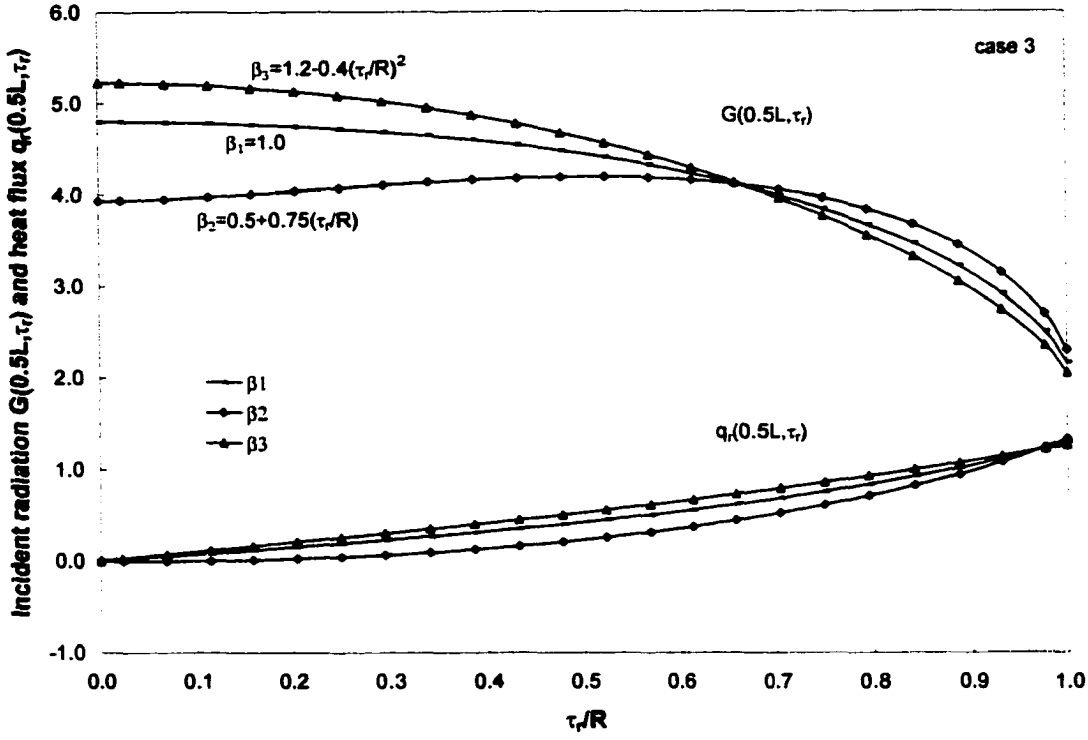

Figure 3-11 The effects of extinction coefficient on the distributions of incident radiation $G(0.5L,\tau_r)$ and heat flux $q_r(0.5L,\tau_r)$ with respect to normalized optical thickness τ_r/R for case 3 in table 3-1.

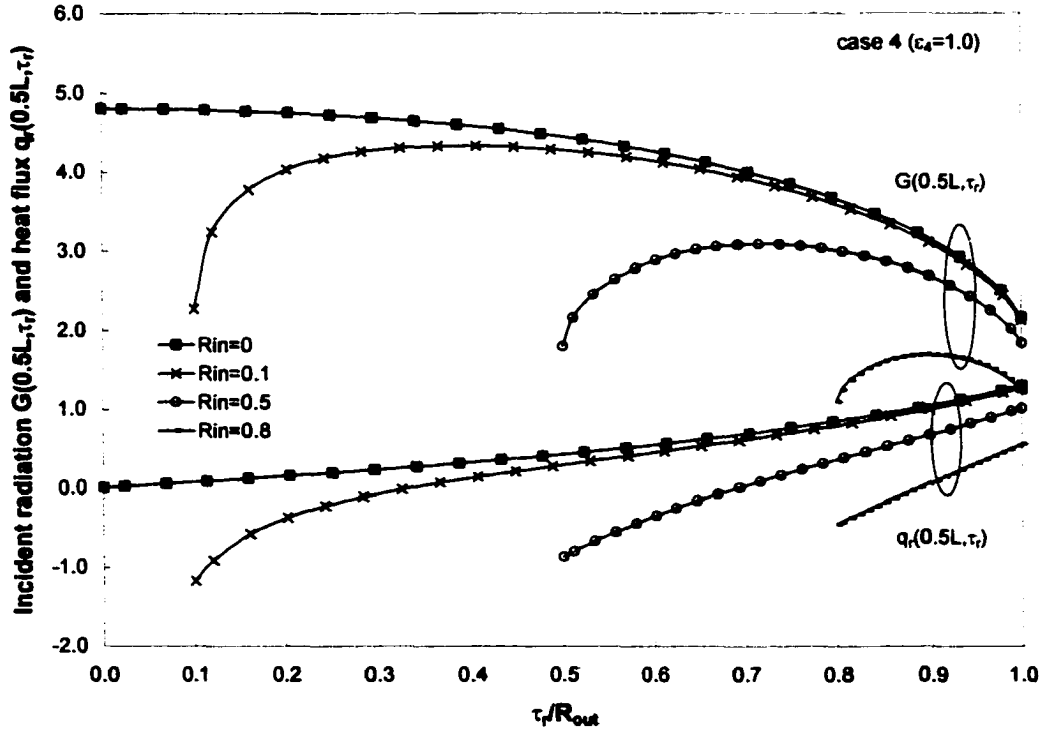

Figure 3-12 The effects of inner cylinder radius on the distributions of incident radiation $G(0.5L,\tau_r)$ and heat flux $q_r(0.5L,\tau_r)$ with respect to normalized optical thickness τ_r/R_{out}, for a hot hollow cylindrical medium enclosed by cold black walls (case 4 in table 3-1).

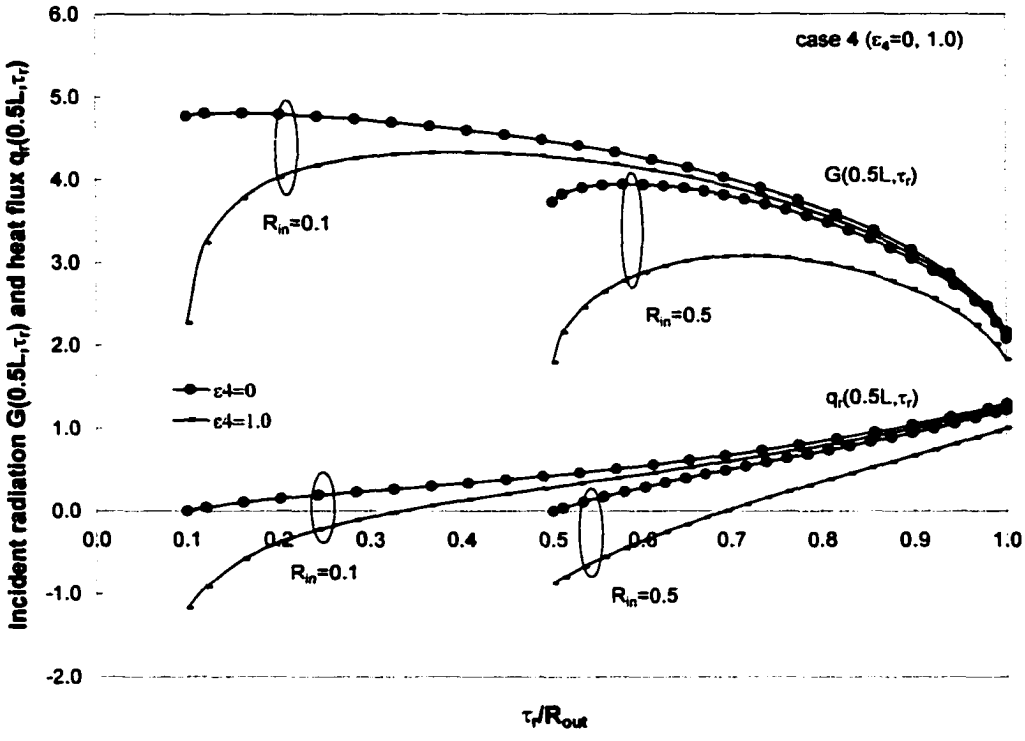

Figure 3-13 The effects of inner wall emissivity on the distributions of incident radiation $G(0.5L,\tau_r)$ and heat flux $q_r(0.5L,\tau_r)$, for a hot hollow cylindrical medium (case 4 in table 3-1).

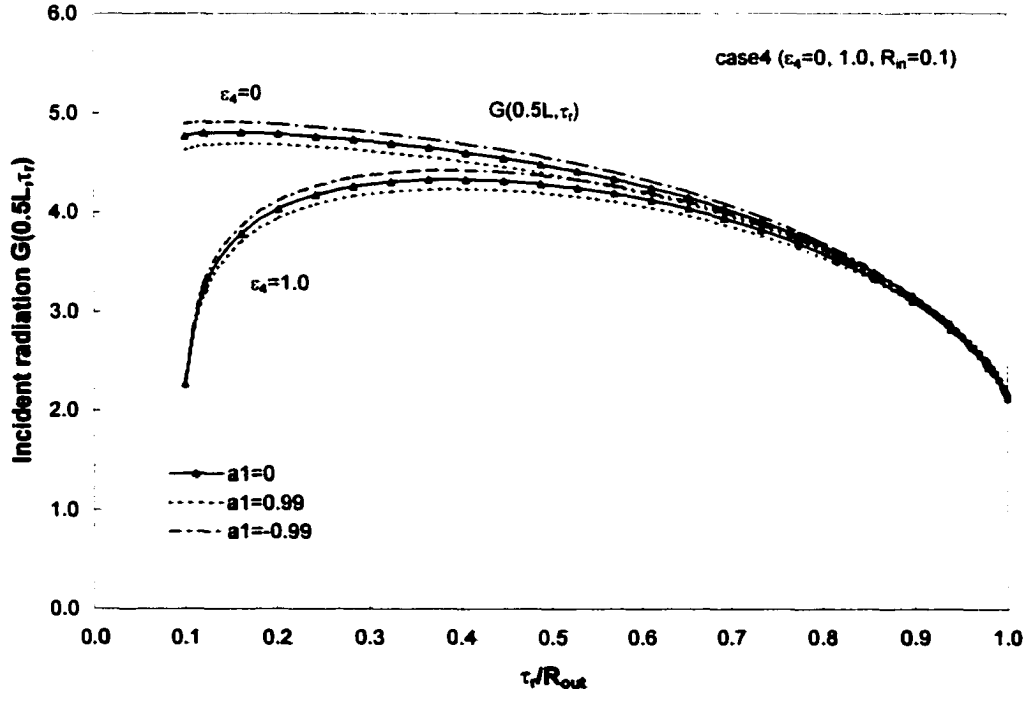

Figure 3-14 The combined effects of inner wall emissivity and linear anisotropic coefficient on incident radiation $G(0.5L,\tau_r)$ for a hot hollow cylindrical medium (case 4 in table 3-1).

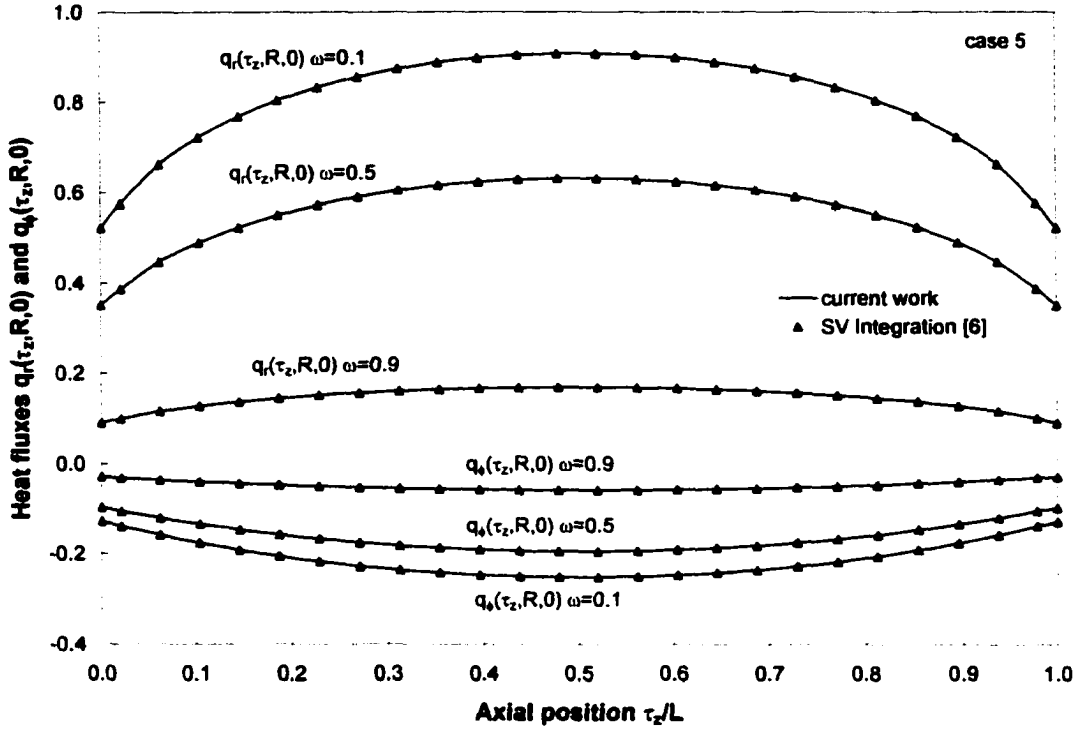

Figure 3-15 The comparison of present work and previous work [6] for the effects of scattering albedo on the distributions of $q_r(\tau_z,R,0)$ and $q_\phi(\tau_z,R,0)$ with respect to τ_z/L for case 5 in table 3-2.

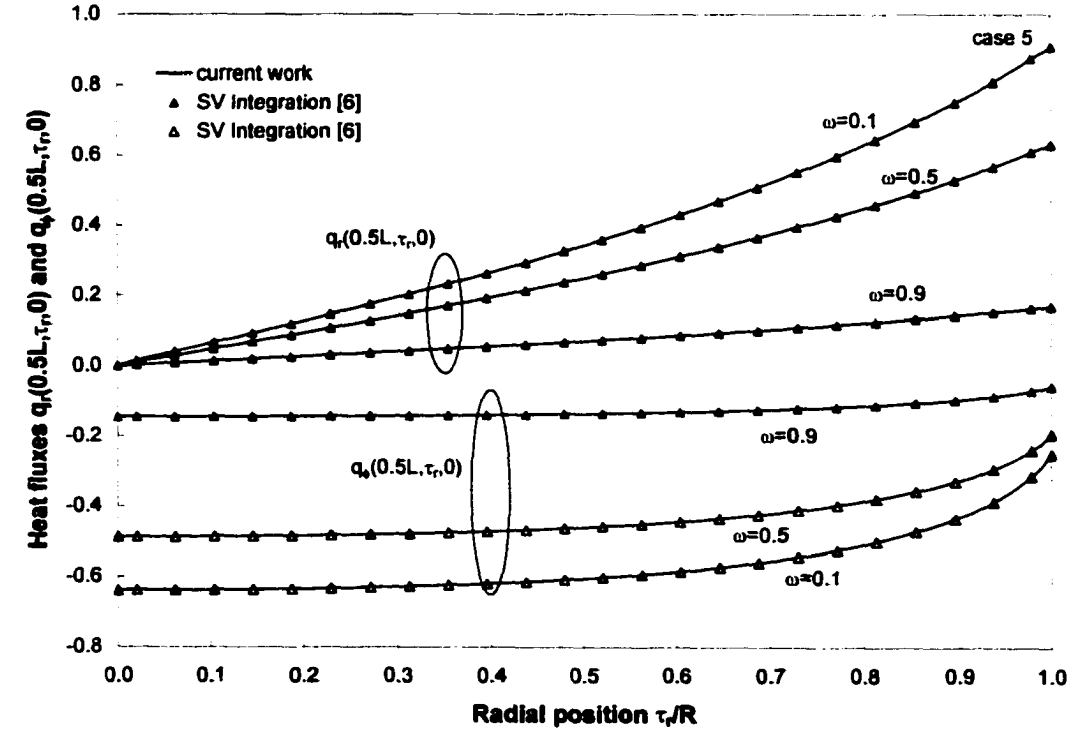

Figure 3-16 The comparison of present work and previous work [6] for the effects of scattering albedo on the distributions of $q_r(0.5L,\tau_r,0)$ and $q_\phi(0.5L,\tau_r,0)$ with respect to radial position for case 5 in table 3-2.

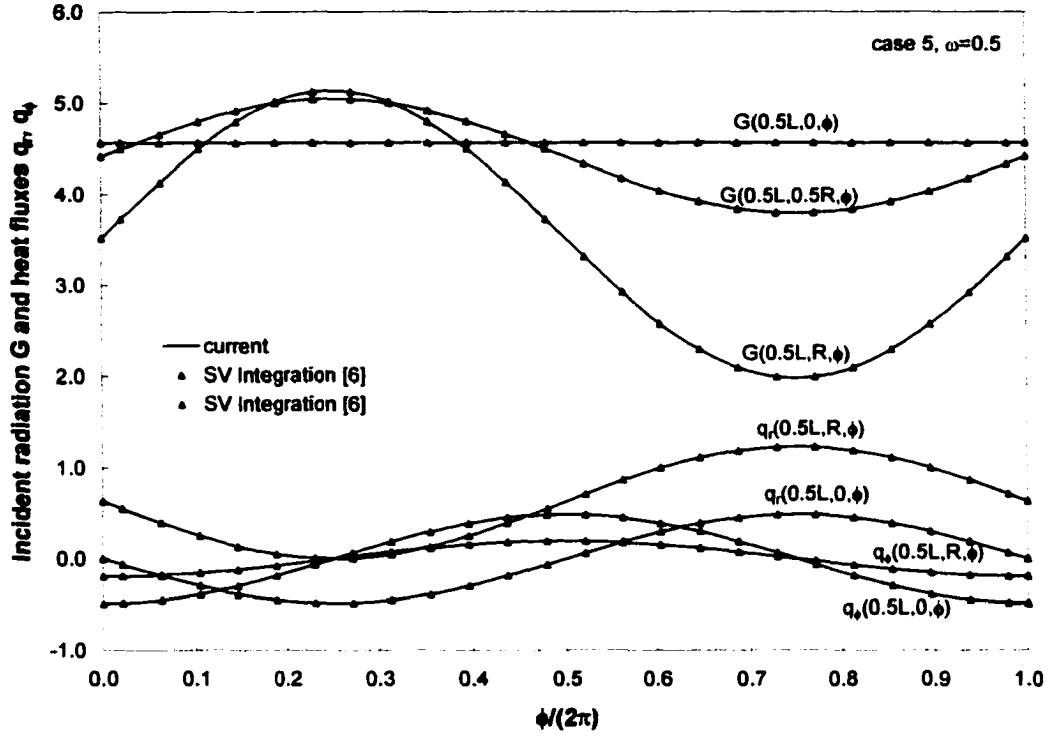

Figure 3-17 The comparison of present work and previous work [6] for the distributions of incident radiation and heat fluxes q_r and q_ϕ at mid-plane τ_z=0.5L, but with different radial positions, with respect to angular coordinate ϕ for case 5 in table 3-2, ω=0.5.

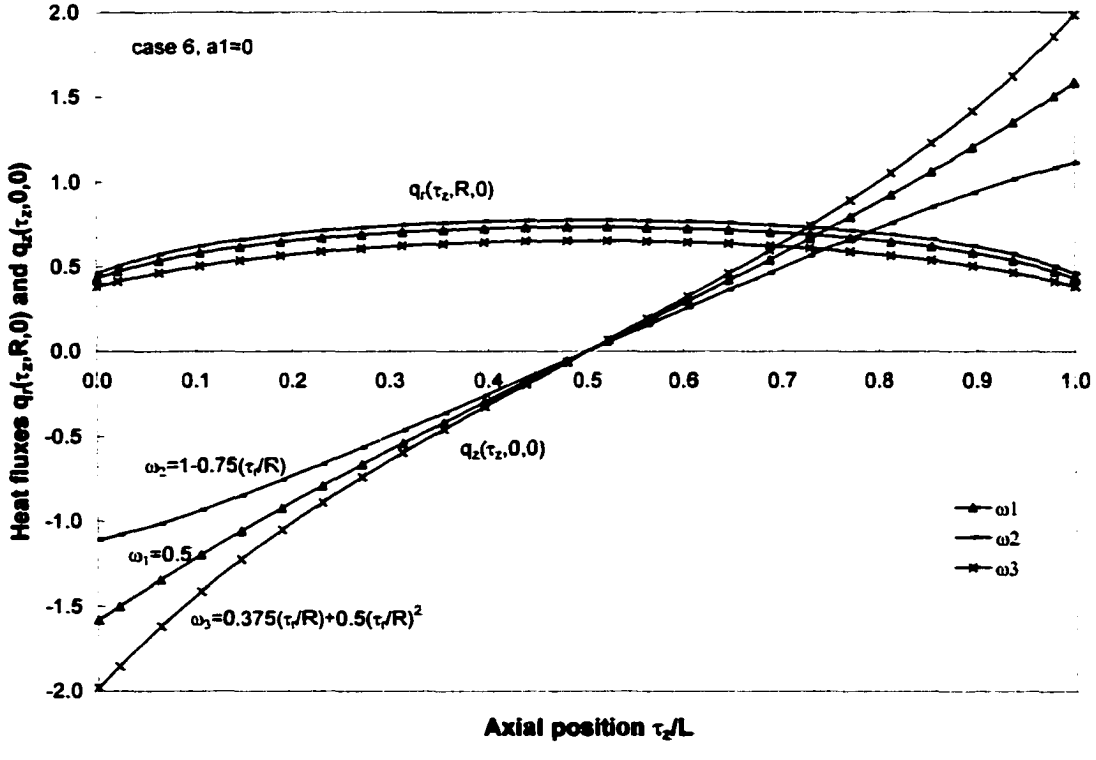

Figure 3-18 The effects of spatial change albedo on the distributions of heat fluxes q_r and q_z with respect to axial position for case 6 in table 3-2, a1=0.

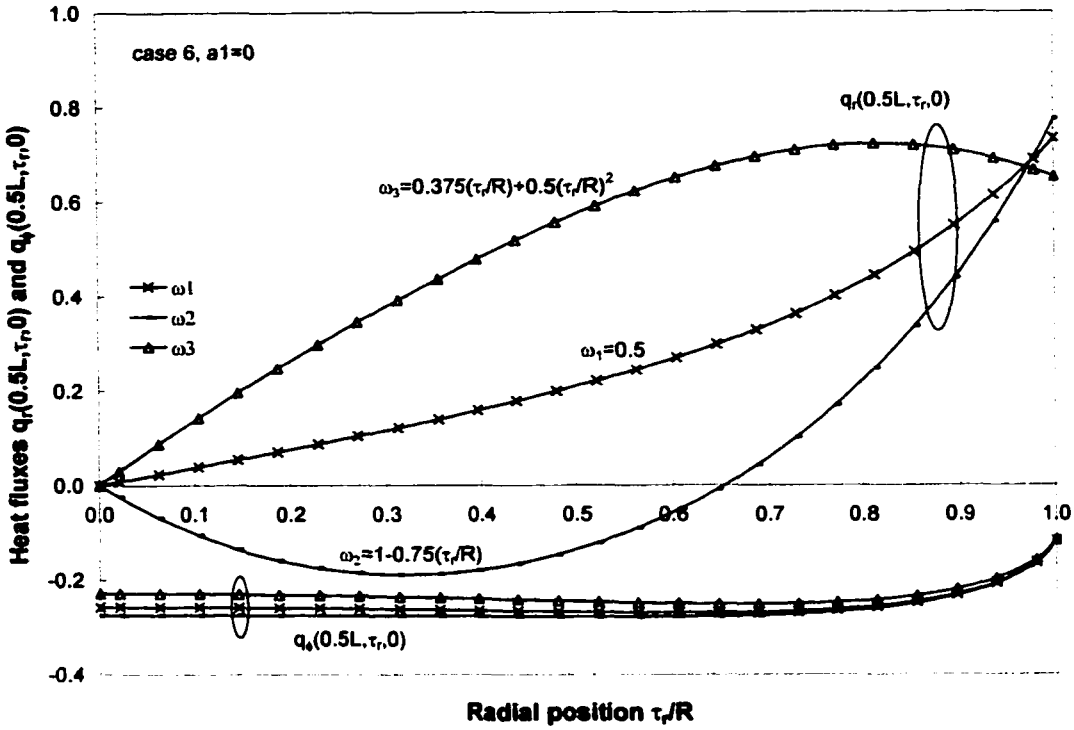

Figure 3-19 The effects of spatial change albedo on the distributions of heat fluxes $q_r(0.5L,\tau_r,0)$ and $q_\phi(0.5L,\tau_r,0)$ with respect to radial position for case 6 in table 3-2, a1=0.

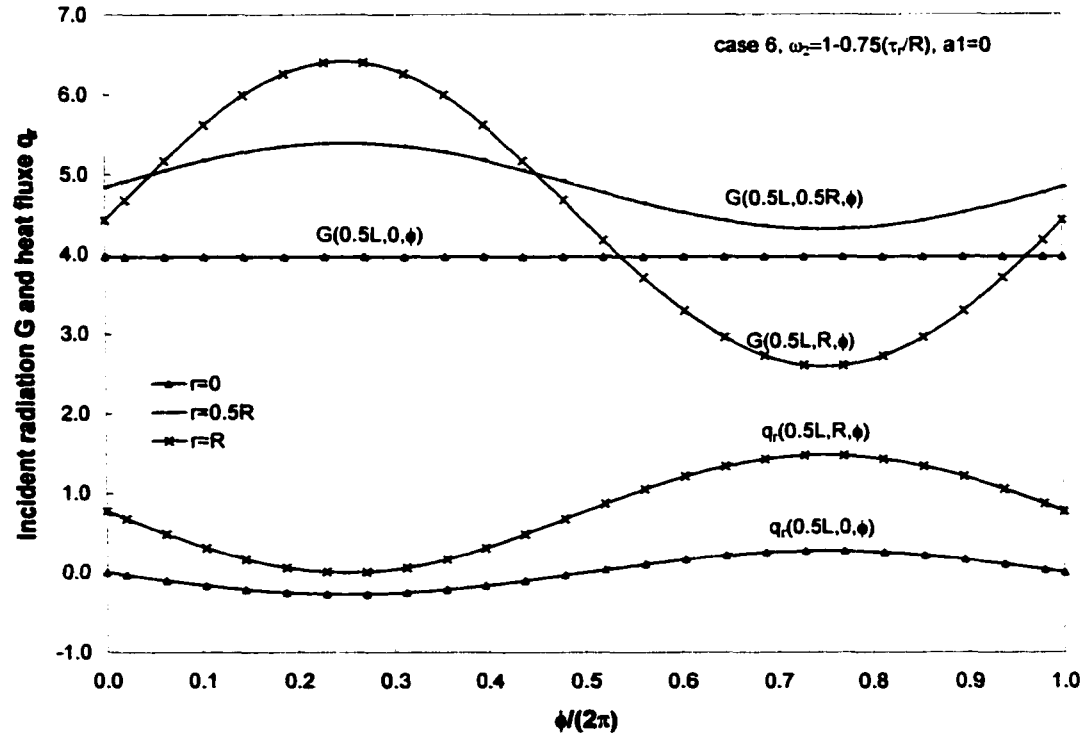

Figure 3-20 The distributions of incident radiation and heat flux q_r at mid-plane τ_z=0.5L, but with different radial position, with respect to angular direction ϕ for case 6 in table 3-2 with spatial change albedo ω_2.

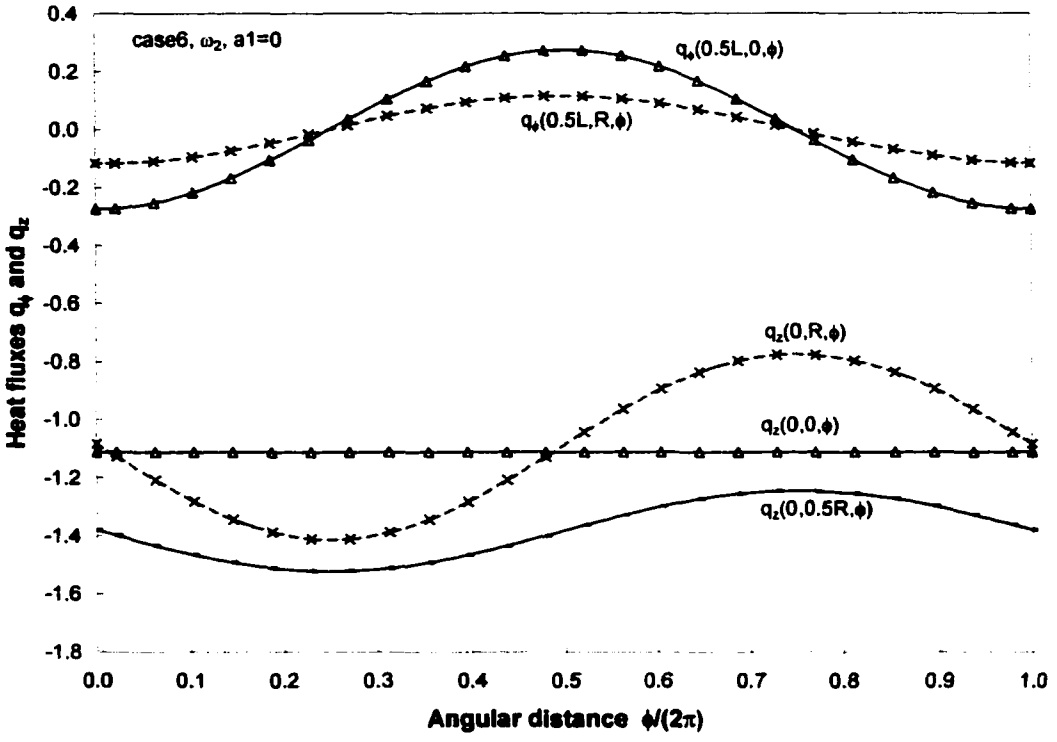

Figure 3-21 The distributions of q_ϕ at mid-plane, q_z at bottom surface, but both with different radial positions, with respect to angular coordinate ϕ for case 6 in table 3-2 with spatial change albedo ω_2.

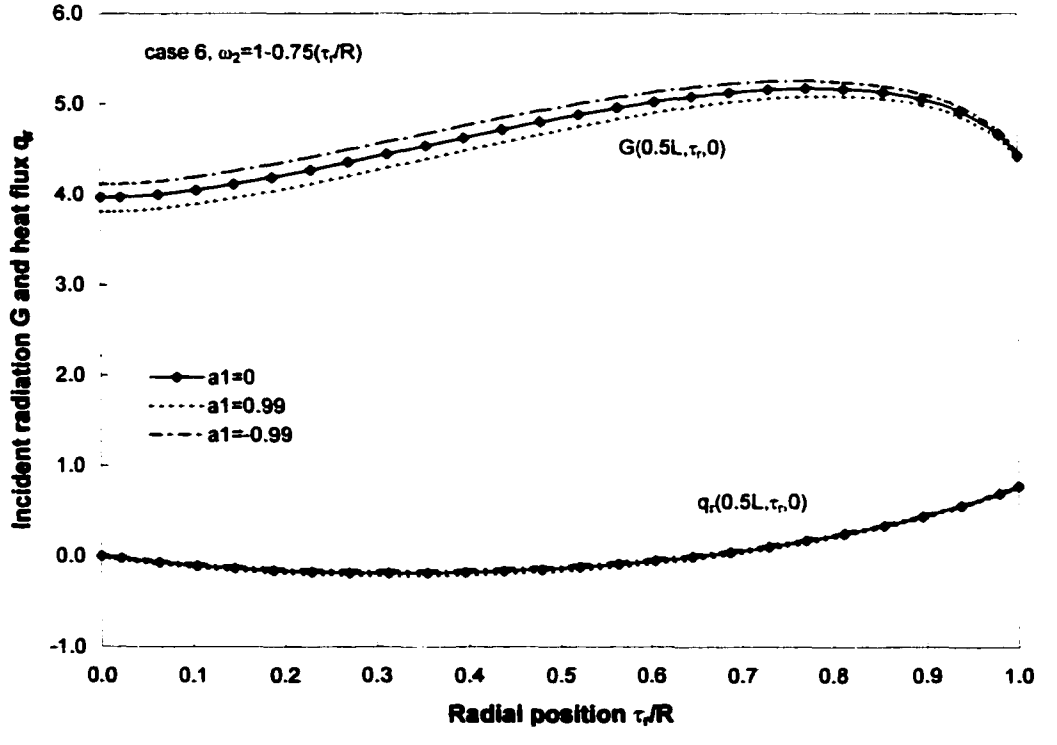

Figure 3-22 The effects of linear anisotropic coefficient on the incident radiation $G(0.5L,\tau_r,0)$ and heat flux $q_r(0.5L,\tau_r,0)$ for case 6 in table 3-2 with spatial change albedo ω_2.

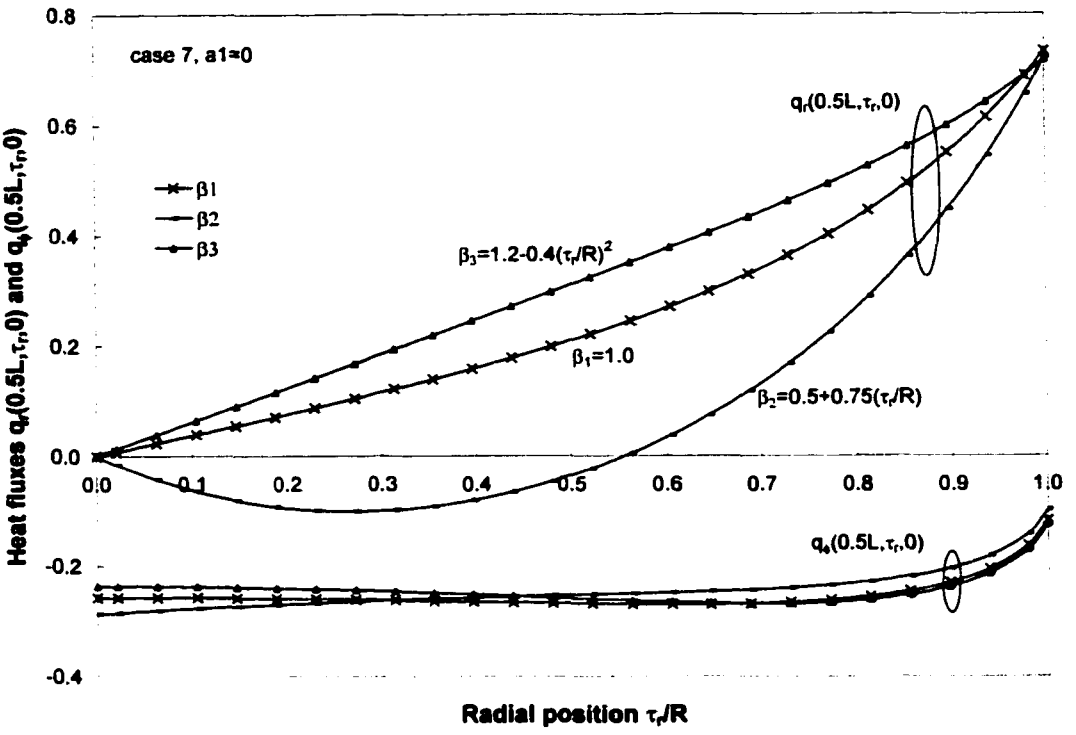

Figure 3-23 The effects of spatial change extinction coefficient on the distributions of heat fluxes $q_r(0.5L,\tau_r,0)$ and $q_\phi(0.5L,\tau_r,0)$ at angular position $\phi=0$ with respect to radial position for case 7 in table 3-2.

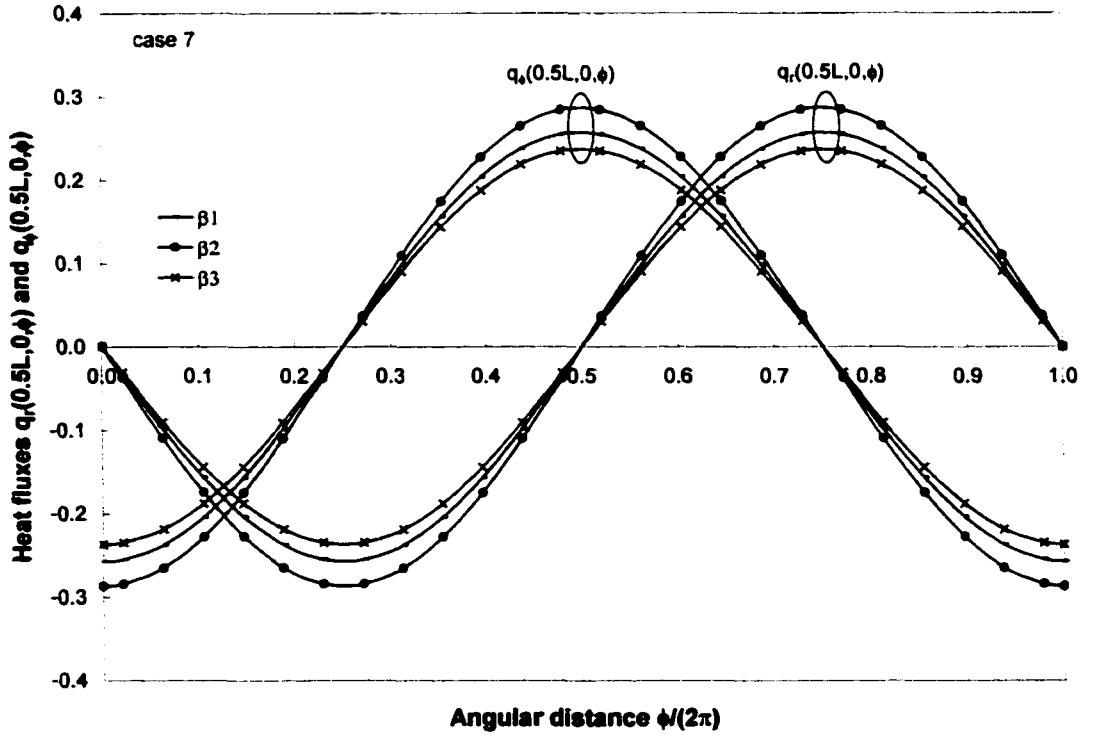

Figure 3-24 The effects of spatial change extinction coefficient on the distributions of heat fluxes $q_r(0.5L,0,\phi)$ and $q_\phi(0.5L,0,\phi)$ with respect to angular position for case 7 in table 3-2.

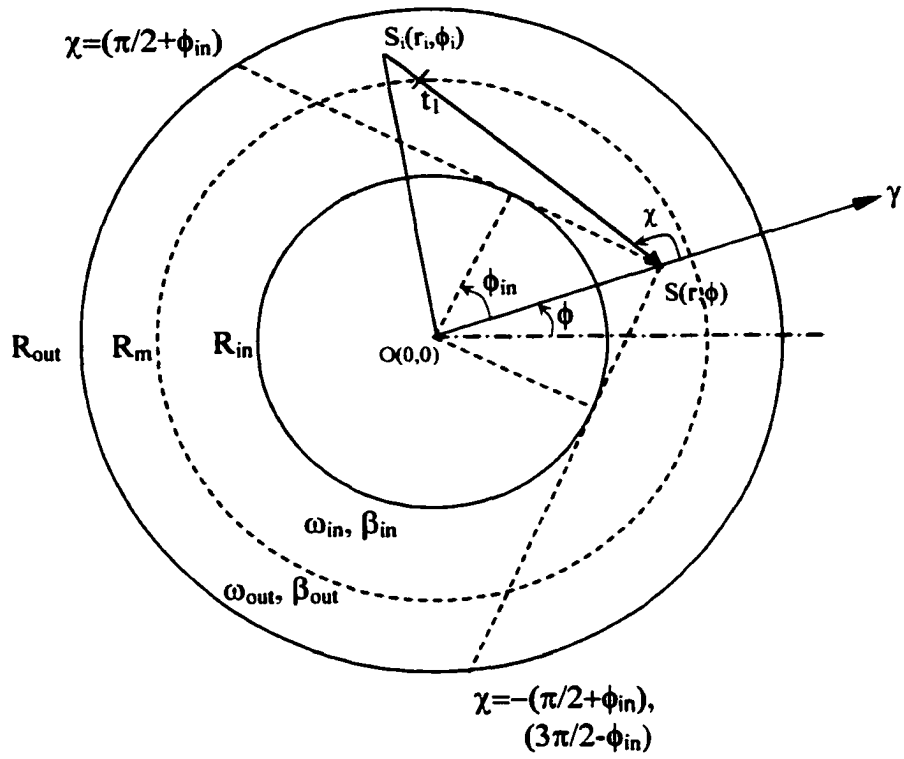

Figure 3-25 Schematic diagram for two-layer hollow cylindrical medium when tracing a ray to compute optical thickness ($r \le R_m$).

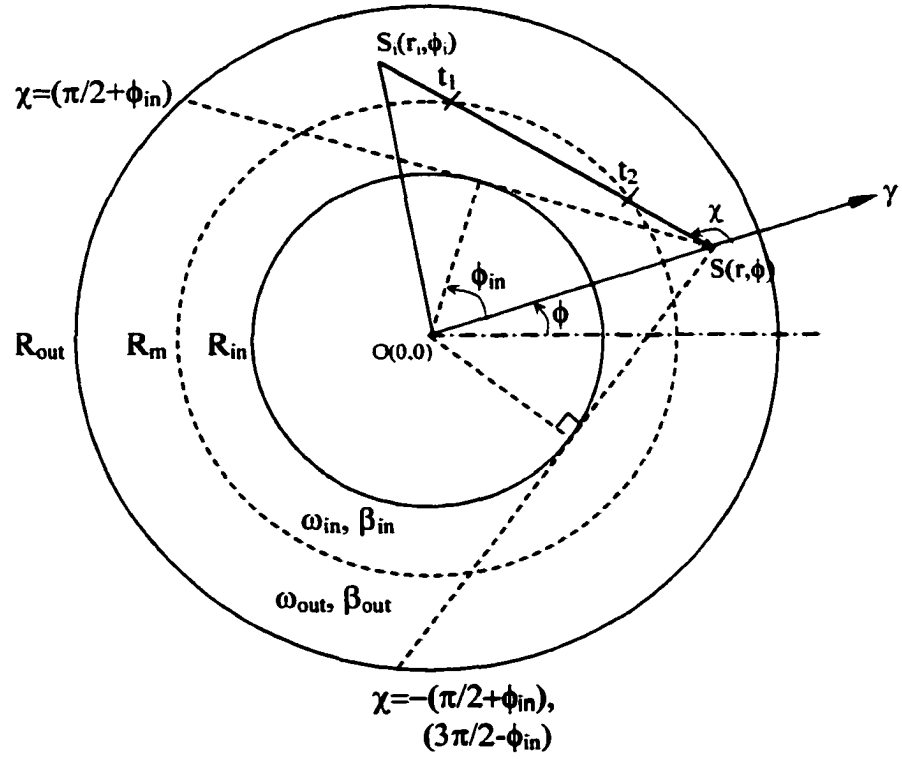

Figure 3-26 Schematic diagram for two-layer hollow cylindrical medium when tracing a ray to compute optical thickness ($r > R_m$).

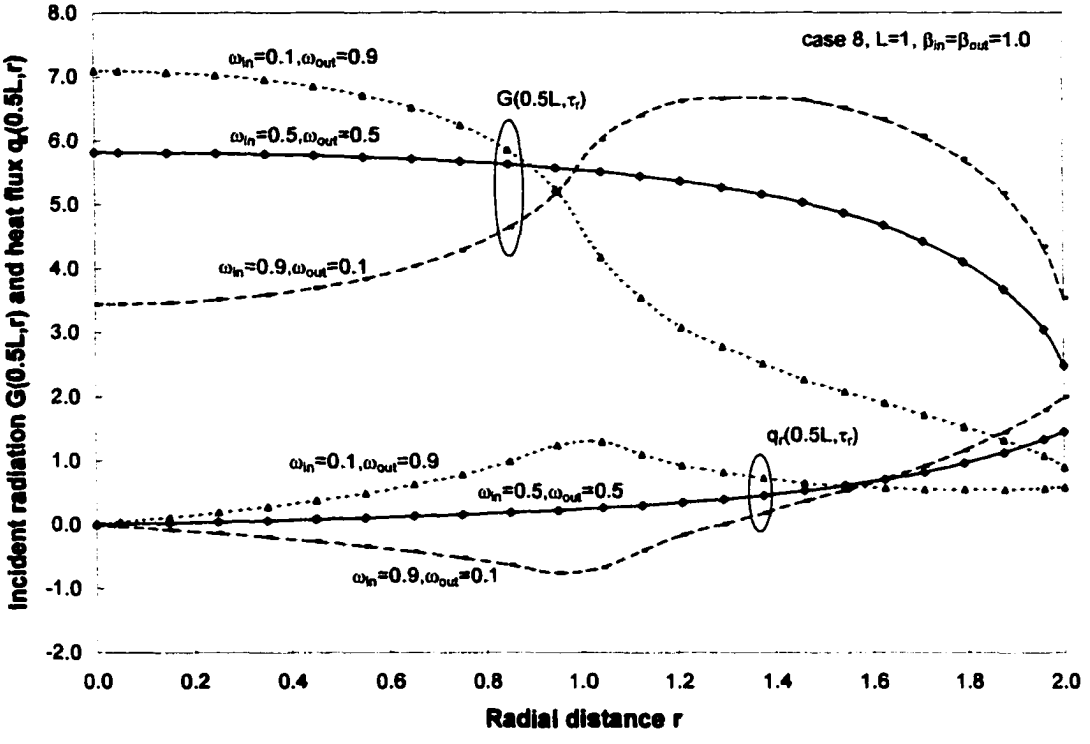

Figure 3-27 The effects of different combinations of scattering albedo on the distributions of incident radiation and heat flux q_r with respect to radial distance for case 8 in table 3-3.

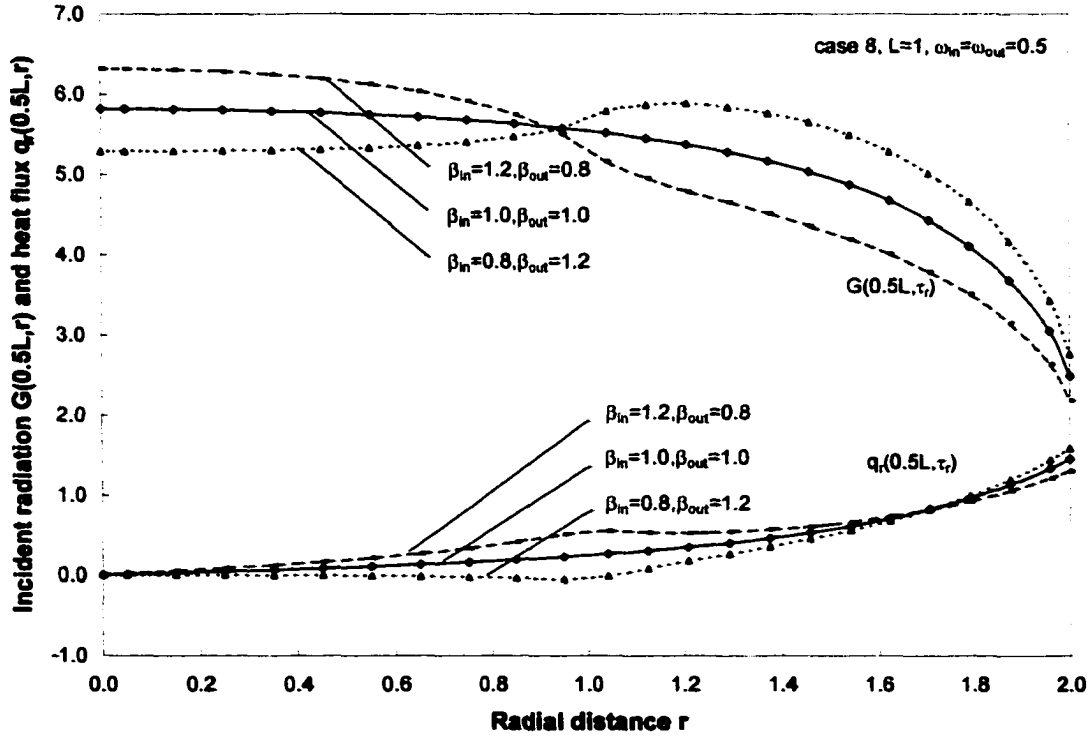

Figure 3-28 The effects of different combinations of extinction coefficient on the distributions of incident radiation and heat flux q_r with respect to radial distance for case 8 in table 3-3.

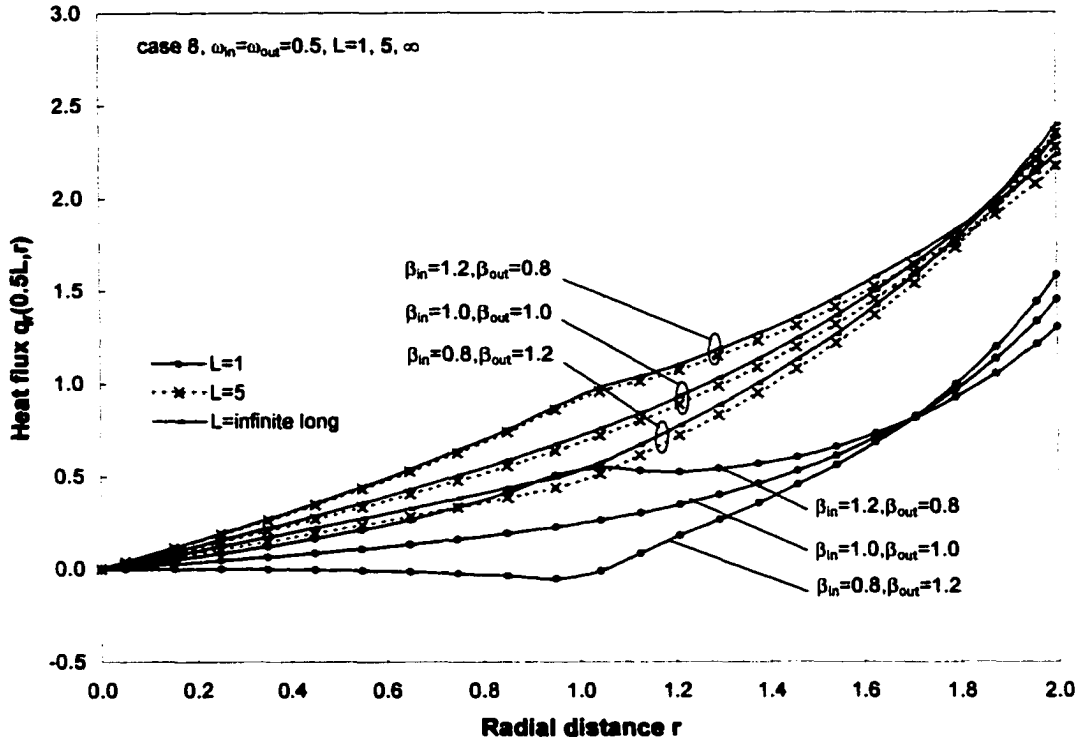

Figure 3-29 The effects of cylinder length on the distributions of heat flux $q_r(0.5L,r)$ with respect to radial distance r for case 8 in table 3-3.

3.7 References:

[3.1] Jenn-Der Lin. Exact expressions for radiative transfer in an arbitrary geometry exposed to radiation. J. Quant. Spectrosc. Radiat. Transfer 1987, Vol. 37, No. 6, pp. 591-601.

[3.2] S. T. Thynell. The integral form of the equation of transfer in finite, two-dimensional, cylindrical media. J. Quant. Spectrosc. Radiat. Transfer 1989, Vol. 42, No. 2, pp. 117-136.

[3.3] Zhiqiang Tan. Radiative heat transfer in multidimensional emitting, absorbing, and anisotropic scattering media-mathematical formulation and numerical method. Journal of Heat Transfer 1989, Vol. 111, No. 1, pp. 141-147.

[3.4] J. M. Zhang and W. H. Sutton. Multidimensional radiative transfer in absorbing, emitting, and linearly anisotropic scattering cylindrical medium with space-dependent properties. J. Quant. Spectrosc. Radiat. Transfer 1994, Vol. 52, No. 6, pp. 791-808.

[3.5] J. Zhang and W. Sutton. Predictions of radiative transfer in two-dimensional non-homogeneous participating cylindrical media based on the S-type integral equation of transfer. ASME/AIAA National Heat Transfer Conference, 1995, Portland, OR. AIAA-95-3519.

[3.6] X.L. Chen and W. Sutton. Radiative transfer in finite cylindrical media using transformed integral equations. Accepted for publication in J. Quant. Spectrosc. Radiat. Transfer.

[3.7] M. N. Ozisik. Radiative transfer and interactions with conduction and convection. Wiley, New York, NY (1973).

[3.8] H. Y. Li, M. N. Ozisik, and J. R. Tsai. Two-dimensional radiation in a cylinder with spatially varying albedo. Journal of Thermophysics and Heat Transfer 1992, Vol. 6, No. 1, pp. 180-182.

[3.9] S. M. Shouman and M. N. Ozisik. Radiative transfer in an isotropically scattering two-region slab with reflecting boundaries. J. Quant. Spectrosc. Radiat. Transfer 1981, Vol. 26, pp. 1-9.

[3.10] P. S. Swathi, T. W. Tong and G. R. Cunnington Jr. Reflection of two-layer composite porous media with linear-anisotropic scattering. J. Quant. Spectrosc. Radiat. Transfer 1987, Vol. 38, No. 4, pp. 273-279.

[3.11] Chih-Yang Wu and Shang-Chen Wu. Radiative transfer in a two-layer medium on a cylinder. Int. J. Heat and Mass Transfer 1993, Vol. 36, No. 5, pp. 1147-1158.

[3.12] J. Zhang and W. Sutton. Thermal Radiation in layered participating cylindrical media using an integral equation method. Journal of International Communications in Heat and Mass Transfer 1995, Vol. 22, pp. 885-894.

3.8 Appendix B

Cosine Equations

Based on the geometric relations [3.4,3.6], the cosines of the angle between the surface normal vector and the intensity direction $\hat{\Omega}$ are given as follows:

$$\cos\theta_1 = \cos(\hat{n}_1, \hat{\Omega}) = \frac{z}{\left[r^2 + r_1^2 - 2rr_1\cos(\phi - \phi_1) + z^2\right]^{1/2}}, \tag{B1a}$$

$$\cos\theta_2 = \cos(\hat{n}_2, \hat{\Omega}) = \frac{L - z}{\left[r^2 + r_2^2 - 2rr_2\cos(\phi - \phi_2) + (L - z)^2\right]^{1/2}}, \tag{B1b}$$

$$\cos\theta_3 = \cos(\hat{n}_3, \hat{\Omega}) = \frac{R_{out} - r\cos(\phi - \phi_3)}{\left[r^2 + R_{out}^2 - 2rR_{out}\cos(\phi - \phi_3) + (z_3 - z)^2\right]^{1/2}}, \tag{B1c}$$

$$\cos\theta_4 = \cos(\hat{n}_4, \hat{\Omega}) = \frac{r\cos(\phi - \phi_4) - R_{in}}{\left[r^2 + R_{in}^2 - 2rR_{in}\cos(\phi - \phi_4) + (z_4 - z)^2\right]^{1/2}}. \tag{B1d}$$

The intensity in the direction of $\hat{\Omega}$ starting from point $s_i(z_i,r_i,\phi_i)$ on the boundary surface i (i=1,2,3,4) to point $s(z,r,\phi)$, yields the following direction cosines.

$$\cos(\hat{e}_z, \hat{\Omega}) = \frac{z - z_i}{\left[r^2 + r_i^2 - 2rr_i\cos(\phi - \phi_i) + (z - z_i)^2\right]^{1/2}}, \tag{B2a}$$

$$\cos(\hat{e}_r, \hat{\Omega}) = \frac{r - r_i\cos(\phi - \phi_i)}{\left[r^2 + r_i^2 - 2rr_i\cos(\phi - \phi\ ) + (z - z_i)^2\right]^{1/2}}, \tag{B2b}$$

$$\cos(\hat{e}_\phi, \hat{\Omega}) = \frac{r_i\sin(\phi - \phi_i)}{\left[r^2 + r_i^2 - 2rr_i\cos(\phi - \phi_i) + (z - z_i)^2\right]^{1/2}}. \tag{B2c}$$

Coordinate Transformation Relations

There are following geometric relations from Figure 3-3 and Figure 3-4:

$$dA_1 = dA_2 = \gamma \cdot d\chi \cdot d\gamma \tag{B3}$$

$$dA_3 = \left[\frac{\gamma_{Ro}}{\cos(\chi - \phi_3 + \phi)} d\chi\right] \cdot \left(\gamma_{Ro} \sec^2 \alpha \cdot d\alpha\right) \quad \text{(B4)}$$

$$dA_4 = \left[\frac{\gamma_{Ri}}{-\cos(\chi - \phi_4 + \phi)} d\chi\right] \cdot \left(\gamma_{Ri} \sec^2 \alpha \cdot d\alpha\right) \quad \text{(B5)}$$

$$d(s_i, s) = \gamma \cdot \sec\alpha \quad \text{(B6)}$$

$$z = -\gamma \cdot \tan\alpha_1, \qquad L - z = \gamma \cdot \tan\alpha_2 \quad \text{(B7a,b)}$$

$$z_3 - z = \gamma_{Ro} \cdot \tan\alpha, \qquad z_4 - z = \gamma_{Ri} \cdot \tan\alpha \quad \text{(B8a,b)}$$

$$R_{out} - r\cos(\phi - \phi_3) = \gamma_{Ro} \cos(\chi - \phi_3 + \phi) \quad \text{(B9)}$$

$$r\cos(\phi - \phi_4) - R_{in} = \gamma_{Ri}\left[-\cos(\chi - \phi_4 + \phi)\right] \quad \text{(B10)}$$

$$r - r_i \cos(\phi - \phi_i) = \gamma(-\cos\chi) \qquad \text{(i=1,2)} \quad \text{(B11a)}$$

$$r - R_{out}\cos(\phi - \phi_3) = \gamma_{Ro}(-\cos\chi), \qquad r - R_{in}\cos(\phi - \phi_4) = \gamma_{Ri}(-\cos\chi) \quad \text{(B11b,c)}$$

$$r_i \sin(\phi - \phi_i) = \gamma(-\sin\chi) \qquad \text{(i=1,2)} \quad \text{(B12a)}$$

$$R_{out}\sin(\phi - \phi_3) = \gamma_{Ro}(-\sin\chi), \qquad R_{in}\sin(\phi - \phi_4) = \gamma_{Ri}(-\sin\chi) \quad \text{(B12b,c)}$$

CHAPTER FOUR

4. ENHANCEMENT OF HEAT TRANSFER: COMBINED CONVECTION AND RADIATION IN THE ENTRANCE REGION OF CIRCULAR DUCTS WITH POROUS INSERTS

The combined convective and radiative heat transfer in the entrance length of a pipe with or without the porous insert is solved by control volume method and integral equation scheme. The results are compared between the pipe flow with the porous insert and flow without the porous insert. The porous insert in a pipe will enhance both the convective and radiative heat transfer. The effects of several important parameters on this enhancement are discussed in detail.

4.1 Introduction

In high temperature systems, an effective way to enhance heat transfer is to add convection-radiation converters (CRC). This technology began in early 1970's due to the shortage of energy and the desire to recover as much as possible of the heat from exhaust gas of industrial furnaces for high efficiency. Earlier authors like Mori et al. [4.1,4.2] suggested adding parallel plates in high temperature gas side of heat exchangers for heat transfer augmentation. The plates receive heat energy from the gas by convection, and then emit radiation to the colder absorbing surface. The metal emissivity is much higher than the gas, so more heat can be recaptured by the absorbing surface. Later Hirano et al. [4.3], Zhang and Ebadian [4.4] proved this efficient way in their research.

Echigo [4.5] improved the enhancement effect by using porous CRC instead of solid plates. Because the large surface area per unit volume of the porous material, the porous CRC can cause a big temperature drop in the gas side. This is not only effective to the energy recovery but also benefits the environment. Later Zhang, Sutton, and Lai [4.6] solved a fully developed pipe flow with a CRC core in the center of the pipe. Their results proved the efficiency of CRC to the enhancement of combined heat transfer modes.

The essential assumptions in the previous research are: the working gas is non-radiating; the porous medium is non-scattering; and fully developed flow is assumed in the pipe. These assumptions are not always valid in actual applications. For example, the working gas may be a participating medium if carbon dioxide or steam is contained in the flow.

Here, the purpose of this study is to consider as many factors as possible to simulate an entrance region, so a more accurate evaluation can be obtained for such a complicated system. The entrance region is numerically solved by control volume method in CFD for both the flow field and the temperature field. The Brinkman type extension of the Darcy law is used with the Navier-Stokes equation to express the velocity field in the whole domain. The working gas is assumed to be radiating and the porous insert is assumed to be absorbing, emitting and scattering. Finally, we present the effects of upstream emissivity, downstream emissivity, Reynolds number, extinction coefficients, scattering albedo and Darcy number contribution to the enhancement of heat transfer.

4.2 Governing Equations

The problem under consideration consists of a circular pipe as shown in Figure 4-1. A porous core is inserted in the middle of the pipe with radius R_m. The hot participating gas enters the pipe with uniform velocity u_{in} and temperature T_{in} and is cooled by the cold pipe wall at constant temperature T_w. Both the fluid and the porous matrix have constant properties. If we consider axisymmetric, laminar, and boundary-layer flow and neglect axial rate of change of viscous stress, the governing equations for fluid and porous layers reduce to the following equations respectively:

Continuity equation

Fluid layer
$$\frac{1}{r}\cdot\frac{\partial(r\cdot v)}{\partial r}+\frac{\partial u}{\partial z}=0 \tag{4-1a}$$

Porous layer
$$\frac{1}{r}\cdot\frac{\partial(r\cdot v)}{\partial r}+\frac{\partial u}{\partial z}=0 \tag{4-1b}$$

Momentum equation

Fluid layer
$$\frac{1}{r}\frac{\partial(r\rho\cdot uv)}{\partial r}+\frac{\partial(\rho\cdot uu)}{\partial z}=-\frac{dp}{dz}+\mu\left[\frac{1}{r}\frac{\partial}{\partial r}(r\frac{\partial u}{\partial r})\right] \tag{4-2a}$$

Porous layer
$$\frac{1}{r}\frac{\partial(r\rho\cdot uv)}{\partial r}+\frac{\partial(\rho\cdot uu)}{\partial z}=-\varphi\frac{dp}{dz}-\varphi\frac{\mu}{K}u+\mu_e\left[\frac{1}{r}\frac{\partial}{\partial r}(r\frac{\partial u}{\partial r})\right] \tag{4-2b}$$

Energy equation

Fluid layer
$$\frac{1}{r}\frac{\partial(r\rho C_p\cdot Tv)}{\partial r}+\frac{\partial(\rho C_p\cdot Tu)}{\partial z}=\frac{1}{r}\frac{\partial}{\partial r}(kr\frac{\partial T}{\partial r})+\frac{\partial}{\partial z}(k\frac{\partial T}{\partial z})-\nabla\cdot\vec{q}_R \tag{4-3a}$$

Porous layer
$$\frac{1}{r}\frac{\partial(r\rho C_p\cdot Tv)}{\partial r}+\frac{\partial(\rho C_p\cdot Tu)}{\partial z}=\frac{1}{r}\frac{\partial}{\partial r}(k_e r\frac{\partial T}{\partial r})+\frac{\partial}{\partial z}(k_e\frac{\partial T}{\partial z})-\nabla\cdot\vec{q}_R \tag{4-3b}$$

where z is the flow direction shown in Figure 4-1, u and v are the velocity components in z or r direction respectively. The terms μ, k, ρ, and C_p are properties of the fluid; φ, K, μ_e

and k_e is the porosity, permeability, effective viscosity and effective conductivity of the porous insert respectively. The Einstein formula can be used to obtain μ_e, but many researchers suggest that μ_e is approximately equal to the viscosity of the fluid. In this work, we assume $\mu_e=\mu$. The following equation is used to compute k_e, the effective thermal conductivity,

$$k_e = \varphi \cdot k_f + (1-\varphi)k_s \tag{4-4}$$

where k_f is the conductivity of the fluid; k_s is the conductivity of solid material of porous insert. The last term in the energy equations (4-3a), (4-3b) is the contribution by thermal radiation and can be computed for gray radiation by the following relation:

$$\nabla \cdot \vec{q}_R = \beta(1-\omega)(4n^2\sigma T^4 - G) \tag{4-5}$$

where $\vec{q}_R$ is the net radiative heat flux; β is the extinction coefficient; ω is the scattering albedo; n is the refractive index, which is assumed as one in this work; σ is the Stefan-Boltzmann constant; and G is the incident radiation.

Due to the boundary-layer flow simplifications, the radial momentum equation has been eliminated. Instead, we use the integrated mass conservation equation below to complete the problem:

$$\int_0^{R_{out}} 2\pi r u \cdot dr = \pi {R_{out}}^2 u_{in} \tag{4-6}$$

The boundary conditions are

At inlet boundary z=0	$u=u_{in}$, $v=0$, $T=T_{in}$
At outlet boundary z=L	outflow boundary condition
At centerline r=0	$\frac{\partial u}{\partial r}=0$, $\frac{\partial T}{\partial r}=0$

At interface $r=R_m$ $\quad u_{fluid}=u_{porous},\quad \mu\frac{\partial u_{fluid}}{\partial r}=\mu_e\frac{\partial u_{porous}}{\partial r}$

$\quad T_{fluid}=T_{porous},\quad k\frac{\partial T_{fluid}}{\partial r}=k_e\frac{\partial T_{porous}}{\partial r}$

At outside wall $r=R_{out}$ $\quad u=v=0,\quad T=T_w$ (4-7)

where the outflow boundary condition is that the region near the outflow boundary exhibits local one-way behavior when Peclet number is sufficiently large according to Patankar [4.10]. So the coefficient a_E is equal to zero (see equation 4-26). We neglect the diffusion at the outflow boundary.

4.2.1 Equations of Radiative Heat Transfer

In order to solve for the radiation source term included in the energy equations, we have to consider the radiative heat transfer equations. Here, we use the same integral method as in previous paper [4.7] or Chapter 3 to calculate the incident radiation and components of net heat flux in the domain. We know that incident radiation and heat flux at a particular point can be evaluated by the integration of the intensity at that point around the whole 4π solid angle. In axisymmetric 2-D cylindrical coordinate system (Figure 4-2), they are expressed in the following forms:

$$G(z,r)=\int_{4\pi} I(z,r,\hat{\Omega})\cdot d\Omega, \tag{4-8a}$$

$$q_r(z,r)=\int_{4\pi} I(z,r,\hat{\Omega})\cdot\cos(\hat{e}_r,\hat{\Omega})\cdot d\Omega, \tag{4-8b}$$

$$q_z(z,r)=\int_{4\pi} I(z,r,\hat{\Omega})\cdot\cos(\hat{e}_z,\hat{\Omega})\cdot d\Omega, \tag{4-8c}$$

where q_r, q_z are the components of net heat flux in r and z direction respectively. $I(z,r,\hat{\Omega})$ is the intensity at position s(z,r) and in $\hat{\Omega}$ direction, which can be computed by

$$I(z,r,\hat{\Omega}) = I_i \exp[-\tau(s_i,s)] + \int_{s_i}^{s} \beta(s')S(s',\hat{\Omega})\exp[-\tau(s',s)]ds' \tag{4-9}$$

where s_i is the boundary point, $\hat{\Omega}$ is the ray direction from start point s_i to end point s, and s' is the intermediate point between s_i and s. I_i is the entering intensity at boundary i (i=1,2,3 for inlet, outlet, and outside boundary respectively). Actually the above equation is the formal solution of the radiative transfer equation expressed by Ozisik [4.9]. The source term in above equation is due to the medium emitting and scattering, which can be expressed as

$$S(s,\hat{\Omega}) \equiv (1-\omega)\frac{n^2\sigma T^4}{\pi} + \frac{\omega}{4\pi}\int_{4\pi} p(\hat{\Omega}'\cdot\hat{\Omega})\cdot I(s,\hat{\Omega}')d\Omega' \tag{4-10}$$

If the linear-anisotropic scattering phase function is assumed

$$p(\hat{\Omega}',\hat{\Omega}) = 1 + a_1\hat{\Omega}\cdot\hat{\Omega}' \tag{4-11}$$

the source term expression in cylindrical coordinate becomes

$$\begin{aligned} &S(s,\hat{\Omega}) = S(z,r,\hat{\Omega}) \\ &= (1-\omega)I_b(T) + \frac{\omega}{4\pi}\left\{G(z,r) + a_1\left[q_r(z,r)\cos(\hat{e}_r,\hat{\Omega}) + q_z(z,r)\cos(\hat{e}_z,\hat{\Omega})\right]\right\} \end{aligned} \tag{4-12}$$

where the optical thickness in equation (4-9) is defined by

$$\tau(s_i,s) = \int_{s_i}^{s}\beta(s')ds', \qquad \tau(s',s) = \int_{s'}^{s}\beta(s'')ds'' \tag{4-13}$$

The radiative boundary conditions are

At inlet z=0, transparent boundary $\quad I_1(0,r) = f_1(r)$ (4-14a)

At outlet z=L, transparent boundary $\quad I_2(L,r) = f_2(r)$ (4-14b)

At the opaque wall r=R_{out} $$I_3(z,R_{out})=\frac{\varepsilon_w\sigma T_w^4}{\pi}+\frac{\rho_w}{\pi}\int_{2\pi}I(z,R_{out})\cos(\hat{e}_r,\hat{\Omega})d\Omega \quad (4\text{-}14c)$$

where f_1 and f_2 are possible externally incident radiations at the inlet and outlet. In order to be compatible with temperature boundary conditions, we assume they can be expressed in the form:

$$f_1=\frac{e_1\sigma T_{in}^4}{\pi}=\frac{\sigma[e_1T_{in}^4]}{\pi},\qquad f_2=\frac{e_2\sigma T^4(L,r)}{\pi}=\frac{\sigma[e_2T^4(L,r)]}{\pi} \quad (4\text{-}14d)$$

where the coefficients e_1 and e_2 are between [0,1] in order to be compatible with different actual situations, for example colder source temperature. When they are both equal to 1.0, we have the maximum externally incident radiations. The detail of solution to these equations will be given later in the numerical section.

4.2.2 Dimensionless Form of Governing Equations

Considerable insight into the physical meaning of this problem may be made through nondimensionalizing the governing equations. By introducing the following dimensionless variables and parameters:

$$\bar{r}=\frac{r}{R_{out}} \qquad \bar{z}=\frac{z}{R_{out}}$$

$$\bar{u}=\frac{u}{u_{in}} \qquad \bar{v}=\frac{v}{u_{in}}$$

$$\theta=\frac{T}{T_{in}} \qquad \bar{p}=\frac{p}{\rho\cdot u_{in}^2}$$

$$\mathrm{Re}=\frac{\rho\cdot u_{in}R_{out}}{\mu} \qquad \mathrm{Pr}=\frac{\mu\cdot C_p}{k}$$

$$Da = \frac{K}{R_{out}^{\ 2}} \qquad Bo = \frac{\rho \cdot C_p u_{in}}{n^2 \sigma T_{in}^{\ 3}}$$

$$\overline{G} = \frac{G}{\sigma T_{in}^{\ 4}} \qquad \overline{q}_r = \frac{q_r}{\sigma T_{in}^{\ 4}}$$

$$\overline{q}_z = \frac{q_z}{\sigma T_{in}^{\ 4}} \qquad \overline{I} = \frac{I}{\sigma T_{in}^{\ 4}}$$

$$\overline{\beta} = \beta \cdot R_{out} \qquad d\overline{s} = \frac{ds}{R_{out}} \qquad \text{(4-15)}$$

The continuity, momentum, and energy equations can be rewritten as follows (Re is Reynolds number, Pr is Prandtl number, Da is Darcy number, and Bo is Boltzmann number).

Continuity equation

Fluid layer
$$\frac{1}{\overline{r}} \cdot \frac{\partial(\overline{r} \cdot \overline{v})}{\partial \overline{r}} + \frac{\partial \overline{u}}{\partial \overline{z}} = 0 \qquad \text{(4-16a)}$$

Porous layer
$$\frac{1}{\overline{r}} \cdot \frac{\partial(\overline{r} \cdot \overline{v})}{\partial \overline{r}} + \frac{\partial \overline{u}}{\partial \overline{z}} = 0 \qquad \text{(4-16b)}$$

Momentum equation

Fluid layer
$$\frac{1}{\overline{r}} \frac{\partial(\overline{r}\overline{u}\overline{v})}{\partial \overline{r}} + \frac{\partial(\overline{u}\overline{u})}{\partial \overline{z}} = -\frac{d\overline{p}}{d\overline{z}} + \frac{1}{\mathrm{Re}}\left[\frac{1}{\overline{r}} \frac{\partial}{\partial \overline{r}}(\overline{r} \frac{\partial \overline{u}}{\partial \overline{r}})\right] \qquad \text{(4-17a)}$$

Porous layer
$$\frac{1}{\overline{r}} \frac{\partial(\overline{r}\overline{u}\overline{v})}{\partial \overline{r}} + \frac{\partial(\overline{u}\overline{u})}{\partial \overline{z}} = -\varphi \frac{d\overline{p}}{d\overline{z}} - \varphi \frac{1}{\mathrm{Re} \cdot Da} \overline{u} + \frac{1}{(\mathrm{Re})_e}\left[\frac{1}{\overline{r}} \frac{\partial}{\partial \overline{r}}(\overline{r} \frac{\partial \overline{u}}{\partial \overline{r}})\right] \qquad \text{(4-17b)}$$

Energy equation

Fluid layer
$$\frac{1}{\overline{r}} \frac{\partial(\overline{r}\overline{v}\theta)}{\partial \overline{r}} + \frac{\partial(\overline{u}\theta)}{\partial \overline{z}} = \frac{1}{\mathrm{Re}\,\mathrm{Pr}}\left[\frac{1}{\overline{r}} \frac{\partial}{\partial \overline{r}}(\overline{r} \frac{\partial \theta}{\partial \overline{r}}) + \frac{\partial^2 \theta}{\partial \overline{z}^2}\right] + \frac{\overline{\beta}(1-\omega)}{Bo}(\overline{G} - 4\theta^4) \qquad \text{(4-18a)}$$

Porous layer
$$\frac{1}{\overline{r}} \frac{\partial(\overline{r}\overline{v}\theta)}{\partial \overline{r}} + \frac{\partial(\overline{u}\theta)}{\partial \overline{z}} = \frac{1}{(\mathrm{Re}\,\mathrm{Pr})_e}\left[\frac{1}{\overline{r}} \frac{\partial}{\partial \overline{r}}(\overline{r} \frac{\partial \theta}{\partial \overline{r}}) + \frac{\partial^2 \theta}{\partial \overline{z}^2}\right] + \frac{\overline{\beta}(1-\omega)}{Bo}(\overline{G} - 4\theta^4) \qquad \text{(4-18b)}$$

where the dimensionless radiation term can be expressed as

$$\overline{G}(\bar{z},\bar{r}) = \int_{4\pi} \bar{I}(\bar{z},\bar{r},\hat{\Omega}) \cdot d\Omega, \tag{4-19a}$$

$$\overline{q}_r(\bar{z},\bar{r}) = \int_{4\pi} \bar{I}(\bar{z},\bar{r},\hat{\Omega}) \cdot \cos(\hat{e}_r,\hat{\Omega}) \cdot d\Omega, \tag{4-19b}$$

$$\overline{q}_z(\bar{z},\bar{r}) = \int_{4\pi} \bar{I}(\bar{z},\bar{r},\hat{\Omega}) \cdot \cos(\hat{e}_z,\hat{\Omega}) \cdot d\Omega, \tag{4-19c}$$

and

$$\bar{I}(\bar{z},\bar{r},\hat{\Omega}) = \bar{I}_i \exp[-\tau(s_i,s)] + \int_{s_i}^{s} \bar{\beta}(s')\bar{S}(s',\hat{\Omega}) \exp[-\tau(s',s)] \cdot d\bar{s}' \tag{4-20}$$

$$\bar{S} = (1-\omega)\bar{I}_b(\theta) + \frac{\omega}{4\pi}\left\{\overline{G}(\bar{z},\bar{r}) + a_1\left[\overline{q}_r(\bar{z},\bar{r})\cos(\hat{e}_r,\hat{\Omega}) + \overline{q}_z(\bar{z},\bar{r})\cos(\hat{e}_z,\hat{\Omega})\right]\right\} \tag{4-21}$$

$$\tau(s_i,s) = \int_{s_i}^{s} \beta(s')ds' = \int_{s_i}^{s} \bar{\beta}(s')\frac{ds'}{R_{out}} = \int_{s_i}^{s} \bar{\beta}(s')d\bar{s}' \tag{4-22}$$

where we have

$$\bar{I}_b(\theta) = \frac{\theta^4}{\pi} \tag{4-23}$$

For momentum and energy equations, the dimensionless boundary conditions become

At inlet boundary $\bar{z} = 0$ $\quad \bar{u} = 1,\ \bar{v} = 0,\ \theta = 1$

At outlet boundary $\bar{z} = \dfrac{L}{R_{out}}$ outflow boundary condition

At centerline $\bar{r} = 0$ $\quad \dfrac{\partial \bar{u}}{\partial \bar{r}} = 0, \quad \dfrac{\partial \theta}{\partial \bar{r}} = 0$

At $\bar{r} = \bar{R}_m = \dfrac{R_m}{R_{out}}$ $\quad \bar{u}_{fluid} = \bar{u}_{porous},\ \dfrac{1}{\mathrm{Re}}\dfrac{\partial \bar{u}_{fluid}}{\partial \bar{r}} = \dfrac{1}{\mathrm{Re}_e}\dfrac{\partial \bar{u}_{porous}}{\partial \bar{r}}$

$$\theta_{fluid} = \theta_{porous},\ \frac{1}{\mathrm{RePr}}\frac{\partial \theta_{fluid}}{\partial \bar{r}} = \frac{1}{(\mathrm{RePr})_e}\frac{\partial \theta_{porous}}{\partial \bar{r}}$$

At outside wall $\bar{r}=1$ $$\bar{u}=\bar{v}=0, \quad \theta=\theta_w=\frac{T_w}{T_{in}} \tag{4-24}$$

For radiation, there are boundary conditions as

At inlet $\bar{z}=0$ $$\bar{I}_1(0,\bar{r})=\bar{f}_1=\frac{e_1\theta_{in}^{\ 4}}{\pi}=\frac{e_1}{\pi} \tag{4-25a}$$

At outlet $\bar{z}=\frac{L}{R_{out}}$ $$\bar{I}_2(\bar{L},\bar{r})=\bar{f}_2=\frac{e_2\theta^4(\bar{L},\bar{r})}{\pi} \tag{4-25b}$$

At the wall $\bar{r}=1$ $$\bar{I}_3(\bar{z},1)=\frac{\varepsilon_w\theta_w^{\ 4}}{\pi}+\frac{\rho_w}{\pi}\int_{2\pi}\bar{I}(\bar{z},1)\cos(\hat{e}_r,\hat{\Omega})d\Omega \tag{4-25c}$$

The above equations are coupled and needed to be solved simultaneously; the detail of the numerical method is discussed below.

4.3 Numerical Methods

Because momentum equations, energy equations and radiative heat transfer equations are solved by different techniques, we'd like to discuss the flow-heat transfer problem and radiative heat transfer problem separately in the following sections.

4.3.1 Numerical Method for Momentum and Energy Equations

The control volume method (SIMPLE) is used to get discretization equations of momentum equations and energy equations. The computing domain is divided into a number of non-overlapping control volumes and each differential equation is integrated over the control volume. The staggered grid and the power-law scheme are adopted. For details refer to Patankar [4.10]. A typical control volume in cylindrical coordinates is

shown in Figure 4-3. The two-dimensional discretization equation may be expressed at a point P in terms of adjacent east, west, south and north neighbors as

$$a_P\Phi_P = a_E\Phi_E + a_W\Phi_W + a_S\Phi_S + a_N\Phi_N + b \tag{4-26}$$

where Φ could be dimensionless velocity $\bar{u}$ or temperature θ. The coefficients are determined by

$$a_E = D_e A(|P_e|) + [-F_e, 0] \qquad a_W = D_w A(|P_w|) + [F_w, 0] \tag{4-27a,b}$$

$$a_N = D_n A(|P_n|) + [-F_n, 0] \qquad a_S = D_s A(|P_s|) + [F_s, 0] \tag{4-27c,d}$$

$$b = S_c \bar{r}\Delta\bar{r}\Delta\bar{z} \tag{4-27e}$$

$$a_P = a_W + a_E + a_S + a_N - S_p \bar{r}\Delta\bar{r}\Delta\bar{z} \tag{4-27f}$$

the power-law formulation in the above equations is

$$A(|P|) = [0, (1 - 0.1|P|)^5] \tag{4-28}$$

where P=F/D called Peclet number. For ***momentum equations*** in both fluid layer and porous layer, F and D are specified as follows

$$F_e = (\bar{r}\bar{u})_e \Delta\bar{r} \qquad F_w = (\bar{r}\bar{u})_w \Delta\bar{r} \tag{4-29a,b}$$

$$F_n = (\bar{r}\bar{v})_n \Delta\bar{z} \qquad F_s = (\bar{r}\bar{v})_s \Delta\bar{z} \tag{4-29c,d}$$

$$D_e = 0 \qquad D_w = 0 \tag{4-30a,b}$$

$$D_n = \frac{\bar{r}_n \Delta\bar{z}}{\mathrm{Re}_n (\delta\bar{r})_n} \qquad D_s = \frac{\bar{r}_s \Delta\bar{z}}{\mathrm{Re}_s (\delta\bar{r})_s} \tag{4-30c,d}$$

But in fluid layer, we have

$$S_c = \frac{\bar{p}_w - \bar{p}_e}{\Delta\bar{z}} \qquad S_p = 0 \tag{4-31a,b}$$

while in porous layer, we have

$$S_c = \frac{\varphi(\bar{p}_w - \bar{p}_e)}{\Delta\bar{z}} \qquad S_p = -\frac{\varphi}{\mathrm{Re}\,Da} \tag{4-31c,d}$$

For ***energy equations***, F and D are calculated by

$$F_e = (\bar{r}\bar{u})_e \Delta\bar{r} \qquad F_w = (\bar{r}\bar{u})_w \Delta\bar{r} \tag{4-32a,b}$$

$$F_n = (\bar{r}\bar{v})_n \Delta\bar{z} \qquad F_s = (\bar{r}\bar{v})_s \Delta\bar{z} \tag{4-32c,d}$$

$$D_e = \frac{\bar{r}_e \Delta\bar{r}}{(\mathrm{Re}\,\mathrm{Pr})_e (\delta\bar{z})_e} \qquad D_w = \frac{\bar{r}_w \Delta\bar{r}}{(\mathrm{Re}\,\mathrm{Pr})_w (\delta\bar{z})_w} \tag{4-33a,b}$$

$$D_n = \frac{\bar{r}_n \Delta\bar{z}}{(\mathrm{Re}\,\mathrm{Pr})_n (\delta\bar{r})_n} \qquad D_s = \frac{\bar{r}_s \Delta\bar{z}}{(\mathrm{Re}\,\mathrm{Pr})_s (\delta\bar{r})_s} \tag{4-33c,d}$$

The above equations are for both the fluid layer and porous layer except using effective value k_e to obtain Prandtl number in the porous layer. As to the source term in energy equations, by using the recommended linearization method by Patankar [4.10], we have

$$S_c = \frac{\bar{\beta}(1-\omega)}{Bo}\left(\bar{G} + 12\theta^{*4}\right) \tag{4-34a}$$

$$S_p = -\frac{16\bar{\beta}(1-\omega)}{Bo}\theta^{*3} \tag{4-34b}$$

where θ^* is the last iteration value of dimensionless temperature.

In order to complete the whole problem specification, we consider pressure correction. Here the total mass conservation equation (4-6) is used to get pressure correction equation and pressure is assumed to be only a function of $\bar{z}$ variable. The velocity component v is computed from the discretization equation of the continuity equation.

It is worth while to note that because the staggered grids are used, the $\bar{u}$, $\bar{v}$, and θ discretization equations are set on different grids. Here the θ grid is normal, $\bar{u}$ grid

is staggered with the normal one in z direction, and $\bar{v}$ grid is staggered with the normal one in r direction.

4.3.1.1 The interface property

The computational domain includes the fluid layer and the porous layer, so obtaining a good representation for the heat flux q_n at the interface n shown in Figure 4-4 is very important to get the correct solution. There are two kinds of grid schemes to deal with this difficulty. One is shown in Figure 4-4 and other is shown in Figure 4-5.

In Figure 4-4, the control volume face n locates exactly on the interface. In this situation, we have the harmonic diffusion coefficient at the interface expressed as

$$\Gamma_n = \frac{\ln(\bar{r}_N/\bar{r}_P)}{\frac{\ln(\bar{r}_n/\bar{r}_P)}{\Gamma_P} + \frac{\ln(\bar{r}_N/\bar{r}_n)}{\Gamma_N}} \tag{4-35}$$

where Γ represents conductivity k in energy equation and viscosity μ in momentum equation.

In Figure 4-5, a line of 'ghost' grid points locate exactly on the interface. They are referred to as ghost is because their $\Delta\bar{r}$ is equal to zero. This scheme can be used only when radial velocity is small enough compared with the axial velocity. As shown in the figure, the grid point P, the south control volume face, and the north control volume face are located at the same interface position. In this case, we do not need to derive special expressions for the interface property. Instead we compute the south coefficient a_s of point P normally but using the porous layer property and compute the north coefficient a_n of point P normally but using the fluid layer property. In doing so, the interface boundary condition will be satisfied automatically.

4.3.2 Numerical Method for Radiative Transfer Equations

The interface for thermal radiation is assumed free and non-reflecting. The medium is enclosed by three bounding surfaces i (i=1, 2, 3 for inlet, outlet and side-wall boundaries respectively), so the solid angle integration for incident radiation could be transformed to surface integration as follows.

$$\bar{G}(\bar{z},\bar{r}) = \sum_{i=1}^{3} \iint_{i} \bar{I}(\bar{z},\bar{r},\hat{\Omega}) \cdot \frac{\cos\theta_i}{\bar{d}^2(s_i,s)} d\bar{A}_i \tag{4-36a}$$

$$\bar{q}_r(\bar{z},\bar{r}) = \sum_{i=1}^{3} \iint_{i} \bar{I}(\bar{z},\bar{r},\hat{\Omega}) \cdot \cos(\hat{e}_r,\hat{\Omega}) \frac{\cos\theta_i}{\bar{d}^2(s_i,s)} d\bar{A}_i \tag{4-36b}$$

$$\bar{q}_z(\bar{z},\bar{r}) = \sum_{i=1}^{3} \iint_{i} \bar{I}(\bar{z},\bar{r},\hat{\Omega}) \cdot \cos(\hat{e}_z,\hat{\Omega}) \frac{\cos\theta_i}{\bar{d}^2(s_i,s)} d\bar{A}_i \tag{4-36c}$$

where $d\bar{A}_i$ is differential dimensionless area; θ_i is the angle between the unit normal vector $\hat{n}_i$ of surface i and the intensity direction $\hat{\Omega}$ (Figure 4-2). The term $\bar{d}(s_i,s)$ is the dimensionless distance from point $s_i(\bar{z}_i,\bar{r}_i,\phi_i)$ on the boundary i (i=1,2,3) to point $s(\bar{z},\bar{r},\phi)$ in the medium and can be computed by

$$\bar{d}(s_i,s) = \left[\bar{r}_i^2 + \bar{r}^2 - 2\bar{r}_i\bar{r}\cos(\phi-\phi_i) + (\bar{z}-\bar{z}_i)^2\right]^{1/2} \tag{4-37}$$

where for 2-D problem here, let ϕ equal zero. Please note that the surface integration involves only the geometry. Radiation properties augment the calculation of the intensity. The cosines in equations (4-36) are listed in the Appendix C [4.7]. By substituting all cosines into the equations, we obtain

$$\bar{G}(\bar{z},\bar{r}) = \iint_{surface1} \bar{I}(\bar{z},\bar{r},\hat{\Omega})\frac{\bar{z}\cdot d\bar{A}_1}{\bar{d}^3(s_1,s)} + \iint_{surface2} \bar{I}(\bar{z},\bar{r},\hat{\Omega})\frac{(\bar{L}-\bar{z})\cdot d\bar{A}_2}{\bar{d}^3(s_2,s)} + \iint_{surface3} \bar{I}(\bar{z},\bar{r},\hat{\Omega})\frac{[\bar{R}_{out}-\bar{r}\cos\phi_3]\cdot d\bar{A}_3}{\bar{d}^3(s_3,s)} \tag{4-38a}$$

$$\bar{q}_r(\bar{z},\bar{r}) = \iint_{surface1} \bar{I}(\bar{z},\bar{r},\hat{\Omega})\frac{\bar{z}[\bar{r}-\bar{r}_1\cos\phi_1]\cdot d\bar{A}_1}{\bar{d}^4(s_1,s)} + \iint_{surface2} \bar{I}(\bar{z},\bar{r},\hat{\Omega})\frac{(\bar{L}-\bar{z})[\bar{r}-\bar{r}_2\cos\phi_2]\cdot d\bar{A}_2}{\bar{d}^4(s_2,s)} + \iint_{surface3} \bar{I}(\bar{z},\bar{r},\hat{\Omega})\frac{[\bar{R}_{out}-\bar{r}\cos\phi_3]\cdot[\bar{r}-\bar{R}_{out}\cos\phi_3]\cdot d\bar{A}_3}{\bar{d}^4(s_3,s)} \tag{4-38b}$$

$$\bar{q}_z(\bar{z},\bar{r}) = \iint_{surface1} \bar{I}(\bar{z},\bar{r},\hat{\Omega})\frac{\bar{z}(\bar{z}-0)\cdot d\bar{A}_1}{\bar{d}^4(s_1,s)} + \iint_{surface2} \bar{I}(\bar{z},\bar{r},\hat{\Omega})\frac{(\bar{L}-\bar{z})(\bar{z}-\bar{L})\cdot d\bar{A}_2}{\bar{d}^4(s_2,s)} + \iint_{surface3} \bar{I}(\bar{z},\bar{r},\hat{\Omega})\frac{[\bar{R}_{out}-\bar{r}\cos\phi_3](\bar{z}-\bar{z}_3)\cdot d\bar{A}_3}{\bar{d}^4(s_3,s)} \tag{4-38c}$$

where $\bar{R}_{out}=1$. To calculate the surface integrations easier and without singularity near the boundary, we use the same coordinate transformation by Chen and Sutton [4.6, 4.7] to transfer the coordinate $(\bar{z}_i,\bar{r}_i,\phi_i)$ (i=1,2,3) of integration to a new coordinate. An angle α is defined as shown in Figure 4-6, then in the projection view of the cylinder (Figure 4-7), the original point is moved from O(0,0) to S($\bar{r}$,ϕ). γ is the distance from S_i to S. χ is the angle shown in the figure. The new defined coordinate (α,γ,χ) is used to obtain transformed integral equations. For more details, see the Appendix C at the end. By doing so, we have

$$\bar{G}(\bar{z},\bar{r}) = \int_{-\pi}^{\pi}\int_{0}^{\gamma_R}\frac{\bar{I}}{\gamma}(-\sin\alpha_1)\cos^2\alpha_1 d\gamma d\chi + \int_{-\pi}^{\pi}\int_{0}^{\gamma_R}\frac{\bar{I}}{\gamma}\sin\alpha_2\cos^2\alpha_2 d\gamma d\chi + \int_{-\pi}^{\pi}\int_{\alpha_1}^{\alpha_2}\bar{I}\cdot\cos\alpha\cdot d\alpha d\chi \tag{4-39a}$$

$$\bar{q}_r(\bar{z},\bar{r}) = \int_{-\pi}^{\pi}\int_{0}^{\gamma_R}\frac{\bar{I}}{\gamma}\sin\alpha_1\cos^3\alpha_1\cos\chi d\gamma d\chi + \int_{-\pi}^{\pi}\int_{0}^{\gamma_R}\frac{\bar{I}}{\gamma}\sin\alpha_2\cos^3\alpha_2(-\cos\chi)d\gamma d\chi + \int_{-\pi}^{\pi}\int_{\alpha_1}^{\alpha_2}\bar{I}\cdot\cos^2\alpha(-\cos\chi)d\alpha d\chi \tag{4-39b}$$

$$\bar{q}_z(\bar{z},\bar{r}) = \int_{-\pi}^{\pi}\int_{0}^{\gamma_R}\frac{\bar{I}}{\gamma}\sin^2\alpha_1\cos^2\alpha_1 d\gamma d\chi + \int_{-\pi}^{\pi}\int_{0}^{\gamma_R}\frac{\bar{I}}{\gamma}(-1)\sin^2\alpha_2\cos^2\alpha_2 d\gamma d\chi + \int_{-\pi}^{\pi}\int_{\alpha_1}^{\alpha_2}\bar{I}\cdot(-\sin\alpha)\cos\alpha\cdot d\alpha d\chi \tag{4-39c}$$

where

$$\gamma_R = \sqrt{\bar{R}_{out}^{\,2} - \bar{r}^2\sin^2\chi} - \bar{r}\cos\chi \tag{4-40}$$

$$\alpha_1 = \arctan\frac{0-\bar{z}}{\gamma},\ \alpha_2 = \arctan\frac{\bar{L}-\bar{z}}{\gamma} \tag{4-41a,b}$$

where γ should be replaced by γ_R in equations (4-41) when calculating α_1 and α_2 limits in the third terms of equations (4-39), which is the surface 3 integration.

Once the new coordinate (α,γ,χ) is known, the old coordinate $(\bar{z}_i,\bar{r}_i,\phi_i)$ can be obtained by

$$\bar{z}_i = \gamma\tan\alpha_i + \bar{z} \qquad (i=1,2) \tag{4-42}$$

$$\bar{r}_i = \sqrt{\bar{r}^2 + \gamma^2 + 2\bar{r}\gamma\cos\chi} \qquad (i=1,2) \tag{4-43}$$

$$\phi_i = \tan^{-1}\frac{\bar{y}_i}{\bar{x}_i}, \quad \text{if } \bar{x}_i > 0 \text{ and } \bar{y}_i > 0 \tag{4-44a}$$

$$\phi_i = 2\pi + \tan^{-1}\frac{\bar{y}_i}{\bar{x}_i}, \quad \text{if } \bar{x}_i > 0 \text{ and } \bar{y}_i < 0 \tag{4-44b}$$

$$\phi_i = \pi + \tan^{-1}\frac{\bar{y}_i}{\bar{x}_i} \quad \text{if } \bar{x}_i < 0 \tag{4-44c}$$

where we have

$$\bar{x}_i = \bar{r}\cos\phi + \gamma\cos(\phi + \chi); \quad \bar{y}_i = \bar{r}\sin\phi + \gamma\sin(\phi + \chi) \tag{4-45}$$

In above equations, ϕ is taken as zero for this 2-D problem. The old coordinate $(\bar{z}_i, \bar{r}_i, \phi_i)$ is required in computing the radiation intensity.

4.3.2.1 Intensity

Considering a radiative ray along the path starting from point $s_i(\bar{z}_i, \bar{r}_i, \phi_i)$ to point $s(\bar{z}, \bar{r}, \phi)$, the radiation intensity once arrived at the point $s(\bar{z}, \bar{r}, \phi)$ is computed by the equation (4-20). Here we have two layers with different properties, so we need to integrate by segments. A step-change extinction coefficient and scattering albedo are assumed in the radial direction as follows:

$$\beta(\bar{z}', \bar{r}') = \beta_{in} = \beta_{porous}, \quad \omega(\bar{z}', \bar{r}') = \omega_{in} = \omega_{porous}, \quad \text{when } 0 \le \bar{r}' \le \bar{R}_m \tag{4-46a}$$

$$\beta(\bar{z}', \bar{r}') = \beta_{out} = \beta_{fluid}, \quad \omega(\bar{z}', \bar{r}') = \omega_{out} = \omega_{fluid}, \quad \text{when } \bar{R}_m \le r' \le \bar{R}_{out} \tag{4-46b}$$

If the line $\overline{s_i s}$ across these two layers, the intensity from start point $s_i(\bar{z}_i, \bar{r}_i, \phi_i)$ to concerned point $s(\bar{z}, \bar{r}, \phi)$ ($\phi = 0$ or omitted for 2-D problem) will go through different layers. The position of intersection is required.

If any point $s'(\bar{z}', \bar{r}', \phi')$ lays on the line $\overline{s_i s}$, then

$$\bar{z}' = \bar{z}_i + (\bar{z} - \bar{z}_i)\cdot t \quad \text{where} \quad 1 \ge t \ge 0 \tag{4-47a}$$

$$\bar{r}' = \sqrt{\bar{x}'^2 + \bar{y}'^2} \tag{4-47b}$$

where

$$\bar{x}' = \bar{x}_i + (\bar{x} - \bar{x}_i)\cdot t = \bar{r}_i \cos\phi_i + (\bar{r}\cos\phi - \bar{r}_i \cos\phi_i)\cdot t \tag{4-47c}$$

$$\bar{y}' = \bar{y}_i + (\bar{y} - \bar{y}_i)\cdot t = \bar{r}_i \sin\phi_i + (\bar{r}\sin\phi - \bar{r}_i \sin\phi_i)\cdot t \tag{4-47d}$$

The intersection point of the line and the circle $\bar{r} = \bar{R}_m$ is determined by

$$\bar{x}'^2 + \bar{y}'^2 = \bar{R}_m{}^2 \tag{4-48a}$$

that is

$$[\bar{r}_i \cos\phi_i + (\bar{r}\cos\phi - \bar{r}_i \cos\phi_i)t]^2 + [\bar{r}_i \sin\phi_i + (\bar{r}\sin\phi - \bar{r}_i \sin\phi_i)t]^2 = \bar{R}_m{}^2 \tag{4-48b}$$

The above equation is solved for t as follows:

$$t_{1,2} = \frac{\bar{r}_i[\bar{r}_i - \bar{r}\cos(\phi - \phi_i)] \pm \sqrt{\bar{r}_i^2[\bar{r}_i - \bar{r}\cos(\phi - \phi_i)]^2 + \gamma^2(\bar{R}_m{}^2 - \bar{r}_i^2)}}{\gamma^2} \tag{4-49}$$

where

$$\gamma = [\bar{r}^2 + \bar{r}_i^2 - 2\bar{r}\bar{r}_i \cos(\phi - \phi_i)]^{1/2} \tag{4-50}$$

In equation (4-49), the '–' operation in the numerator goes with solution t_1 and the '+' operation goes with solution t_2. So the root t_2 is always greater than t_1. We may consider three situations. One is no solution or both t_1 and t_2 do not belong to [0,1], so there is no intersection between line $\overline{s_i s}$ and middle cylindrical plane $\bar{r} = \bar{R}_m$; another situation is only one of t_1 and t_2 belongs to [0,1], so there is only one intersection point; the last situation is both of t_1 and t_2 fall in the range [0,1], so there are two intersection points. From systematic analysis of equation (4-49), we have following possibilities:

If $\bar{r} \le \bar{R}_m$ (Figure 4-8)

1) When $t_1, t_2 \notin [0,1]$

$$\bar{I}(\bar{z},\bar{r},\hat{\Omega}) = \bar{I}_i \exp\left[-\bar{\beta}_{in}\bar{d}(s_i,s)\right] + \int_0^1 \bar{\beta}_{in}\bar{S}(\omega_{in})\exp\left[-\bar{\beta}_{in}(1-t)\bar{d}(s_i,s)\right]\bar{d}(s_i,s)dt \quad (4\text{-}51a)$$

2) When only $t_1 \in [0,1]$

$$\begin{aligned}\bar{I}(\bar{z},\bar{r},\hat{\Omega}) &= \bar{I}_i \exp\left\{-\left[\bar{\beta}_{out}t_1 + \bar{\beta}_{in}(1-t_1)\right]\bar{d}(s_i,s)\right\} + \\ &\int_0^{t_1} \bar{\beta}_{out}\bar{S}(\omega_{out})\exp\left\{-\left[\bar{\beta}_{out}(t_1-t) + \bar{\beta}_{in}(1-t_1)\right]\bar{d}(s_i,s)\right\}\bar{d}(s_i,s)dt + \\ &\int_{t_1}^1 \bar{\beta}_{in}\bar{S}(\omega_{in})\exp\left[-\bar{\beta}_{in}(1-t)\bar{d}(s_i,s)\right]\bar{d}(s_i,s)dt\end{aligned} \quad (4\text{-}51b)$$

If $\bar{r} \geq \bar{R}_m$ (Figure 4-9)

3) When no solution or $t_1, t_2 \notin [0,1]$

$$\bar{I}(\bar{z},\bar{r},\hat{\Omega}) = \bar{I}_i \exp\left[-\bar{\beta}_{out}\bar{d}(s_i,s)\right] + \int_0^1 \bar{\beta}_{out}\bar{S}(\omega_{out})\exp\left[-\bar{\beta}_{out}(1-t)\bar{d}(s_i,s)\right]\bar{d}(s_i,s)dt \quad (4\text{-}51c)$$

4) When only $t_2 \in [0,1]$

$$\begin{aligned}\bar{I}(\bar{z},\bar{r},\hat{\Omega}) &= \bar{I}_i \exp\left\{-\left[\bar{\beta}_{in}t_2 + \bar{\beta}_{out}(1-t_2)\right]\bar{d}(s_i,s)\right\} + \\ &\int_0^{t_2} \bar{\beta}_{in}\bar{S}(\omega_{in})\exp\left\{-\left[\bar{\beta}_{in}(t_2-t) + \bar{\beta}_{out}(1-t_2)\right]\bar{d}(s_i,s)\right\}\bar{d}(s_i,s)dt + \\ &\int_{t_2}^1 \bar{\beta}_{out}\bar{S}(\omega_{out})\exp\left[-\bar{\beta}_{out}(1-t)\bar{d}(s_i,s)\right]\bar{d}(s_i,s)dt\end{aligned} \quad (4\text{-}51d)$$

5) When both $t_1, t_2 \in [0,1]$

$$\begin{aligned}\bar{I}(\bar{z},\bar{r},\hat{\Omega}) &= \bar{I}_i \exp\left\{-\left[\bar{\beta}_{out}t_1 + \bar{\beta}_{in}(t_2-t_1) + \bar{\beta}_{out}(1-t_2)\right]\bar{d}(s_i,s)\right\} + \\ &\int_0^{t_1} \bar{\beta}_{out}\bar{S}(\omega_{out})\exp\left\{-\left[\bar{\beta}_{out}(t_1-t) + \bar{\beta}_{in}(t_2-t_1) + \bar{\beta}_{out}(1-t_2)\right]\bar{d}(s_i,s)\right\}\bar{d}(s_i,s)dt \\ &\int_{t_1}^{t_2} \bar{\beta}_{in}\bar{S}(\omega_{in})\exp\left\{-\left[\bar{\beta}_{in}(t_2-t) + \bar{\beta}_{out}(1-t_2)\right]\bar{d}(s_i,s)\right\}\bar{d}(s_i,s)dt + \\ &\int_{t_2}^1 \bar{\beta}_{out}\bar{S}(\omega_{out})\exp\left[-\bar{\beta}_{out}(1-t)\bar{d}(s_i,s)\right]\bar{d}(s_i,s)dt\end{aligned} \quad (4\text{-}51e)$$

Now we obtain all basic equations to solve this problem. In order to evaluate those coupled equations in above sections, grids 42×18 divide the domain. Fluid layer and porous layer use different grid sizes. Piecewise second order Lagrange polynomial interpolation is assumed for the incident radiation, heat fluxes and entering intensity at the boundaries. 20 point Gauss-Legendre quadrature is used to integrate radiative equations and the iteration method is used to solve all equations simultaneously. It is found that the solution is stable while the criterion is set very small (10^{-5} to 10^{-8}). The values of incident radiation and heat fluxes on the boundaries are obtained by direct computation from the integrals same as in our previous papers [4.7, 4.8]. The corner point values, which are the values at the intersection point of boundaries, are obtained by multidimensional extrapolation.

4.4 Results and Discussions

In order to evaluate the augmentation of heat transfer by using porous insert, the following calculation of the dimensionless bulk temperature is necessary

$$\theta_b = \frac{\int_0^1 \bar{u}\theta\bar{r}d\bar{r}}{\int_0^1 \bar{u}\bar{r}d\bar{r}} \tag{4-52}$$

The total Nusselt number is related to the total heat flux through the cooling wall

$$Nu_T = \frac{q_w D_{out}}{k(T_b - T_w)} = \frac{2q_w R_{out}}{k(\theta_b - \theta_w)T_{in}} \tag{4-53}$$

where

$$q_w = q_{wc} + q_{wr} \tag{4-54}$$

In the above equation, q_{wc} and q_{wr} are the contributions of convection and radiation respectively. They are determined by

$$q_{wc} = -k\frac{\partial T}{\partial r}\Big|_w = -(\frac{kT_{in}}{R_{out}})\frac{\partial \theta}{\partial \bar{r}}\Big|_w \tag{4-55a}$$

$$q_{wr} = \bar{q}_r(z, R_{out}) \cdot \sigma T_{in}^4 \tag{4-55b}$$

Further, we define

$$Nu_c = \frac{q_{wc} D_{out}}{k(\theta_b - \theta_w)T_{in}} = \frac{2}{(\theta_w - \theta_b)}\frac{\partial \theta}{\partial \bar{r}}\Big|_w \tag{4-56a}$$

$$Nu_r = \frac{q_{wr} D_{out}}{k(\theta_b - \theta_w)T_{in}} \tag{4-56b}$$

By the first law of thermodynamics, we have the overall energy balance equation for the entire geometry as

$$\dot{m}C_p(T_{bin} - T_{bout}) + Q_{radiation,z=0} - Q_{radiation,z=L} = 2\pi R_{out}\int_0^L q_w dz \tag{4-57}$$

where T_{bin} and T_{bout} are the inlet and outlet mean bulk temperature respectively, Q_{rin} and Q_{rout} are the radiation energy at the inlet and outlet respectively, computed by

$$Q_{radiation,z=0} = \sigma T_{in}^4 \int_0^1 \bar{q}_z(0, \bar{r}) \cdot (2\pi R_{out}^2 \bar{r}) d\bar{r} \tag{4-58a}$$

$$Q_{radiation,z=L} = \sigma T_{in}^4 \int_0^1 \bar{q}_z(L, \bar{r}) \cdot (2\pi R_{out}^2 \bar{r}) d\bar{r} \tag{4-58b}$$

In order to have detail knowledge about the effects of the porous insert, we have to know the actual combined convection and radiation heat transfer without the porous insert in the pipe. Because of the limited data in the literature, the following situation is considered to obtain necessary information first.

4.4.1 Combined Heat Transfer without Porous Insert

The computations are carried out on the clear in-pipe flow without porous insert, which is the combined convection and radiation heat transfer in the entrance with simultaneously developing velocity and temperature field. The following values of flow and geometry parameters are adopted: Re=100~1000, T_{in}=1200K, T_w=500~800K, ε_w=0.2~0.8, R_{out}=0.1m, L=0.8m, β_{fluid}=0, 0.5, 5m^{-1}, ω_{fluid}=0~0.2, e_1=0.05~1.0, e_2=0.05~0.4 (based on the extinction coefficient of the flue gas, the emissivity of the gas may range from 0.05 to 0.39, but if the inlet is close to the combustion chamber, the upstream coefficient e_1 may equal to 1.0), a1=0, the fluid properties are assumed to be the properties of dry air at temperature 1000K, ρ=0.363kg/m^3, C_p=1104.60J/kg-K, k=0.0641W/m-K, μ=41.538×10^{-6} kg/s-m. We will discuss the validation of the method and the influences of some important parameters below.

In order to validate the present code, a special case without radiation was run. These given conditions represent the pure convective developing flow in the entrance region of a clear tube. The results are compared with Kays [4.11], Ulrichson and Schmitz [4.12], which are discussed in the book by Kakac and Yener [4.13], and shown in Figure 4-10. The results of the current work fall between that of above mentioned two works. Kays results were obtained by solving the combined entrance region problem and employing Langhaar's velocity profiles [4.14]. He neglected the effect of the radial velocity component, so the local Nusselt number is over estimated. Ulrichson and Schmitz used values for the axial velocity component also taken from the work of Langhaar, but computed the radial component from the continuity equation. Actually

from the discussions of the book [4.13], differences of local Nusselt number among many investigators are observed near the inlet. This is due to the tremendous changes of velocity and temperature fields and strong sensitivity of parameters where close to the inlet. The results of current code are achieved by solving continuity equation, momentum equation and energy equation together. The velocity developing along the flow direction is shown in Figure 4-11. The current results are compared with Manohar's [4.15] and found in good agreement.

4.4.1.1 The upstream and downstream externally incident radiation

For the radiative heat transfer, there are several important parameters that have strong effects on the final results. One is the boundary conditions specified at the inlet and outlet. Most investigators assume upstream and downstream incoming radiation as black body source, that is e_1 and e_2 are assumed to be 1.0 in the equation (4-14d). But in industry applications, this is not always true. Assuming e_1 and e_2 equal to 1.0 strongly affects the analysis results.

The inlet and exit boundary conditions for radiative heat transfer depend on a number of factors. If a region up or downstream beyond the porous insert is large, in comparison to the adjacent area normal to the flow, while the gas is radiatively transparent, then the incident radiation will appear to originate from radiatively black walls. This could result in a colder temperature radiatively than the continuous average inlet or exit gas temperature. If the same external relatively large (in comparison to the flow area) region has a luminous combustion or an optically thick gas, then the condition will appear as radiatively black at the gas temperature. If the same region is of the same

order of size as the flow area while the walls are not black (for example refractory brick) or the gas is semi-transparent, then the up or downstream radiative problem must be solved prior to input to the current combined problem. Here, the radiation is specified as an incident radiative intensity at either end of the duct being analyzed. Thus, any of the conditions above can be replicated.

If we fix the coefficient e_2=0.05 and cooling wall emissivity ε_w=0.8, then the effect of upstream externally incident radiation on the radiative heat flux q_{wr} at the wall is shown in Figure 4-12. This effect is even larger than the effect of cooling wall temperature in almost half a length of the pipe near the inlet. In another half length of the pipe at the outlet side, the effect of the wall temperature increases with z coordinate. We can see that in the most entrance region, the radiative flux q_{wr} is positive, which means the radiant heat is transferred from the hot flue gas to the wall. But in the case of e_1=0.05 and T_w=800K, the radiative flux q_{wr} is negative even at both inlet and outlet sides except near the middle of the length. This phenomenon means that the radiant heat is transferred from the wall to the hot gas at both ends area because the wall and gas emit most of the energy out to the upstream and downstream.

Figure 4-13 and Figure 4-14 shows the distributions of radiative heat flux q_z (kW/m^2) at the inlet and outlet respectively. At the inlet, the effects of upstream coefficient e_1 are still larger than the effects of cooling wall temperature. When e_1 is 0.4 or 1.0, the q_z is positive at both wall temperatures 500K and 800K. The radiant heat comes into the domain from upstream. When e_1 is 0.05, the radiant heat will emit out to the upstream whether the wall temperature is 500K or 800K. With the increase of the wall temperature, the heat flux q_z decreases. At outlet, as expected, the effects of wall

temperature are much larger than the effects of upstream coefficient e_1 as shown in Figure 4-14. The radiative heat flux q_z is positive at the outlet, so the radiant heat is transferred from the domain to the downstream. With the increase of wall temperature and e_1, the heat flux q_z increases. Because the large scale, the q_z is almost constant in these figures. The actual distribution of q_z is shown in Figure 4-15 for the case e_1=0.05 and T_w=800.

The distributions of net radiative heat flux component q_z along the flow direction at different upstream incident radiation cases are shown in Figure 4-16. When the coefficient e_1 is 0.05, the heat flux at centerline r=0 is negative at inlet and positive at outlet, which means the hot gas emits radiant heat to both upstream and downstream. When the upstream coefficient e_1 is 1.0, the domain gets the most radiant energy from the upstream.

When the hot gas emits radiant heat to the upstream and downstream in the case e_1=0.05 and T_w=800, the development of temperature field in the entrance is shown in Figure 4-17. The gas temperature drops fast near the inlet as shown in the figure. At the midpoint of the flow, the temperature drops to a little higher than the wall temperature. At the outlet, the gas temperatures of some points are even lower than the wall temperature because of self-emission to the downstream.

If we fix the upstream coefficient e_1=0.4 and cooling wall emissivity ε_w=0.8, the combined effects of downstream coefficient e_2 and cooling wall temperature are shown in Figure 4-18. The downstream coefficient e_2 only affects the radiative heat flux q_{wr} at the wall in the range close to the outlet as shown in the figure. Unlike the upstream emissivity, the effect of downstream emissivity is smaller than the effect of cooling wall

temperature even near the outlet. The radiative flux q_{wr} increases with the increase of downstream coefficient e_2 especially at the outlet.

4.4.1.2 The emissivity and temperature of the cooling wall

The effects of cooling wall temperature and emissivity on the radiative heat flux q_{wr} at the wall are shown in Figure 4-19. If we assume both upstream and downstream coefficient $e_1=e_2=0.05$, then when the wall temperature is 500K, the radiant heat is transferred from the hot gas to the wall in the most entrance region. When the wall temperature is 800K, the radiant heat is transferred from the wall to the gas except at several points in the middle. This is because most of the radiant heat is emitted out to upstream and downstream as we stated before, and the wall emissivity is much higher than the gas emissivity. The effect of wall emissivity is smaller than the effect of wall temperature as shown in the figure. With the decrease of the wall emissivity, a more uniform heat flux at and along the wall is achieved.

The combined effects of wall temperature and emissivity on the distributions of net radiative heat flux component q_z along the flow direction are shown in Figure 4-20. With the increase of wall temperature, the radiant heat emitted out to the upstream and downstream by the gas will increase. Increasing the cooling wall temperature forces more radiant heat from the hot gas transferred to the inlet and outlet and less radiant heat is transferred to the wall, or even the gas to accept radiation from the wall. It is also interesting to note that at a high temperature 800K, the larger wall emissivity lets more radiant heat be emitted to upstream and downstream. But at low temperature 500K, the

larger wall emissivity has less radiant heat going upstream and downstream. This means other factors than the wall emission may play an important role.

4.4.1.3 The extinction coefficient of the fluid

The extinction coefficient of the fluid also influences the final results. The effects of the coefficient on the radial flux at the wall and axial flux along the z direction are shown in Figure 4-21 and Figure 4-22 respectively. The effects of extinction coefficient are smaller than the effects of wall temperature near the inlet and outlet, but are in the same magnitude as that of wall temperature in the middle of the pipe. The extinction coefficient has stronger influence on the axial component of net radiative heat flux than that on the radial component of the net flux as shown in the figures. This is because the total optical thickness in z direction ($=\beta_f L$) is much larger than the optical thickness in r direction ($=\beta_f R$). With the increase of the extinction coefficient, the radiative heat energy transferred from upstream will decrease and the energy transferred to downstream will increase as shown in Figure 4-22. In the middle of the pipe, the increase of the extinction coefficient does not bring the increase but decrease of both radial and axial components of the net flux.

4.4.1.4 The scattering albedo of the fluid

The effects of the single scattering albedo on the radiative heat flux at the wall are much smaller than that of other parameters as shown in Figure 4-23. So considering the gas as non-scattering will not cause big errors. But at the inlet and outlet, there exist some differences of results among different scattering albedo values. Increasing

scattering albedo causes both the heat flux transferred to the wall near the inlet and heat flux transferred from the wall near the outlet to decrease. That means larger scattering albedo results more uniform distributed radiative heat flux as expected.

4.4.1.5 Reynolds number

The effects of Reynolds number as well as the effects of cold wall temperature on the radiative heat flux on the wall are shown in Figure 4-24. The effects of wall temperature are larger than that of Reynolds number in the area close to the inlet and outlet. In reverse, Reynolds number has stronger influence than wall temperature in the middle of duct as shown in the figure. The heat flux at the wall will increase with the increase of Reynolds number. This is due to the fact that larger Reynolds number means larger mass flow rate and more hot gas flowing through.

The effects of Reynolds number on both of the convective and radiative heat transfer are shown in Figure 4-25. With the increase of Reynolds number, convective and radiative heat fluxes increase. But the largest increase of convective flux occurs near the inlet, while the largest increase of radiative flux happens near the outlet. At the same Reynolds number, radiative heat flux is 2~6 times of the convective heat flux. This factor decreases with the increase of Re number near the inlet, but increases with Re number near the outlet. So in the heat transfer calculation of high temperature equipment, neglecting radiative transfer may be damaging.

Due to the existence of radiation, the temperature field has been changed, so the convective heat transfer is enhanced compared with pure convection cases as shown

in Figure 4-26. The convective Nusselt number is about 6% higher in the combined radiation and convection situation.

4.4.2 Combined Heat Transfer with Porous Insert

The computations are carried out on the in-pipe flow with a porous insert. The following values of flow and geometry parameters are adopted: Re=100~1000, T_{in}=1200K, T_w=500~800K, ε_w=0.8, R_{out}=0.1m, $\overline{R}_m = 0.2,0.5$, L=0.8m, Da=10^{-4}~1.0, φ=0.875, $k_e=5k_f$, $\beta_{in}=\beta_{porous}$=200,400$m^{-1}$, $\omega_{in}=\omega_{porous}$=0.5,0.8, β_{fluid}=0.5m^{-1}, ω_{fluid}=0, $e_1=e_2$=0.05~0.4, a1=0, the fluid properties are assumed to be the properties of dry air at temperature 1000K as before.

With the porous insert, the flow field has been changed as shown in Figure 4-27 for a non-dimensional porous radius $\overline{R}_m = 0.5$ and Darcy number Da=0.01. The dimensionless velocity is developing in the flow direction in the figure. As the fluid flows in the z direction, some of it will flow from the porous domain to the non-porous domain; we can see the dimensionless velocity $\overline{u}$ decreases in the porous domain but increases in the non-porous domain as z increases.

Under the same parameters, the comparison of temperature fields between pure convection and combined convection-radiation cases with and without the porous insert is made as shown in Figure 4-28. At clear flow case (R_m=0), the radiation effect is small and cause the core temperature to drop. By using the insert, the radiation effect is increased and causes the porous core temperature to drop a lot. The porous insert is emitting significant heat to the receiving wall by radiation. The convective Nusselt numbers in the pure convection and combined convection-radiation cases with and

without the insert are shown in Figure 4-29. If consider combined convection-radiation heat transfer, the use of the insert cause the temperature gradient near the wall to increase, so the convection is improved. If consider pure convective heat transfer, in most area, the convective Nusselt number is increased due to the use of the porous insert. The temperature developing speed is different because the geometry is changed by using the porous insert, so in a short area near the inlet, the convective Nusselt number is decreased.

The comparison between the clear flow and the flow with the porous insert ($\overline{R}_m = 0.5$) for convective and radiative heat flux at the wall is shown in Figure 4-30. With the porous insert, the convective heat transfer is enhanced up to 20% at the outlet. This enhancement increases with the coordinate z. The radiative heat transfer in the porous insert case is about 1.6~2.8 times of that in the clear fluid case. It is interesting to note that the radiative transfer enhancement decreases with the coordinate z except near the inlet. The increases for the convective and radiative Nusselt number are also shown in Figure 4-31. In the porous insert case, the convective Nusselt number can be increased up to 55% at the outlet and radiative Nusselt number can be more than 2 times of that in the clear fluid case.

The distributions of radiant heat from upstream and downstream in the cases of flow without porous insert and flow with porous insert are shown in Figure 4-32. At the inlet, q_z is negative, that means there is radiant heat emitting from the domain to the upstream. With the porous insert, this outgoing energy increases to 2.2~7.5 times of that without the porous insert. At the outlet, q_z is positive and the radiant heat emits out to the downstream. With the porous insert, this downstream-going energy increases too, but not

as much as the upstream-going energy at the outlet. It will increase from 2% to 20% with the most at the porous domain as shown in the figure.

From the discussions above, we know that porous insert is a benefit to the combined heat transfer at above parameters situation. Those parameters will influence these benefits, because the velocity field and temperature field will be changed if those parameters change especially at the entrance range. The effects of some important parameters on the results are discussed in the following subsections.

4.4.2.1 The radius of the porous insert

If the dimensionless radius of the porous insert is 0.2 rather than 0.5, the flow field in this case is shown in Figure 4-33. Compared with Figure 4-27, the difference is the speed of the velocity development in both the porous domain and non-porous domain. When $\overline{R}_m = 0.2$, the velocity in the porous domain is more developed than that of $\overline{R}_m = 0.5$. On the other hand, the flow field in clear area of $\overline{R}_m = 0.2$ case is less developed than that of $\overline{R}_m = 0.5$ case.

The temperature field in this case is shown in Figure 4-34. The temperature in the porous domain is much smaller than the temperature in the clear flow area. As stated previously, the fluid transfers the heat energy to the porous insert, which emits the thermal energy to the cold wall, upstream, and downstream depending on the externally incident radiation from upstream and downstream.

The distributions of radiative heat fluxes to the wall at different radius are shown in Figure 4-35. The radiative heat flux when $\overline{R}_m = 0.2$ is about 1.1~1.3 times of that of clear flow, while the heat flux when $\overline{R}_m = 0.5$ is about 1.6~2.7 times of that of

clear flow. The enhancement of convective heat flux when $\overline{R}_m = 0.2$ is also smaller than that of convective flux when $\overline{R}_m = 0.5$.

4.4.2.2 The upstream externally incident radiation

The externally incident radiation at the inlet and outlet boundaries will influence the radiative heat transfer. As we discussed before, the upstream coefficient e_1 has much stronger effects on the final results than the downstream coefficient e_2. The comparison of the effects on the distributions of radiative and convective heat transfer at the wall is shown in Figure 4-36. We can see that the convective heat transfer is almost the same at three different upstream coefficients (e_1). The radiative heat flux increases with the increase of upstream coefficient e_1. The largest enhancement of the radiative flux happens near the inlet.

The effects of the porous insert at different upstream externally incident radiation values are shown in Figure 4-37. At lower incident radiation case, the effect of the porous insert is larger than that of the porous insert at higher incident radiation condition especially near the inlet. The reason for this is due to the shield effect of the porous insert on the radiation from upstream and is shown in Figure 4-38. When the upstream coefficient e_1 is 0.4, the radiant energy comes into the domain if no porous insert. But with a $\overline{R}_m = 0.2$ porous insert, the total coming energy will decrease a lot because the shield effect of the porous insert. At somewhere of the porous domain, the radiation even comes out to the upstream. The shield effect of the porous insert is stronger at higher externally incident radiation as shown in the figure. So when there

exists strong radiation coming from upstream, using the porous insert will bring less or no benefits.

4.4.2.3 The cooling wall temperature

Increasing the cooling wall temperature will result in the radiative heat flux to the wall decreases as shown in Figure 4-39. At some points, the radiant heat is even transferred from the wall to the gas. With the porous insert, the radiative flux to the wall will be increased to 1.1~2.0 time of the original flux without the insert. If the original flux is from the wall to the fluid, then with the porous insert, this absolute amount of the flux is decreased. The largest increment due to the insert is near the inlet. The wall temperature has little effects on this increment.

4.4.2.4 Reynolds number

The distributions of dimensionless velocity $\bar{u}$ with respect to $\bar{r}$ at different z locations are illustrated in Figure 4-33 and Figure 4-40 for Re=1000 and Re=100 respectively. As the fluid flows in the z direction, some of it will flow from the porous domain to the non-porous domain, we can see the dimensionless velocity $\bar{u}$ decreases in the porous domain but increases in the non-porous domain in both the figures. When Re=100, the flow field gets fully developed at the outlet for dimensionless $\bar{L} = 8$ as shown in Figure 4-40. Because the velocity lines at z=3/4L and z=L are almost the same.

The distributions of outlet temperature with respect to radial coordinate at Re=500, 1000 with and without the porous insert are shown in Figure 4-41. The temperature in the porous domain is much smaller that that in the fluid domain due to the

radiation of the porous insert. The benefits of the insert are larger at higher Reynolds number. The distributions of the mean temperature at different Reynolds number values are also shown in Figure 4-42.

The effects of Reynolds number on the enhancement of radiative heat flux are shown in Figure 4-43. The enhancement of the radiative flux increases with Reynolds number. The heat flux with the porous insert could be about 1.1~1.38 times of that without the insert when Re=1000, while about 1.03~1.2 times when Re=100.

4.4.2.5 The scattering albedo of the porous insert

The effects of the scattering albedo of the porous insert on the radiative heat transfer are shown in Figure 4-44. We can see that smaller albedo cause larger radiative heat flux from the gas to the cooling wall. Although this effect is not big, choosing the material with smaller scattering albedo for the porous insert brings higher efficiency for the total heat transfer. Still, this effect is stronger near the inlet than the outlet.

4.4.2.6 The extinction coefficient of the porous insert

The extinction coefficient of the porous insert has effects on the enhancement of radiative heat transfer too, although not big as shown in Figure 4-45. Increasing the extinction coefficient has the same effects as decreasing the scattering albedo. Larger extinction coefficient brings bigger benefits to the heat transfer as shown in the figure especially near the inlet. So choosing porous material with large extinction coefficient and small scattering albedo for the insert is good to the heat transfer enhancement.

4.4.2.7 Darcy number Da

The effects of Darcy number are important for all porous materials. The developments of the flow field at Da=0.001, 0.01, and 0.1 are shown in Figure 4-46, Figure 4-33, and Figure 4-47 respectively. It is interesting to note that when Darcy number is 0.001 and 0.01, some of the fluid will flow from the porous domain to the clear domain. So, the velocity in the center of clear domain increases, while the velocity in the porous domain decreases in the entrance range. When Darcy number is 0.1, the porous insert allows more fluid to flow through. So, the velocity in the porous domain will increase just like the center of clear domain as shown in Figure 4-47. The mass flow rate in the porous domain increases with Darcy number when get fully developed.

The effects of Darcy number on the radiative heat transfer are shown in Figure 4-48. To increase Darcy number will enhance the heat transfer to the wall. When Darcy number is increased from 0.0001 to 0.01, the radiative heat flux increases from 1.05~1.23 times of clear flow to 1.10~1.38 times of clear flow. But if Darcy number further increased from 0.01 to 0.1, the radiative heat flux increases a little. The heat flux of Darcy number 1.0 remains the same as Darcy number 0.1.

The decreasing of bulk mean temperature along the flow passage is shown in Figure 4-49. Larger Darcy number will cause bigger mean temperature drop through the flow passage. So more gas enthalpy is captured and transferred to the cooling wall by radiation.

If we fix the outlet dimensionless pressure as zero, the relative pressure distributions along the flow direction at different Darcy numbers are shown in Figure 4-50. The pressure drop of Darcy number being 0.1 is almost the same as that without

porous insert. When Darcy number is 0.01, the pressure drop is about 1.09~1.18 times of the pressure drop of clear flow. This is an acceptable value for industry application. But when Darcy number is 0.001, the pressure drop increases a lot to about 1.23~1.35 times of that of clear flow. This will largely increase the consuming power of the flow system.

Large Darcy number will benefit the radiative heat transfer enhancement, but the value of Da is normally much less than unity. Weinert and Lage [4.16] in 1994 reported a sample of compressed aluminum foam of 1mm thick, which has a Da number about 8 and is 'hyper-porous medium'. The material called Berl saddles has a relatively big permeability of 1.3×10^{-7}~$3.9\times10^{-7}m^2$, a porosity of 0.68~0.83, and a Da number about 10^{-5} [4.17]. A kind of ceramic foam, the material of which is Cordierite ($2Al_2O_3{\cdot}5SiO_2{\cdot}2MgO$) has been investigated by Hoffmann [4.18] to find its properties are: porosity=0.875, particle diameter=8.33×10^{-4}m, and apparent absorption coefficient=$197m^{-1}$. By using Kozeny's equation, its permeability is calculated to be around $1.65\times10^{-7}m^2$ and so the Darcy number is about 1.65×10^{-5} if defined by K/R_{out}^2 here. The ceramic foam called cordierite (manufactured by Bridgestone Tyre Co. Ltd) was made into a plate sample and investigated by Kamiuto etc. [4.19]. Its properties are: porosity=0.879, pore diameter=$(2.82\sim6.35)\times10^{-3}$m, extinction coefficient=$212.3m^{-1}$, and albedo is about 1.0. By using Kozeny's equation, its permeability is calculated and the result is about $1.04\times10^{-5}m^2$. The Darcy number is about 1.04×10^{-3} here. From the radiative heat transfer and pressure drop point of view, the Da number is the bigger the better. In this work, the properties of the porous medium are adopted according to the properties of cordierite as stated above. The relationship of these properties of porous material is very complicated and need specific experimental investigation.

4.4.3 Error Analysis

In above numerical computation, we use 42×18 grids to divide the domain for dimensionless R_m=0.2 porous insert. Then we use more grids 80×38 to divide the domain for the same case. The results are compared and an average error about 0.093 percent is obtained. It took about 16 hours for 42×18 case, but about 70 hours for 80×38 case in Digital Fortran 5.0 on a generic PC with 1 GB memory and an AMD Athlon™ XP 1.2 GHz processor. So the grid size of 42×18 is convergence and save a lot of compute time.

We assume Peclet number is large and outflow boundary condition at exit boundary. Doing so is to let the coefficient a_E=0, which means the axial diffusion is neglected. In order to evaluate the error caused by assuming sufficiently large Peclet number, we extend the flow passage from $\overline{L}=8$ to $\overline{L}=12$, and compute the same case to compare the results. The velocity and temperature fields agree well in these two cases of dimensionless length 8 and 12. At the same positions the biggest velocity difference is about 0.38 percent and the biggest temperature difference is about 1 percent. So we conclude that the outflow boundary condition will not cause big errors as expected by Patankar [4.10] and is an effective way to deal with flow exit boundaries.

At the inlet of the flow, uniform velocity and temperature distributions are assumed. Actually in practical application, this is impossible. The flow will slow down in the upstream beyond the porous insert. To analyze the error caused by this inlet condition, the same case as uniform distributions is computed again but assuming a split flow with the inlet velocity in the porous domain to be 20% and 30% of the inlet velocity in fluid domain for Da=0.001. Based on the previous numerical results, a split flow with

the inlet velocity in the porous domain to be 80% and 90% of the inlet velocity in clear domain is assumed for Da=0.01. The results are compared in the velocity fields. For Da=0.001 and Re=1000, after z=0.22L (dimensionless length is 8), the velocity profiles are almost the same in the three cases of assuming porous inlet velocity equal 1.0, 0.3, and 0.2 (clear domain inlet velocity equal 1.0). For Da=0.01 and Re=100, after z=0.1L, the velocity profiles are the same in the three cases of porous inlet velocity being 1.0, 0.9, and 0.8. In the case of Da=0.01 and Re=1000, for more than half way of L, the velocity profiles exist much difference in above three cases. This is because the total developing region is increased at higher Reynolds number. But we can see that when assuming porous inlet velocity being 0.9, the velocity of some points inside the porous domain is increased along the flow direction. This is impossible in actual situation and means the assumed inlet velocity is smaller than the actual inlet velocity. So for super-porous medium with large Da=0.01, assuming uniform inlet velocity being 1.0 as Alkam etc. did in their paper [4.20] may not cause big errors.

In current work, we assume constant properties for flue gas. But the temperature change is not small, doing so may cause certain errors. In a general case of T_{in}=1200K, T_w=500K, Re=1000, Da=0.01 and dimensionless R_m=0.2 shown in Figure 4-42, the inlet bulk mean temperature (dimensionless) is 1.0 and the outlet bulk mean temperature is 0.74. The property at 1000K is used in the computation. The following values are estimated: Re_{in}/Re_{1000}=74%, Re_{1000}/Re_{out}=84%, Pr_{1000}/Pr_{in}=99.2%, Pr_{out}/Pr_{1000}=99.8%, so there have certain errors caused by assuming constant Reynolds number if our working fluid is gas. The continuous property change with the temperature should be considered in the future work.

4.5 Conclusions

In this chapter, a combined convective and radiative heat transfer computing scheme is provided and used to solve combined problems, with and without the porous insert. For the situation without the insert, combined heat transfer in the entrance length with simultaneously developing velocity field and temperature field is computed. The effects of several important parameters are discussed. At certain conditions (smaller upstream externally incident radiation and higher wall temperature), the cooling wall will give radiant heat to the flue gas even when the gas temperature is higher than the wall temperature. So the radiative inlet and outlet boundary conditions are very important to the radiative heat transfer.

The combined heat transfer in the entrance length with the porous insert is also formulated and computed. With the porous insert, the radiative heat transfer and convective heat transfer are both enhanced. With a $\overline{R}_m = 0.5$ porous insert, the convective Nusselt number can be increased up to 55% and the radiative Nusselt number can be increased up to 150%. The porous insert can provide a shield effect to the coming in radiation from upstream; the enhancement effect is larger at lower upstream incident radiation than that at higher upstream incident radiation. If externally upstream incident radiation is high (above certain value), using the porous insert has small enhancement effects or no effects. The large extinction coefficient and small scattering albedo of the porous material benefit the enhancement effect of the insert. Increasing Darcy number of the porous insert will also benefit this enhancement effect.

4.6 Nomenclature

a	coefficients of discretization equations
a_l	linear anisotropic scattering coefficient
A	differential surface area, m^2
Bo	Boltzmann number
C_p	constant pressure specific heat, J/(kg K)
d	distance, m
Da	Darcy number
e	coefficient related to externally incident radiation and defined in equation (4-14d)
G	incident radiation, W/m^2
I	the radiation intensity, W/m^2
k	thermal conductivity, W/(m K)
L	the cylinder height, m
m	mass rate of the fluid, kg/s
n	refractive index
Nu	Nusselt number
p	pressure, N/m^2
Pr	Prandtl number
q	net radiative heat flux, or components of net radiative heat flux, W/m^2
Re	Reynolds number
R_m	the porous insert radius, m
R_{out}	the outside cylindrical radius, m
S	radiation source term, W/m^2

T temperature, K

u velocity in z direction, m/s

v velocity in r direction, m/s

Greek symbols

α the specified angle, transformed coordinate

β extinction coefficient, 1/m

ε the emissivity of the surface

θ dimensionless temperature K, or angle between surface normal vector and the intensity direction

γ the specified distance, transformed coordinate

μ absolute viscosity, N s/m^2

ρ density kg/m^3, or surface reflectivity

τ optical thickness

φ porosity

χ the specified angle, transformed coordinate

ω single scattering albedo

Ω the unit vector of the intensity direction, or the solid angle

Superscript

$^-$ non-dimensional quantity

Subscripts

b	black body, or bulk
e	effective
E	east neighbor
f	fluid
i	surface i
in	inlet, or inside porous domain
N	north neighbor
out	outlet, or outside fluid domain
r	radial direction
R	at out radius position
s	solid material
S	south neighbor
wc	convective and wall
wr	radiative and wall
z	axial direction
w	wall
W	west neighbor

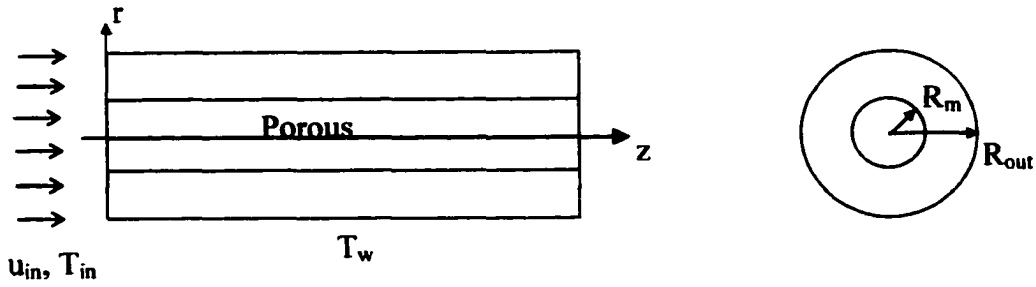

Figure 4-1 Schematic diagram of the flow system and coordinates.

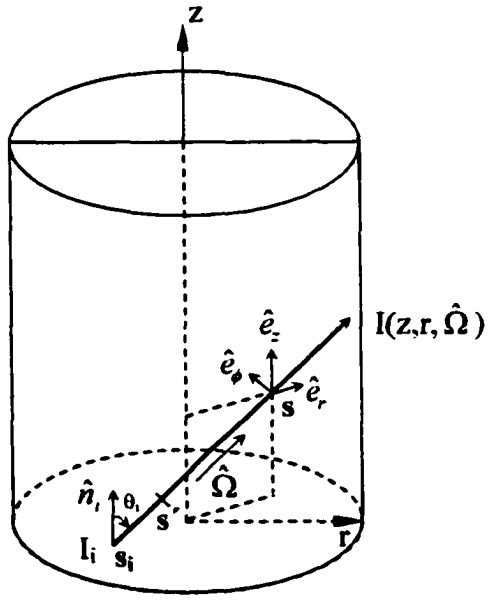

Figure 4-2 Schematic diagram of the cylindrical coordinate and the radiant ray direction.

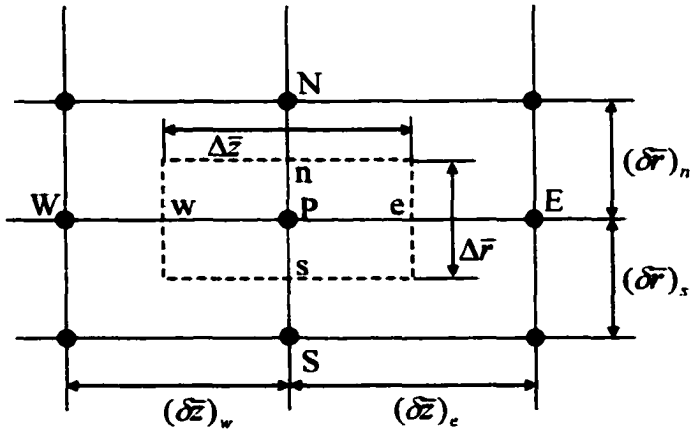

Figure 4-3 A typical control volume in cylindrical coordinate.

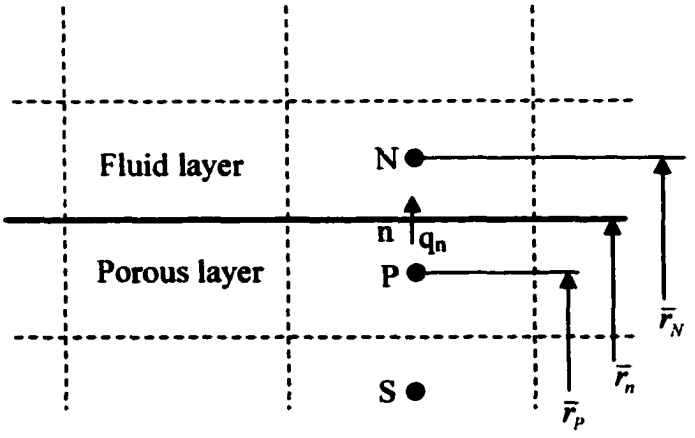

Figure 4-4 Illustration of the heat flux at the interface between the fluid layer and porous layer.

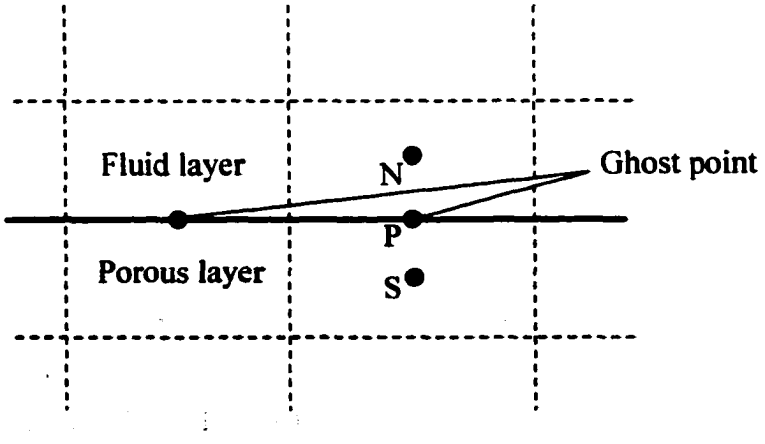

Figure 4-5 Illustration of the 'ghost' point at the interface between the fluid layer and porous layer.

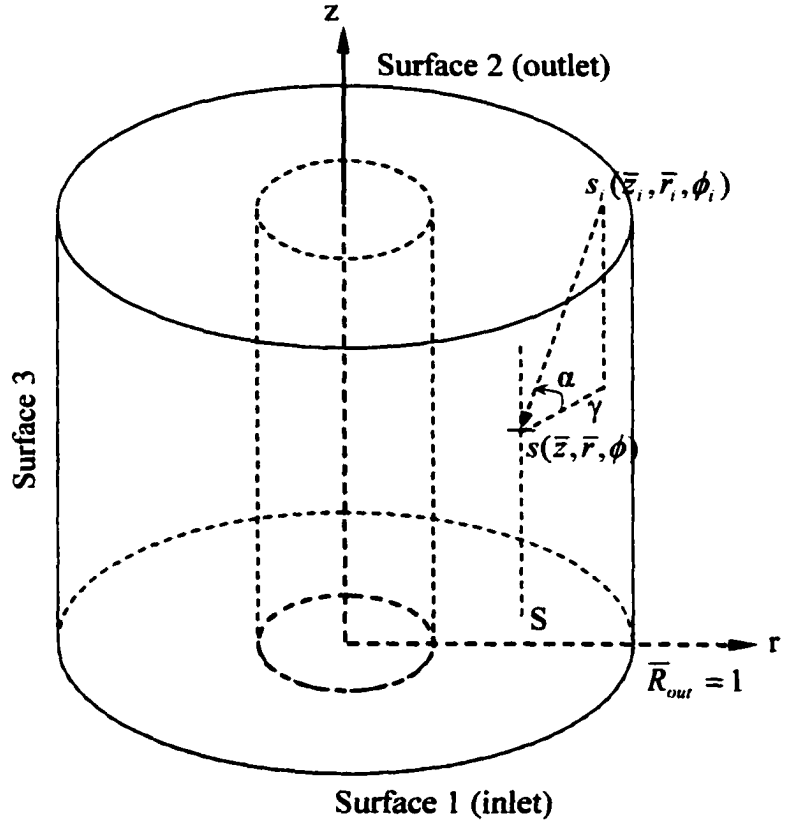

Figure 4-6 Schematic diagram of the transformed coordinates.

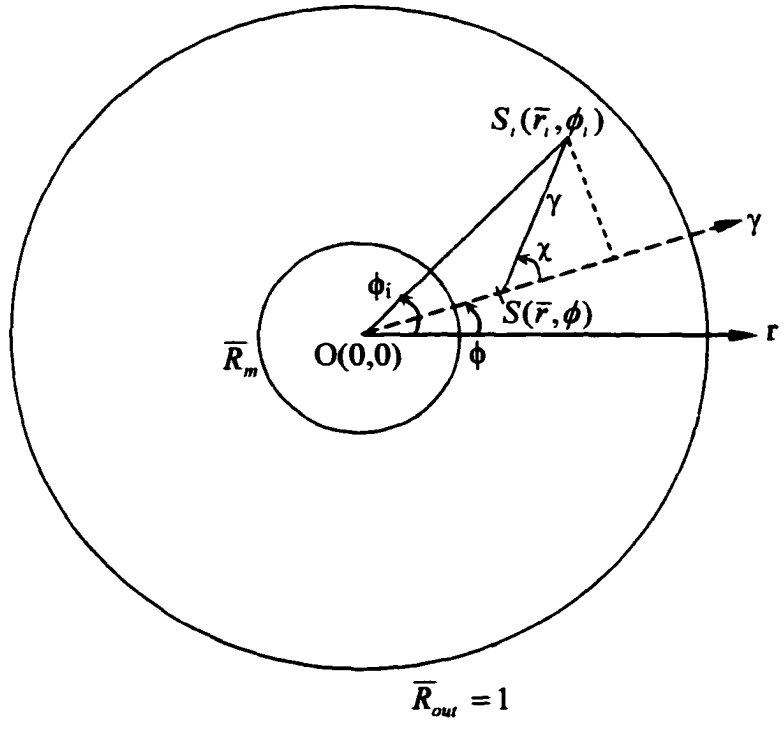

Figure 4-7 Top view of the transformed coordinates, S and S_i are the projection points of s and s_i.

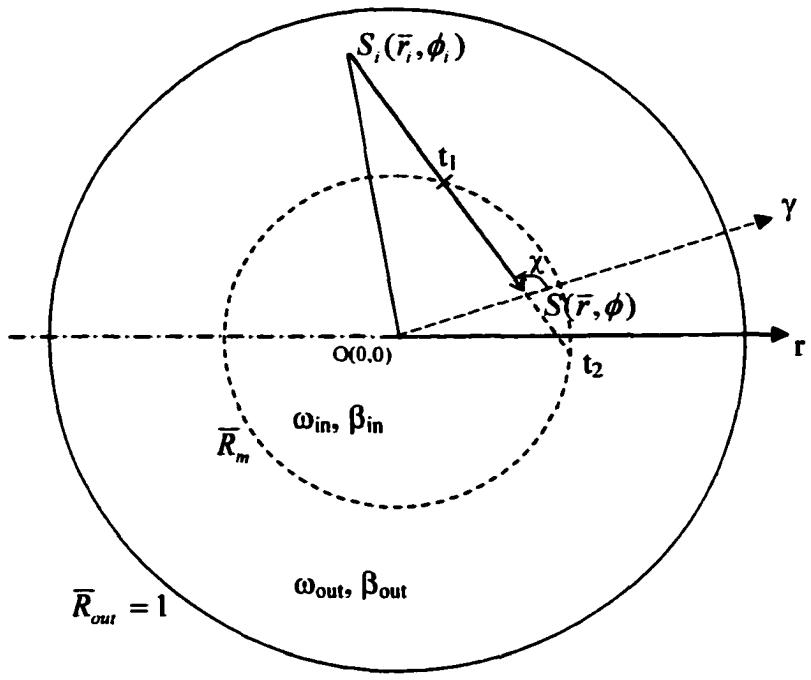

Figure 4-8 Schematic diagram for two-layer media when tracing a ray to compute optical thickness ($r \le R_m$).

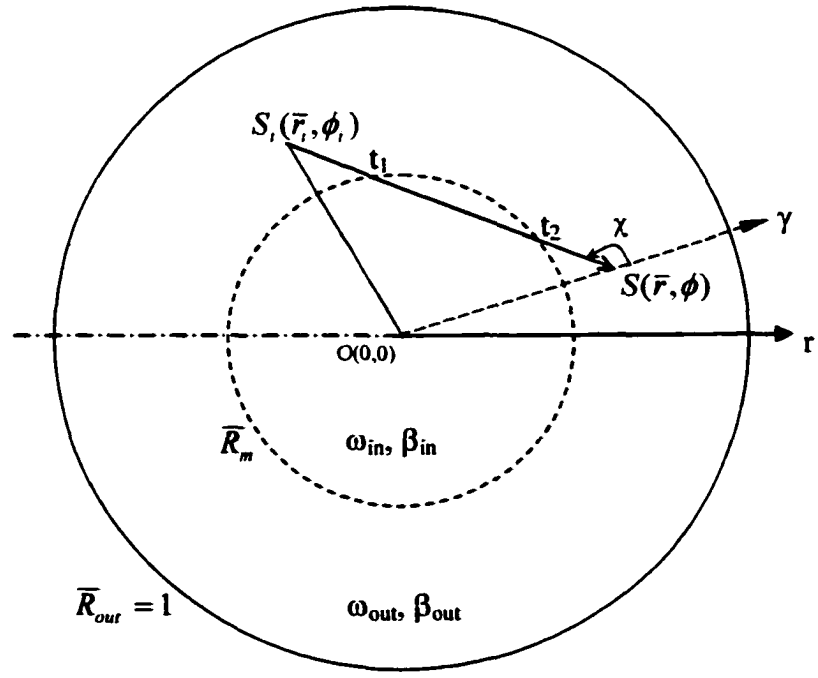

Figure 4-9 Schematic diagram for two-layer media when tracing a ray to compute optical thickness ($r > R_m$).

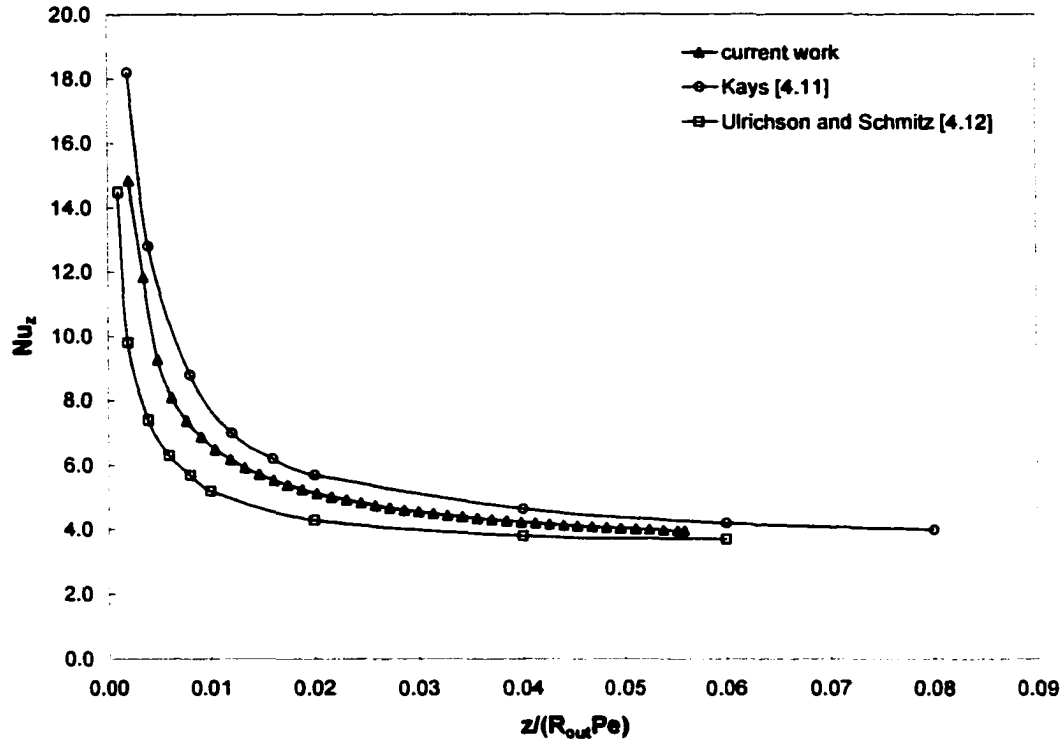

Figure 4-10 The comparison of current work with Kays etc. for the laminar flow in the entrance region with simultaneously developing velocity and temperature profiles.

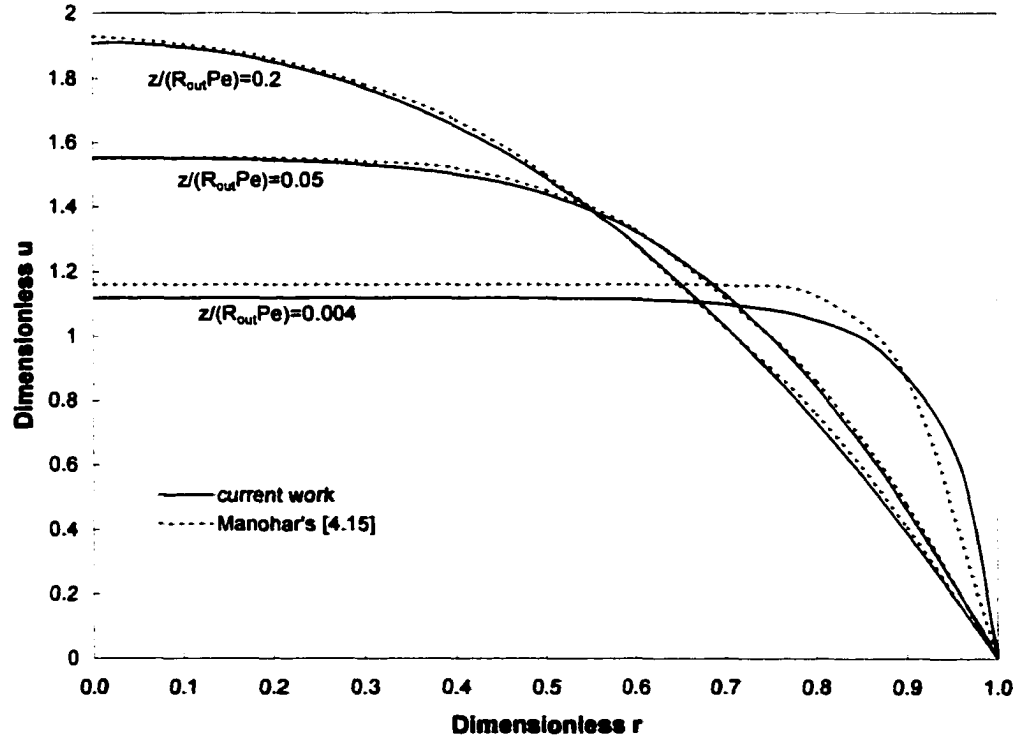

Figure 4-11 The comparison of velocity developing profiles for Pr=0.7158 and constant wall temperature T_w=500K.

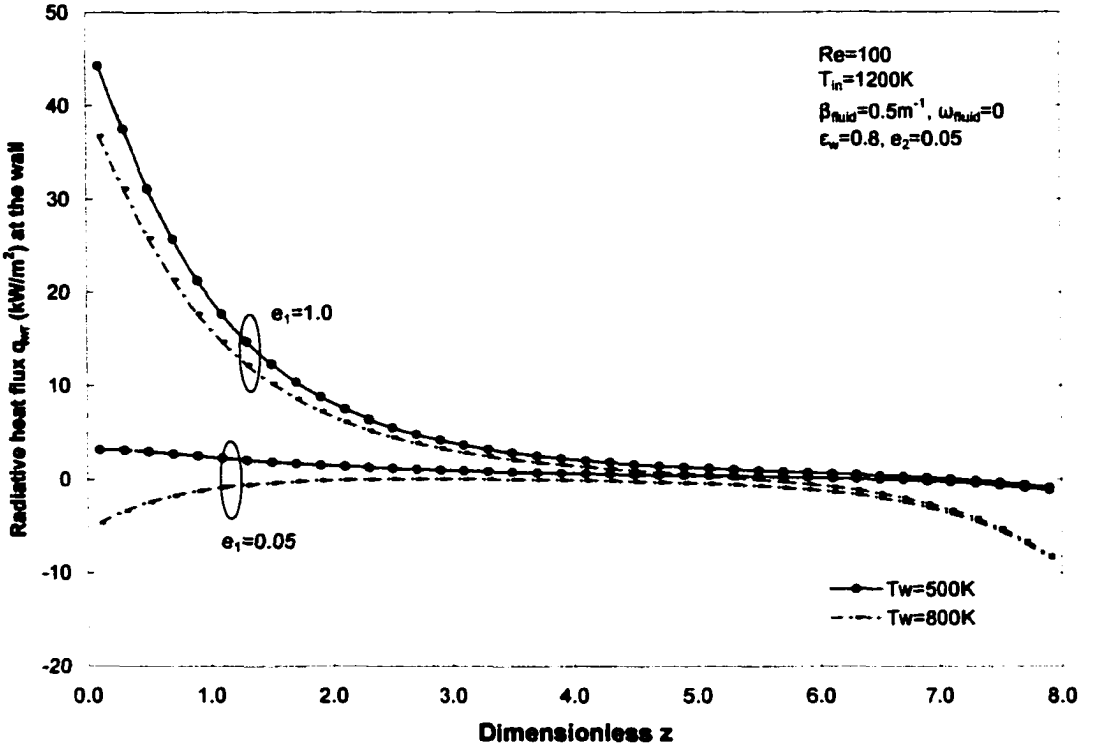

Figure 4-12 The distributions of radiative heat flux along the wall at different upstream externally incident radiation conditions.

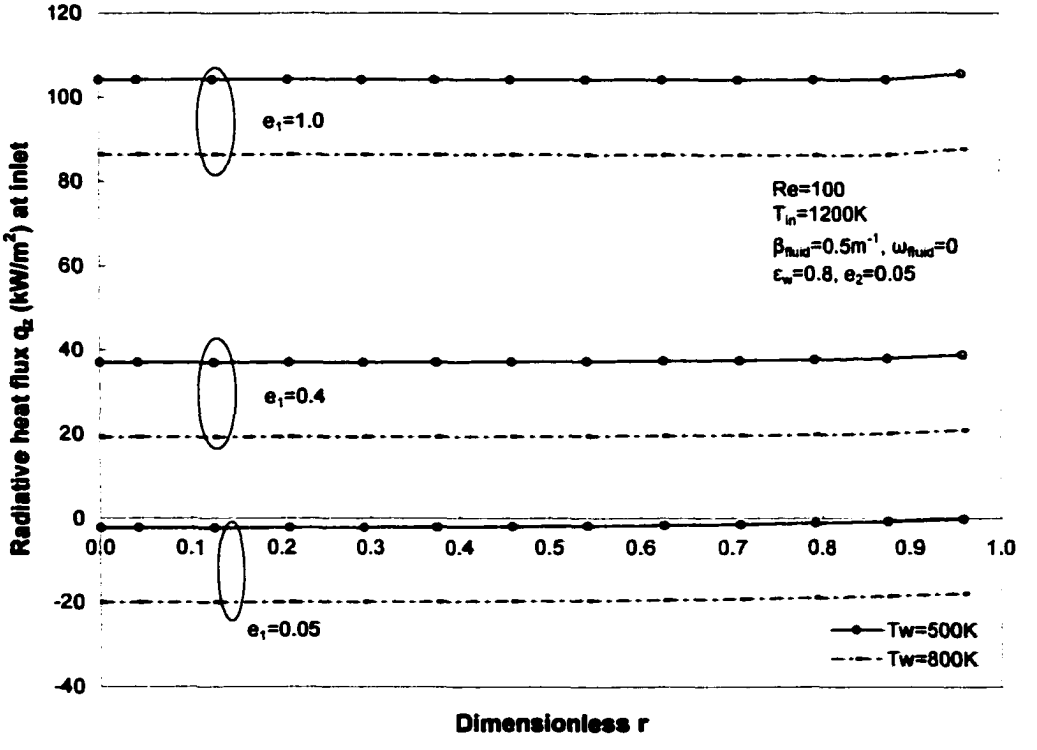

Figure 4-13 The distributions of radiative heat flux from upstream along radial coordinate at different upstream incident radiation conditions.

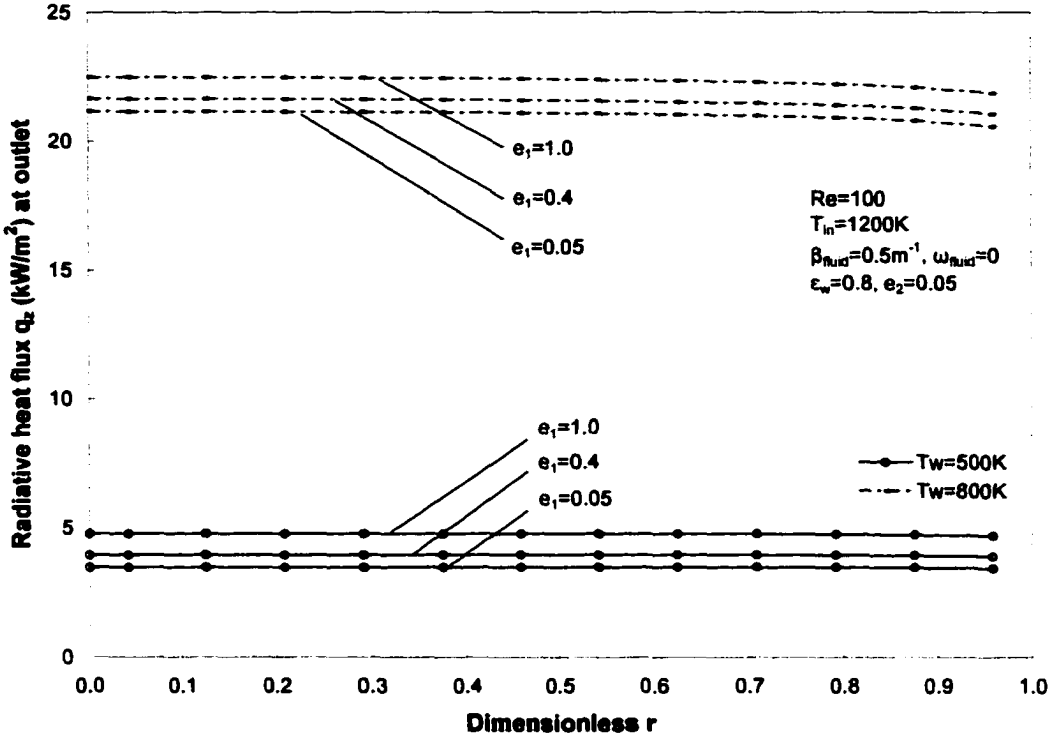

Figure 4-14 The distributions of radiative heat flux to downstream along radial coordinate at different upstream incident radiation conditions.

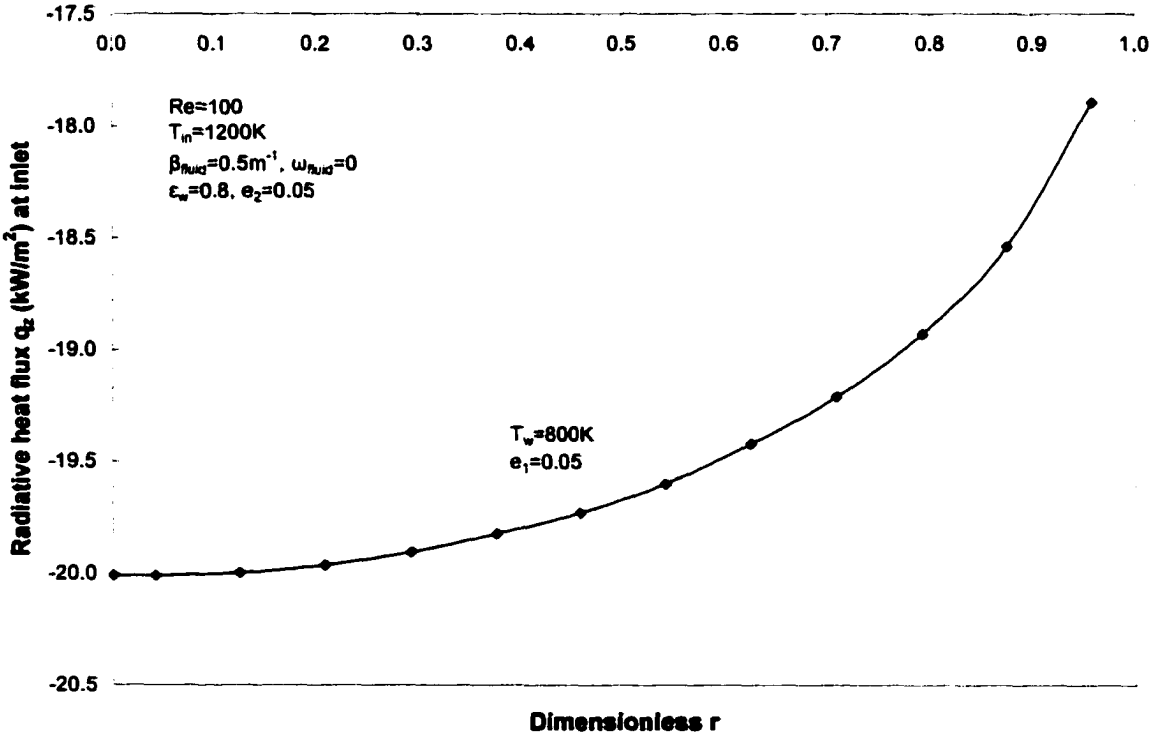

Figure 4-15 The distribution of radiative heat flux from upstream along radial coordinate when e_1=0.05 and T_w=800K.

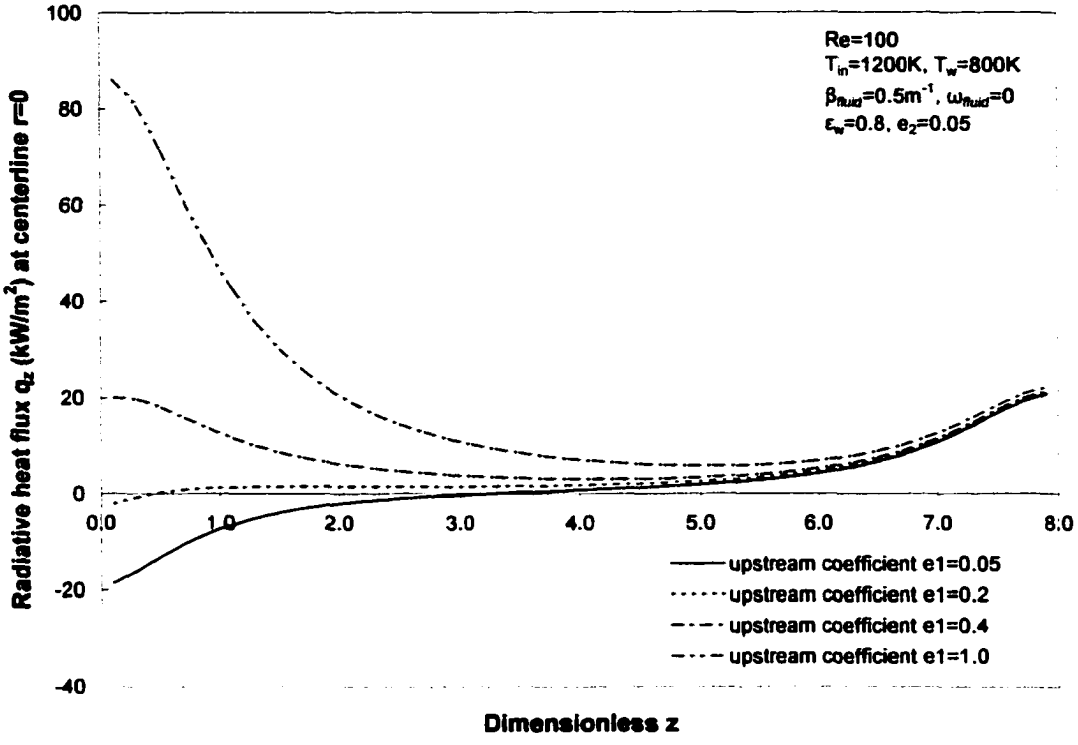

Figure 4-16 The distributions of net heat flux component q_z along axial direction at different upstream incident radiation conditions.

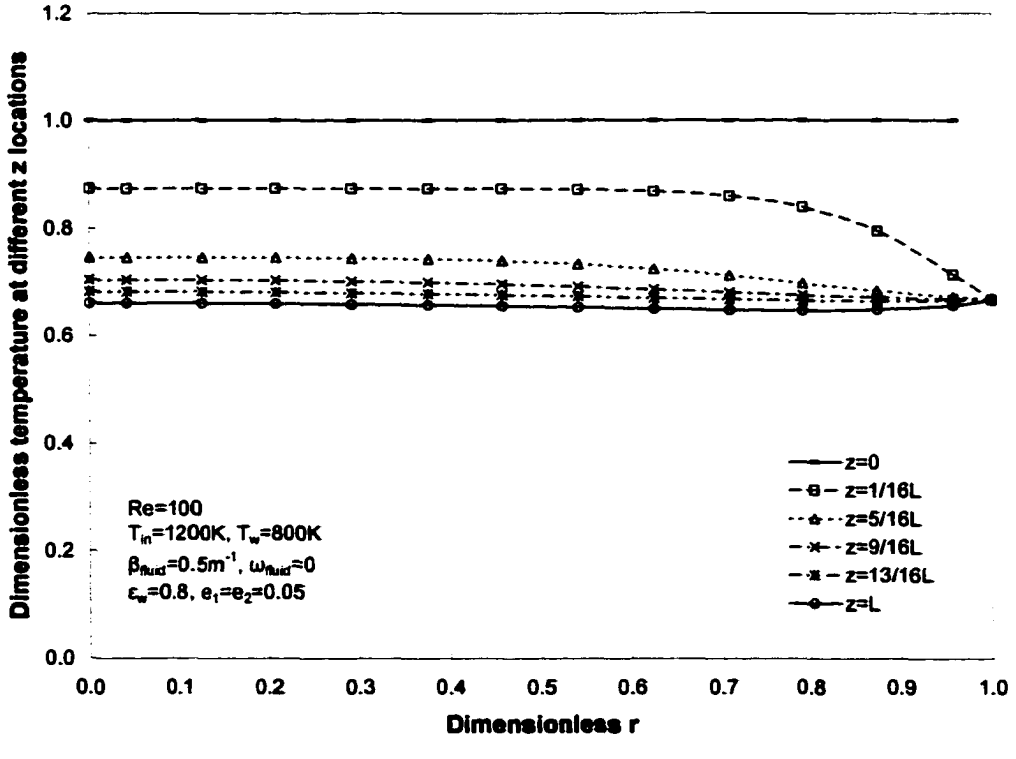

Figure 4-17 The temperature developing profiles for Re=100, e_1=0.05 and T_w=800K.

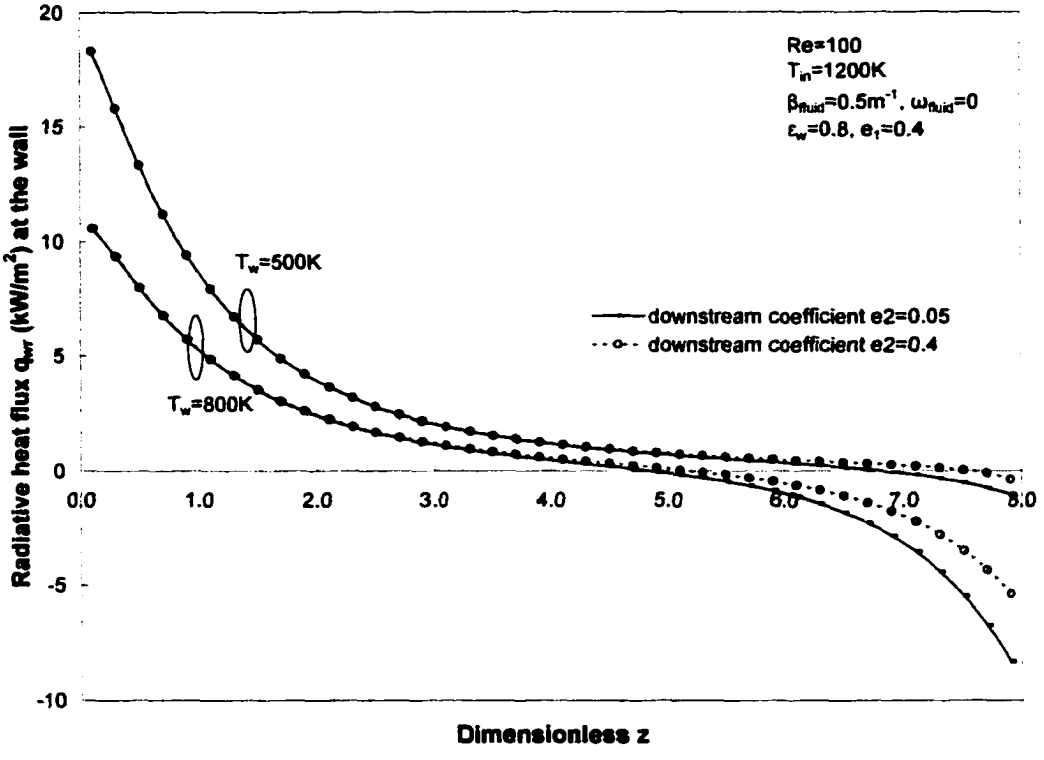

Figure 4-18 The distributions of radiative heat flux along the wall at different downstream incident radiation conditions.

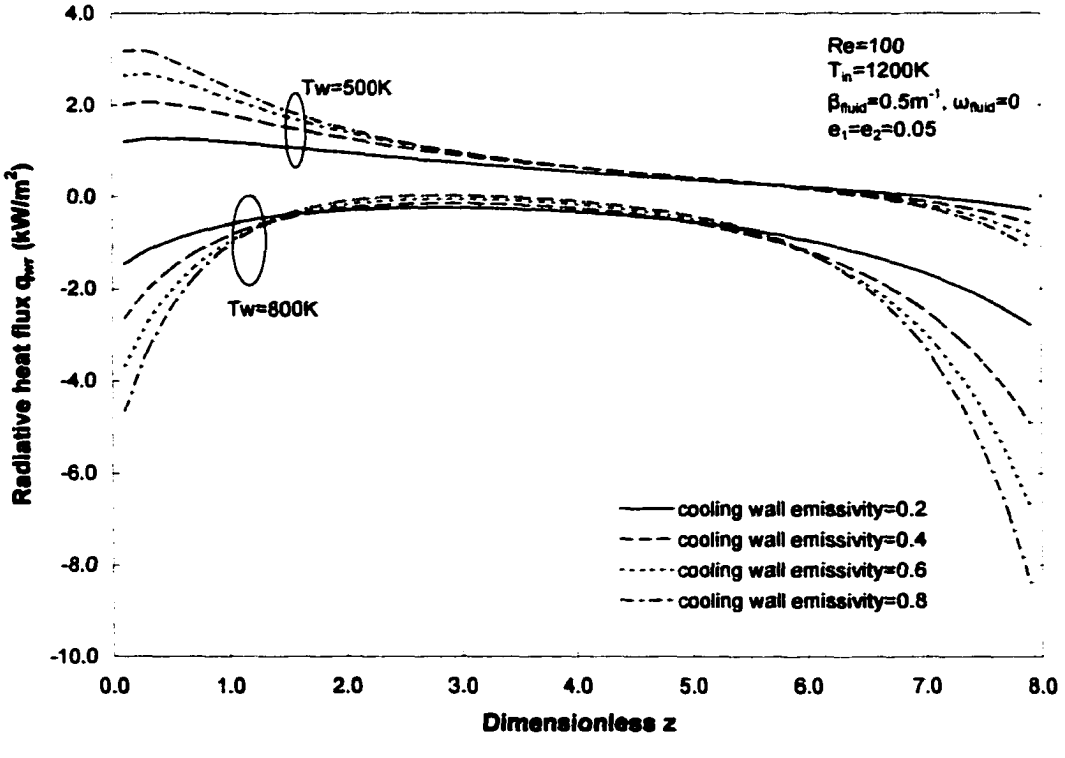

Figure 4-19 The distributions of radiative heat flux along the wall at different wall temperature and emissivity conditions.

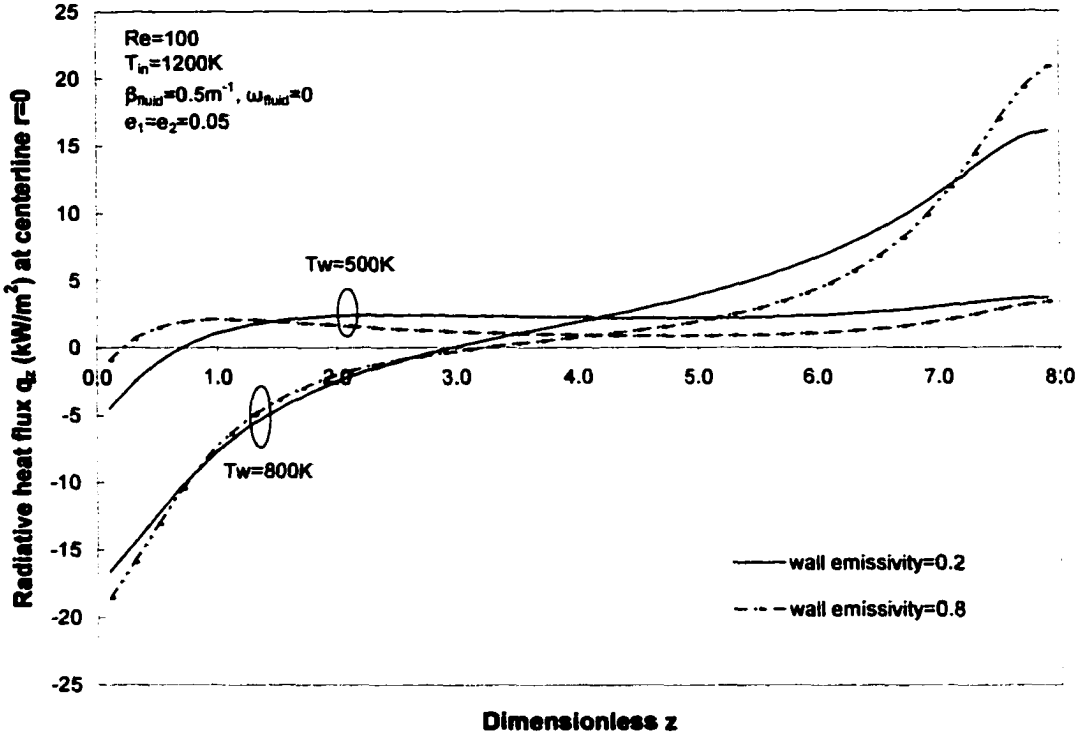

Figure 4-20 The distributions of net heat flux component q_z along axial direction at different wall temperature and emissivity conditions.

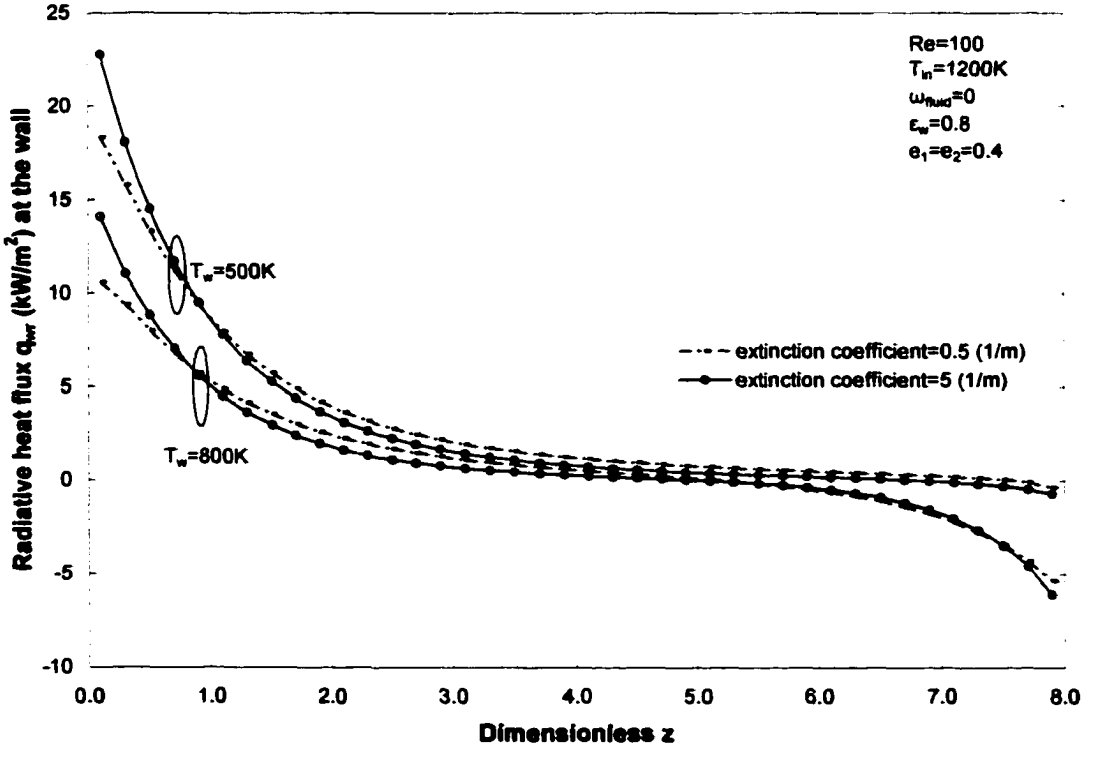

Figure 4-21 The distributions of radiative heat flux along the wall at different fluid extinction coefficients.

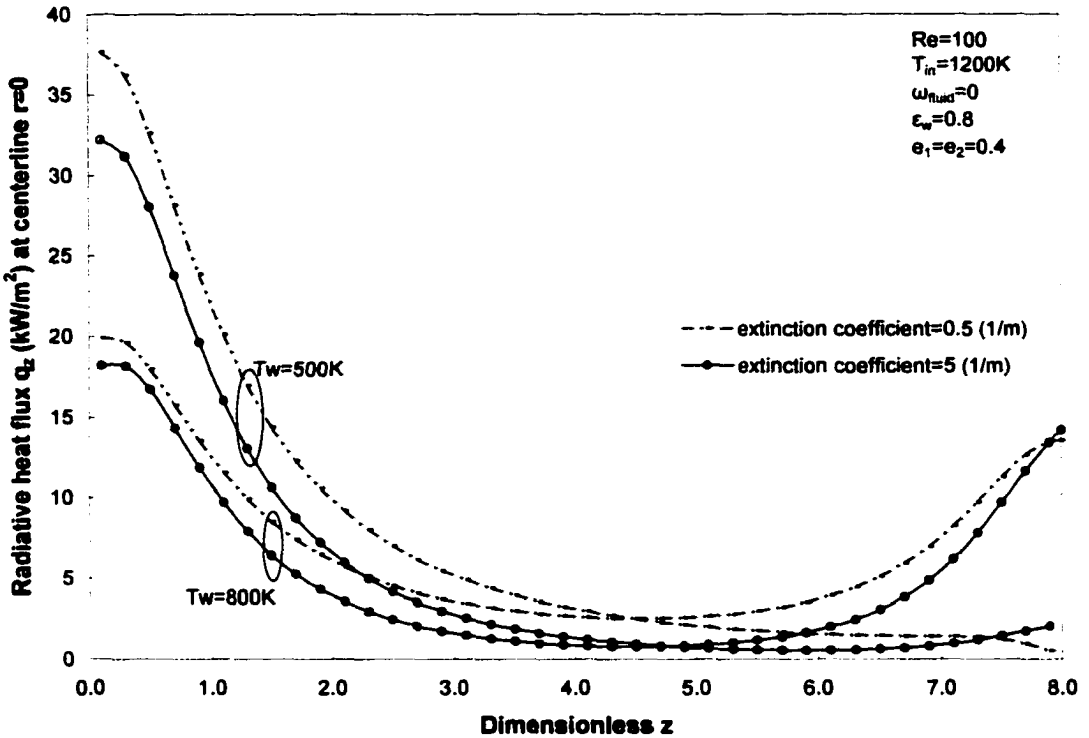

Figure 4-22 The distributions of net heat flux component q_z along axial direction at different fluid extinction coefficients.

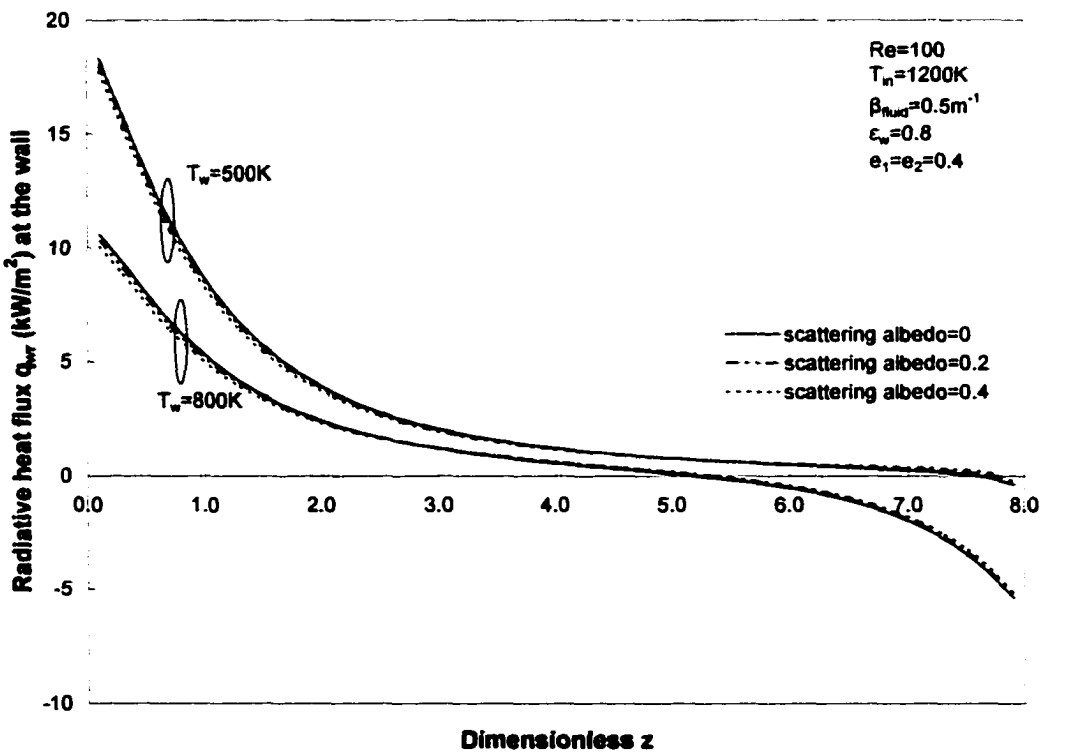

Figure 4-23 The distributions of radiative heat flux along the wall at different fluid scattering albedos.

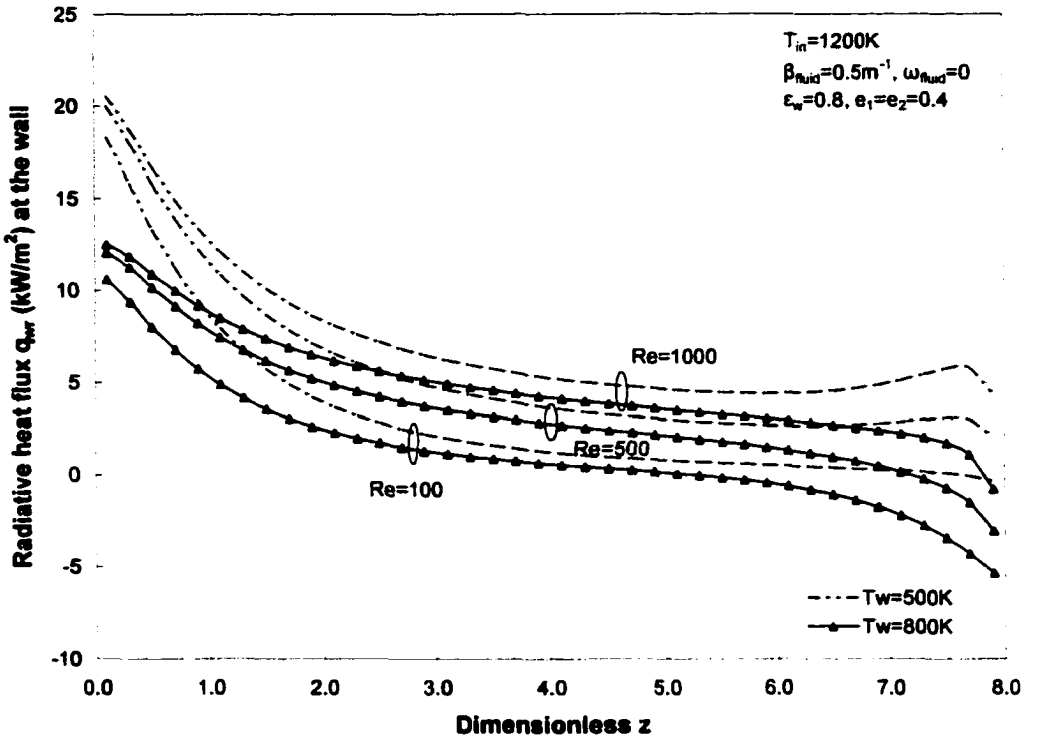

Figure 4-24 The distributions of radiative heat flux along the wall at different Reynolds numbers.

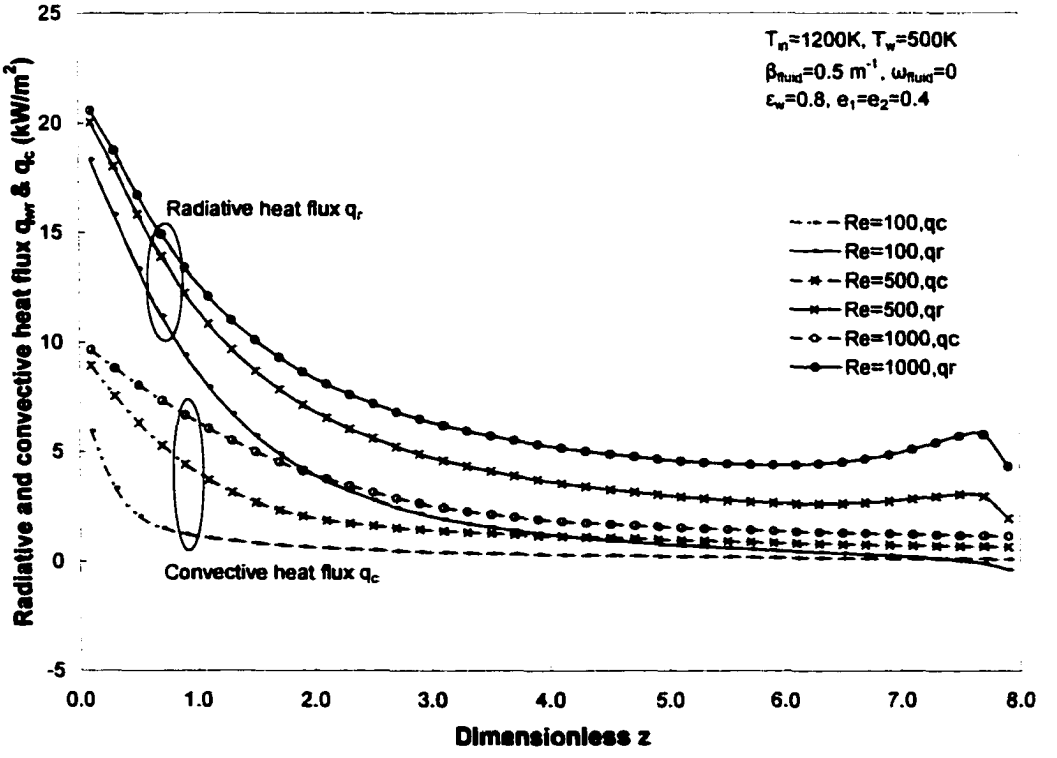

Figure 4-25 The distributions of convective and radiative heat flux along the wall at different Reynolds numbers

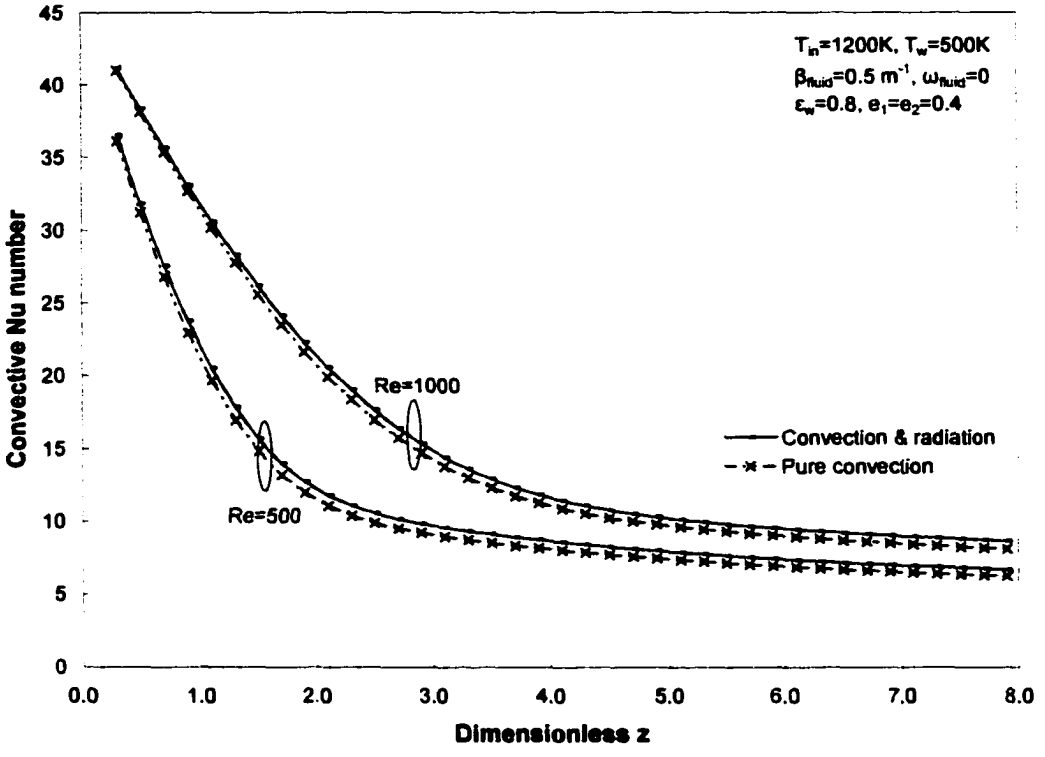

Figure 4-26 The comparison of convective Nusselt number between pure convection and combined convection-radiation.

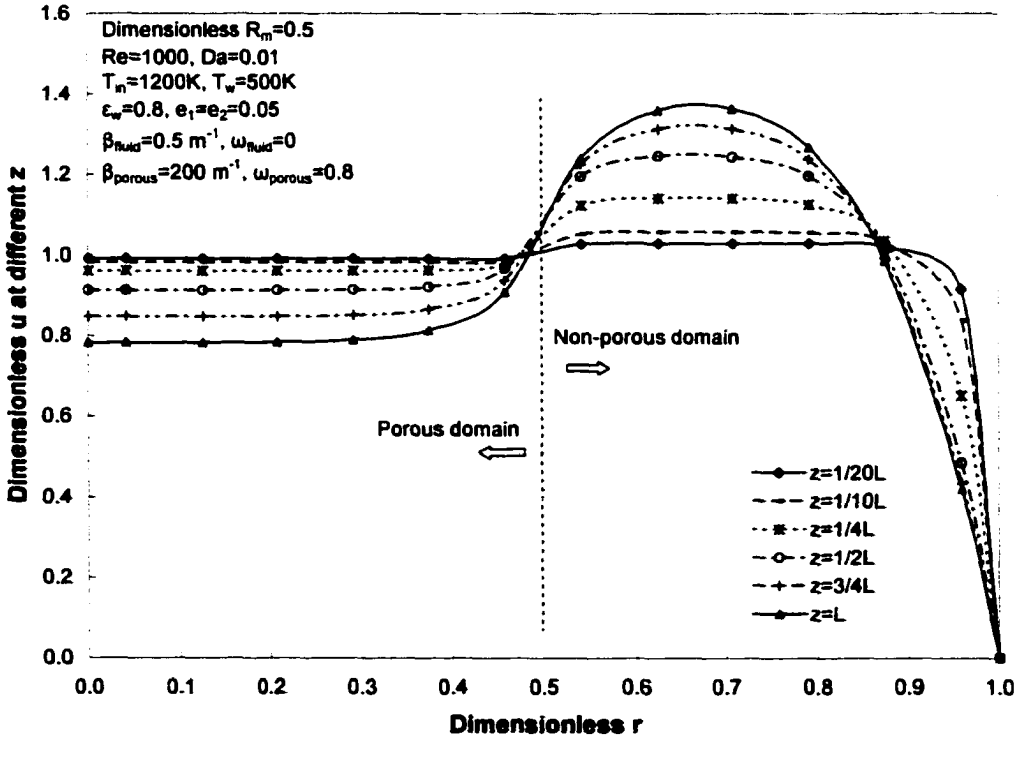

Figure 4-27 The velocity developing profiles for in-pipe flow with the porous insert R_m=0.5(dimensionless).

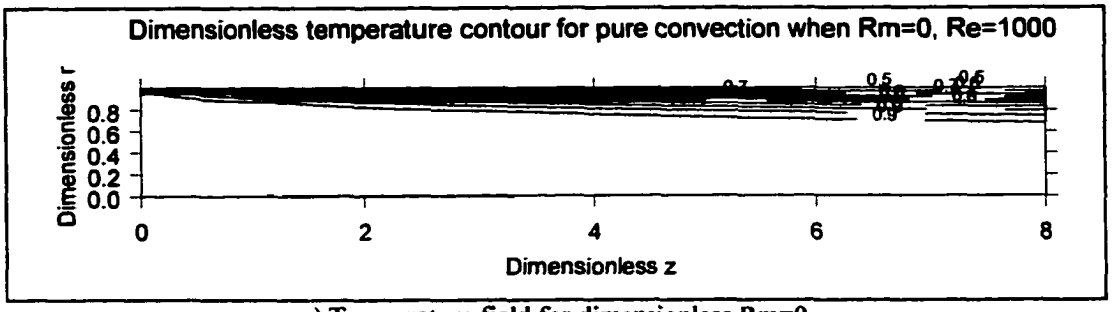

a) Temperature field for dimensionless Rm=0

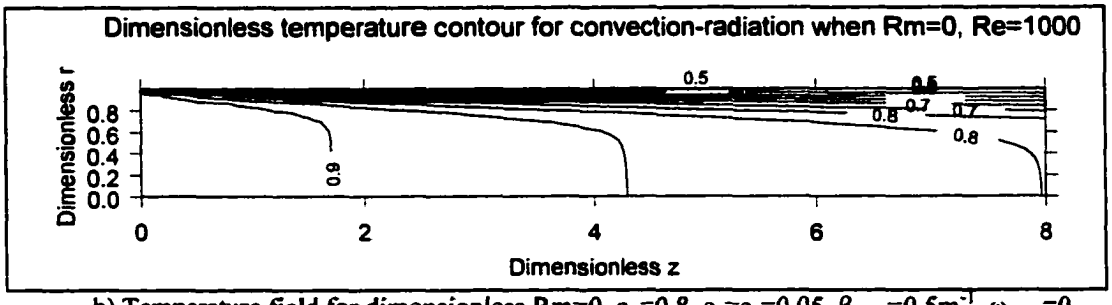

b) Temperature field for dimensionless Rm=0, ε_w=0.8, e_1=e_2=0.05, β_{fluid}=0.5m^{-1}, ω_{fluid}=0

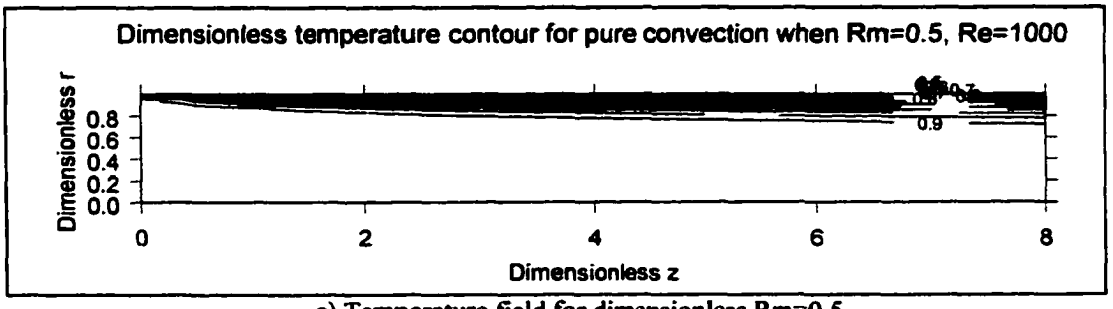

c) Temperature field for dimensionless Rm=0.5

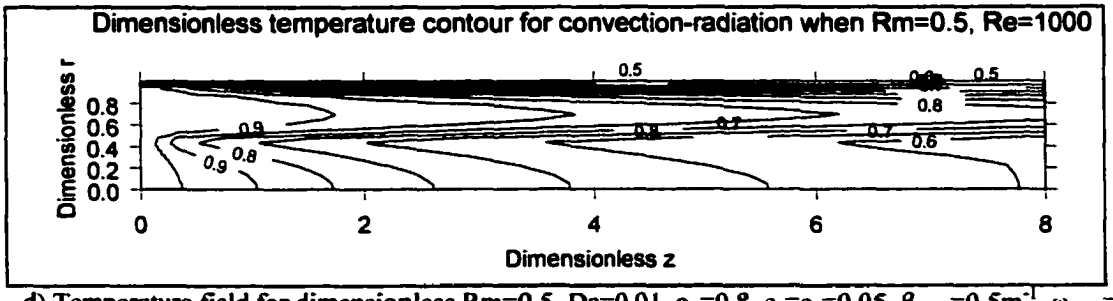

d) Temperature field for dimensionless Rm=0.5, Da=0.01, ε_w=0.8, e_1=e_2=0.05, β_{fluid}=0.5m^{-1}, ω_{fluid}=0, β_{porous}=200m^{-1}, ω_{porous}=0.8

Figure 4-28 The comparison of temperature fields between pure convection and combined convection-radiation cases with and without porous insert (T_{in}=1200K, T_w=500K)

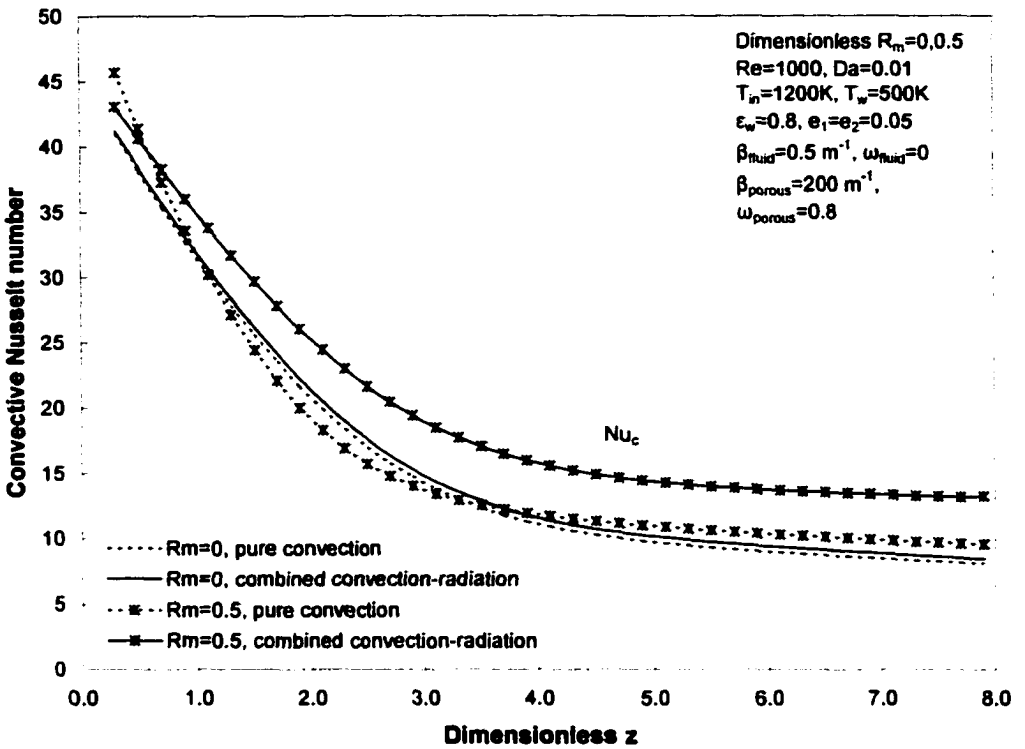

Figure 4-29 The comparison of convective Nusselt number between pure convection and combined convection-radiation cases with and without porous insert.

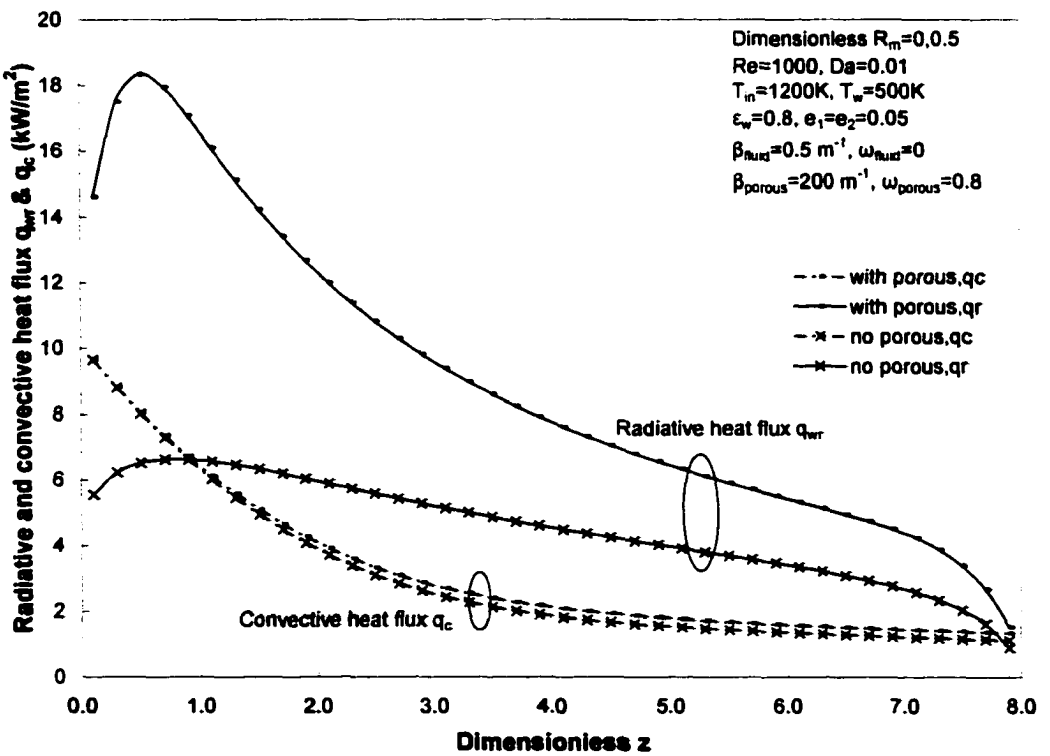

Figure 4-30 The distributions of convective and radiative heat fluxes at the wall for the pipe with and without the porous insert.

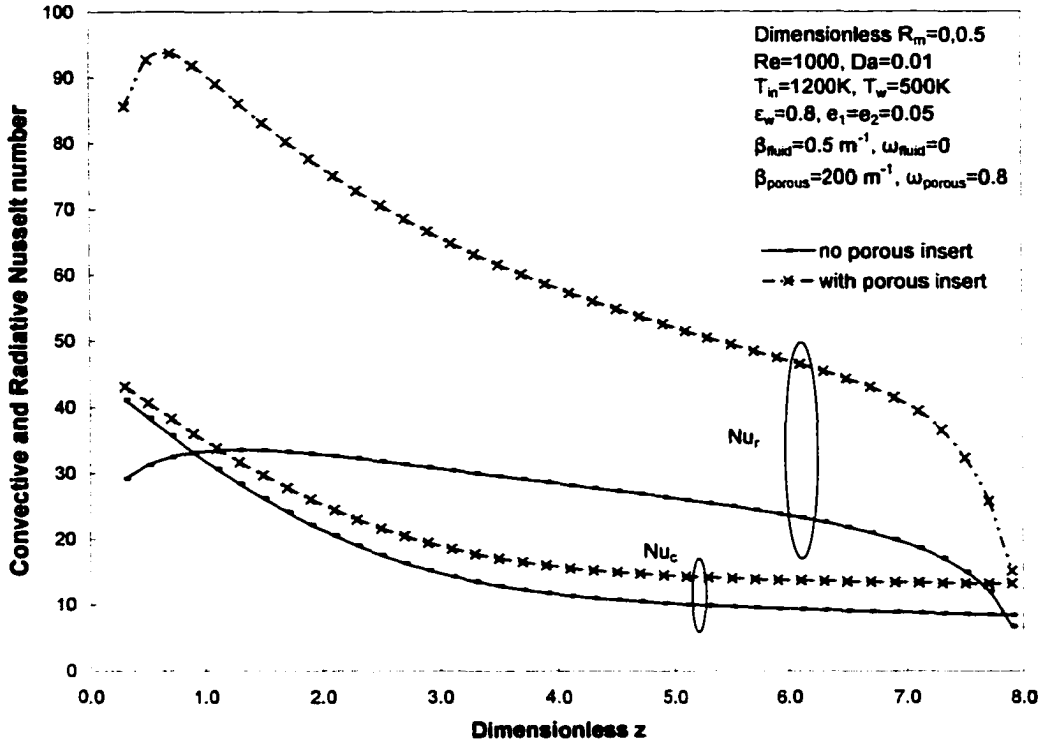

Figure 4-31 The comparison of convective and radiative Nusselt number between the cases with and without the porous insert.

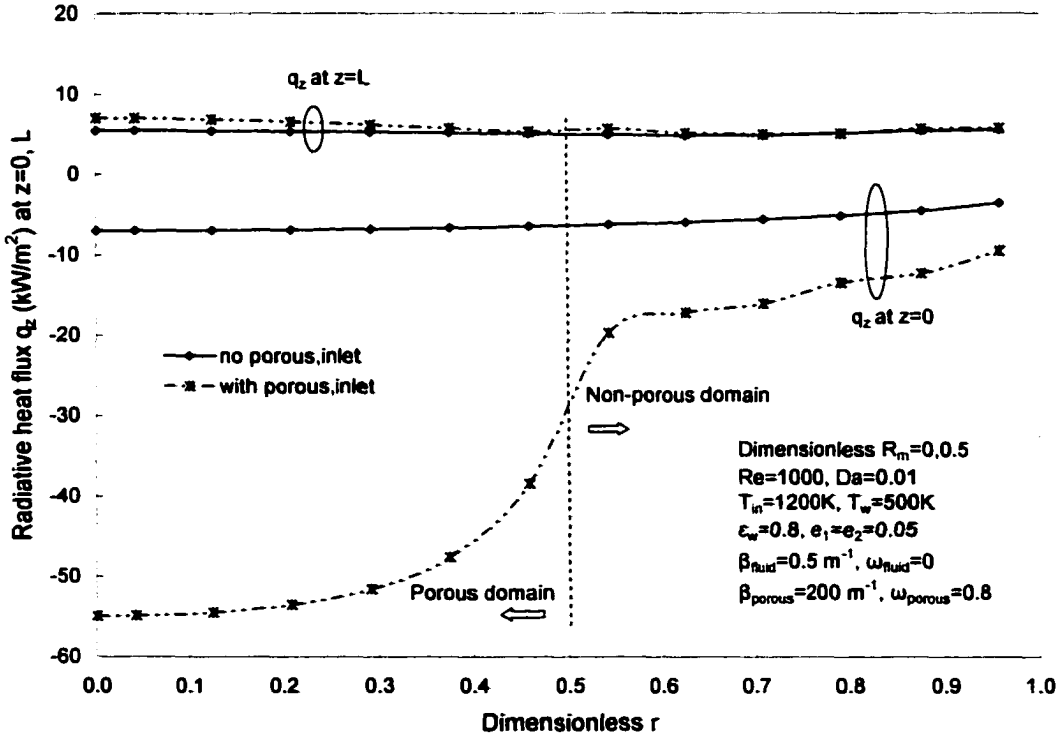

Figure 4-32 The distributions of net flux component q_z at the inlet and outlet for cases with and without the porous insert.

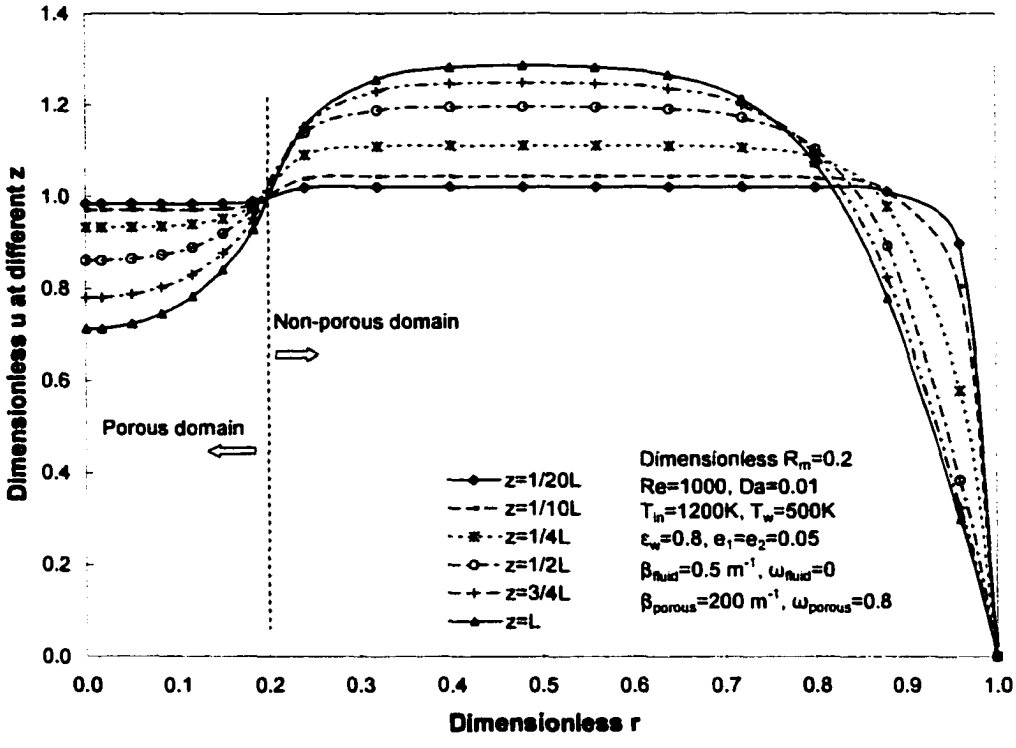

Figure 4-33 The velocity developing profiles for in-pipe flow with the porous insert R_m=0.2(dimensionless).

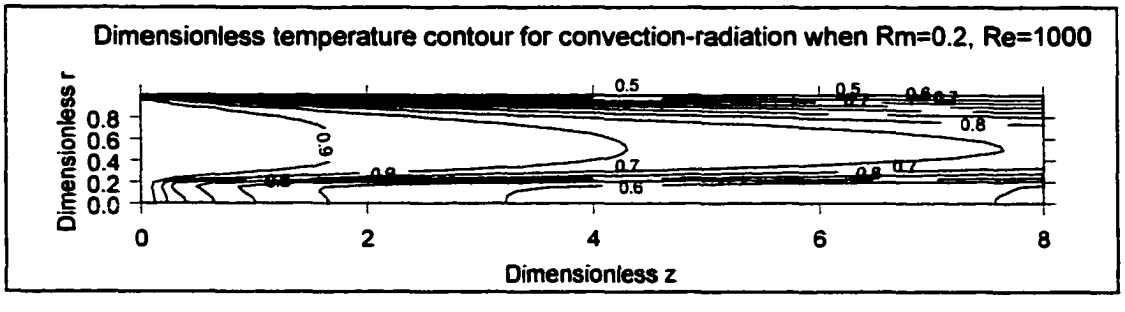

Figure 4-34 The temperature developing field for in-pipe flow with the porous insert (Da=0.01, T_{in}=1200K, T_w=500K, ε_w=0.8, e_1=e_2=0.05, β_{fluid}=0.5m^{-1}, ω_{fluid}=0, β_{porous}=200m^{-1}, ω_{porous}=0.8).

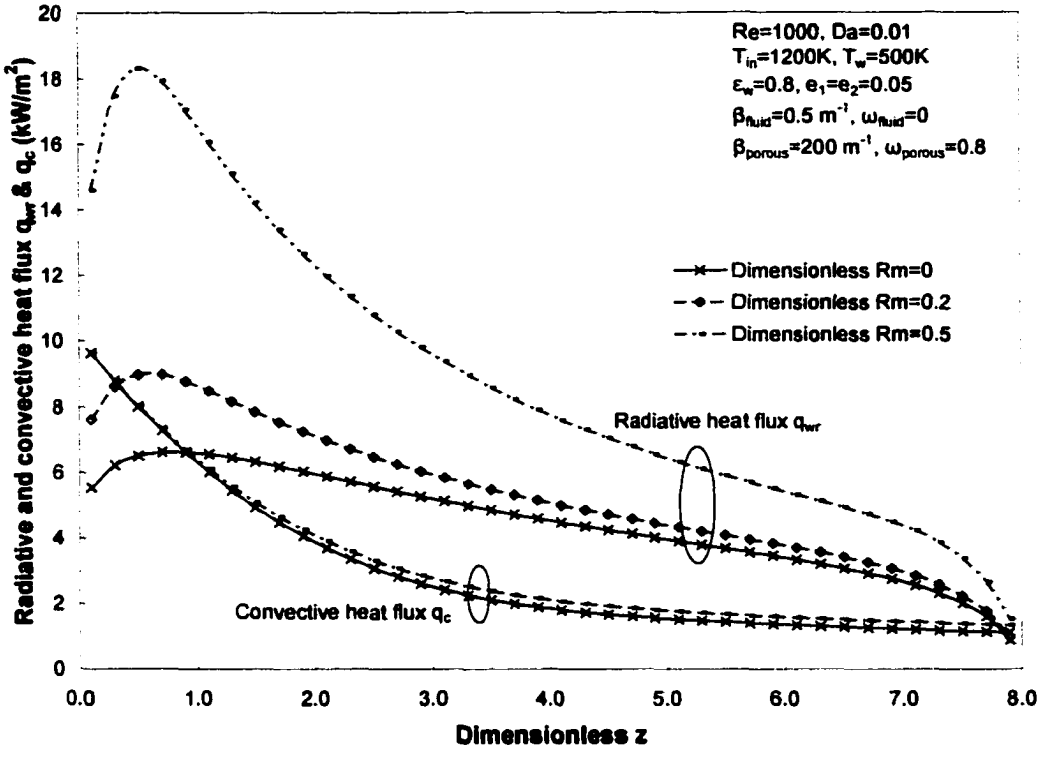

Figure 4-35 The distributions of convective and radiative heat fluxes along the wall at different dimensionless R_m.

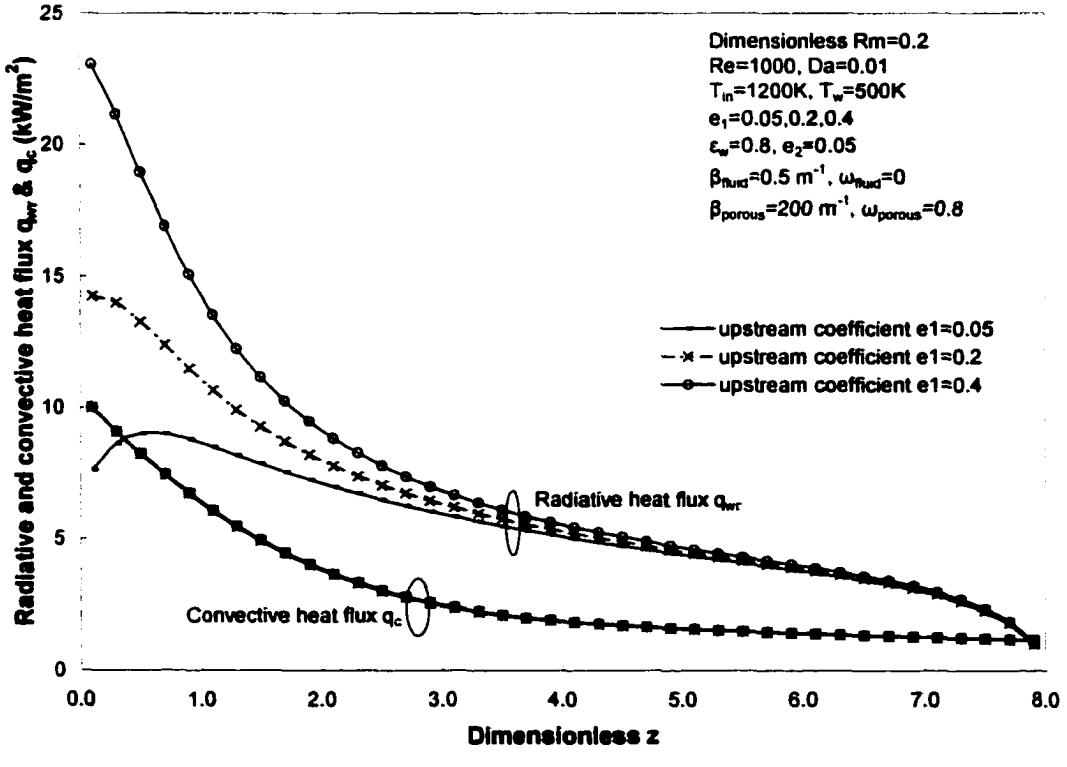

Figure 4-36 The distributions of convective and radiative heat fluxes at different upstream incident radiation conditions with R_m=0.2.

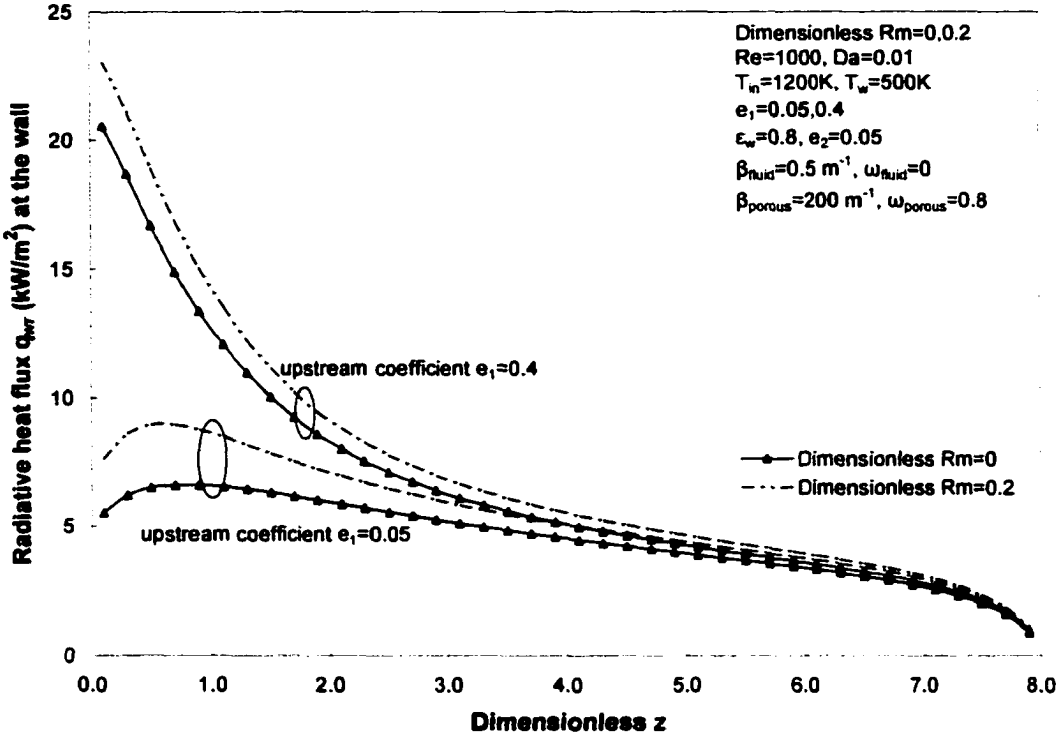

Figure 4-37 The comparison of radiative heat fluxes with and without the porous insert at different upstream incident radiation conditions.

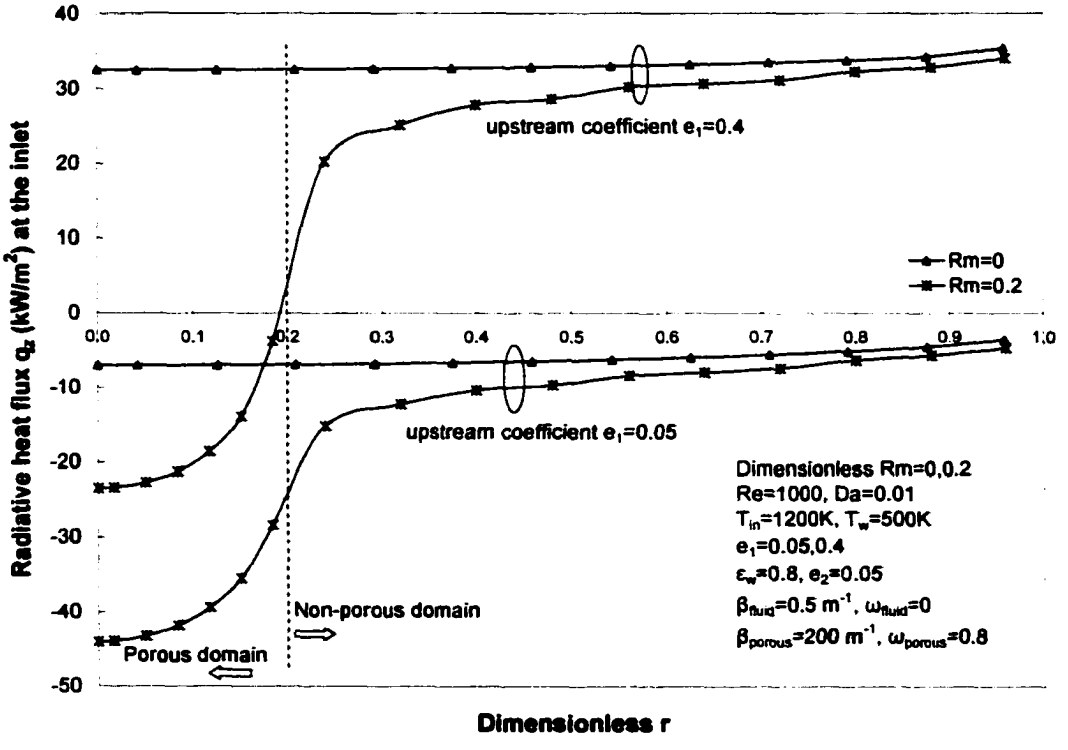

Figure 4-38 The distributions of net flux component q_z at the inlet at different upstream incident radiation conditions.

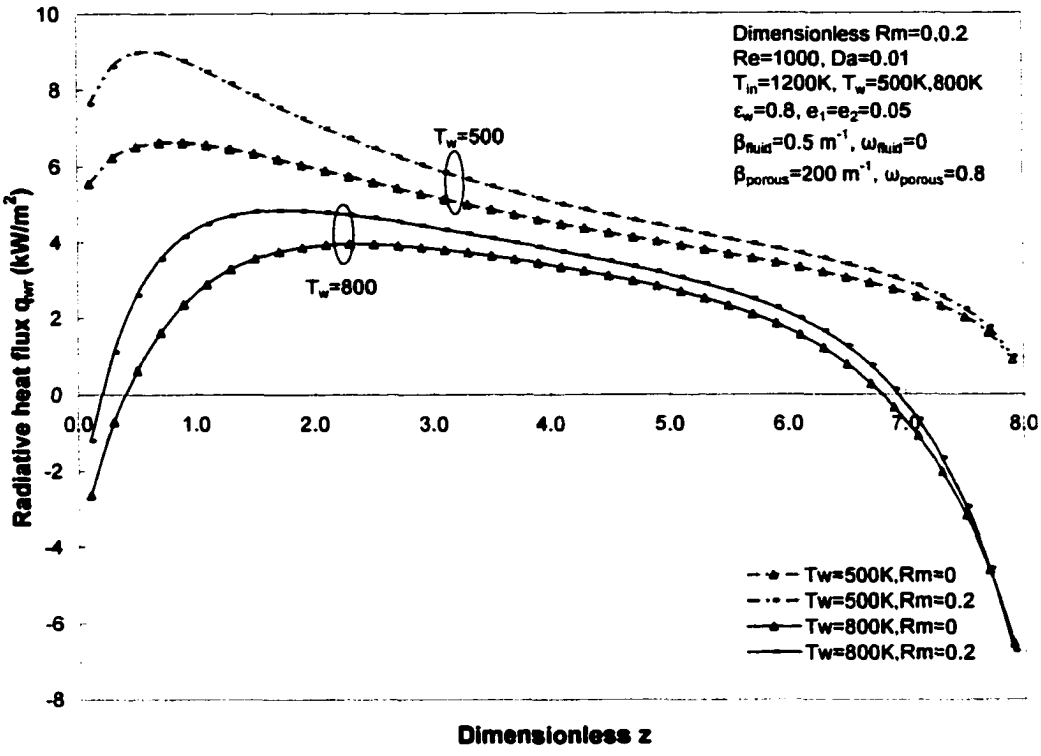

Figure 4-39 The distributions of radiative heat flux at the wall for T_w=500K and 800K.

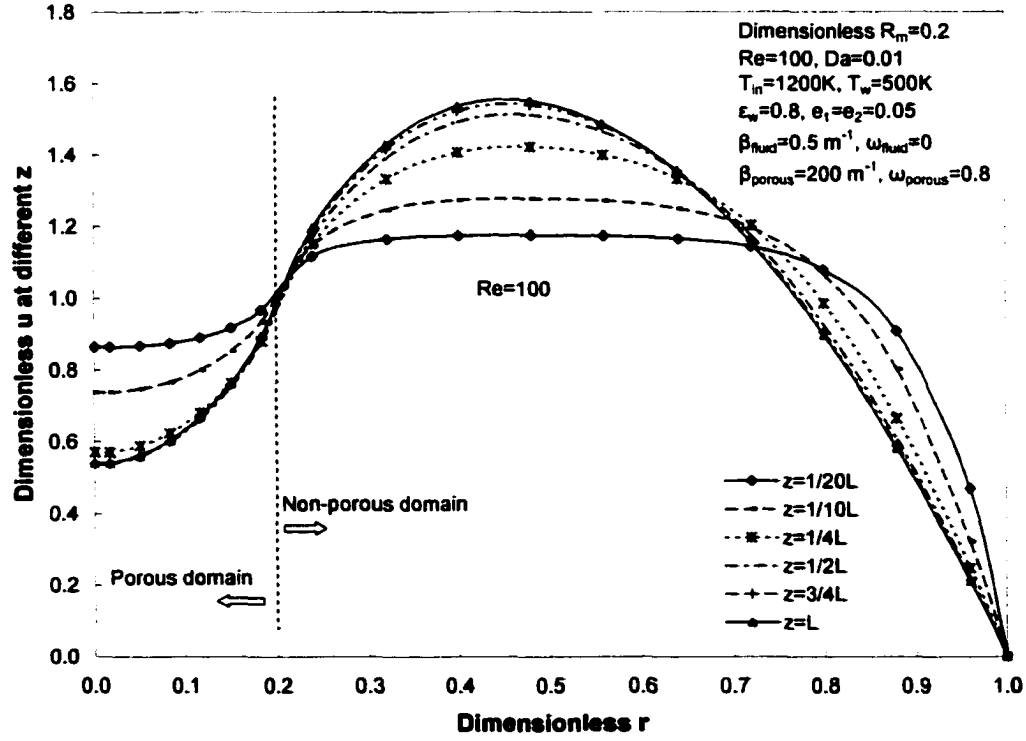

Figure 4-40 The velocity developing profiles for in-pipe flow with the porous insert R_m=0.2(dimensionless) and Re=100.

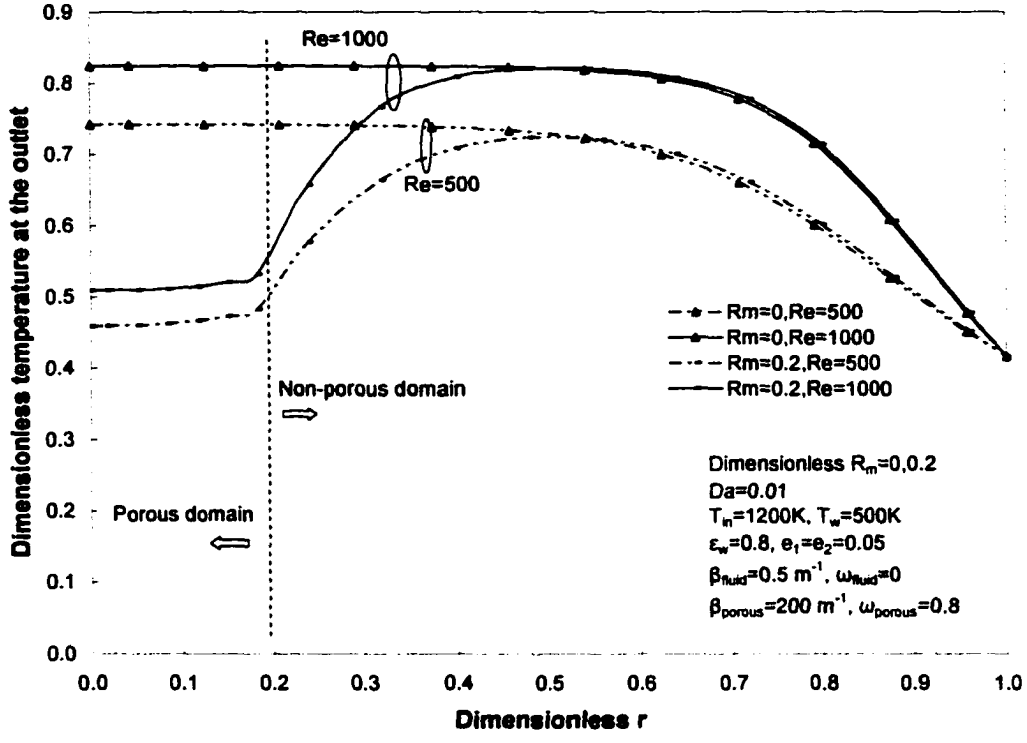

Figure 4-41 The comparison of outlet temperature at different Reynolds numbers.

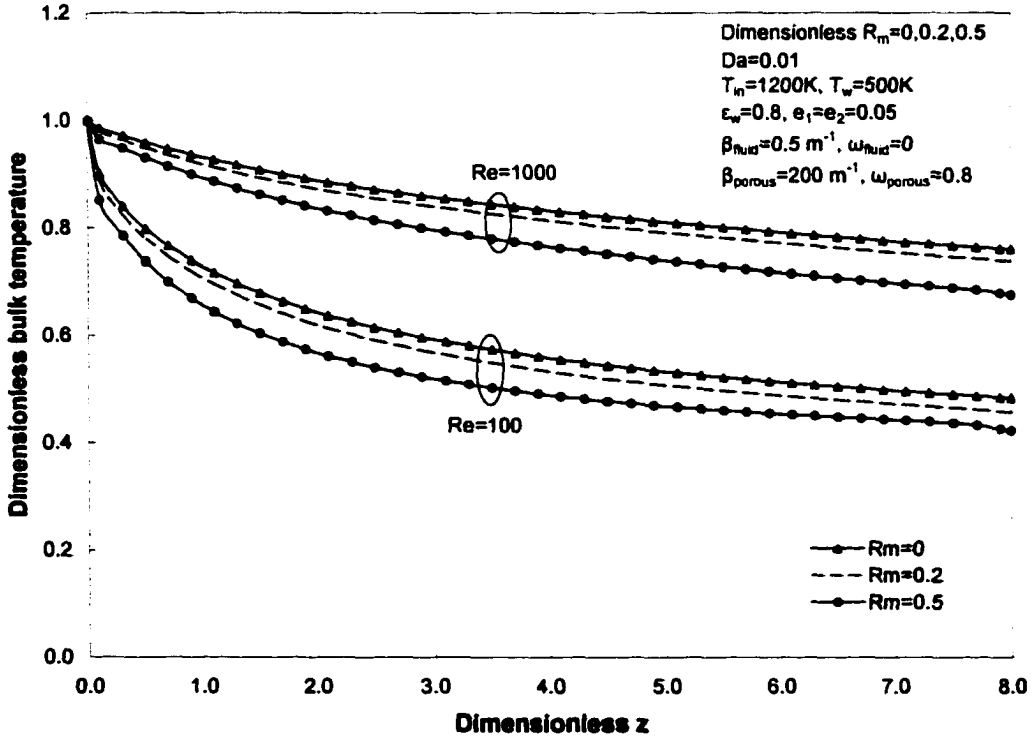

Figure 4-42 The distributions of bulk mean temperature at different Reynolds numbers.

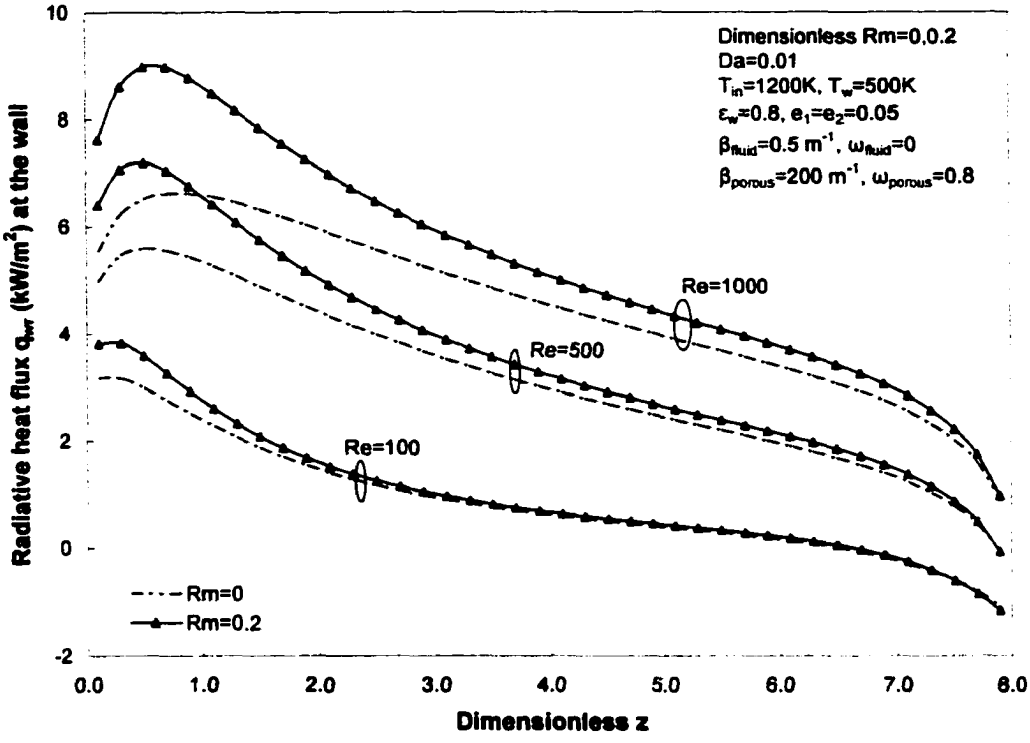

Figure 4-43 The comparison of the enhancement of radiative heat flux by the porous insert at different Reynolds numbers.

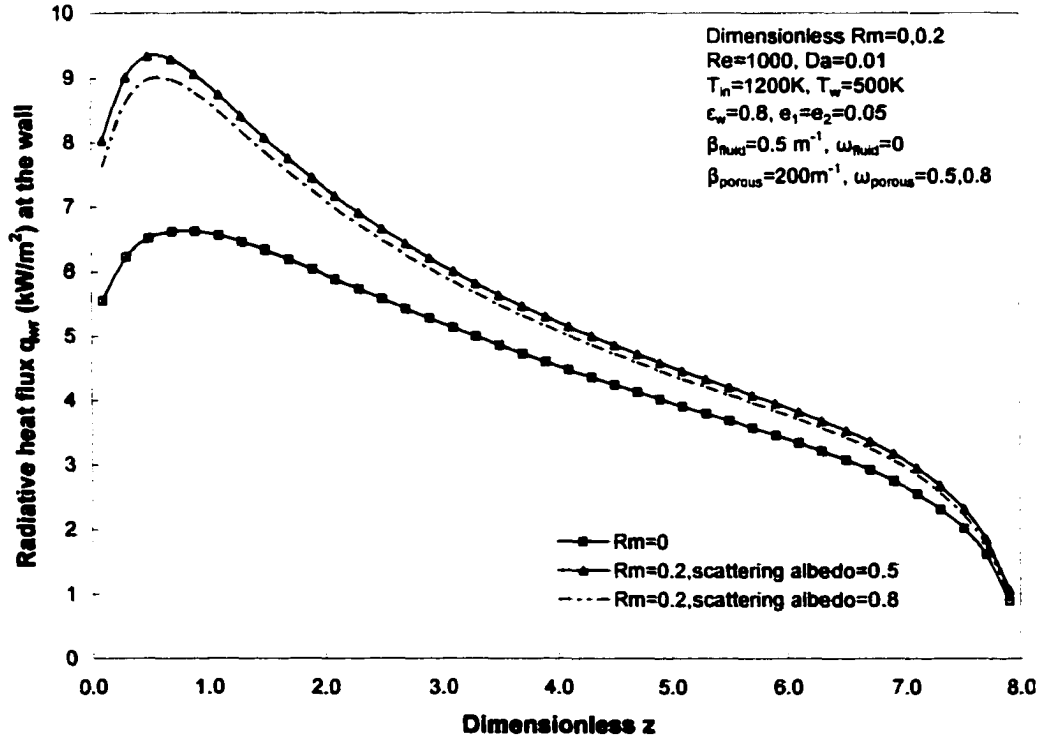

Figure 4-44 The distributions of radiative heat flux at the wall under different porous scattering albedo conditions.

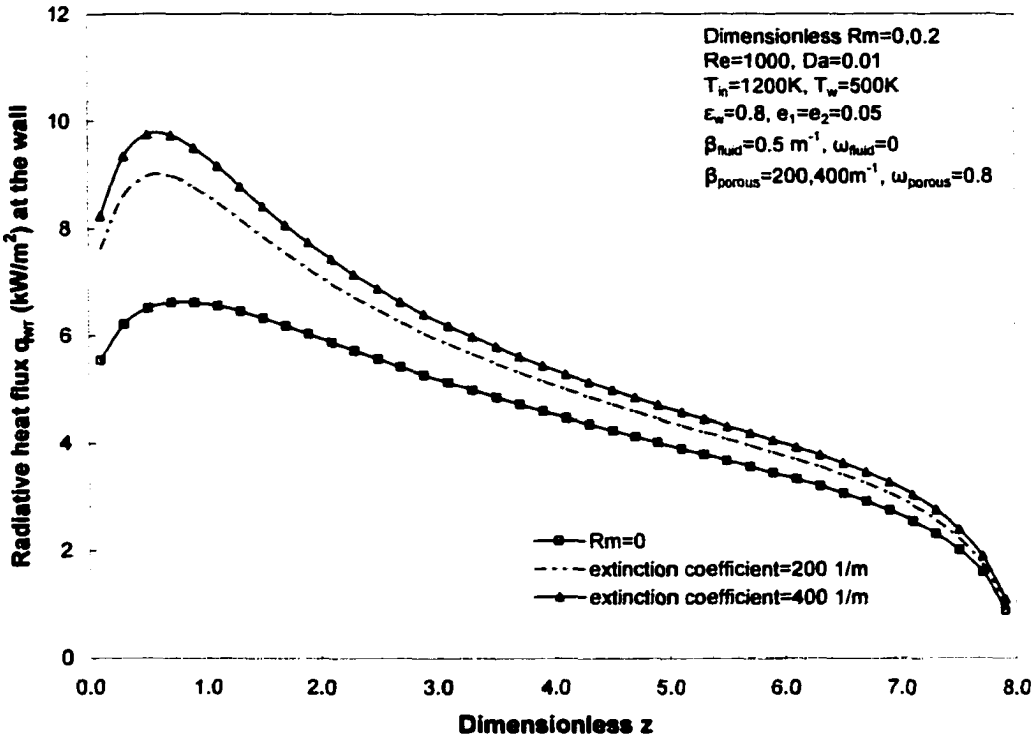

Figure 4-45 The distributions of radiative heat flux at the wall under different porous extinction coefficients.

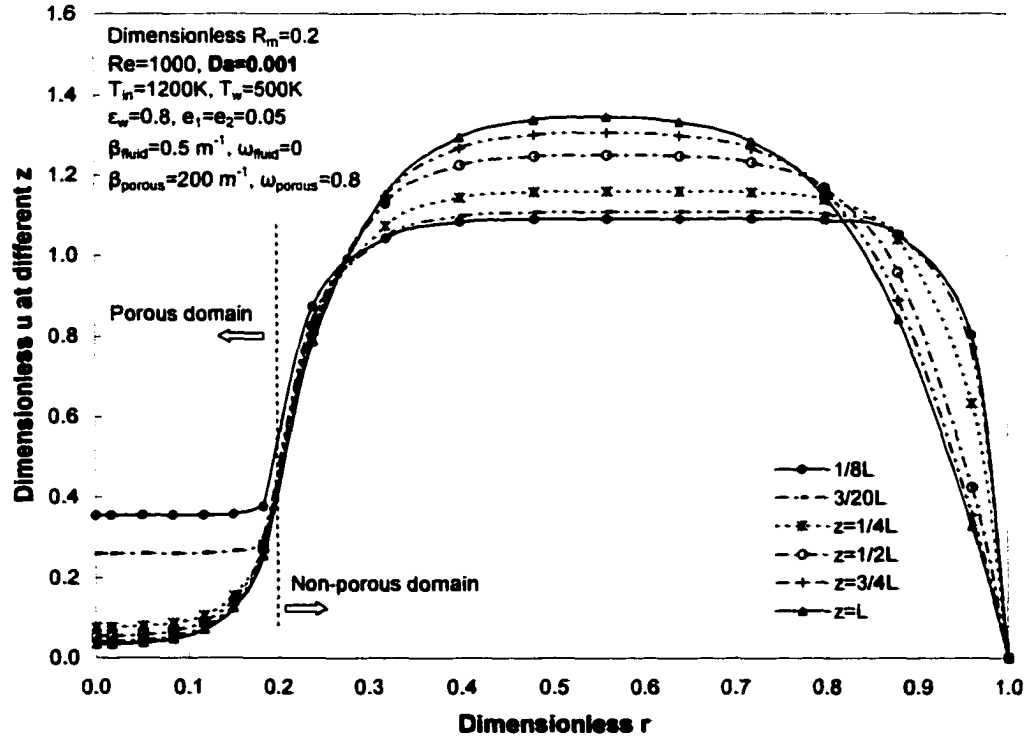

Figure 4-46 The velocity developing profiles for in-pipe flow with the porous insert R_m=0.2(dimensionless) and Da=0.001.

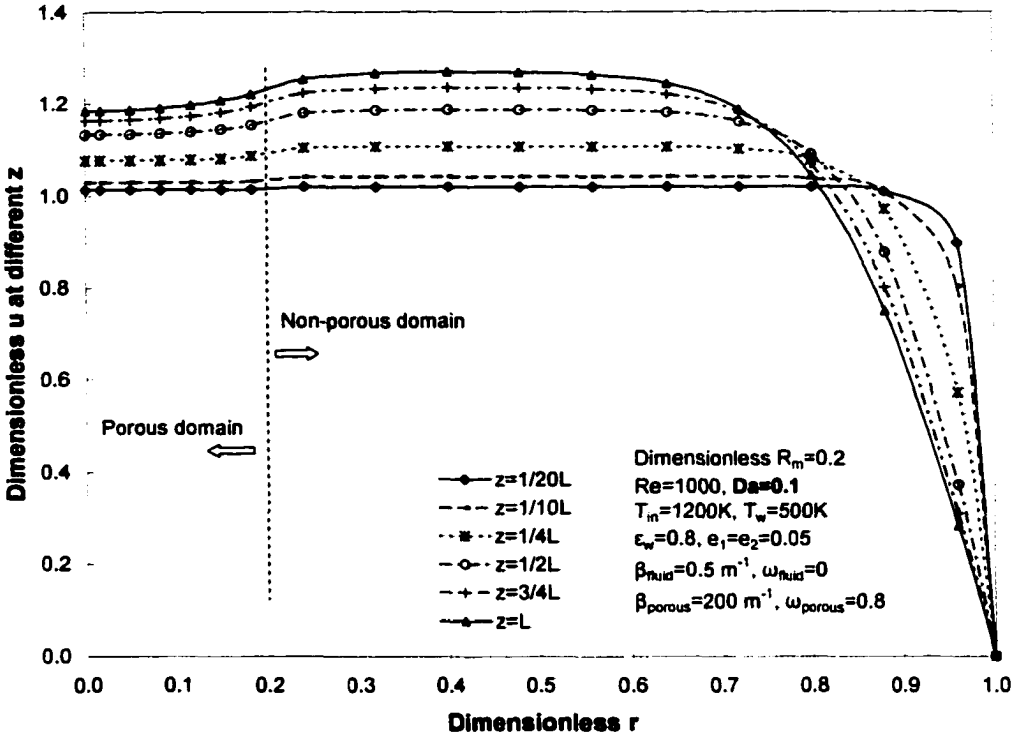

Figure 4-47 The velocity developing profiles for in-pipe flow with the porous insert R_m=0.2(dimensionless) and Da=0.1.

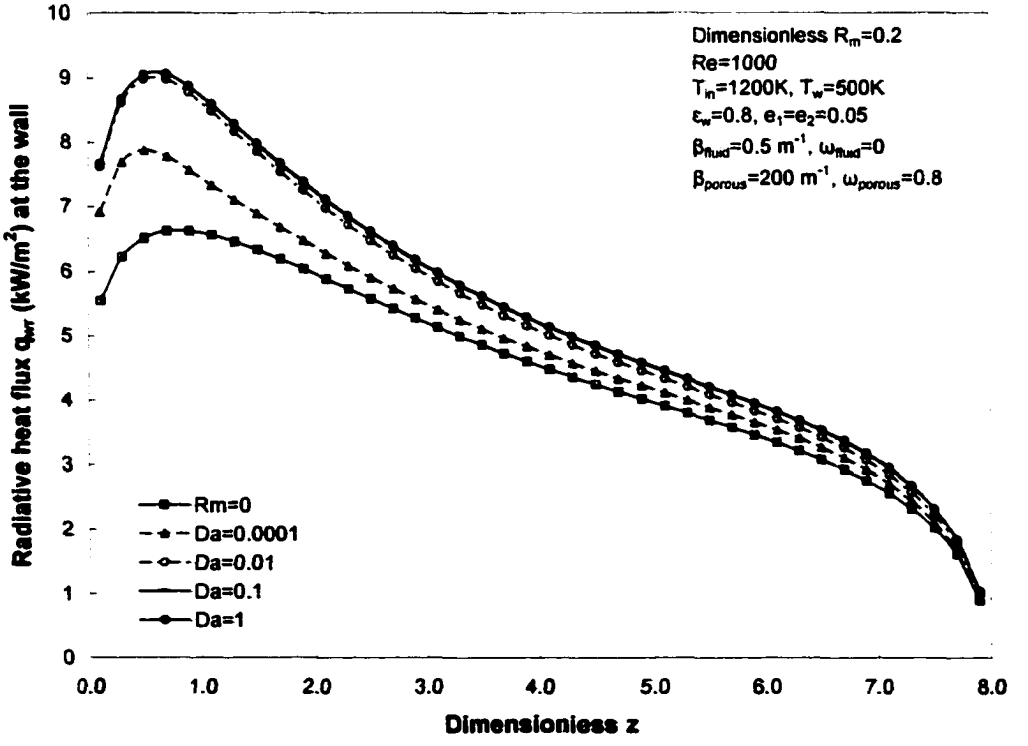

Figure 4-48 The distributions of radiative heat flux at different Darcy numbers.

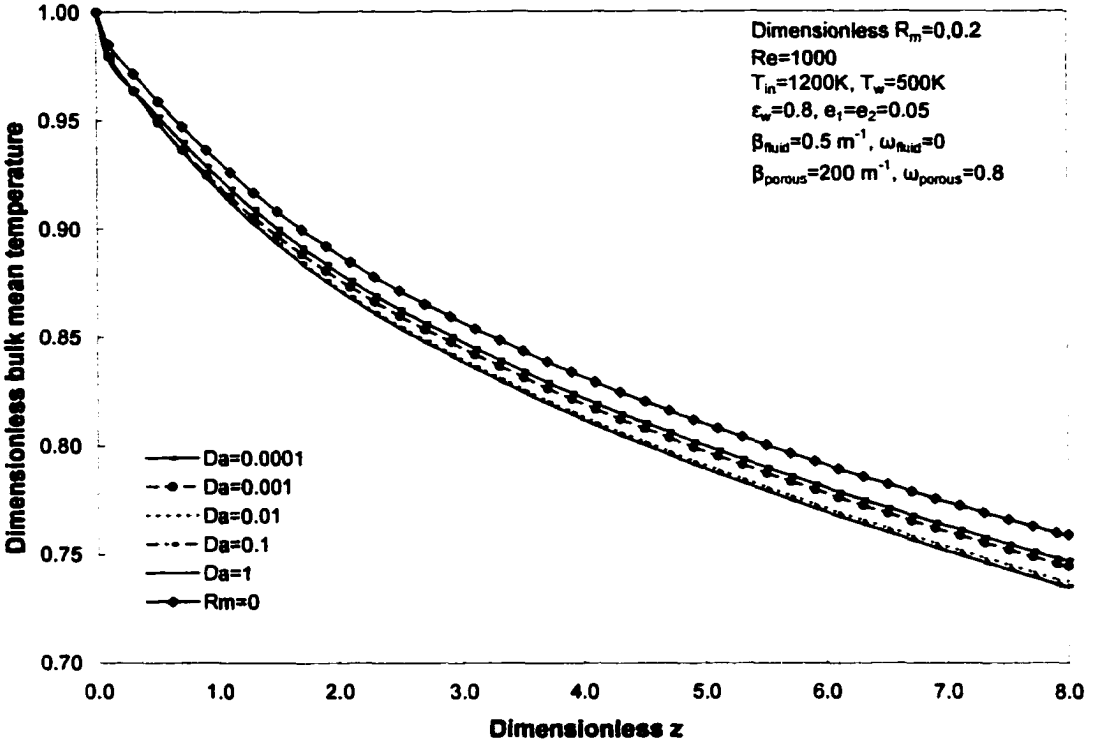

Figure 4-49 The distributions of bulk mean temperature at different Darcy numbers.

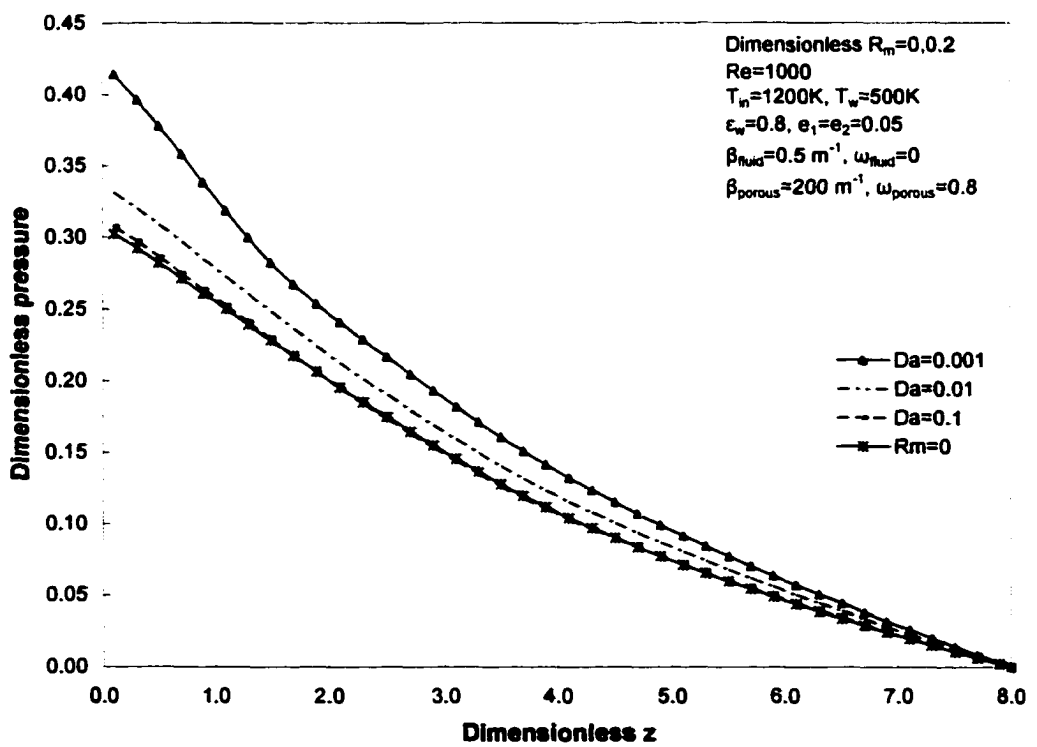

Figure 4-50 The distributions of relative pressure at different Darcy numbers.

4.7 References:

[4.1] Y. Mori, T. Taira and K. Watanabe, Heat exchanger augmentation by radiation plates, ASME Paper No. 76-HT-3, Proceedings of the ASME-AIChE National Heat Transfer Conference, St. Louis, Missouri (August 1976).

[4.2] Y. Yamada, M. Akai, and Y. Mori, Shell-and-tube side heat transfer augmentation by the use of wall radiation in a cross flow shell-and-tube heat exchanger, J. of heat transfer, Nov. 1984.

[4.3] M. Hirano, T. Miyauchi and Y. Takahira, Enhancement of radiative heat transfer in the laminar channel flow of non-gray gases, Int. J. Heat Mass Transfer 1988, Vol. 31, No. 2, pp. 367-374.

[4.4] H. Y. Zhang and M. A. Ebadian, Convective-radiative heat transfer in the thermal entrance region of the semicircular duct with streamwise internal fins, Int. J. Heat Mass Transfer 1991, Vol. 34, No. 12, pp. 3135-3142.

[4.5] R. Echigo, Effective energy conversion method between gas enthalpy and thermal radiation and application to industry furnaces, Proceedings of the 7th International Heat Transfer Conference, Sep. 1982, Munich, Vol. 6, pp. 361-366.

[4.6] J. M. Zhang, W. H. Sutton, and F. C. Lai, Enhancement of heat transfer using porous convection-to-radiation converter for laminar flow in a circular duct, Int. J. Heat Mass Transfer 1997, Vol. 40, No. 1, pp. 39-48.

[4.7] X. L. Chen and W. Sutton, Radiative transfer in finite cylindrical media using transformed integral equations, accepted for publication by J. Quant. Spectrosc. Radiat. Transfer.

[4.8] W. Sutton and X. L. Chen, A general integration method for radiative transfer in 3-D non-homogeneous cylindrical media with anisotropic scattering, submitted for publication to J. Quant. Spectrosc. Radiat. Transfer.

[4.9] M. N. Ozisik. Radiative transfer and interactions with conduction and convection. Wiley, New York, NY (1973).

[4.10] S. V. Patankar, Numerical heat transfer and fluid flow, Hemisphere Publishing Corporation, Washington New York London, 1980.

[4.11] W. M. Kays, Numerical solutions for laminar-flow heat transfer in circular tubes, Trans. ASME, 1955, Vol. 77, pp. 1265-1274.

[4.12] D. L. Ulrichson and R. A. Schmitz, Laminar-flow heat transfer in the entrance region of circular tubes, Int. J. Heat Mass Transfer 1965, Vol. 8, pp. 253-258.

[4.13] S. Kakac and Y. Yener, Convective heat transfer, Boca Raton, Fla. CRC Press, 1995.

[4.14] H. L. Langhaar, Steady flow in the transition length of a straight tube, J. Appl. Mech., Trans. ASME, 1942, Vol. 9, pp. 4-55.

[4.15] R. Manohar, Analysis of laminar-flow heat transfer in the entrance region of circular tubes, Int. J. Heat Mass Transfer 1969, Vol. 12, pp. 15-22.

[4.16] A. Weinert and J. L. Lage, Porous aluminum-alloy based cooling devices for electronics, SMU-MED-CPMA Inter. Rep. 1.01/94, Southern Methodist University, Dallas, TX. [1.5.3]

[4.17] M. Kaviany, Principles of heat transfer in porous media, *Mechanical engineering series*, 1991 Springer-Verlag New York Inc.

[4.18] J. G. Hoffmann, R. Echigo, H. Yoshida, and S. Tada, Experimental study on combustion in porous media with a reciprocating flow system, Combustion and Flame (1997), 111: 32-46.

[4.19] K. Kamiuto, M. Sato, and M. Iwamoto, Determination of the radiative properties of high-porosity materials by use of the emerging-intensity fitting method, J. Quant. Spectrosc. Radiat. Transfer 1989, Vol. 42, No. 6, pp 477-482.

[4.20] M. K. Alkam and M. A. Al-nimr, Transient non-Darcian forced convection flow in a pipe partially filled with a porous material, Int. J. Heat Mass Transfer 1998, Vol. 41, No. 2, pp. 347-356.

4.8 Appendix C

Cosine Equations

Based on the geometric relations [4.7], the cosines of the angle between the surface normal vector and the intensity direction $\hat{\Omega}$ are given as follows:

$$\cos\theta_1 = \cos(\hat{n}_1, \hat{\Omega}) = \frac{z}{\left[r^2 + r_1^2 - 2rr_1\cos(\phi - \phi_1) + z^2\right]^{1/2}}, \tag{C1}$$

$$\cos\theta_2 = \cos(\hat{n}_2, \hat{\Omega}) = \frac{L - z}{\left[r^2 + r_2^2 - 2rr_2\cos(\phi - \phi_2) + (L - z)^2\right]^{1/2}}, \tag{C2}$$

$$\cos\theta_3 = \cos(\hat{n}_3, \hat{\Omega}) = \frac{R_{out} - r\cos(\phi - \phi_3)}{\left[r^2 + R_{out}^2 - 2rR_{out}\cos(\phi - \phi_3) + (z_3 - z)^2\right]^{1/2}}. \tag{C3}$$

The intensity in the direction of $\hat{\Omega}$ starting from point $s_i(z_i,r_i,\phi_i)$ on the boundary surface i (i=1,2,3) to point $s(z,r,\phi)$, yields the following direction cosines.

$$\cos(\hat{e}_z, \hat{\Omega}) = \frac{z - z_i}{\left[r^2 + r_i^2 - 2rr_i\cos(\phi - \phi_i) + (z - z_i)^2\right]^{1/2}}, \tag{C4}$$

$$\cos(\hat{e}_r, \hat{\Omega}) = \frac{r - r_i\cos(\phi - \phi_i)}{\left[r^2 + r_i^2 - 2rr_i\cos(\phi - \phi\ ) + (z - z_i)^2\right]^{1/2}}, \tag{C5}$$

$$\cos(\hat{e}_\phi, \hat{\Omega}) = \frac{r_i\sin(\phi - \phi_i)}{\left[r^2 + r_i^2 - 2rr_i\cos(\phi - \phi_i) + (z - z_i)^2\right]^{1/2}}. \tag{C6}$$

For axisymmetric 2-D problem, ϕ equal zero in above equations and equation (C6) is not required.

Coordinate Transformation Relations

There are following geometric relations for coordinate transformation:

$$dA_1 = dA_2 = \gamma \cdot d\chi \cdot d\gamma \tag{C7}$$

$$dA_3 = \left[\frac{\gamma_R}{\cos(\chi - \phi_3 + \phi)} d\chi\right] \cdot \left(\gamma_R \sec^2 \alpha \cdot d\alpha\right) \tag{C8}$$

$$\bar{d}(s_i, s) = \gamma \cdot \sec\alpha \qquad (i=1,2) \tag{C9}$$

$$\bar{d}(s_3, s) = \gamma_R \cdot \sec\alpha \tag{C10}$$

$$\bar{z} = -\gamma \cdot \tan\alpha_1, \qquad \bar{L} - \bar{z} = \gamma \cdot \tan\alpha_2 \tag{C11}$$

$$\bar{R}_{out} - \bar{r}\cos(\phi - \phi_3) = \gamma_R \cos(\chi - \phi_3 + \phi) \tag{C12}$$

$$\bar{r} - \bar{r}_i \cos(\phi - \phi_i) = \gamma(-\cos\chi) \qquad (i=1,2) \tag{C13}$$

$$\bar{r} - \bar{R}_{out} \cos(\phi - \phi_3) = \gamma_R(-\cos\chi) \tag{C14}$$

$$\bar{z}_3 - \bar{z} = \gamma_R \cdot \tan\alpha \tag{C15}$$

where let $\phi = 0$ for 2-D problem, point $S(\bar{r}, \phi)$ will becomes $S(\bar{r}, 0)$ in Figure 4-7.